

**ZIRCONIA-YTTRIA-ALUMINO SILICATE GLASS-BASED
ERBIUM-DOPED FIBRES AS A MEDIUM FOR Q-SWITCHED
AND MODE-LOCKED PULSE GENERATION**

KAVINTHERAN A/L THAMBIRATNAM

**THESIS SUBMITTED IN FULFILLMENT OF THE
REQUIREMENTS FOR THE DEGREE OF
DOCTOR OF PHILOSOPHY**

**DEPARTMENT OF PHYSICS
FACULTY OF SCIENCE
UNIVERSITY OF MALAYA
KUALA LUMPUR**

2014

ORIGINAL LITERARY WORK DECLARATION

Name of Candidate: **KAVINTHERAN A/L THAMBIRATNAM**

I/C/Passport No: **830408-14-6007**

Registration/Matric No.: **SHC100104**

Name of Degree: **DOCTOR OF PHILOSOPHY**

Title of Project Paper/Research Report/Dissertation/Thesis ("this Work"):

"ZIRCONIA-YTTRIA-ALUMINO SILICATE GLASS-BASED ERBIUM-DOPED FIBRES AS A MEDIUM FOR Q-SWITCHED AND MODE-LOCKED PULSE GENERATION"

Field of Study: **FIBER OPTIC**

I do solemnly and sincerely declare that:

- (1) I am the sole author/writer of this Work,
- (2) This Work is original,
- (3) Any use of any work in which copyright exists was done by way of fair dealing and for permitted purposes and any excerpt or extract from, or reference to or reproduction of any copyright work has been disclosed expressly and sufficiently and the title of the Work and its authorship have been acknowledged in this Work,
- (4) I do not have any actual knowledge nor do I ought reasonably to know that the making of this work constitutes an infringement of any copyright work,
- (5) I hereby assign all and every rights in the copyright to this Work to the University of Malaya ("UM"), who henceforth shall be owner of the copyright in this Work and that any reproduction or use in any form or by any means whatsoever is prohibited without the written consent of UM having been first had and obtained,
- (6) I am fully aware that if in the course of making this Work I have infringed any copyright whether intentionally or otherwise, I may be subject to legal action or any other action as may be determined by UM.

(Candidate Signature)

Date:

Subscribed and solemnly declared before,

Witness's Signature

Date:

Name **PROFESSOR DR HARITH AHMAD**

Designation

Witness's Signature

Date:

Name **PROFESSOR DR SULAIMAN WADI HARUN**

Designation

ABSTRACT

In this research, the fabrication and characterization of zirconia–yttria–alumino silicate glass-based erbium-doped fibres as well as their application as the gain media for compact fast and ultra-fast pulsed sources is presented.

The fabrication process is similar to that of a conventional erbium doped fibre, with the ZrO_2 co-dopants incorporated into the silica host during solution doping. Morphological studies of the drawn fibres reveal a core with a diameter of approximately 10 μm . Tunneling electron microscope scanning shows the presence of ZrO_2 rich micro-crystallites, while X-ray diffraction analysis indicates the formation of tetragonal ZrO_2 structures. Spectral characterization of the fibres show attenuation peaks at 980 nm and 1550 nm, with sample designated ZEr-B having absorption rates of 22.0 dB/m and 53.0 dB/m at 980 and 1550 nm respectively as well as a fluorescence life-time of 10.86 ms, as well as a W-profile refractive index.

A 3 m long ZEr-B fiber with a dopant concentration of about 3880 ppm/wt is used to generate an amplified spontaneous emission spectrum. The fibres amplified spontaneous emission spectrum output differs substantially from that of a conventional erbium doped fibre of the same length, rising to a peak region at 1530 nm, followed by a short ‘plateau’ before decreasing. As a fibre amplifier a gain of around 28.0 dB near 1530 nm and a relatively flat gain of between 22.0 to 25.0 dB at the plateau region is obtained, together with a noise figure of approximately 14.1 dB for an input signal of -30 dBm. The fiber can also generate a single-longitudinal mode output, ranging from 1533.8 nm to 1545.0 nm at output powers of more than -8.9 dBm with an average signal-to-noise ratio of more than 50 dB. Additionally, the fiber allows non-linear interactions to occur at lower signal intensities than normal, with a four-wave-mixing output adhering to theoretically predicted models. The average four-wave-mixing power level is -45 dBm at approximately 1565 nm, with a non-linear coefficient of $14 \text{ W}^{-1}\text{km}^{-1}$ with chromatic and dispersion slopes of 28.45 ps/nm.km and 3.63 ps/nm².km.

The erbium-doped zirconia fiber is also used in conjunction with graphene and single-walled carbon nanotubes based passive saturable absorbers to generate fast and ultrafast pulses is examined. Using a 3 m long ZEr-B with single-walled carbon nanotubes suspended in a polymer host generates Q-switched pulses with a repetition rate of 14.20 kHz and corresponding pulse width of 8.6 μs at a maximum pump power of 141.8 mW, as well as an

average pulses output power of 270.0 μW and maximum pulse energy of 19.02 nJ. Using the graphene based saturable absorber gives a 50.1 kHz pulse train with a pulse width, energy and peak power of 4.6 μs , 16.8 nJ and 3.6 mW respectively. When mode-locked, the ZEr-B combined with the graphene based saturable absorber generates ultrafast pulses with an average output power, pulse energy and peak power of approximately 1.6 mW, 23.1 pJ and 31.6 W respectively as well as a pulse width of 730 fs and repetition rate of the pulses is 69.3 MHz. Using the single-walled carbon nanotubes composite as a saturable absorber gives mode-locked pulses with a repetition rate and peak power of 17.74 MHz and 14.09 W as well as average output power of 180 μW and pulse duration of approximately 720 fs at the full-width at half maximum point, with a pulse energy of 0.01 nJ. The generated pulses are stable and consistent, and allow them to be deployed with a high degree of confidence and reliability in multiple practical applications.

ABSTRAK

Di dalam penyelidikan ini, pembuatan dan pencirian gentian berdopan erbium berasaskan gelas zirconia–yttria–alumino silicate serta aplikasinya sebagai bahan aktif bagi sumber berdenyut cepat dan ultra-cepat yang padat dibentangkan.

Proses pembuatan gentian ini adalah hampir sama seperti gentian berdopan erbium yang lazim, dengan penggabungan dopan ZrO_2 ke dalam gentian silica semasa process pendopan cecair. Analisa morfologi bagi gentian yang ditarik menunjukkan bahagian teras dengan diameter sebanyak 10 μm . Analisa ‘Tunneling Electron Microscope Scanning’ menunjukkan kehadiran struktur kristal mikro yang kaya dalam ZrO_2 manakala analisa penuraian X-Ray mengesahkan pembentukan struktur ZrO_2 berbentuk tetragon. Pencirian spectra gentian yang ditarik menunjukkan puncak pelemahan pada 980 nm dan 1550 nm, dengan sampel ZEr-B mempunyai kadar penyerapan sebanyak 22.0 dB/m dan 53.0 dB/m pada 980 dan 1550 nm serta jangkamasa pendaflour selama 10.86 ms dan indeks biasan berprofil-W yang biasa.

Gentian ZEr-B sepanjang 3 m dengan ketumpatan dopan sebanyak 3880 ppm/wt digunakan untuk menghasilkan spektra amplified spontaneous emission. Spektra yang diperolehi daripada adalah amat berbeza daripada gentian berdopan erbium biasa, dengan puncak pada 1530 nm disertai bahagian datar yang pendek sebelum berkurang. Apabila digunakan sebagai pembesar optik, gentian EDZF berkebolehan untuk memberi penambahan sebanyak 28.0 dB di rantau 1530 nm, dengan penambahan yang agak malar di antara 22.0 hingga 25.0 dB di rantau mendatar, serta nilai hingar sebanyak 14.1 dB bagi isyarat masuk setinggi -30 dBm. ZEr-B juga dapat menghasilkan output jenis single-longitudinal mode daripada 1533.8 nm hingga 1545.0 nm diperolehi pada kuasa -8.9 dBm dan nisbah isyarat kepada hingar yang lebih daripada 50 dB. Di samping itu, ZEr-B juga membolehkan interaksi tidak linear berlaku pada kuasa isyarat yang rendah, dengan penjanaan fenomena four-wave-mixing seperti yang dijangkakan dalam teori. Kuasa purata four-wave-mixing adalah sebanyak -45 dBm pada 1565 nm, dengan nilai pemalar tidak linear yang sebanyak $14 \text{ W}^{-1}\text{km}^{-1}$ serta cerun kromatik dan penguraian sebanyak 28.45 ps/nm.km dan 3.63 ps/nm².km..

ZEr-B juga digunakan bersama graphene dan single-walled carbon nanotubes sebagai saturable absorber yang pasif bagi menjana denyutan yang cepat dan ultra-cepat. Menggunakan ZEr-B sepanjang 3 m dan single-walled carbon nanotubes yang diampai

dalam polimer dapat menghasilkan denyutan Q-switched dengan kadar pengulangan 14.20 kHz serta lebar denyutan sepanjang 8.6 μ s pada kuasa pam makisma sebanyak 141.8 mW, pada kuasa purata sebanyak 270.0 μ W, dengan tenaga denyutan sebanyak 19.02 nJ. Penggunaan saturable absorber berasaskan graphene memberikan kadar denyutan sebanyak 50.1 kHz serta lebar denyutan, tenaga denyutan dan kuasa puncak denyutan sebanyak 4.6 μ s, 16.8 nJ dan 3.6 mW. Apabila mode-locked, ZEr-B bersama saturable absorber berasaskan graphene memberikan kuasa output purata, tenaga denyutan dan kuasa puncak sebanyak 1.6 mW, 23.1 pJ dan 31.6 W serta lebar denyutan sebanyak 730 fs and pada kadar denyutan 69.3 MHz. Menggunakan saturable absorber jenis single-walled carbon nanotubes memberikan denyutan mode-locked dengan kadar denyutan dan kuasa puncak sebanyak 17.74 MHz dan 14.09 W pada kuasa purata sebanyak 180 μ W dan masa denyutan 720 fs pada full-width at half maximum serta tenaga denyutan sebanyak 0.01 nJ. Denyutan yang dihasilkan adalah stabil dengan kuasa yang malar, dan ini membolehkannya digunakan dengan kadar keyakinan yang tinggi serta dapat diharapkan dalam pelbagai aplikasi yang praktik.

ACKNOWLEDGEMENTS

First and foremost, I must convey my sincerest and most heartfelt appreciation and gratitude to my supervisor, Prof Dr. Harith Ahmad. He guided me, encouraged me and imparted his knowledge and wisdom to me. He thought me not only the value and worth of research, but also the importance of doing one's best and persevering through all odds until the finish line. I must also take this opportunity to acknowledge my other supervisor for his silent support and counsel, Prof. Dr. Sulaiman Wadi Harun. In addition, I would also like to thank Dr. Mukul Chandra Paul for his significant contribution and help, especially in Chapter 2, the fabrication of the Zirconia–Yttria–Alumino Silicate Glass-Based Erbium-Doped Fibres, as well as its characterization. I thank my colleagues, Ahmad Zarif Zulkifli and especially Noor Azura Awang, for her assistance in measuring the non-linear parameters of the optical fibres and I also thank my family, V Thambiratnam a/l V. V. Ratnam, Padmadevi a/p Navaratnam and Paavitha a/p Thambiratnam for their patience and support.

I would also like to take this opportunity to thank the Photonics Research Centre, University of Malaya for their generous funding that enabled me to complete this thesis within the stipulated time-frame.

Contents

Abstract	3
Abstrak	5
Acknowledgements	7
List of Figures	11
List of Tables	19
List of Abbreviations.....	20
1. Introduction	23
1.1 Introduction.....	23
1.2 In-Line Optical Amplification.....	24
1.3 The Impetus for the Development of Zirconia–Yttria–Alumino Silicate Glass- Based Erbium-Doped Fibres.....	27
1.4 Fast and Ultrafast Pulsed Fibre Lasers	29
1.5 Objective and Scope of Work	30
1.6 Thesis Overview.....	32
2. Fabrication and Characterization of Zirconia–Yttria–Alumino Silicate Glass-based Erbium-doped Fibres	34
2.1 Introduction.....	34
2.2 Fabrication of the EDZF.....	35
2.2.1 Pre-Fabrication: Selection and Preparation of Host Material	36
2.2.2 The MCVD Process.....	42
2.2.3 Solution Doping	48
2.2.4 Oxidation, Dehydration and Sintering.....	50
2.2.5 Collapsing of the Preform.....	51
2.2.6 Drawing of the Optical Fibre	52
2.3 Characterization of the EDZFs.....	56
2.3.1 Morphological and Physical Analysis of the EDZF.....	56

2.3.2	Spectral Measurement and Characterization of the EDZF	61
2.3.3	Measurement of Refractive Index Profile.....	66
2.4	Summary and Conclusion.....	68
3.	Zirconia–Yttria–Alumino Silicate Glass-based Erbium-doped Fibre as an Amplifier, Laser and Non-Linear Gain Medium.....	71
3.1	Introduction.....	71
3.2	EDFA Theory.....	71
3.2.1	Characteristics of Er^{3+} ions in a Silica Glass Matrix.....	72
3.2.2	Energy Levels of Er^{3+} Ions in Silica Host Matrix	74
3.2.3	Er^{3+} Rate Equations	76
3.2.4	Absorption and Emission Cross Sections	82
3.2.5	ASE.....	84
3.2.6	Signal Gain.....	86
3.2.7	NF.....	88
3.3	The EDZF as a Fibre Amplifier, Fibre Laser and Non-Linear Medium	91
3.3.1	ASE Characteristics of the EDZF	92
3.3.2	Gain and NF Characteristics of the EDZF.....	106
3.3.3	The EDZF as an SLM Fibre Laser	110
3.3.4	The EDZF as a Non-Linear Gain Medium	119
3.4	Summary and Conclusion.....	131
4.	Generation of Fast and Ultra-Fast Pulses using Passive Saturable Absorbers and the Zirconia–Yttria–Alumino Silicate Glass-based Erbium-doped Fibre	134
4.1	Introduction.....	134
4.2	Pulse Generation in Fibre Lasers	135
4.2.1	Q-Switched Fibre Lasers	136
4.2.2	Mode-Locked Fibre Lasers.....	141
4.3	Saturable Absorbers.....	144
4.3.1	Graphene as a Passive Saturable Absorber.....	149

4.3.2	Carbon Nanotubes as a Passive Saturable Absorber	156
4.4	The EDZF as an Passively Pulsed Fibre Laser	160
4.4.1	The EDZF as a Passively Q-Switched Fibre Laser	160
4.4.2	The EDZF as a Passively Mode-Locked Fibre Laser.....	172
4.5	Conclusion	180
5.	Summary and Conclusion	183
5.1	Introduction.....	183
5.2	Summary.....	183
5.2.1	Revisiting the EDZF Fabrication Process.....	184
5.2.2	Examining the Behavior of the Active Ions in the EDZF when Exposed to Pump Wavelengths.....	186
5.2.3	Employing the EDZF as a Gain Medium for Compact Fast and Ultrafast Pulse Lasers using Graphene and SWCNT based Saturable Absorbers.....	188
5.3	Conclusion	191
References	192
Appendix 1	206
Appendix 2	207

LIST OF FIGURES

Figure 1: Typical transmission bands in optical fibres	26
Figure 2: Tetrahedron structure of SiO_2 , which has 4 oxygen ions connected to a single silicon ion. The solid lines represent the O^{2-} to O^{2-} bonds, while the dashed lines represent bonds between the Si^{4+} and O^{2-} ions.	37
Figure 3: Viscosity of oxide glasses with glass transition (T_g) and softening (T_s) temperature	38
Figure 4: Effect of common dopants on refractive index of the silica host.	39
Figure 5: The relationship between the dopant concentrations and the ZDW of the silica host	41
Figure 6: Vapor pressure of different source chemicals against temperature	44
Figure 7: MCVD system setup, with glass working lathe	45
Figure 8: Deposition efficiency GeO_2 against tube temperature	47
Figure 9: Particle trajectories in silica substrate tube.	48
Figure 10: Collapsed substrate tube after deposition	52
Figure 11: Fibre drawing tower configuration, with dual-coating cups.	53
Figure 12: Summarized process flowchart for EDZF fabrication	55
Figure 13: ZEr-A (<i>above left</i>) and ZEr-B (<i>above right</i>) (<i>both highlighted by the red boxes</i>) sample fibres as seen without any magnification. Due to the fibres being very thin, they are not easily visible, even when placed on a contrasting background. As such, the red box is used to highlight the fibres in the figures above.	56
Figure 14: View of the surface of the two EDZFs (ZEr-A, <i>above left</i> , and ZEr-B, <i>above right</i>) under 200x magnification.	57

Figure 15: The microstructure of the core region of optical fibre preforms ZEr-A (<i>above left</i>) and ZEr-B (<i>above right</i>).	58
Figure 16: TEM spectroscopic analysis of ZEr-B.	59
Figure 17: XRD curve obtained for ZEr-B preform, with small diffraction peak at 2θ of $\sim 30^\circ$.	59
Figure 18: Phase-diagram of $\text{SiO}_2\text{-ZrO}_2$ system obtained using the Fact-Sage software	60
Figure 19: Setup of the Bentham spectral attenuation measurement system	62
Figure 20: Spectral attenuation curve of ZEr-A (<i>above, left</i>) and ZEr-B (<i>above, right</i>)	64
Figure 21: Fluorescence curves of the (a) ZEr-A and (b) ZEr-B fibres at a pump power level of 100 mW.	65
Figure 22: The fluorescence decay curves of the (a) ZEr-A and (b) ZEr-B fibres at a pump power level of 100 mW.	65
Figure 23: Schematic diagram of refracted near field set up	67
Figure 24: Refractive index profile of the EDZF. The profile given above is that of the ZEr-B sample	68
Figure 25: (a) Silicate glass structure based on (Si^{4+} , O^{2-}) network formers with no additional glass formers present. It can be seen that all ions are bridged, thus making it almost impossible to integrate new ions into the structure. (b) Silicate glass structure based on the same network formers, but now with alkali ions incorporated as network modifiers. It can be seen here that the bridging ions have now become non-bridging ions, making the addition of dopant ions significantly easier.	73
Figure 26: Partial energy diagram for the trivalent erbium ion.	74

Figure 27: Energy level diagram corresponding to the pumping rates. Radiative and absorptive transitions are denoted by solid lines, while the dashed lines denotes non-radiate transitions	77
Figure 28: (a) Absorption and emission cross-sections of Er^{3+} ions suspended in an Al-Ge-Er based silica host matrix. The absorption and emission cross-sections peaks at 1530 nm, which is typical for Er^{3+} ions near the 1550 nm region. (b) Comparison of emission cross sections of Er^{3+} ions in silica, fluoride and tellurite glass hosts.	83
Figure 29: Total forward- and backward- propagating ASE power as a function of position along a 14 m length of an erbium-doped fibre pumped at 980 nm with 20 mW of power.	85
Figure 30: Experimental setup for ASE spectrum measurement and analysis with 3 m long EDF	92
Figure 31: ASE spectrum from 1490 to 1610 nm from 3 m long EDF under various LD powers	93
Figure 32: ASE spectrum from 1500 to 1550 nm from 3 m long EDF under various LD powers	95
Figure 33: Experimental setup for ASE spectrum measurement and analysis with 3 m long EDZF	96
Figure 34: ASE spectrum from 1500 to 1610 nm from 3 m long EDZF under various LD powers	97
Figure 35: ASE spectrum from 1490 to 1610 nm from 3 m long EDZF and 3 m long EDF at pump power of 76.0 mW	98
Figure 36: Energy level diagram showing absorption and emissions at wavelengths longer than the C-band region.	99

Figure 37: ASE spectrum from 1490 to 1610 nm from 3 m long EDZF and 3 m long EDF at pump power of 108.6 mW	100
Figure 38: ASE spectrum from 1490 to 1610 nm from 3 m long EDZF and 3 m long EDF at pump power of 140.0 mW	101
Figure 39: ASE spectrum from 1490 to 1610 nm from 3 m long EDZF and 3 m long EDF at pump power of 170.1 mW	101
Figure 40: ASE spectrum from 1500 to 1600 nm from 2 m and 3 m long EDZF at pump power of 76.0 mW	103
Figure 41: ASE spectrum from 1500 to 1600 nm from 2 m and 3 m long EDZF at pump power of 108.7 mW	103
Figure 42: ASE spectrum from 1500 to 1600 nm from 2 m and 3 m long EDZF at pump power of 140.0 mW	104
Figure 43: ASE spectrum from 1500 to 1600 nm from 2 m and 3 m long EDZF at pump power of 170.1 mW	104
Figure 44: Excess 980 nm pump power as a function of the input 980 nm pump power for the 2 m and 3 m long EDZFs	106
Figure 45: Experimental setup for gain and NF measurement of 3 m long EDZF	107
Figure 46: Gain of the EDZF imparted to Low (-30 dBm) signal and High (0 dBm) input signals.	108
Figure 47: NF of the EDZF imparted to Low (-30 dBm) signal and High (0 dBm) input signals	109
Figure 48: Experimental setup of the proposed SLM fibre laser	111
Figure 49: Setup of the C-band TBFG	112
Figure 50: C-band TBFG. The TBFG itself is embedded in the polymer layer (<i>highlighted by the red box</i>), which serves as a medium to transfer the	

strain and compression experienced by the metal plate when it is bent, without damaging the C-band FBG itself.	113
Figure 51: Tunability of the SLM fibre laser from 1533.8 nm to 1545.0 nm	114
Figure 52: Frequency spectra of the SLM fibre laser obtained using an RF-SA (a) before the addition of the saturable absorbers and (b) with SA1 and SA2 present in the laser cavity	115
Figure 53: 3-dimensional plot of the EDZF based SLM fibre laser's output power and wavelength against time. The measurements are taken at 10 minute intervals over a period of two and a half hours.	116
Figure 54: (a) plot of output wavelength over time, (b) plot of output power against time.	117
Figure 55: Setup of the self-heterodyne linewidth measurement technique	118
Figure 56: Linewidth measurement of the output from the SLM fibre laser	118
Figure 57: Experimental setup for non-linear coefficient measurement	125
Figure 58: Obtained P_{FWM} at different signal wavelengths and fixed pump wavelength	126
Figure 59: The typical output spectra at P_p and P_s , as well as the generated idlers C_1 and S_2 , with P_p kept constant at 1560 nm and P_s varied from 1552 nm – 1567 nm. C_1 wavelengths are obtained by the equation $\omega_3 = 2\omega_1 - \omega_2$, while S_2 wavelengths are obtained from the formula $\omega_4 = 2\omega_2 - \omega_1$.	128
Figure 60: FWM conversion efficiency versus wavelength detuning	129
Figure 61: Normalized FWM efficiency against the input signal frequency.	130
Figure 62: Nonlinear coefficients with varying the frequency spacing.	130
Figure 63: Generation of the Q-switched pulse as a function of the lamp current, resonator loss, population inversion and photon flux levels against time.	137

- Figure 64: Different stages of Q-switching (a) population inversion build-up, (b) sustainment of complete population inversion and (c) release of energy, resulting in excited population dropping back to the ground level and a release of energy in the form a high energy pulse. Note that the above described system is for a bulk laser, however the same operating principles also applies to a Q-switched fibre laser. 138
- Figure 65: Mechanism of mode-locking: (a) the output signal of the laser when the modes oscillate independently of each other, resulting in a CW output, and (b) output when there is a fixed phase shift, locking the mode together and generating a mode-locked output pulse. 143
- Figure 66: Energy levels of a saturable absorber under excited state absorption. σ_{gs} is the ground state absorption coefficient, while σ_{es} is the absorption coefficient of the excited state. τ is the excited state lifetime 146
- Figure 67: 2-D graphene as the structural base for other carbon structures graphite (3D); SWCNTs (1D); and fullerene (buckyballs) (0D) 150
- Figure 68: (a) Schematic representation of strong and weak σ – and π – bonds in graphene, and (b) the atomic structure of graphene. 151
- Figure 69: (a) The first Brillouin Zone in graphene, and (b) The electron dispersion calculated for the first Brillouin Zone in graphene 152
- Figure 70: Setup for optical deposition of graphene layer to form the saturable absorber 154
- Figure 71: Raman spectrum of the deposited graphene layer on the face of the fibre ferrule. 155
- Figure 72: (a) The spot image of the graphene layer, and (b) the face of the fibre ferrule as observed using an optical fibre scope. The graphene layer on the

<p>fibre ferrule is visible as the black parts over what would be the core of the fibre. The oily residue, at the left hand and the edges of the image are the leftover traces of the NMP solution.</p>	156
Figure 73: ‘Rolling’ of SWCNT from a sheet of graphene	157
Figure 74: (a) SWCNT/PEO saturable absorber on the face of the fibre ferrule, and (b) the Raman spectroscopy confirming the presence of the SWCNTs.	159
Figure 75: Q-switched EDZF fibre laser with SWCNT/PEO based saturable absorber	161
Figure 76: Repetition rate and pulse width at pump powers of (a) 95.1 mW, (b) 110.3 mW and (c) 141.8 mW.	163
Figure 77: Pulse Repetition Rate (kHz) and Pulse Width (μ s) as a function of the pump power.	164
Figure 78: Pulse energy (nJ) and average output power (μ W) as a function of the pump power.	165
Figure 79: Q-switched EDZF fibre laser with graphene based saturable absorber	166
Figure 80: Optical spectrum of Q-switched pulses from the EDZF laser incorporating a graphene based saturable absorber.	167
Figure 81: Output pulse train of the Q-switched pulses from the EDZF laser incorporating a graphene based saturable absorber.	168
Figure 82: Average output power against the pump power	168
Figure 83: Pulse repetition rate and pulse width against the pump power	170
Figure 84: Pulse energy and peak power against the pump power	171
Figure 85: Mode-locked EDZF fibre laser with graphene based saturable absorber	172
Figure 86: Optical spectrum of the EDZF mode-locked fibre laser at a pump power of 100 mW using the graphene based saturable absorber	174

Figure 87: Autocorrelation trace of the mode-locked pulses, obtained from the mode-locked EDZF using the graphene based saturable absorber, against with sech^2 fitting	175
Figure 88: RF spectrum of the mode-locked pulse obtained from the mode-locked EDZF with the graphene based saturable absorber, taken at a 1 GHz span	176
Figure 89: RF spectrum at the fundamental repetition rate of 69.3 MHz with an 80 kHz frequency span and resolution of 300 Hz	176
Figure 90: Optical spectrum of the EDZF mode-locked fibre laser at a pump power of 100 mW using the SWCNT/PEO based saturable absorber	177
Figure 91: Autocorrelation trace of the mode-locked pulses, obtained from the mode-locked EDZF using the graphene based saturable absorber, against with sech^2 fitting	178
Figure 92: RF spectrum of the mode-locked pulse obtained from the mode-locked EDZF with the SWCNT/PEO based saturable absorber, taken at a 300 GHz span. The fundamental harmonic frequency is 17.74 MHz.	179
Figure 93: RF spectrum at the fundamental repetition rate of 17.74 MHz with an 60 kHz frequency span and resolution of 300 Hz	180

LIST OF TABLES

Table 1: List of Oxidation Reactions in the MCVD Process	47
Table 2: Doping levels within core region of the preforms	61

LIST OF ABBREVIATIONS

The following are the list of abbreviations and acronyms used in this document:

AM	Amplitude Modulated
AOM	Acousto-Optic Modulator
ASE	Amplified Spontaneous Emission
CCD	Charge Coupled Device
CGCRI	Central Glass and Ceramic Institute
CNT	Carbon Nanotube
CVD	Chemical Vapor Deposition
CW	Continuous Wave
DBR	Distributed Bragg Reflector
DUT	Device-Under-Test
DWDM	Dense Wavelength Division Multiplexing
EDF	Erbium Doped Fibre
EDFA	Erbium Doped Fibre Amplifier
EDZF	Erbium Doped Zirconia-Yttria-Alumino Silicate Fibre
EOM	Electro-Optic Modulator
EPMA	Electron Probe Micro-Analysis
FBG	Fibre Bragg Gratings
FEGSEM	Field-Emission Gun Scanning Electron Microscopy
FM	Frequency Modulated
FWHM	Full-Width at Half Maximum
FWM	Four-Wave-Mixing
FOAs	Fibre Optic Amplifiers
FOPA	Fibre Optic Parametric Amplifier
GPIO	General Purpose Interface Bus
GVD	Group Velocity Dispersion
He-Ne	Helium-Neon
IMG	Index Matching Gel
InGaAs	Indium-Galium-Arsenide
IR	Infrared

LD	Laser Diode
MCVD	Modified Chemical Vapor Deposition
MFC	Mass Flow Controller
MFD	Mode Field Diameter
MI	Modulation Instability
NA	Numerical Aperture
NF	Noise Figure
NMP	N-MethylPyrrolidone
NPR	Non-Polarization Rotation
OC	Optical Circulator
OE	Opto-Electronic
OH	Hydroxyl
OSA	Optical Spectrum Analyzer
OVD	Outside Vapor-Deposition
PC	Polarization Controller
PCVD	Plasma Chemical Vapor Deposition
PEO	Polyethylene Oxide
PMCVD	Plasma Modified Chemical Vapor Deposition
PVA	Polyvinyl Alcohol
R&D	Research and Development
RF	Radio Frequency
RFSA	Radio Frequency Sepctrum Analyzer
RI	Refractive Index
SBS	Stimulated Brillouin Scattering
SESAM	Semiconductor Saturable Absorber Mirror
SLM	Single-Longitudinal Mode
SMF	Single-Mode Fibre
SNR	Signal-To-Noise Ratio
SOA	Semiconductor Optical Amplifier
SPM	Self Phase Modulation
SRS	Stimulated Raman Scattering
SWCNT	Single-Walled Carbon Nanotube
TEM	Tunneling Electron Microscopy
TFBG	Tunable Fibre Bragg Grating

TIR	Total Internal Reflection
Ti:Sapphire	Titanium:Sapphire
TLS	Tunable Fibre Laser
VPAD	Vapor Phase Axial Deposition
WDM	Wavelength Division Multiplexer
XPM	Cross Phased Modulation
XRD	X-Ray Diffraction
ZDW	Zero Dispersion Wavelength

1. INTRODUCTION

1.1 Introduction

Light has long been a medium for communication over long distances, capable of sending information quickly over expanses that would take days to traverse. Almost every civilization in history has used light in one form or another as a means of communicating quickly, and there is no doubt that light had played an integral part in shaping the development of the world to what it is today.

As a result of the speed in which messages could be transmitted using light, the earliest examples of communication by light was inevitably in war. One of the oldest known examples of this application of light was by the Greek armies, who sent messages by reflecting light of their polished shields in flashes to one another. As the world continued to develop, however, more and more beneficial applications for light communication were developed. Sailors regularly used lamps to communicate when travelling the oceans at night, while messengers and couriers used flashes of light to communicate messages, thus transmitting information much faster than if done by hand. In fact, the potential for communicating by light was so great that in the 1900's, the British Army developed the Mance Heliograph, a device that used light to allow instantaneous communication at distances of almost 50 km [1]. Even Alexander Graham Bell had toyed with the idea of transmitting speech using a beam of light, as early as 1880 [2].

The benefits of light as a medium to transfer information were significant. The properties of light as a high-speed, high-capacity tool for communication were long well known and in the mid-1960s proposals for optical communication via dielectric wave-guides and optical fibres fabricated from glass were made almost simultaneously, with theoretical models confirming their potential capacities. However, using light as a medium of transmitting information over a glass 'tube' remained a pipe-dream for a long time, with the main barrier being loss – up until the 1960s, loss in glass was still in the order of 1000 dB/km, much larger than the 5 to 10 dB/km in the more common coaxial cable at the time.

All this changed in January of 1966. Charles K. Kao and his colleague, George Hockham, demonstrated that the inherent loss in glass could potentially be removed. As a

result of their research, they concluded that the fundamental limitation for light attenuation in glass was less than 20 dB/km [3]. This proved to be the catalyst needed to jumpstart optical communications, and which also eventually led to Charles receiving the 2009 Nobel prize for groundbreaking achievement concerning the transmission of light in fibres for optical communication. It was this advancement in optical fibres as well as a parallel development in semiconductor lasers that gave birth to the high speed broadband networks which we enjoy today. Since the 60s, more and more attention and resources were focused on optical communications, technological advances were quickly being made, and by 1979, further progress in fabrication technology resulted in a loss of only 0.2 dB/km in the 1550 nm region [4], which is the minimum loss level allowed by the fundamental process of Rayleigh scattering [5]. This would be a crucial point, as it would set the stage for the development and eventual adaptation of optical systems as the dominant means of communications today.

1.2 In-Line Optical Amplification

While the glass fibres that would carry the optical signal now enjoyed very low losses, the realization of a globally spanning network of optical fibres could still not be realized. The reason for this was the cumulative effect of losses. Although the loss per km in fibres was now very low, the long distances that signals needed to traverse in these fibres meant that the total attenuation encountered by the optical signal would become significantly high over long distances, thus degrading the signal. When considering the fact that global optical networks would have to span distances in excess of thousands of kilometers, the degradation of the signal's power would be to the extent that the information in the signal would become buried in the background noise. In order to allow for long distance transmissions, a way had to be found to overcome the loss of the signal power over long distances. Simply sending a very strong signal from the source would not be a viable option, as the cost of building such a source would be excessive and impractical, and the intensity emitted from the source would be at levels high enough to actually damage the optical fibre.

The solution to this problem would come in the form of amplifiers. Unlike very strong sources, amplifiers could be placed at intervals along the fibre transmission line, boosting the signal by moderate levels such that it could overcome the losses of a section of the fibre,

before being boosted again for the next stage of the journey. This would be a much more practical solution, as the cost of these amplifiers would be quite affordable, and the intensity of the amplified signal not so high as to damage the optical fibre. Early systems used electronic regenerators for this purpose. These devices would be placed at intervals along the transmission line, and would convert an incoming optical signal into an electronic signal. The signal would then be Amplified, Reshaped and Retimed (3R) before being converted into an optical signal and transmitted along the fibre to the next stage. As a result of this repetitive process, electronic regenerators were often referred to as optical communications repeaters, and during the early years of optical communications proved to be a crucial component in optical networks [6], [7], [8].

However, 3R repeaters were bit rate sensitive, and as such needed to be replaced as and when transmission capacities needed to be boosted. This problem was further complicated with the advent of Dense Wavelength Division Multiplexing (DWDM) systems quickly exposed a limitation of these devices. The problem lay in the conversion of the optical signal to an electronic signal; this process could not differentiate between different wavelengths. As such, when only a single wavelength was present in the system, the electronic regenerator could carry out its function with no problems. Multiple signals on the other hand would be combined by the regenerator, overloading the device and corrupting the data in the signals – in a worst case scenario, damaging the device itself. Thus, a new means of amplification would be needed. To address this problem, researchers now looked at new methods such as Raman amplification [9], [10] Semiconductor Optical Amplifiers (SOAs) [11], [12] and Fibre Optic Parametrical Amplifiers (FOPAs) [13]. While these efforts were successful in overcoming the technical limitations of the electronic regenerator, their cost and complexity still remained prohibitive and as such there was very little incentive to adopt these technologies.

It was not until the late 80s and early 90s that a low-cost and commercially viable alternative to the electronic regenerator was developed in the form of the Erbium Doped Fibre Amplifier (EDFA) [14]. EDFAs provide a wide amplification bandwidth and can be easily spliced to conventional silica fibres as they themselves are based on silica fibres. This makes them highly compatible devices, allowing them to be integrated into current optical infrastructure easily. The EDFA was developed by D. N. Payne and colleagues in 1987 [15], and has the advantage of amplifying signals at the region of 1550 nm, which by chance coincides with the third low-loss window of communications in optical fibres as shown in Figure 1. Furthermore, EDFAs could be pumped at 980 or 1480 nm – this means that the

EDFA can be pumped by laser sources that are of relatively low-cost and easily mass producible. Due to their all optical nature, the overall performance of the EDFA is better than that of the regenerators, with better gain ratios as well as improved Noise Figures (NFs).

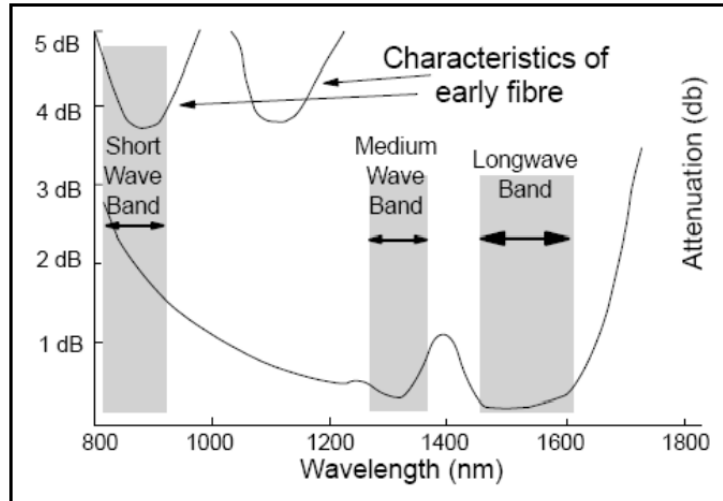


Figure 1¹: Typical transmission bands in optical fibres

Since its conception, the EDFA has been continuously researched on and improved. By 1995, less than a decade later, most optical communication links had migrated away from the electronic repeater and replaced it with the EDFA. In addition to the advantages already inherent to the EDFA, it was discovered that EDFAs also had better installation spans of 100 to 200 km as compared to the span installation electronic repeaters, which were only 30 to 50 km. At the same time, the optical nature of the EDFA also contributed less noise to the optical link, and thus provided significant cost savings and improved the overall performance of the system.

However, even with this significant advancement in optical amplification technology, EDFAs still had their shortcomings. Although a far improvement over the electronic regenerators, EDFAs did have a substantial limitation, in that the silica glass host could only support low concentrations of the active ion, erbium. Should the concentration of the erbium ions exceed a certain limit, detrimental effects such as concentration quenching would occur, severely reducing the performance of the EDFA. Substantial efforts are being made to overcome this problem, as a highly-doped EDFA would have a high potential for developing compact and cost effective amplifiers, which would in turn increase the overall performance

¹ Source: H. J. Dutton, IBM Redbook: Understanding Optical Communications, IBM, 1998.

profitability of current optical communications systems. An Erbium Doped Fibre (EDF) with a high active ion dopant concentration would also find significant use many novel applications, such as in the development of Single-Longitudinal Mode (SLM) fibre lasers as well as Q-switched and mode-locked pulse lasers, which require as short as possible laser cavity in order to generate an optimal output.

In this regard, researchers are now focusing their efforts towards the development of highly-doped EDFs. A number of alternative glasses have been suggested as candidate host matrices for the development of highly-doped EDFs, such as alumina, phosphorus, telluride and bismuth [16], [17], [18], [19], [20] and these new fibres have already shown significant promise, in sustaining high erbium ion concentrations without the onset of concentration quenching. However, the different host matrices of these fibres results in a new problem – incompatibility. These glasses are typically termed as ‘soft-glass’ fibres, and are very difficult, if not close to impossible to splice to conventional optical fibres. As a result of this, there is now a search for a host material that is compatible with conventional silica Single-Mode Fibres (SMFs), yet at the same time capable of sustaining high active ion concentrations.

1.3 The Impetus for the Development of Zirconia–Yttria–Alumino Silicate Glass-Based Erbium-Doped Fibres

While conventional EDFAs have already seen a significant uptake in the commercial optical communications systems, the need for a compact and more cost-effective EDFA is now driving the development of EDFs with high active ion dopant concentrations. This would allow the EDFA to impart significant gain to passing signals, while at the same time retaining a compact form-factor.

Increasing the concentration of the erbium ions in the silica host matrix is not as easy as it sounds, as the glass structure can only sustain a limited amount of active ions. This is not a physical problem however – the glass structure can in fact sustain a very high number of erbium ions in its structure. The problem lies instead in a phenomenon known as ion clustering, or cluster formation [21], which has been mentioned earlier. Ion clustering occurs when active ions such as erbium or other lanthanides are present in high concentrations, and

in this scenario the active ions would tend to group towards each other, forming micro-crystalline clusters. This will in turn lead to another phenomenon, known as concentration quenching that is highly detrimental to the fibre as it reduces the overall performance and ability of the active ions to impart gain to a propagating signal [22].

In this regard, the element Zirconia has now become a highly promising candidate as a co-dopant for creating this highly-doped yet compatible EDF. Early studies have already shown that adding Zirconia or ZrO_2 ions as co-dopants in silica fibres creates a zirconia-yttria-alumino silicate fibre that can easily sustain a high active ion concentration, exceeding 3800 ppm/wt in some cases [23], without the onset of concentration quenching. At the same time, as the host material is still silica glass, thus allowing the developed fibre to have excellent compatibility with conventional fibres used in optical networks today, and also have high mechanical strength and chemical corrosion resistance as well as exhibiting non-hygroscopic characteristics. Studies have also shown that EDFs fabricated using a yttria-alumino silicate fibre as the glass host have a high index of refraction of around 1.45 over the visible and near infrared spectrum [24], [25] and can therefore amplify more DWDM channels than materials with a lower refractive index. This is due to the addition of the ZrO_2 ions, which tend to exhibit wide emission and absorption bandwidths into the host matrix, as predicted by the Fuchtbauer–Ladenberg relationship [26], [27] and Judd–Ofelt theory [28], [29].

The presence of the ZrO_2 micro-crystalline structures in the EDF would also play an important role in the generation of non-linear optical phenomena in this fibre. While conventional SMFs or EDFAs [14] exhibit this phenomena only when exposed to signals of very high intensity, the inclusion of the ZrO_2 micro-crystalline structures would, in theory, allow for these effects to be observed at lower intensity signals. In this regard, a particularly interesting non-linear effect that may be seen is the Four-Wave Mixing (FWM) effect. The FWM effect is an optical Kerr effect, occurring in the absence of significant photo-absorption effects [14]. It may be possible to generate the FWM effect in the Erbium Doped Zirconia-Yttria-Alumino Silicate Fibre (EDZF) if the erbium ions can be suppressed, thus allowing the propagating signal to interact with the ZrO_2 micro-crystalline structures. Under these conditions, two propagating signals would, in theory, give rise to a new signal known as an idler whose wavelength does not coincide with those of the originally propagating wavelengths [30], [31]. The ability of the EDZF to generate the FWM effect would give the fibre tremendous potential for use in the development of new fibre based wavelength sources, thus expanding the applications of the EDZF its current limited scope of merely acting as a

compact optical amplifier towards new and novel applications such as multi-wavelength sources and wavelength converters.

It is also prudent to note that the compact size of the highly-doped EDZF offers another application to the fibre that has yet to be explored; the generation of fast and ultra-fast pulsed fibre lasers. Pulsed fibre lasers have tremendous potential for a multitude of applications, but in order to create a compact and cost-effective as possible system, the generation of the pulsed output should be passive in nature. Achieving this in turn requires as short as possible laser cavity, and the EDZF would thus be a highly suitable candidate for reducing the size of the laser cavity while at the same time allowing the other components of the fibre laser to be commercially procured. This keeps the cost of the laser low while still allowing it to operate at its optimum capacity.

1.4 Fast and Ultrafast Pulsed Fibre Lasers

Laser sources can operate in two possible modes – either generating an output in the form of a Continuous Wave (CW), or in the form of a pulse. Recently, fibre lasers capable of generating fast and ultra-fast pulses have become the focus of tremendous research efforts due to their significant applications in a multitude of areas such as communications, metrology, manufacturing and material processing as well as medicine and health [32], [33], [34], [35]. Traditionally, pulsed laser systems have always been bulk lasers, the most common being the Titanium:Sapphire (Ti:Sapphire) laser. Although these lasers have impressive commercial specifications, such as being capable of generating pulses 100 fs long with repetition rates of up to 80 MHz, they also carry significant limitations and constraints. Among the key limitations that bulk laser have is that they are naturally large, and also complex as well as very costly to build and operate, and at the same time highly sensitive, requiring precise alignment of their optical components as well as substantial cooling and maintenance. To top it all, most of these lasers do not reach their theoretical outputs, even when operated at optimal conditions.

As a result of this, focus has now turned towards the development of fibre lasers capable of generating fast and ultra-fast pulses. These lasers are typically Q-switched or mode-locked, and in most cases actively modulated [36], [37], [38]. However, the cost and

bulk added to the system by active modulators has seen increasing levels of interest in the development of passively modulated fast and ultra-fast fibre lasers. Passively modulated fibre lasers can be achieved by various techniques, such as the Non-Polarization Rotation (NPR) technique [39] and Semiconductor Saturable Absorber Mirrors (SESAMs) [40], [41] and more recently by saturable absorbers made from the allotropes of carbon in the form of graphene or Carbon Nanotubes (CNTs). Graphene in particular has emerged as a practical and highly cost-effective saturable absorber that can be used to develop passively pulsed fibre lasers. Such are the inherent capabilities of graphene that a single atomic layer of graphene can generate the desired Q-switched or mode-locked pulses without the high complexity and costs incurred by other passive modulators such as SESAMs. Furthermore, graphene based saturable absorbers also possess impressive optical characteristics such as ultrafast recovery times and a very wide operational wavelength range as a result of the gapless behavior of the graphene atomic layer [42], [43]. CNTs, which are formed from graphene layers, also exhibit the same properties and advantages as graphene and can thus be used to generate the desired pulses from a fibre laser.

However, in order to develop these compact fast and ultra-fast pulsed lasers, a short as possible cavity length is desired, so as to reduce the losses in the cavity that will affect the performance of the system. This would be especially important in generating mode-locked pulses, where the cavity losses must be delicately balanced so as to obtain the desired ultra-fast pulses. While the earlier mentioned highly-doped EDFs such as those based on the telluride and bismuth hosts could be used to realize these pulsed lasers, their incompatibility with conventional fibre components prevents their widespread applications. It is here that the EDZF would be highly beneficial as a compact highly doped EDF that is also very compatible with conventional silica fibres. Combining the EDZF with saturable absorbers for passively generating pulses will indeed allow for the realization of compact fast and ultra-fast fibre lasers.

1.5 Objective and Scope of Work

As discussed in the earlier section, the EDZF has high potential for enabling a multitude of novel applications. As such, the overall focus of this work would be to gain an insight into its

behavior and characteristics, before using this novel EDF in a number of selected applications. These factors form the basis for the motivation behind this work, which is to investigate this new fibre for possible applications such as realizing a compact SLM fibre laser and compact optical amplifiers as well as devices for ultra-short pulses and even as a non-linear medium for realizing more advanced applications such as wavelength converters. There are three main objectives to this work, which are given as follows:

1. The first objective of this work is to revisit the fabrication process of the EDZF. Understanding the fabrication process of the EDZF will give valuable insights into the morphology and behavior of the EDZF, as well as understand better the roles played by the various glass modifiers, nucleating agents and active ion dopants. Subsequently, the physical and optical of the prepared EDZFs will be determined and analyzed. This will consist of an in-depth study on the physical morphology of the fibre, both at the macro- and micro-levels, as well as characteristics inherent to the structure and composition of the fibre, such as the refractive index, luminescence and decay rates.
2. The second objective of the study will be to examine the behavior of the active ions in the EDZF when exposed to pump wavelengths. This examination will look into the Amplified Spontaneous Emission (ASE) generated by the fibre, as well as its operation as an optical amplifier. Where possible, a comparison will be made with a conventional EDF of the same length, to illustrate the difference in the performance of the two fibres due to the varying active ion concentrations. Another key focus of this objective would be the generation of a SLM output from an EDZF based fibre laser, as this will have significant real-world applications. In addition, the non-linear characteristics of the EDZF will also be studied, specifically the FWM effect. This is in-line with the hypothesis that the EDZF will exhibit non-linear phenomena due to the incorporation of the ZrO_2 rich micro-crystalline structures in the matrix of the glass host.
3. The third and final objective of this research is to use the EDZF as the gain medium for compact fast and ultrafast pulse lasers, built using saturable absorbers made from graphene and Single-Walled Carbon Nanotubes (SWCNTs). The goal of this objective would be to combine the thin passive saturable absorber together with the compact, high performance EDZF to create a cost-effective and compact pulsed laser source that is still robust enough to be used in the field. The EDZF will be examined as a possible gain

media for both Q-switched and mode-locked pulse lasers, and used together with either a graphene or SWCNT based saturable absorber as a mechanism to obtain the desired pulsed. Should this objective be achieved, it will undoubtedly open up significant potential fast and ultra-fast EDZF based laser sources in many real-world applications such as manufacturing, communications, range-finding, medicine and spectroscopy, to name just a few.

It is very important to take note that a study like this can encompass a significantly wide area. Therefore, it is crucial that the scope of the work be well defined and focused, or else the objectives originally set out for cannot be reached. One may be tempted to explore all possible variations and avenues of a particular aspect or setup, but this will ultimately consume time and resources and drive the research further away from the goal. As such, the various limitations and scopes of this research are indicated in their relevant chapters, along with their justifications.

1.6 Thesis Overview

This thesis is structured around three main chapters, barring the introduction and concluding chapters.

The first main chapter, Chapter 2, will examine the fabrication process of the EDZF. As the fibre is based on a conventional silica fibre, thus a major portion of the fabrication process is highly conventional. The Modified Chemical Vapor Deposition (MCVD) process is employed, along with solution doping to incorporate the various glass modifiers as well as dopants and nucleating agents. The obtained tube is then collapsed before being drawn in the same manner as a conventional fibre laser. A physical characterization of the fibre is described in this chapter, examining various aspects of the developed EDZF such as its molecular structures and morphology, as well as examining some of the more fundamental optical properties of the fibre such as luminescence, decay rates and refractive indices.

The second main chapter of this work would be Chapter 3. In this chapter, the various optical properties of the fibre are studied. As an EDF in nature, thus conventional parameters such as Gain, NF and ASE are examined. The performance of the EDZF as the gain medium

for a conventional fibre laser is examined, and also its performance in generating a SLM output. Finally, the chapter will also examine the non-linear characteristics of the EDZF that arise due to the inclusion of Zr^{2+} ions within the matrix of the glass host, focusing specifically on the FWM effect.

This final major chapter of this work, Chapter 4, will finally examine the application of the EDZF in fast and ultra-fast pulsed fibre lasers. The EDZF will be used in conjunction with passive saturable absorbers formed from graphene and SWCNTs, and will be operated in both the Q-switched and mode-locked regimes. Finally, a brief summary of the findings of this work will be compiled, together with any limitations encountered and any future works that can be carried out.

In all three chapters, a theoretical background will be presented first, covering the various fundamentals of each chapter before the chapter moves on towards the experimental procedures and the analysis of the results. In this manner, each chapter is designed to be standalone, and if the need arises, can serve as a reference source.

2. FABRICATION AND CHARACTERIZATION OF ZIRCONIA–YTTRIA–ALUMINO SILICATE GLASS-BASED ERBIUM-DOPED FIBRES

2.1 *Introduction*

While in-line amplifiers have now become a common-place technology in optical communications networks, significant research efforts are still being made to further improve and enhance their performance. A key focus of research is the development of Fibre Optic Amplifiers (FOAs) with high erbium dopant concentrations to aid in the development of compact, high performance and low cost FOAs and fibre amplifiers. However, increasing erbium dopant concentration gives rise to a number of detrimental effects, the most significant of these being concentration quenching [21] and cluster formation [22]. These effects not only result in a drastic reduction of the amplifier's optical performance, but also degrade the fibre physically, inducing various effects such as cracking in the core region of the fibre [23]. In order to overcome these limitations, fibres based on soft glass hosts other than silica were examined as possible host fibres or co-dopants, so as to obtain high erbium dopant concentrations without the detrimental effects of concentration quenching and clustering. While these new fibres were able to achieve this goal, they have inherent drawbacks that would eventually make them unsuitable for practical use, such as a significant incompatibility in splicing for example with conventional silica fibres or requiring pump wavelengths not commonly used by the industry. As a result of these new drawbacks, researchers and scientists were forced to return to the drawing board, and are now looking at co-dopants that can be incorporated into a silica glass host matrix to increase the erbium dopant concentration without triggering the effects of concentration quenching and cluster formation, while at the same time maintaining the structural properties and characteristics of a conventional silica fibre. In this regard, the element Zirconia has now become the focus of extensive research, as its introduction as a co-dopant into a conventional silica host that will allow the fibre to sustain active ion concentrations substantially higher than those found in conventional silica fibres, while still maintaining the compatibility as well as mechanical strength, chemical corrosion resistance and non-hygroscopic characteristics of an SMF.

In this chapter, the fabrication and characterization of the EDZF will be the primary focus. The following section will revisit the fabrication process, providing an insight into the creation of the EDZF as well as the various techniques and constraints encountered during the fabrication of this fibre. Subsequently, the physical characteristics of the fibre are examined, such as its structure, morphology and compositions. This is then followed by an examination of the optical characteristics of the fibre, such as its luminescence, decay rates and refractive indices. It must be noted that the optical characteristics examined in this chapter are not the optical performance characteristics of the EDZF, such as its ASE, gain and NF. This will instead be the focus on the next chapter, which is dedicated solely to this aspect of the EDZF.

2.2 *Fabrication of the EDZF*

The fabrication and characterization of the EDZF is carried out under the supervision of Dr. Mukul Paul of the Central Glass and Ceramic Institute (CGCRI), Kolkata, India as well as members of his research team². Due to the availability of facilities, the fabrication of the fibers as well as certain characterization tests were carried out at the CGCRI, and some tests being carried out at the University of Malaya.

The fabrication process of the EDZF is a three step process, beginning with a MCVD process [25] to prepare a porous glass host. This is followed by solution doping, where the necessary glass modifiers and nucleating agents are added to the glass host. At this stage also, erbium ions are incorporated into the glass host to turn it into an active medium. Finally, the glass host, with the incorporated glass formers, modifiers and active ions is sintered and collapsed to form the fibre preform. In addition to these three steps, certain pre- and post-fabrication steps must also be undertaken if a high quality EDZF is to be obtained. In the pre-fabrication process, a high quality host material must first be selected, and the selected glass tube must be thoroughly cleaned to remove any contaminants that will affect the fibre before it undergoes the MCVD process. In the post-fabrication process, the fibre preform is drawn using a drawing tower, and then coated with a polymer layer to protect and preserve the pristine strength of the fibre.

² Fabrication of the fiber was carried out with Dr. Mukul C. Paul (my external co-supervisor) and members of the CGCRI. All tables and figures presented in the chapter are sourced from Dr. Mukul C. Paul, unless otherwise stated.

2.2.1 *Pre-Fabrication: Selection and Preparation of Host Material*

The proper selection and preparation of the host material plays a crucial role in ensuring the high quality and optimal performance of the fabricated fibre. The host material used for the fabrication of optical fibres can be categorized into three broad groups – silica glasses, non-silica glasses and plastics or polymers. Typically, fused silica, which is also known as amorphous silicon dioxide, is the preferred choice for a host material as it has a number of highly advantageous characteristics:

- Fused silica has a wide wavelength range with good optical transparency, from 200 nm to 3000, with extremely low absorption and scattering losses at the order of 0.2 dB/km in the near-infrared spectral region of approximately 1550 nm. It can also be made transparent at the 1400 nm region by ensuring a low concentration of Hydroxyl (OH) groups³ in the fibre.
- Fused silica fibres can be drawn at temperatures of between 1600°C and 2000°C from silica based preforms, making them suitable for high temperature processing. They are also easy to fusion splice, with low average losses of 0.1 dB or better, making them a highly preferred fibre for deployment in commercial optical networks.
- Fibres based on fused silica glass possess amazingly high mechanical strength against pulling and bending, highly stable chemically and also not hygroscopic. Furthermore, the structure of the host material readily accepts various dopant materials, making it suitable for the fabrication of specialty optical fibres such as EDFs.
- Fused silica fibres also have a very high optical damage threshold, which is important in the development of fibre amplifiers and lasers. It also has a particularly low Kerr non-linearity factor, which is highly beneficial in preventing detrimental non-linear effects from occurring in the fibre, which will in turn affect the quality of the transmission.

³ Conversely, inducing a high concentration of OH groups will make the fused silica fibre transparent for wavelengths in the Ultraviolet (UV) region.

Vitreous or fused silica (SiO_2) glass is made by cooling molten glass in such a manner that it does not crystallize, but rather remains in an amorphous state, with the viscosity of the molten glass increasing to a level where the glass molecules can no longer rearrange themselves in the form of a liquid due to fast cooling. SiO_2 has a silicon-oxygen tetrahedron network structure, with a coordination number of 4. The tetrahedron structure of the SiO_2 molecules links at all four corners, forming a continuous 3-dimensional network as shown in Figure 2.

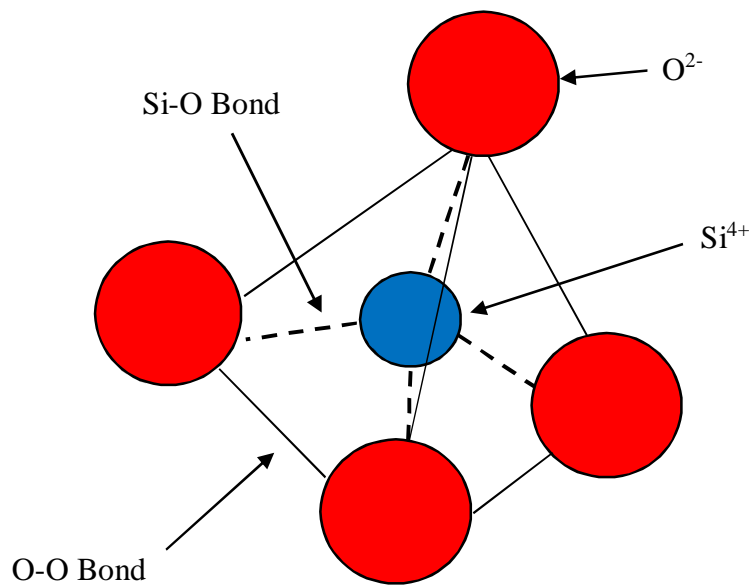


Figure 2: Tetrahedron structure of SiO_2 , which has 4 oxygen ions connected to a single silicon ion. The solid lines represent the O^{2-} to O^{2-} bonds, while the dashed lines represent bonds between the Si^{4+} and O^{2-} ions.

In the SiO_2 structure, the shortest Si-O link is approximately 0.162 nm, while the shortest O-O link is approximately 0.265 nm [44]. Each oxygen atom moves in two degrees of freedom, thus giving the SiO_2 its various absorption bands. It is these characteristics that give fused silica glass its highly desirable characteristics. Vitreous germanium or GeO_2 , a non-silica glass also possesses a similar tetrahedral structure, with the same coordination number of 4. However, the ionic diameter of the germanium atom is larger than that of the silicon ion, thus making the Ge-O bond length slight greater at about 0.175 nm [45]. The structure of GeO_2 glass is more compact than SiO_2 glass, thereby making the interstitial volume of GeO_2 slightly less

than that of SiO_2 . This manifests as structural defects in GeO_2 glass, as a result of the formation of Ge-Ge bonds, thus reducing the overall popularity of GeO_2 based glass.

The viscosity of GeO_2 glass is near to that of SiO_2 glass, as shown in the viscosity curves of Figure 3. The glass transition temperatures (T_g) and softening temperatures (T_s) of both glasses are also shown in Figure 3.

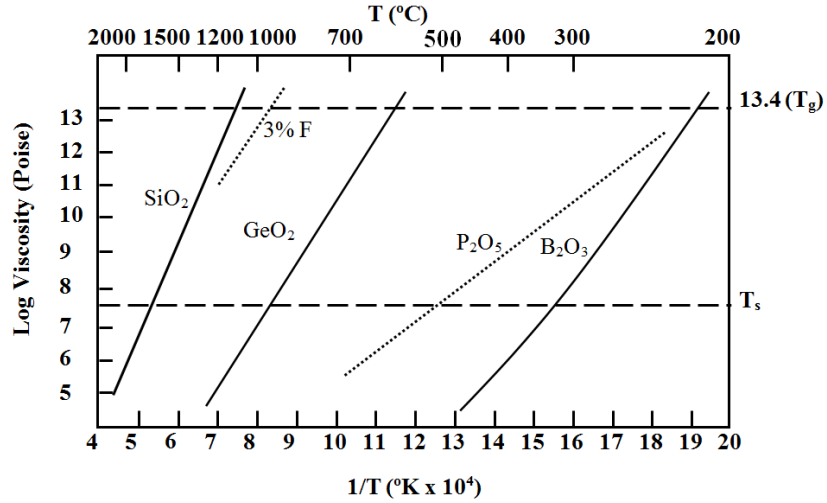


Figure 3: Viscosity of oxide glasses with glass transition (T_g) and softening (T_s) temperature

From the figure, it can be seen that GeO_2 glass has a transition temperature of between 550 to 600°C, while SiO_2 glass has a higher transition temperature at about 1100°C. Adding a minor amount of F (of about 3%) will lower the temperature of SiO_2 glass to below 1000°C, making the fabrication process slightly easier. The glass softening temperatures for GeO_2 and SiO_2 glass ranges at around 1000°C and slightly higher than 1600°C. B_2O_3 glass has much lower transition and softening temperatures, at around 200 and 300°C, making the fabrication process easier, but making the glass difficult to splice to conventional fibres. These characteristics become a very important factor in the selection of the host material.

Another important factor that must be considered in the fabrication of the EDZF is the refractive index of the fibre. In order to fabricate an optical fibre, two fused silica glass layers are needed, namely the inner layer (core) and the outer layer (cladding). It is here that the problem lies, as the core must have a higher refractive index than the cladding to ensure that Total Internal Reflection (TIR) is always preserved and thereby trapping light within the core layer [46]. At the same time, both

the core and cladding layers must be compatible in terms of their viscosity and thermal expansion coefficients in order to preserve the physical integrity of the fibre, thus ruling out the use of different host materials for the core and cladding sections of the fibre. To overcome this problem, the refractive indices of the host material for the core and cladding layers are instead controlled using Refractive Index (RI) modifying agents, which are typically added to the core layer during fabrication process to increase its RI and thus preserving TIR. The best RI modifying agents for fused silica fibres are found to be those oxides that are similar in dimension to SiO_2 itself, such as GeO_2 , P_2O_5 or Al_2O_3 . The RI can be changed by varying the percentages of the different dopants in the glass host, as shown in Figure 4. From the figure, it can be seen that increasing the concentration of dopants such as GeO_2 and P_2O_5 in the silica host will increase the RI of the core layer, while increasing the concentration of B_2O_3 and F dopants in the silica host will have the opposite effect, reducing the RI of the glass [5].

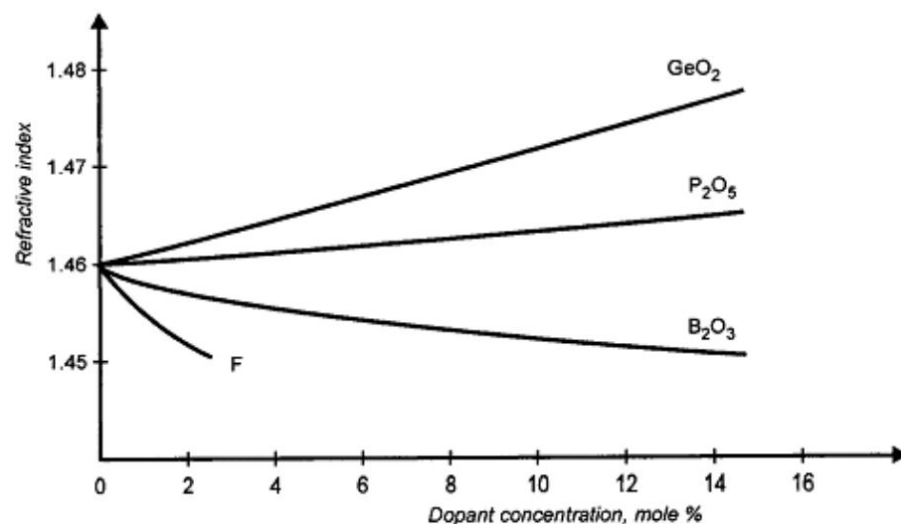


Figure 4⁴: Effect of common dopants on refractive index of the silica host.

Thus, the choice is left to the manufacturer of the fibre, whereby the RI of the core can be increased, or the RI of the cladding decreased. The typical modifying agents used in the fabrication of commercial optical fibres are Al_2O_3 , GeO_2 , P_2O_5 , or B_2O_3 , which forms aluminosilicate, germanosilicate, phosphosilicate or borosilicate glass. It is also prudent to note that F is typically the preferred agent for fabricating low-RI

⁴ Source: G. E. Keiser, Optical Fibre Communication, 2nd Ed., New York: McGraw Hill, 1991.

claddings as opposed to B_2O_3 , as B_2O_3 possesses minor Infrared (IR) absorption characteristics which in turn will affect the transmission of light at the 1500 nm region. Furthermore, F ions are also used as glass formers, as they harden the fibre, allowing it easier drawing [47].

The same agents that are responsible for modifying the RIs of the core and cladding also play an important role in the fabrication of fibres doped with active ions such as Er_2O_3 . These fibres, also known as rare-earth doped fibres, are crucial in the development of active fibre systems, such as fibre amplifiers and fibre lasers. In order to fabricate rare-earth doped fibres, a pure silica host cannot be used as it typically exhibits low solubility levels for rare earth ions. The reason for this is the structure of a pure silica glass host, which adheres closely to the ‘continuous random network’ model as proposed by Zacharison [48]. In this model, the structural tetrahedrons as illustrated in Figure 2 will share a bridging oxygen ion, thus forming a rigid network. As trivalent rare-earth ions, such as Er^{3+} ions require the coordination of 6 to 8 oxygen ions, thus the introduction of Er^{3+} ions into the silica matrix will result in the silica tetrahedron being displaced to allow the dopant ion to bond to six oxygen ions. This will allow a coordination balance to be achieved, with the 3+ charge of the erbium ion being balanced by three -1 charges from the oxygen ions, with two oxygen atoms behaving as a single charge⁵. As there are not enough ‘non-bridging’ oxygen ions in the structural matrix of silica, thus the Er^{3+} ions will tend to share oxygen ions, which in turn leads to a clustering of the rare earth ions. The close proximity of the Er^{3+} ions now allows energy to be transferred among these ions through Er-O-Er bonds, which reduces the ability of the Er^{3+} ions to impart energy to photons propagating through the doped fibre. This is the phenomenon known as concentration quenching, and the effects of concentration quenching and clustering limit the amount of Er^{3+} ions that can be incorporated homogenously into a pure silica fibre to only a about a hundred ppm/wt [49], [50]. As such, increasing the concentration of Er^{3+} ions in a silica host will require a change to the atomic structure of the silica host; typically by adding an additional ion into the tetrahedral structure. Both aluminum and phosphorous ions can be used as co-dopants in this manner, surrounding the Er^{3+} ion and shielding its charge. Trivalent Al^{3+} ions will act as a substitute for the Si^{4+} ions in the glass network, so that the three Aluminum ions can compensate for the charge

⁵ In this regard, the three -1 charges will thus be the contribution of six oxygen ions.

imbalance when in close proximity with the Er^{3+} ion. Phosphorous ions also play a similar role if incorporated into the glass structure, forming a P_2O_5 tetrahedron [49], [51]. Today, alumina-silicate glass has become the industry standard and preferred choice for the fabrication of rare-earth doped fibres for conventional applications.

In addition to the refractive index difference between the core and cladding layer as well as the ability to incorporate rare-earth ions, another important consideration in the development of the host material for the EDZF is the total dispersion of the material. The total dispersion, which comprises of material dispersion and waveguide dispersion, should be kept as close as possible to zero when selecting various dopants as well as their levels of concentration. The relationship between the Zero Dispersion Wavelength (ZDW) with respect to various dopant concentrations is shown in Figure 5.

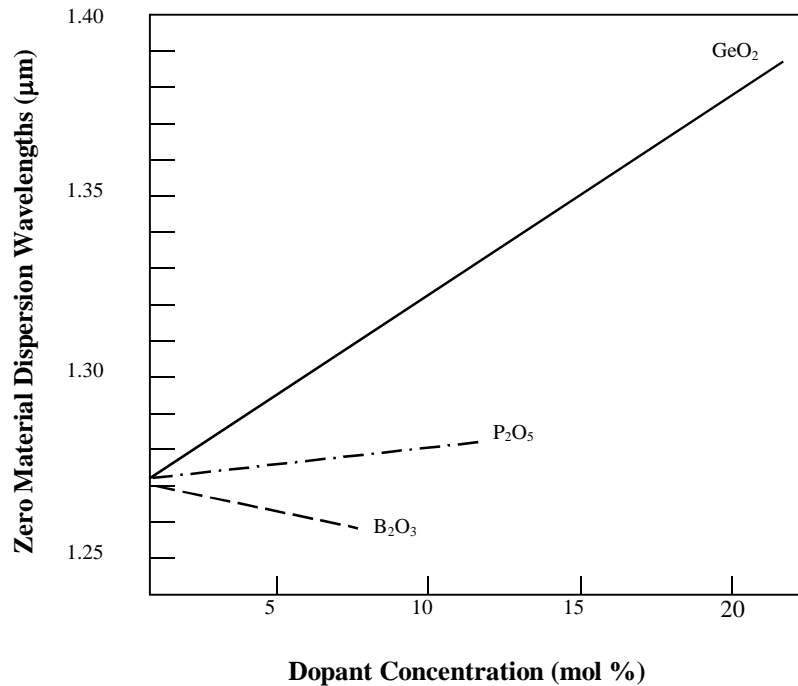


Figure 5: The relationship between the dopant concentrations and the ZDW of the silica host

It can be seen clearly that increasing the concentration of dopants such as GeO_2 and P_2O_5 in the silica host will result in the ZDW shifting towards the longer wavelength region, while higher concentrations of B_2O_3 dopants will in turn shift the ZDW of the silica host towards the shorter wavelength region. Therefore, the concentration of

these dopants in the fabrication process is carefully controlled to allow the desired ZDW wavelength to be achieved.

Based on these criteria, the selected host material for the fabrication of the EDZF is a silica glass, which is procured in the form of a hollow silica substrate tube, with an outer diameter of about 20 mm and an inner diameter of about 16 mm. Once the selection of the host tube has been completed, the tube is cleaned thoroughly, to remove any contaminants, before being placed in the lathe of the MCVD rig. Upon mounting the tube securely, the next stage of the fabrication process begins, which is the deposition of the soot layer by the MCVD technique.

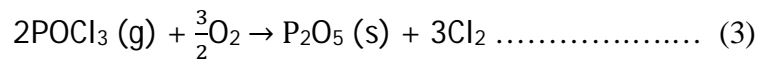
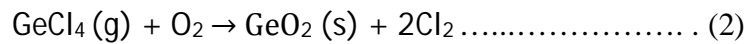
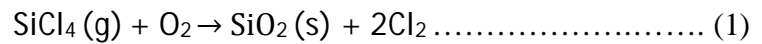
2.2.2 *The MCVD Process*

The principle behind the MCVD technique, or for that matter most Chemical Vapor Deposition (CVD) techniques, is that the selected vaporization of certain precursors by a significant difference in the vapor pressure between the desired precursor and the rest will create a very pure form of the material [52]. The purity of the precursor is essential as contaminants; in particular transition metal impurities can have a very detrimental effect on the performance of the fabricated fibre - such that even a few parts per billion of these impurities can induce significant losses of anywhere between 0.1 dB/km up to 2.7 dB/km over wide spectral ranges. Appendix 1 provides a summary of the optical losses induced by common transition metal impurities in silica optical fibres, as well as their peak absorption ranges.

Of the CVD techniques employed for producing optical fibres of very high quality, the MCVD technique is the most common [53]. First demonstrated at Bell Laboratories in early 1974 [54], the MCVD technique is based on thermal chemical vapor reactions in which two gases, typically SiCl_4 and O_2 , are mixed at high temperatures of above 1450°C to produce SiO_2 . Although there are many other vapor deposition process used commercially as well, such as Outside Vapor-Deposition (OVD) [55], Vapor Phase Axial Deposition (VPAD) [56], Plasma-activated Chemical Vapor Deposition (PCVD) [57] and Plasma Modified Chemical Vapor Deposition (PMCV) [58], the MCVD process is particularly advantageous as it allows the fine tuning of the various dopants and chemicals that are being used to fabricate the fibres,

making it highly suitable for Research and Development (R&D) activities. At the same time, the MCVD technique is also very robust, making it more than capable of handling the demands of preform production on a commercial scale if the need arises. Furthermore, the process can be carried out manually or automatically, depending on the requirements of the user; this gives the system great flexibility, while at the same time maintaining its simplicity, allowing it to fabricate preparing preforms with all possible types of geometries, including specialty preforms now in demand for EDFA and sensors applications.

The MCVD system used in the fabrication of the EDZF consists of two main components⁶: a liquid bubbler and an external burner. O₂, N₂ and CCl₂F₂ gasses are fed through liquid SiCl₄, GeCl₄ & POCl₃ in the bubbler to generate SiO₂, GeO₂ & P₂O₅. The chemical reactions involved are described below:



where equations 1, 2 and 3 represent the thermal oxidation of chloride gas precursors to solid oxides [52]. The individual oxidation processes are chemically complete once certain thermal conditions are met; however the thermal equilibrium constants for the individual reactions differ, making the chemical kinetics complicated when the gases are mixed together [59]. The halide vapors obtained are highly toxic, and have high vapor pressures at room temperature, dependent on the temperature as shown in Figure 6:

⁶ The setup of the MCVD system is typical, and does not differ in any way from conventional MCVD system configurations.

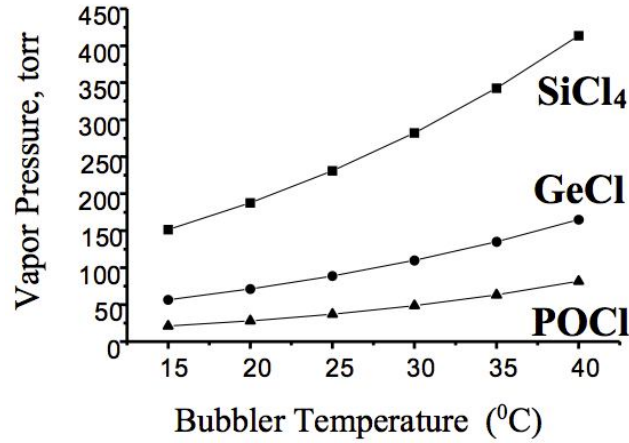


Figure 6: Vapor pressure of different source chemicals against temperature

The vapor pressure of respective chemicals is calculated from the following equation:

$$\log_{10} P = \frac{A-B}{C+t} \dots\dots\dots(4)$$

where A , B & C are constants and t is temperature in degrees centigrade ($^{\circ}\text{C}$). Thermal Mass Flow Controllers (MFCs) are used to control the vapor separation. The vapor precursors are channeled into the hollow glass tube, which slowly rotated by the MCVD rig while at the same time being heated by an external burner which travels along the length of the tube as it turns⁷. The optimum deposition temperature range for the MCVD process is $1350 - 1400^{\circ}\text{C}$, with a variation of the pre-sintering temperature from 1300 to 1450°C . The diameter of the tube used is typically between 12 to 30 mm. The setup of the MCVD rig is given in Figure 7.

⁷ The burner used is a quartz flue, burning a hydrogen oxygen mixture.

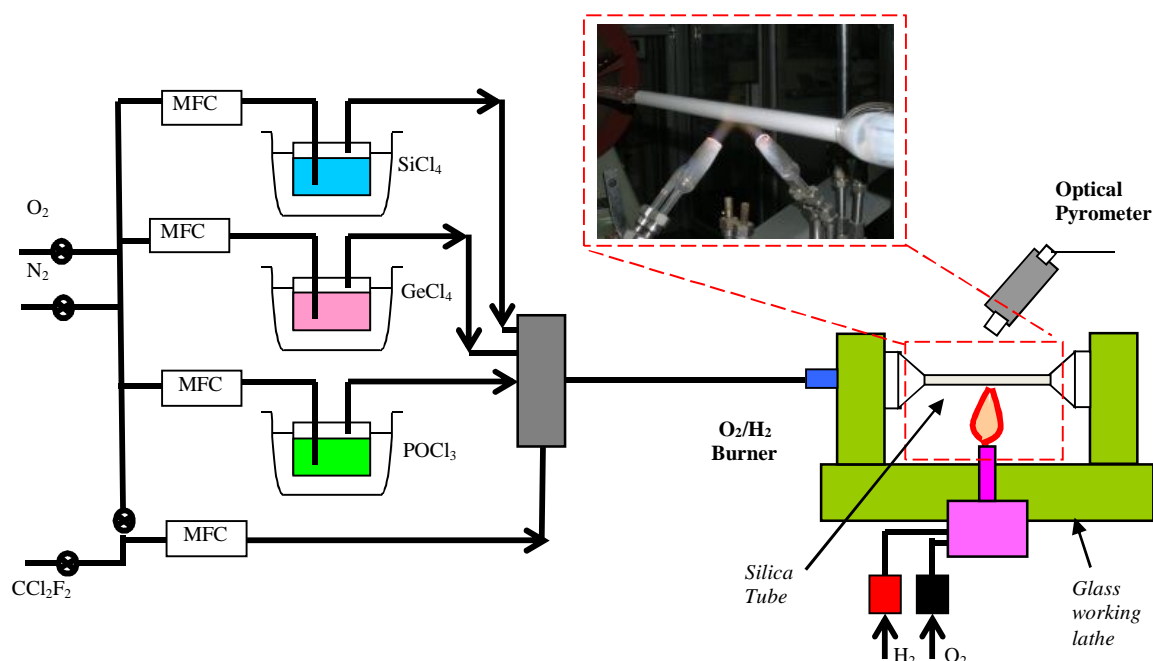
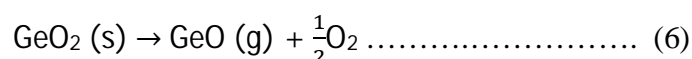


Figure 7⁸: MCVD system setup, with glass working lathe

As the precursor vapors are heated in the hollow tube, two additional chemical processes also occur at this stage, namely Cl_2 disassociation and GeO_2 evaporation. The chemical reactions for these two processes are given as follows:



As the oxide particles formed through the reactions in 1, 2 and 3 are heated under the right thermal conditions; they grow in size, from a few nanometers to a range of between 0.1 and 0.5 μm during Brownian coagulations in the gas-particle stream [52]. The distribution of the sub-micron particles along the inner wall of the hollow silica tube is determined by the temperature distribution along the path of the hollow tube, as well as the gas flow rate. In order to ensure the deposition of a layer of sub-micron

8 Image modified from that in H. Ahmad, M. C. Paul, N. A. Awang, S. W. Harun, M. Pal and K. Thambiratnam, "Four-Wave-Mixing in Zirconia-Yttria-Aluminum Erbium," *J. Europ. Opt. Soc. Rap. Public.*, vol. 7, pp. 12011-1 - 12011-8, 2012.

particles (also called soot) with a uniform as possible surface and thickness, the gas flow rates inside the silica tube must carefully controlled to maintain the laminar flow in all cross sections along the substrate.

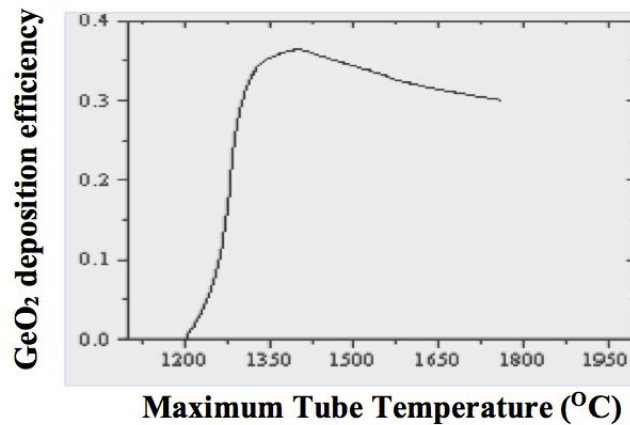
The deposition process is carried out using the forward deposition method, where the oxy-hydrogen burner is maintained at a temperature of between 1250-1300°C and moved along the direction of reactant flow the containing SiCl₄, GeCl₄, POCl₃ vapors. Doing so will allow the soot particles formed by oxidation of input gas mixture to be deposited downstream of the burner and allow the partial sintering of the porous layer to take place simultaneously during deposition. The total flow of SiCl₄ & GeCl₄ was controlled for deposition of core layers of different thickness having the same RI values while the proportion of GeCl₄ vapor with respect to SiCl₄ was varied for adjusting the Numerical Aperture (NA) of the preform. The deposition temperature of SiO₂-GeO₂ core layer was in the range of 1250°C to 1300°C. Since deposition and partial sintering took place in the same pass of the burner, the experimental parameters during deposition had significant influence on the composition and relative density of the porous layer. A dopant control program was worked out to adjust NA values to within the range of 0.15-0.25 with a core diameter of between 5.0-6.0 μm. The relative density of the soot layer estimated on the basis of the RE concentration that ranges between 0.30 to 0.50. This was important to reduce core-clad interface defect. A summary of the oxidization reactions in the MCVD process is given in Table 1.

As the burner traverses further, the particulate layer is sintered and vitrified, forming a pore-free layer of glass with a thickness around 10 microns. When the burner reaches the end of its travel, it quickly returns and the traverse is repeated. The concentration of the dopants can be changed in each pass to get desired refractive indices of the cladding and core glasses. The reaction rate largely depends on the tube temperature with associated flow pattern of the reactant vapors. The deposition efficiency of GeO₂ versus silica tube temperature is shown in Figure 8.

Table 1: List of Oxidation Reactions in the MCVD Process

Reaction Type	Reaction Description	Oxidation Reaction
A	Reactions for etching process when inside surface of silica tube is cleaned	$\text{CCl}_2\text{F}_2 (\text{g}) + \text{O}_2 = \text{Cl}_2 + \text{F}_2 + \text{CO}_2$ (Freon gas)
		$\text{SiO}_2 (\text{silica tube}) + 2\text{F}_2 = \text{SiF}_4(\text{g}) + \text{O}_2$ (Silicon dioxide) (Silicon tetra fluoride)
B	Reactions for deposition of cladding layers	$\text{SiCl}_4(\text{g}) + \text{O}_2 = \text{SiO}_2(\text{s}) + 2\text{Cl}_2$ (Silicon tetrachloride)
		$\text{SiO}_2(\text{s}) + 2\text{F}_2 = \text{SiF}_4(\text{g}) + \text{O}_2$
		$3\text{SiO}_2(\text{s}) + \text{SiF}_4 = 2\text{Si}_2\text{O}_3\text{F}_2 (\text{s})$ (Fluorinated silica compound)
		$4\text{POCl}_3 (\text{g}) + 3\text{O}_2 = 2\text{P}_2\text{O}_5 (\text{s}) + 6\text{Cl}_2$
C	Reactions for deposition of core layer	$\text{SiCl}_4(\text{g}) + \text{O}_2 = \text{SiO}_2(\text{s}) + 2\text{Cl}_2$
		$\text{GeCl}_4(\text{g}) + \text{GeCl}_4(\text{g}) + \text{O}_2 = \text{GeO}_2(\text{s}) + 2\text{Cl}_2$

Source: Data obtained from the work of Andrew Simon Webb and Giusy Origlio

**Figure 8:** Deposition efficiency GeO₂ against tube temperature

The deposition rate is optimized with respect to the temperature where higher temperatures cause dopant vaporization in the simultaneous sintering process. Deposition at lower temperatures results in the reaction being inefficient, especially for GeCl₄. Downstream from the hot zone that is near to the burner, the tube walls are cooler than the vapor stream, and some of the suspended glass particles are deposited on the tube surface. The deposition is caused by thermophoresis, a phenomenon in which a suspended particle experiences a net force in the direction of decreasing

temperature due to a greater rate of collisions with gas molecules on the hot side of each particle. This is illustrated in Figure 9.

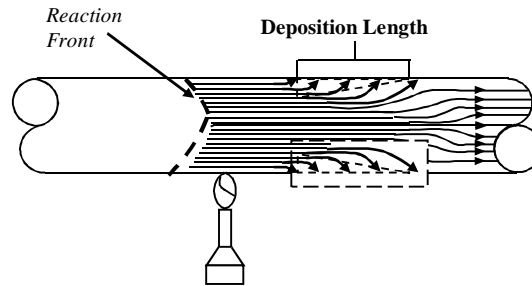


Figure 9: Particle trajectories in silica substrate tube.

Once the porous soot layer has been deposited on the inner layer of the silica substrate tube, the tube is then carefully removed from the glass lathe. The tube, together with its porous silica layer, will now undergo the solution doping technique to incorporate the glass modifiers Al_2O_3 , ZrO_2 and Y_2O_3 , as well as the Er_2O_3 ions into the host matrix.

2.2.3 Solution Doping

The solution doping process will allow for the incorporation of glass modifiers and active ions into the yttria-alumino silicate host material that was fabricated in the previous section. The active ions will allow the EDZF to be used as a host material for fibre lasers and amplifiers, while glass modifiers such as ZrOCl_2 will allow for the desired active ion concentrations to be achieved without the detrimental effects of clustering and concentration quenching.

A special set-up was used in the solution-doping process so that the solution could be poured into the tube at a uniform rate to avoid imperfections as well as reduce the probability of concentration variations along the length of the preform. The draining rate of the solution is also controlled after completion of dipping for the same reasons. To incorporate the desired quantity of Er^{3+} ions, an alcoholic-water (1:5) mixture at a suitable strength was used to form $\text{ErCl}_3 \cdot 6\text{H}_2\text{O}$, $\text{ZrOCl}_2 \cdot 8\text{H}_2\text{O}$ &

$\text{AlCl}_3 \cdot 6\text{H}_2\text{O}$. The strength of $\text{ErCl}_3 \cdot 6\text{H}_2\text{O}$ was varied between 0.005 M to 0.010 M, while the strength of the $\text{ZrOCl}_2 \cdot 8\text{H}_2\text{O}$ & $\text{AlCl}_3 \cdot 6\text{H}_2\text{O}$ complexes was adjusted to between 0.1 M to 1.0 M. The ratio of the Er^{3+} and Al^{3+} ions is typically maintained at a ratio of 1:10 or above. Small amounts of Y_2O_3 and P_2O_5 are added to the mixture as well, serving as nucleating agents to increase the phase separation with generation of the Er_2O_3 doped micro crystallites in the core matrix of optical fibre preform. The dipping time is varied from between 0.45 to 1.50 hours, depending on the thickness of porous core. The time period was increased with increase in core thickness to allow sufficient time for diffusion through the porous layer which takes place due to capillary action. It was observed that as the strength of the solution is increased, so too does the viscosity and surface tension of the solution by a considerable amount, with the viscosity ranging between 1.98 to 7.25 cps for a variation of the concentration of AlCl_3 in the ethanolic solution from 0.15 M to 0.58 M. As a result of this, a good adhesion of the porous layer to the inner wall of the substrate tube is necessary when using a solution with a high AlCl_3 concentration. As such, during the deposition of the porous core layer, the substrate tube and its deposited layers are also partially sintered at a high temperature⁹ in the backward direction¹⁰.

The substrate tube with the porous layer is left to 'soak' in the solution for about 1 hour, which is typically sufficient time to ensure that saturation of the developed pores in the porous layer is complete. Subsequent to soaking, the substrate tube is removed and the ethanol solvent is removed from the substrate N_2 gas to flow through the tube for approximately 15-30 minutes at room temperature. Once this is complete, the substrate tube will now undergo oxidization, dehydration and sintering before being collapsed to form the fibre preform.

⁹ The intensity and duration of the partial sintering is dependent on two factors: the desired porosity of the desired layer, as well as the strength of the solution used. In this case, a partial sintering is carried out at a temperature of between 1400 and 1600°C.

¹⁰ Pre-sintering is carried out in the backward direction, while deposition is carried out in the forward direction.

2.2.4 *Oxidation, Dehydration and Sintering*

Following solution doping, the substrate tube now undergoes oxidation, dehydration and sintering in order to form the glassy core layer. The substrate tube, which has undergone the solution doping process, is again mounted on the lathe of the MCVD rig.

Oxidation

Oxidation was done at a temperature of 800°C to 1000°C in presence of excess O₂ for conversion of the halide or nitrate salts present in the pores into their corresponding oxides. During the oxidation process, the temperature is carefully adjusted and monitored so that no sintering takes place; otherwise, OH⁻ ions may become trapped in the porous layer. This is detrimental, as the presence of OH⁻ will have an effect on the opacity of the fibre, and if sintering takes place, the OH⁻ may become trapped in the collapsed pores – in the worst case scenario, this would render the entire fibre unusable.

Dehydration

Once oxidized, the substrate now undergoes dehydration using a careful combination of temperature, Cl₂:O₂ ratio and time period. The dehydration parameters were experimented to determine the best conditions for an optimal dehydration. The dehydration temperature was varied between 800 and 1100°C with a Cl₂:O₂ ratio of, while the Cl₂:O₂ ratio of was adjusted from 3.5:1 to 1.5:1. The dehydration time was also varied from between one to two hours. It was determined that optimal dehydration of the substrate was obtained at a temperature of about 900°C and a Cl₂:O₂ ratio of 2.5:1, carried out over a period of one hour. This would yield an OH⁻ content of very much less than 1 ppm in the glass core. In the same manner as the oxidation step, care must be maintained to ensure that the dehydration temperature and Cl₂:O₂ ratio does not become very high as this will cause a large amount of the Er³⁺ ions deposited in the porous core layer to evaporate in the form of halides, with the rate of evaporation depending on the K_p value of the associated halogenation reactions.

Sintering

Sintering is the final step before the collapsing of the preform, and involves the gradual heating of the deposited layer within the tube up to the sintering temperature in the presence of O_2 and He to facilitate the sintering process. The sintering temperature is set between 1400 to 1600°C, which is typical for a fibre with a SiO_2 - GeO_2 core¹¹. In most cases, $GeCl_4$ is also supplied at a controlled rate and temperature of between 1250 to 1350°C during the sintering process. The presence of $GeCl_4$ allows the concentration of GeO_2 in the core region to be increased, which can be used to either adjust the numerical aperture of the preform while at the same time compensating for the evaporation of GeO_2 . Once the sintering process is complete, a glassy layer is formed on the inner layer of the substrate tube, and the tube is now ready to be collapsed to form the preform.

2.2.5 Collapsing of the Preform

The final stage in fabricating the EDZF preform is to collapse the substrate tube with the glassy core layer. Because the EDZF is essentially a silica optical fibre, similar to any other silica optical fibre available today, thus the collapsing of the substrate tube is done in a similar manner to that typically seen in the industry. To collapse the tube, the temperature of the oxy-hydrogen burners are increased to above 2000°C and the tube is made to traverse the burner for its entire length 3 to 4 times. During each pass, the traversing speed of the burner was reduced, from 4 cm/min to 2 cm/min over subsequent passes. The collapsing phenomenon is shown in Figure 10, and occurs as a result of the inward viscous flow of mass driven by surface tension as well as the pressure differences between the internal and external portions of the tube.

¹¹ In case of a fibre core with high concentrations of P, sintering can be carried out at temperatures lower than 1400°C.

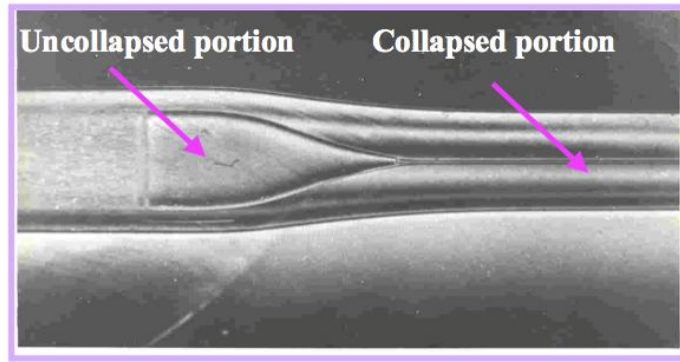


Figure 10: Collapsed substrate tube after deposition

During the collapsing process, it is very important to control of the flow of the additional O_2 as well as tube temperature and pressure differences between the inside and outside portions of the tube so as to maintain the circular geometry of the core, cladding layers and overall preform along the whole collapsing length. In addition, a small flow of $GeCl_4$ is also maintained to neutralize the evaporation of GeO_2 from the core at higher temperatures and reduce the extent of the dip at the center.

Once the collapsing process has been completed, the obtained preform can now be drawn into a fibre. This is described in the next section.

2.2.6 Drawing of the Optical Fibre

The EDZF reform is drawn in a similar manner as to any other optical fibre. The schematic of the fibre drawing process is shown in Figure 11. The completed preform is mounted onto the top of a drawing tower, and secure in a heating furnace. The furnace will heat the preform to between 2000 to 2200°C, allowing it to become viscous enough that the fibre strand may be extracted by a capstan puller from the preform. A pyrometer, together with a temperature regulator, is used to measure and control the heating of the preform. The drawn fibre is then measured using a diameter measuring device, which is connected to a speed regulator. Therefore, if the diameter of the fibre becomes too thin or thick, the drawing speed is adjusted until the diameter is once again at the desired value.

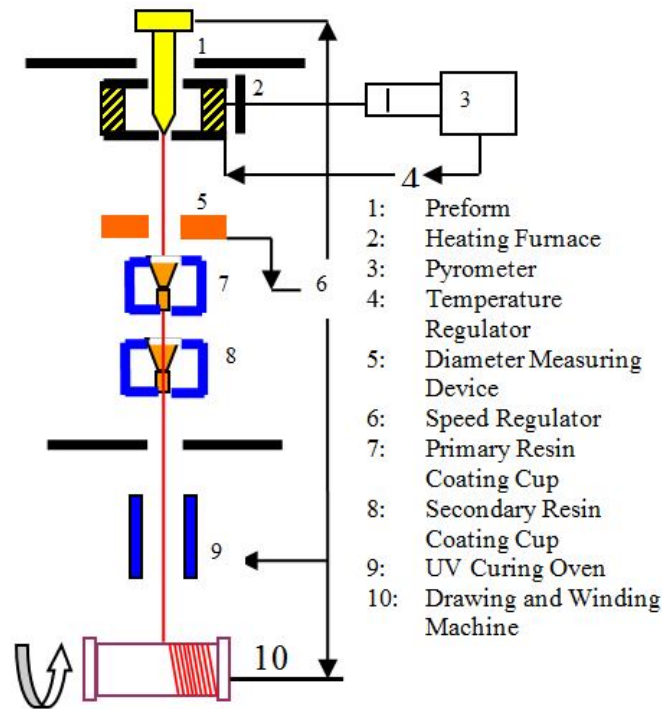


Figure 11: Fibre drawing tower configuration, with dual-coating cups.

Once the optimum diameter has been achieved, the fibre is then coated on-line with a protective polymer coating. In order to do this, the fibre is channeled through the first coating cup, which contains the primary resin coating, and then subsequently through the second coating cup which contains the secondary resin coating¹². As the fibre continues along the drawing path, it will now pass through a UV curing oven, which will cure the primary and secondary resin coatings. It must be noted that until the fibre is drawn and coated with its protective resin or polymer cover, it risks being contaminated. Therefore, special care must be taken in designing the furnaces so that they themselves do not become a source of particle contamination, which will significantly degrade the fibre strength. The final product is then wound along a drum by a winding machine.

¹² The deposition of the acrylate can be done using either the 'Wet-on-Wet' method or 'Wet-on-Dry' method. The 'Wet-on-Wet' method, as the name implies, involves the deposition of the second polymer layer on top of the first layer before it has been cured, thus the two layers are cured together at the same time. The 'Wet-on-Dry' method on the other hand entails the deposition and curing of the first layer, before the second layer is deposited and cured. The 'Wet-on-Wet' approach allows for a quicker deposition process, although it carries an inherent risk, whereby if the inner layer does not cure properly, it would affect the overall integrity of the protective polymer coating. On the other hand, the 'Wet-on-Dry' method is slower, but guarantees a stronger coating. In this work however, the 'Wet-on-Wet' method is applied as the risk of the inner polymer coating failing is deemed negligible.

Control of the fibre diameter is important in a steady-state drawing process where mass-conservation is necessary. During steady-state process, the following relation is derived from mass-conservation rule:

$$\frac{D^2}{d^2} = \frac{v}{V} \dots\dots\dots(7)$$

where D and d are the preform and fibre diameters, while v and V are preform feed down and fibre drawing speeds. Due to local fluctuations, a steady state can sometimes not be achieved at all; this can result non-uniformities in the preform diameter. As this will affect the overall performance of the EDZF, thus it is important to ensure that the diameter of the drawn fibre is measured and controlled precisely, with very tight dimensional tolerances. The fibre drawing speed is typically between 30 m/min to 600 m/min, although in industrial production setups higher drawing speeds can be obtained¹³.

The Ultraviolet (UV) curable resins used for the fabrication of the EDZF are acrylate resins, and are necessary to protect the fibre from contact and foreign particles, as these will affect the life of the fibre in terms of strength and static fatigue. Furthermore, the fibre needs to be protected from microbending, and as such the coating must be concentric and bubble free around the fibre as well as having stable performance under different environments. For the primary coating, Desolite DP-1004 resin is used, while the secondary coating is fabricated from Desolite DS-2015 resin. The primary coating, which is the softer inner layer, protects the fibre and a hard outer layer ensures good mechanical properties. The uniformity of the coating is maintained by adjusting the flow pressure of the inlet gases into the primary and secondary coating resin cups and also by properly aligning the position of primary and secondary coating cup units during the drawing process. A laser concentricity monitor controls the coating process. Bubbles may be formed at the interface of the fibre surface and the hard coating because of the way the coating liquid moves surrounding the surface of the fibre, although this is easily overcome by controlling the pressure and keeping the viscosity of the liquid constant during the drawing

¹³ Industrial fibre drawing techniques use drawing speeds of up to 2000 m/min in a 20 m high tower with proper drawing tension and fibre cooling.

process before it enters the UV curing oven. As a final step, the fibres are wound on a precision spooling machine. The fabrication of the EDZF can be summarized as in Figure 12.

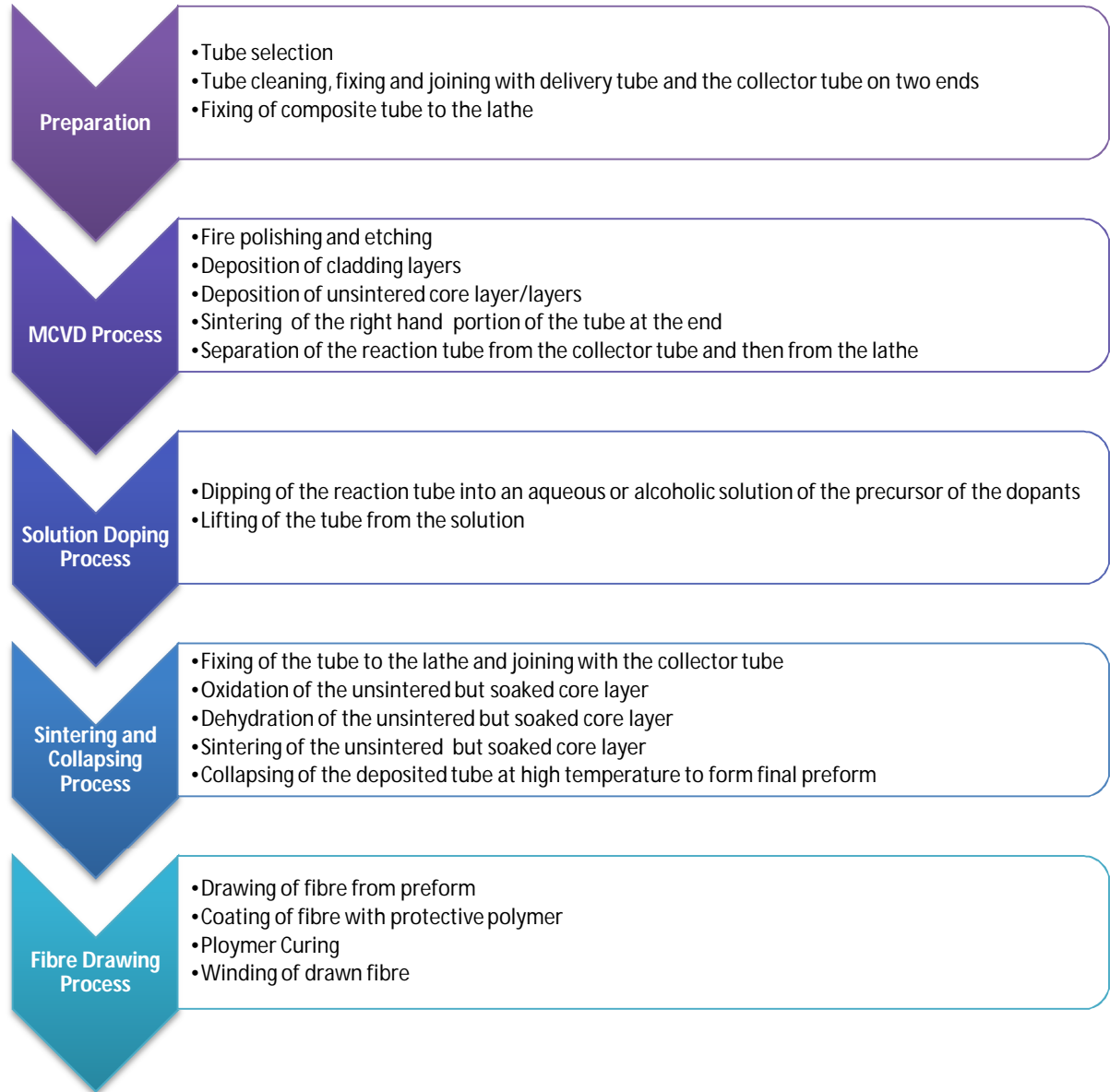


Figure 12: Summarized process flowchart for EDZF fabrication

The following section details the characterization of the EDZF's morphology and spectral characteristics.

2.3 Characterization of the EDZFs

In this work, two EDZF samples (ZEr-A and ZEr-B) are fabricated with increasing the doping levels of Er_2O_3 and ZrO_2 while maintaining almost the same content of Al_2O_3 with changing the composition of the soaking solution of a mixture of $\text{ErCl}_3 \cdot 6\text{H}_2\text{O}$ and $\text{ZrOCl}_2 \cdot 8\text{H}_2\text{O}$. Both EDZF spools are approximately 100 m long. The fabricated samples are characterized for both their physical morphology as well as spectral characteristics. The analysis of the optical performance of the two EDZFs, such as the gain and noise figure is not examined here, but will instead become the focus of the following chapter.

2.3.1 Morphological and Physical Analysis of the EDZF

Before an in-depth analysis is carried out on the fabricated fibre, a simple visual inspection is first carried out. Figure 13 shows the samples of the ZEr-A and ZEr-B fibres as seen normally, without any visual aids or magnification.



Figure 13: ZEr-A (above left) and ZEr-B (above right) (both highlighted by the red boxes) sample fibres as seen without any magnification. Due to the fibres being very thin, they are not easily visible, even when placed on a contrasting background. As such, the red box is used to highlight the fibres in the figures above.

It can be seen that the both the ZEr-A and ZEr-B fibres are formed as expected. Visual inspection of the lateral surfaces of the fibre reveals a smooth polymer layer, thereby indicating that there are no bubbles or other deformities present in the polymer coating.

The surfaces of the fabricated EDZFs are also examined using an Olympus BX51 operating 200x magnification. The images obtained are shown in Figure 14.

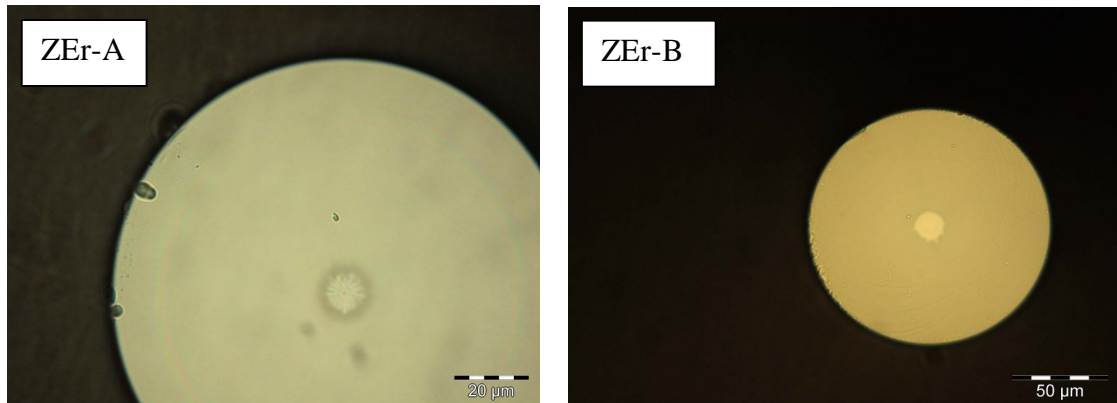


Figure 14: View of the surface of the two EDZFs (ZEr-A, *above left*, and ZEr-B, *above right*) under 200x magnification.

It can be seen that the microscopic views of the two EDZFs are very much similar, with both EDZFs having a very distinct core, surrounded by the cladding. Both EDZFs have a core diameter of approximately 10 μm , taking the internal ring of the core. It can also be seen that the core is homogeneous and shows no observable defects at the interface between the silica cladding and the core. Therefore it can be construed that in physical terms, the fabricated fibre is well within its design parameters.

However, of greater concern is the morphology of the crystalline structures formed within the EDZFs. As ZrO_2 can sustain the crystalline nature of the host matrix at high temperatures, comparable to those required for the collapsing of the substrate rod and also for the drawing of the fibre, it is thus expected that the ZrO_2 will retain crystalline nature in some portions of the core glass matrix of preform as well as the fibre. The core region morphology of selected ZEr-A and ZEr-B preform samples, developed without any thermal treatment or annealing, is studied using Field-Emission Gun Scanning Electron Microscopy (FEGSEM). An analysis of the

microstructures in the doping region of the preforms tested is given in Figure 15. It can be seen clearly from the figure that the ZEr-B fibre, which is richer in ZrO_2 micro-crystallites than the ZEr-A fibre, has micro-crystallite structures with better defined boundaries than that of the ZEr-A fibre, as is to be expected. The presence of the ZrO_2 micro-crystallites is an important factor, as this will affect the non-linear characteristics of the EDZF.

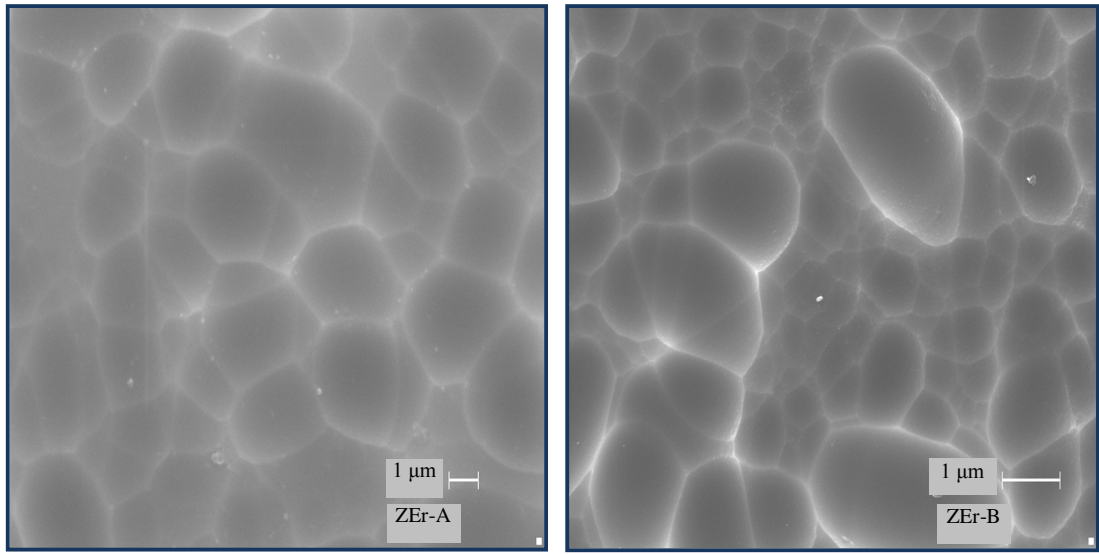


Figure 15: The microstructure of the core region of optical fibre preforms ZEr-A (*above left*) and ZEr-B (*above right*)¹⁴.

The presence of the ZrO_2 micro-crystallites in the ZEr-B after the drawing process is confirmed by Tunneling Electron Microscopy (TEM), as shown in Figure 16.

X-Ray Diffraction (XRD) is also carried out on samples of the fibre preform, and the XRD curve obtained is shown in Figure 17. From the curve, a small diffraction peak is detected at a 2θ value of about 30° , indicating the formation of tetragonal ZrO_2 in the host matrix [60]. In bulk zirconia-silicate ($\text{ZrO}_2\text{--SiO}_2$) glass, phase-separation has been observed at temperatures below the onset of crystallization that also results in structural homogeneity. This phenomenon, known as phase separation or immiscibility, is a phenomenon that is known to exist in amorphous binary systems. However in some $\text{ZrO}_2\text{--SiO}_2$ system, immiscibility exists even in the stable liquid phase above the melting point.

¹⁴ Figure adapted from that in H. Ahmad, M. C. Paul, N. A. Awang, S. W. Harun, M. Pal and K. Thambiratnam, "Four-Wave-Mixing in Zirconia-Yttria-Aluminum Erbium," *J. Europ. Opt. Soc. Rap. Public.*, vol. 7, pp. 12011-1 - 12011-8, 2012.

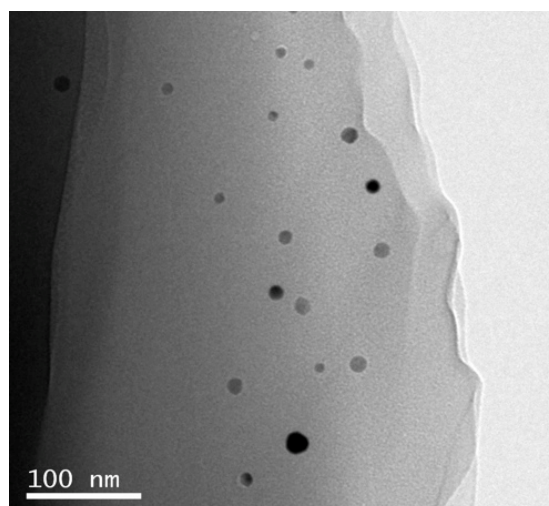


Figure 16: TEM spectroscopic analysis of ZEr-B¹⁵.

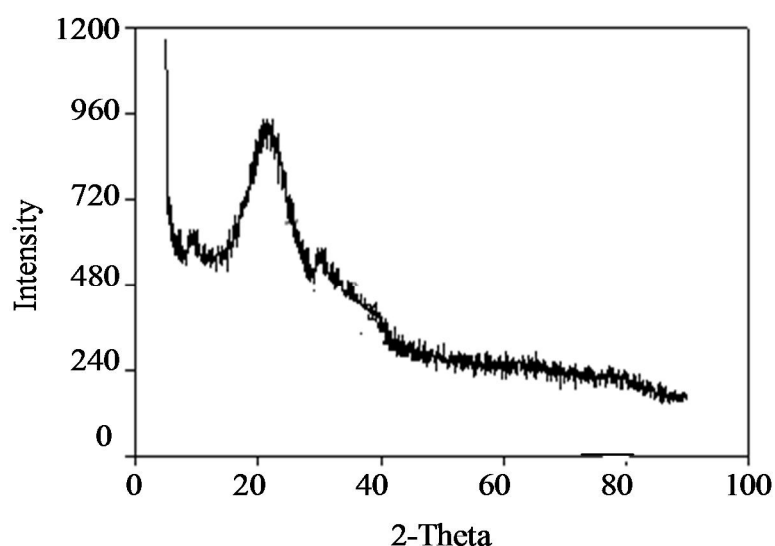


Figure 17: XRD curve obtained for ZEr-B preform, with small diffraction peak at 2θ of $\sim 30^\circ$.

The phase diagram of $\text{ZrO}_2\text{--SiO}_2$ system, obtained from the evaluation of the FactSage software¹⁶ is given in Figure 18. It can be seen that a stable immiscibility zone exists at a molarity ratio of 60–80 mole% in favor to SiO_2 (or alternatively, 40–20% mole% in favor of ZrO_2) up to temperatures of about 2250°C . The stable immiscibility zone extent to temperatures lower than the melting point and gives a metastable

¹⁵ Figure adapted from that in Chapter 2: Nano-Engineered Glass-Based Erbium Doped Optical Fibers for Study of Multi-Channel Amplification and Four-Wave Mixing Phenomena, M. C. Paul, M. Pal, K. Thambiratnam, S. W. Harun, N. A. Awang, S. Das, S. K. Badhra, H. Ahmad and J. K. Sahu. Rare Earths: New Research (Chemistry Research and Applications: Materials Science and Technologies) (Zhaosen Liu (Editor)) Nova Science Publishers Inc. (1 July 2013, Hauppauge, New York, No. of pages: 289, ISBN-10: 162618996X)
¹⁶ www.factsage.com

immiscibility zone in a wide composition range where phase separation normally occurs in an amorphous state.

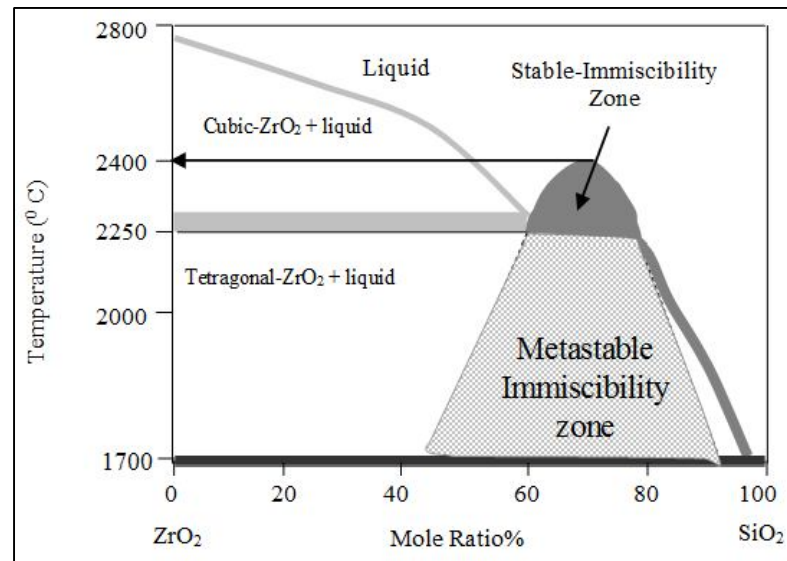


Figure 18: Phase-diagram of SiO₂-ZrO₂ system obtained using the Fact-Sage software

It is worth noticing the different forms in which the ZrO₂ crystallites can take in the system, depending on the temperature. At a high temperature of 2350°C and above, the ZrO₂ molecules take on a cubic structure, while at a lower temperature range of between 1170°C to 2250°C, the molecules take on a tetragonal structure instead and a mono-clinic structure when the temperature is below 1170°C. This represents a serious problem in the fabrication process - the shift from the tetragonal to monoclinic phases occurs very fast and will incur an increase of between 3 to 5% in volume. This rapid increase, encountered during the cooling process as the temperature drops quickly from more than 2400°C to less than 1000°C, results in significant cracking in the drawn fibre, especially in the core region as this is where the concentration of the ZrO₂ crystallites is highest and can essentially destroy the mechanical properties of the fibre. However, this problem can be overcome by adding a minute amount of Y₂O₃, or even oxides such as MgO, CaO, which can suppress the changes in the crystalline structure and thus preserve the integrity of the fibre. It is also expected that the separated ZrO₂ and Al₂O₃ phase in the EDZF will mix together when heated at high temperatures. Generally, the homogeneous ZrAl_xO_y amorphous mixture is thermodynamically more stable than the separated two phases, and thus the two

separated phases ZrO_2 and Al_2O_3 will tend to mix into a homogeneous mixture before crystallization.

In addition to the physical structure of the fibre, the concentration levels of the various dopants in the EDZFs are analyzed through Electron Probe Micro-Analysis (EPMA). The obtained results from the EPMA are given in Table 2.

Table 2: Doping levels within core region of the preforms

Preform	Al_2O_3 (mole%)	ZrO_2 (mole%)	Er_2O_3 (mole%)
ZEr-A	0.25	0.65	0.155
ZEr-B	0.24	2.21	0.225

It can be seen from the results of the EPMA given in Table 2 that the ZEr-A and ZEr-B contain almost similar amounts of Al_2O_3 with dopant concentrations of between 0.24-0.25 mole%. However, the ZrO_2 dopant concentration in the ZEr-B fibre is higher, at 2.21 mole% as compared to only 0.65 mole% in the ZEr-A fibre. Similarly, the Er_2O_3 dopant concentrations for ZEr-A and ZEr-B are 0.155 and 0.225 mole% respectively, as is to be expected.

The next section will detail the measurement and characterization of the spectral properties of the EDZF.

2.3.2 Spectral Measurement and Characterization of the EDZF

Spectral characterization of the EDZF will give an understanding of the optical properties of the EDZF. It must be noted that the spectral characterization of the EDZF investigates only the spectroscopic properties of the fibre, such as absorption coefficient, fluorescence and fluorescence decay curves, and does not include optical signal measurements such as the ASE or the gain and noise figure levels. Spectral characterization of the EDZF is carried out with the use of a Bentham spectral loss system, which has the advantage of modularity. The system consists of a chopped white light source, a monochromator, launch optics, detectors and a lock in amplifier. The whole system is controlled by software, allowing for easier control and also

providing real-time measurement and computation of the spectral losses at any wavelength in dB/Km. Figure 19 provides the schematic setup of the system.

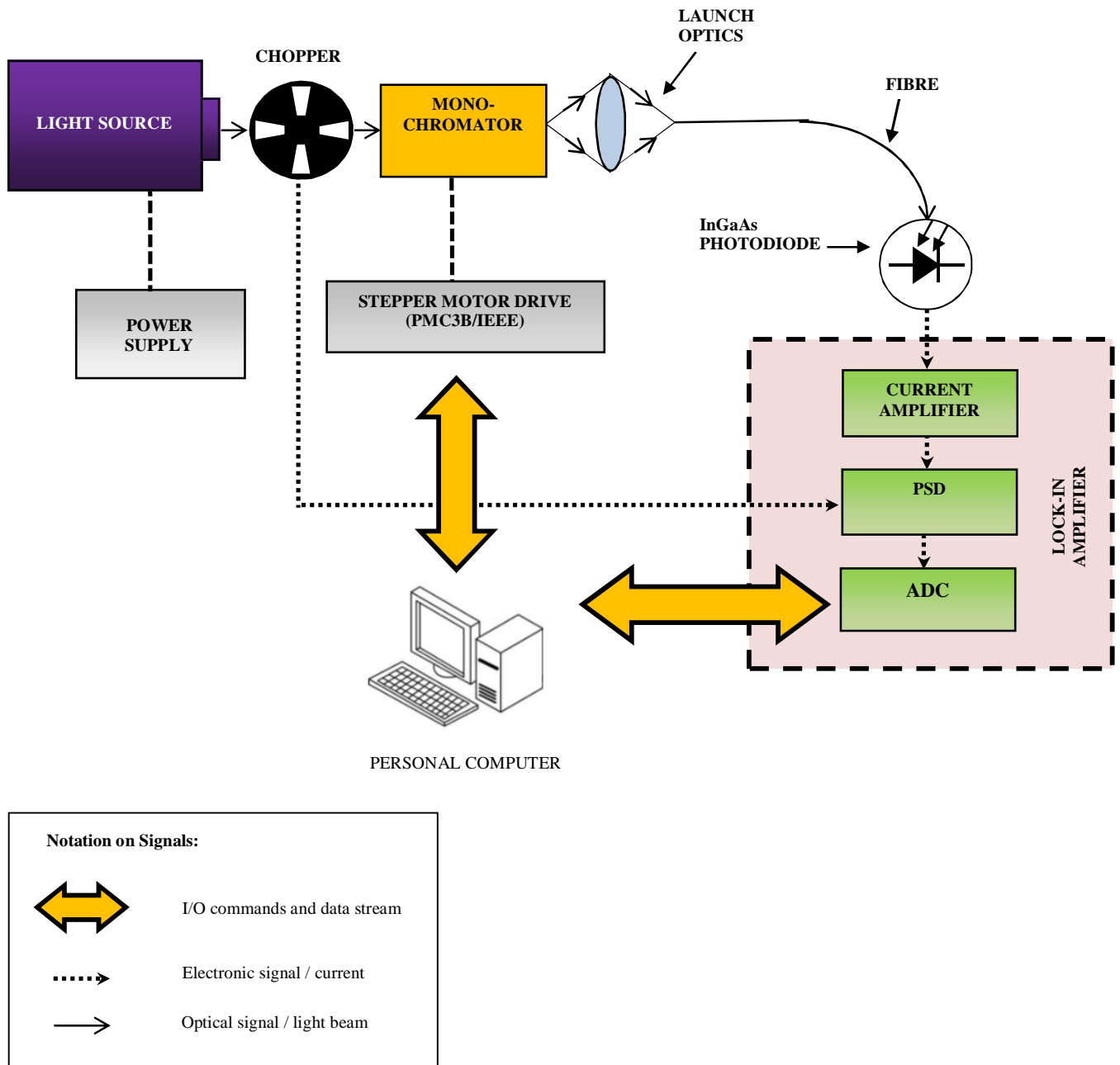


Figure 19: Setup of the Bentham spectral attenuation measurement system

The system uses a 10 W quartz halogen light source with an aspheric lens as the primary light source for the system. The light source is powered with a constant 8.5 A current, and provides a stable output with fluctuations of less than +0.1% over an 8-hour period. The monochromator system consists of Czerny Turner optical

configuration which has a 300 mm focal length mount with 69 mm x 69 mm plain diffraction gratings, variable slits, adjustable from 0.01 mm to 5.5 mm and a stepper motor for controlled wavelength selection. An optical chopper is placed between the quartz light source and the monochromator. The monochromator is controlled by a PMC3B/IEEE¹⁷ stepper motor driver, which in turn is controlled by a personal computer. The output of the monochromator is connected to the launch optics, which includes a precision x-y-z positioner¹⁸, which will focus the light into the fibre under test. The fibre being tested is held in a bare fibre chuck capable of holding fibres with diameters from a few microns up to a maximum of 250 μm . An Indium-Gallium-Arsenide (InGaAs) photodiode with a 2 mm housing diameter is connected to the fibre chuck together with an adaptor. The LS4A lock-in-amplifier used in this setup uses a programmable current preamplifier, connected to a voltage sensitive lock in the module as well as an integrated analog to digital converter. The integrating analog to digital converter digitizes the lock-in output and passes it to the computer, allowing for the maximum use of the signal information available and for the computer to conduct digital averaging straight away. The software controlling the lock-in amplifier is based in a personal computer, which also controls the entire system via the IEEE/488 General Purpose Interface Bus (GPIB) interface.

The operation of the spectral measurement system begins with the selection of the starting and finishing wavelengths, as well as the spectral resolution and signal averaging period. Automatic zero routines will address any drift in electronic offsets by making a zero level measurement prior to each spectral run. The modulated white light is then allowed to pass through the monochromator before being launched into one end of the fibre under test. The light emerging from the other end of the fibre is collected by the large area InGaAs diode and the resulting signal amplified by a lock-in-amplifier. The spectral curve is obtained from the lock-in amplifier is then computed and stored by the computer. The fibre at the detector end is then taken out and a short length is selected, cleaved and reinserted in the detector assembly, after which a new spectral curve measurement is run and the obtained data stored.

The spectroscopic properties such as absorption coefficient, fluorescence and fluorescence decay curves of the fabricated fibres can be measured by the system. When placed under test, the ZEr-A fibre shows a peak at 980 nm, with a loss of about

¹⁷ IEEE designates that the driver can be controlled by an IEEE/488 General Purpose Interface Bus (GPIB)

¹⁸ Adjustments of the x-y-z positioner are carried out manually.

16.5 dB/m, as well as a second peak at 1550 nm with a spectral attenuation of around 27.5 dB/m. The ZEr-B fibre sample also shows two attenuation peaks, the first occurring at 980 nm, with a loss of about 22.0 dB/m, while the second occurs at 1550 nm, with a loss of around 53.0 dB/m. These results are as expected, as the spectral attenuation curve of the fibre will be heavily influenced by the concentration of Erbium ions within the fibre. It is worthwhile to note that both fibres also show a peak at 800 nm, approximately 6.0 dB/m for the ZEr-A and 8.0 dB/m for the ZEr-B. The spectral attenuation curves of both fibres are shown in Figure 20.

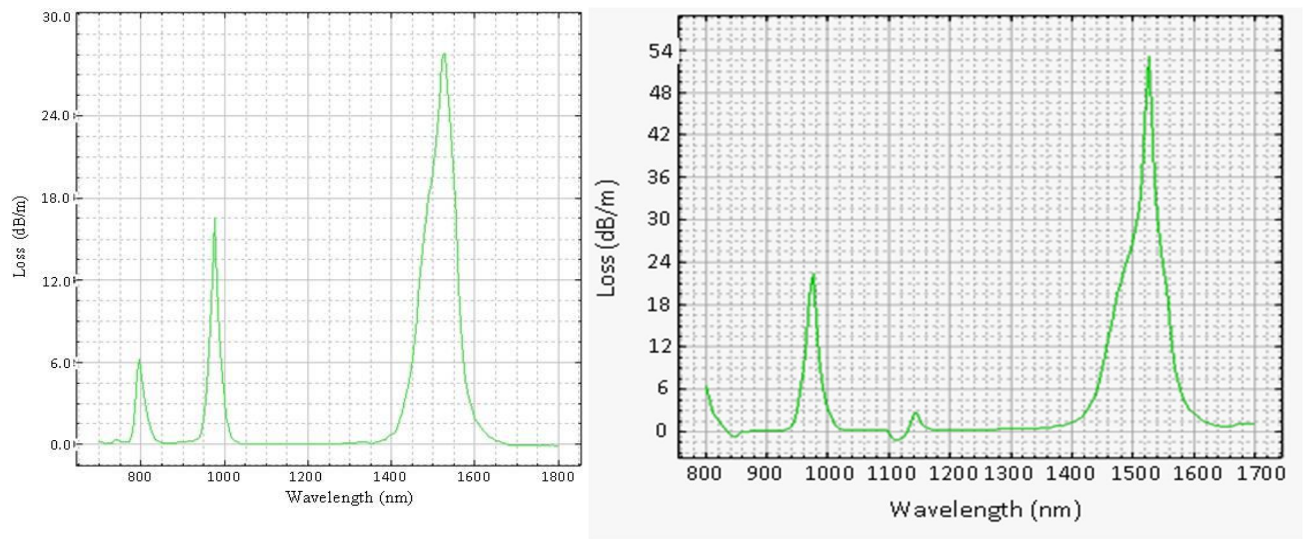


Figure 20: Spectral attenuation curve of ZEr-A (*above, left*) and ZEr-B (*above, right*)¹⁹

The fluorescence spectra of the fibre samples were measured by laterally pumping, the fibres at 980 nm and a power of 100 mW. The fluorescence curves for both fibres are shown in Figure 21, while Figure 22 shows the fluorescence decay curves of both.

¹⁹ Figure modified from that in H. Ahmad, M. C. Paul, N. A. Awang, S. W. Harun, M. Pal and K. Thambiratnam, "Four-Wave-Mixing in Zirconia-Yttria-Aluminum Erbium," *J. Europ. Opt. Soc. Rap. Public.*, vol. 7, pp. 12011-1 - 12011-8, 2012.

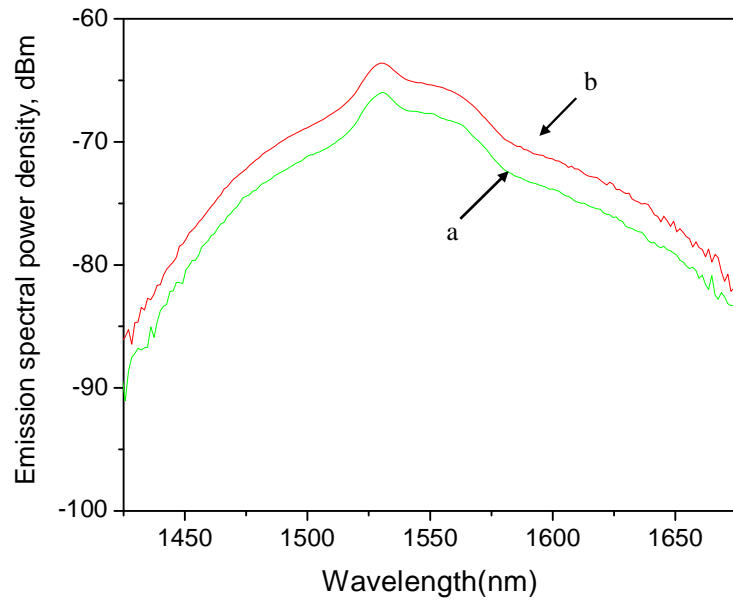


Figure 21: Fluorescence curves of the (a) ZEr-A and (b) ZEr-B fibres at a pump power level of 100 mW²⁰.

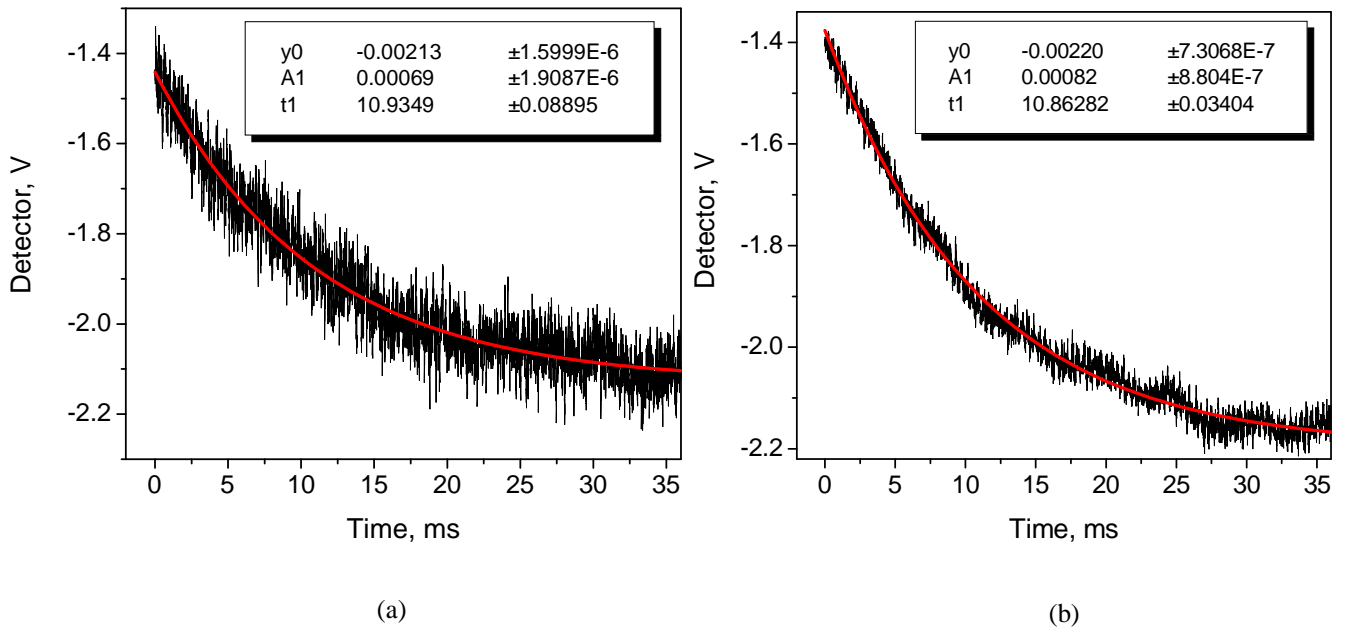


Figure 22: The fluorescence decay curves of the (a) ZEr-A and (b) ZEr-B fibres at a pump power level of 100 mW²¹.

20 Figure modified from that in H. Ahmad, M. C. Paul, N. A. Awang, S. W. Harun, M. Pal and K. Thambiratnam, "Four-Wave-Mixing in Zirconia-Yttria-Aluminum Erbium," *J. Europ. Opt. Soc. Rap. Public.*, vol. 7, pp. 12011-1 - 12011-8, 2012.

21 Figure modified from that in H. Ahmad, M. C. Paul, N. A. Awang, S. W. Harun, M. Pal and K. Thambiratnam, "Four-Wave-Mixing in Zirconia-Yttria-Aluminum Erbium," *J. Europ. Opt. Soc. Rap. Public.*, vol. 7, pp. 12011-1 - 12011-8, 2012.

It can be seen from the figures that the two fibres, ZEr-A and ZEr-B, show almost the same fluorescence life-times of 10.93 and 10.86 ms respectively. Fibre ZEr-B however, which has higher doping levels of Er_2O_3 and ZrO_2 , shows a slight shorter fluorescence life-time. These results indicate that the concentration-quenching phenomenon, which is typically associated with high Er^{3+} ions concentrations, is strongly reduced through an increase in the doping levels of ZrO_2 .

2.3.3 *Measurement of Refractive Index Profile*

The measurement of the fibre's refractive index profile is obtained by the refracted near field method, with the setup of the system given in Figure 23. The measurement system consists of a 0.5 W Helium-Neon (He-Ne) laser as the light source, with a quarter wavelength plate placed just after the light source to change the polarization of the light beam from linear to circular. The circularly polarized light is then focused by using launch optics, consisting of lenses with an aperture of about $10\text{ }\mu\text{m}$ as well as a reasonable NA, together with a 50X objective at the surface of the fibre under test. The fibre itself is placed in a liquid cell filled with glycerol, which has a refractive index of 1.471, higher than that of the fibre. A part of the focused light is transmitted through this fibre while the rest is refracted into the air through the cladding, forming a light cone around the fibre. The liquid cell, together with the fibre is moved using a stepper motor with an accuracy of $\pm 1\text{ }\mu\text{m}$ so that the focused light spot traverses across the fibre core. A central stopper fixed on the center of the light collecting lenses blocks the guided light from the core, so that only the refracted light emerges and is collected by the receiving optics. The receiving optics focuses the collected light onto a detector, and the signal from the detector is amplified before being routed to an XY detector. The power of the refracted light varies in accordance with the refractive index at the point where the cell's light spot is focused on the front surface of the fibre. A complete scanning along the diameter of the fibre gives a profile from which the refractive index of the core and cladding layer can be accurately determined, along with the dimensional ratio of the fibre.

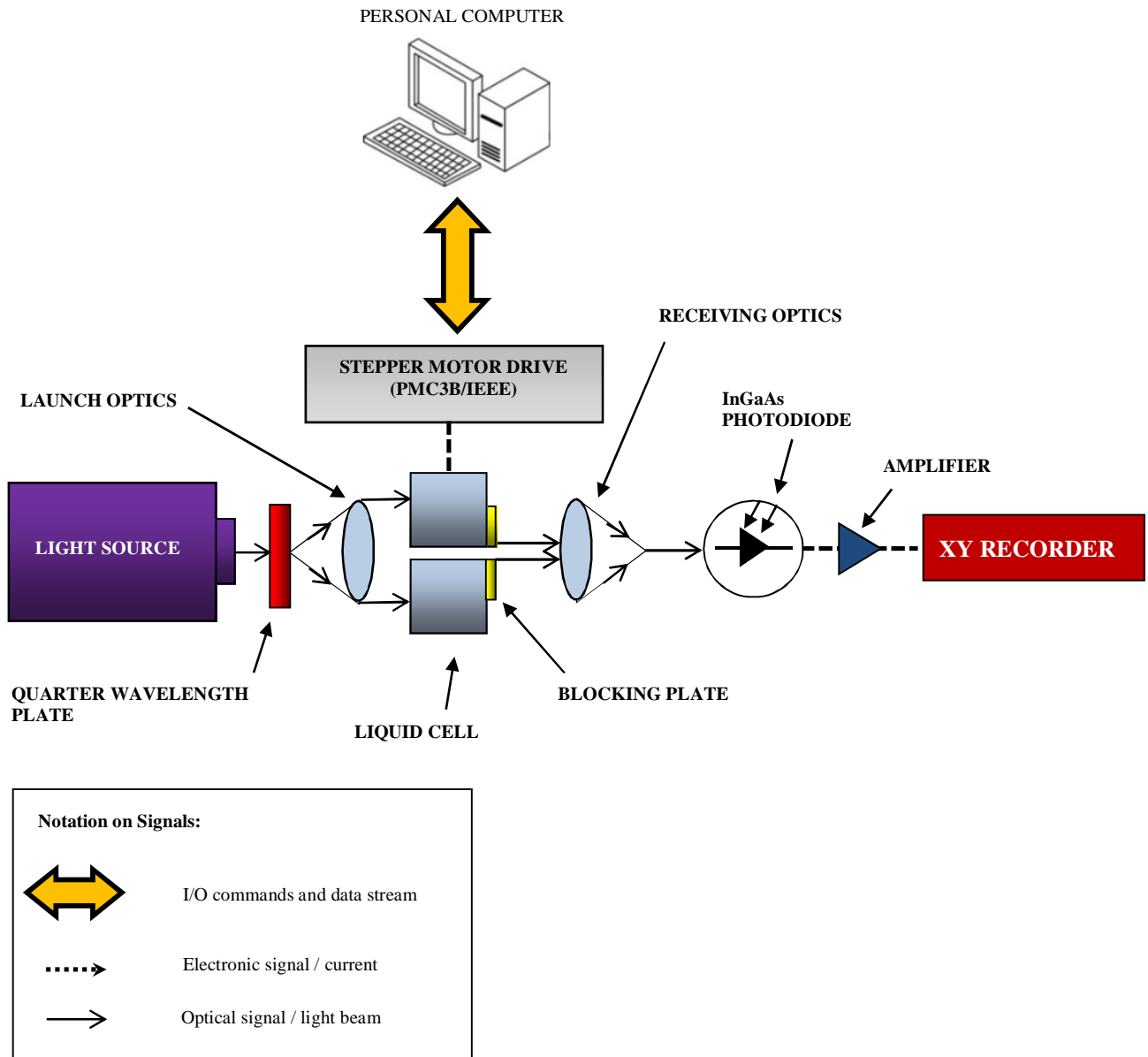


Figure 23: Schematic diagram of refracted near field set up

From the refractive index values of core and cladding layer, the numerical aperture of the fibre can be determined as follows:

$$NA = \sqrt{(n_1^2 - n_2^2)} \dots\dots\dots(.8)$$

where n_1 and n_2 are the refractive index values of the core and cladding layer respectively. The cladding dimension of the fibre is equal to the distance between two points from which the refractive index becomes lower, relative to silica level, and the

core dimension is equal to the distance between two points from which refractive index becomes higher, relative to the cladding layer. Figure 24 shows the refractive index of the fibre as measured by the above setup.

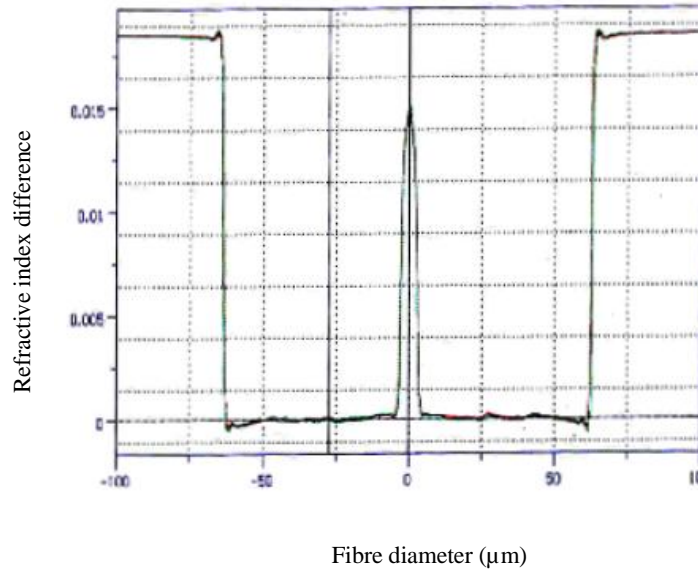


Figure 24: Refractive index profile of the EDZF. The profile given above is that of the ZEr-B sample²²

As can be seen from the figure, the refractive index profile of the ZEr-B, as well as the ZEr-A fibres follows the standard W-profile.

2.4 Summary and Conclusion

In this chapter, the fabrication of the EDZF is first analysed. The fabrication process is carried out by using the same processes in which conventional fibres and EDFs are fabricated, with only a minor change being made during the solution doping process before the developed porous layer is sintered, collapsed and drawn into a fibre.

²² Figure modified from that in H. Ahmad, M. C. Paul, N. A. Awang, S. W. Harun, M. Pal and K. Thambiratnam, "Four-Wave-Mixing in Zirconia-Yttria-Aluminum Erbium," *J. Europ. Opt. Soc. Rap. Public.*, vol. 7, pp. 12011-1 - 12011-8, 2012.

The process begins with a hollow silica tube with good optical transparency, relatively high drawing temperatures and good mechanical strength and non-hygroscopic properties as the base material. The tube is cleaned and then made to undergo the MCVD process, where O_2 , N_2 and CCl_2F_2 gasses are fed through $SiCl_4$, $GeCl_4$ & $POCl_3$ in a liquid form in the bubbler to generate SiO_2 , GeO_2 & P_2O_5 gases. The deposition process is carried out using an oxy-hydrogen burner at a temperature of 1250-1300°C along the direction of the reactant flow containing the $SiCl_4$, $GeCl_4$, $POCl_3$ vapors. A dopant control program was used to adjust the NA values to within the range of 0.15-0.25 with a core diameter of between 5.0-6.0 μm , with the relative density of the soot layer estimated on the basis of RE concentration ranging between 0.30 to 0.50. Once the porous soot layer has been deposited on its inner layer, the tube is then made to undergo the solution doping process. An alcoholic-water mixture at a ratio of 1:5 with a suitable strength was used to form $ErCl_3 \cdot 6H_2O$, $ZrOCl_2 \cdot 8H_2O$ & $AlCl_3 \cdot 6H_2O$, with the strength of the $ErCl_3 \cdot 6H_2O$ was adjusted between 0.005 M to 0.010 M, while the strength of the $ZrOCl_2 \cdot 8H_2O$ & $AlCl_3 \cdot 6H_2O$ complexes adjusted to between 0.1 M to 1.0 M. Small amounts of Y_2O_3 and P_2O_5 are also added to serve as nucleating agents. Subsequently, the doped tube is now oxidized at 800°C to 1000°C before being dehydrated using a careful combination of temperature, $Cl_2:O_2$ ratio and selected time period, and finally undergoing a sintering process at a temperature of between 1400 to 1600°C. The completed tube is then collapsed at a temperature of above 2000°C to form the preform. Fibre drawing is carried out using a drawing tower, and the drawn fibre is measured using a diameter measuring device, and coated with Desolite DP-1004 resin as the primary coating as well as Desolite DS-2015 resin as the secondary coating.

Two fibres are drawn, ZEr-A and ZEr-B, with different dopant concentrations. Visual inspection of the lateral surfaces of the both fibres shows a smooth polymer layer, indicating that no bubbles or other deformities present in the polymer coating and a very distinct core with a diameter of approximately 10 μm under microscopic view. The core region morphology of selected ZEr-A and ZEr-B preform is studied FEGSEM, and the ZEr-B fibre is seen to have micro-crystallite structures with better defined boundaries than the ZEr-A fibre, owing to its higher ZrO_2 ion concentrations. The presence of the ZrO_2 rich micro-crystallites is further confirmed by TEM scanning. XRD analysis of the preform samples shows a small diffraction peak is detected at a 2θ value of about 30° , indicating the formation of tetragonal ZrO_2 in the

host matrix. An EPMA analysis of the preform samples gives an almost equivalent level of Al_2O_3 dopants in both fibres, at about 0.24-0.25 mole%. However, the ZEr-B preform has significantly higher ZrO_2 and Er_2O_3 dopant concentrations, at approximately 2.21 mole% and 0.155 mole% respectively, as compared to concentrations of only 0.65 mole% and 0.225 mole% for the same dopants in the ZEr-A fibre.

Spectral characterization of the EDZF, carried out with the use of a Bentham spectral loss system, gives details on the absorption coefficient, fluorescence and fluorescence decay curves of the fabricated fibres. The ZEr-A fibre shows a peak at 980 nm with a loss of about 16.5 dB/m as well as a second peak at 1550 nm with a spectral attenuation of around 27.5 dB/m. Similarly, the ZEr-B fibre sample also shows two attenuation peaks at the same wavelengths, with attenuation rates of around 22.0 dB/m and 53.0 dB/m at 980 nm and 1550 nm respectively and also a peak at 800 nm, with spectral attenuations of 6.0 and 8.0 dB/m. Measured fluorescence life-times are 10.93 and 10.86 ms for the ZEr-A and ZEr-B fibres respectively. The slightly shorter lifetime of the ZEr-B fibre, which can be attributed to the higher dopant concentrations of that fibre, is crucial as it indicates that the concentration-quenching phenomenon typical associated with high Er^{3+} ions concentrations is strongly reduced in the presence of high ZrO_2 doping levels. Examination of the refractive index profile of the ZEr-B, as well as the ZEr-A fibres gives a standard W-profile that is to be expected of the optical fibre.

In the following chapter, the application of the EDZF as an active medium will be examined. Due to the ZEr-B's higher dopant concentration, all subsequent research will be carried out using this fibre. Of particular interest would be to use the EDZF as a gain medium for the development of a compact SLM fibre laser, as the high dopant concentrations in the EDZF will allow the cavity length of the proposed laser to be reduced significantly, a crucial criteria for the generation of the SLM output. The next chapter will also examine the possible application of the EDZF as a non-linear medium, as the incorporation of the ZrO_2 rich micro-crystalline structures in the host matrix will allow non-linear phenomena to manifest in light signals of relatively low intensity, whereas the same phenomena will only manifest itself in conventional SMFs at much higher intensities. This makes the EDZF a particularly useful candidate for the development of exotic all-optical components such as wavelength converters.

3. ZIRCONIA–YTTRIA–ALUMINO SILICATE GLASS-BASED ERBIUM-DOPED FIBRE AS AN AMPLIFIER, LASER AND NON-LINEAR GAIN MEDIUM

3.1 *Introduction*

While the focus of this research is primarily aimed towards the understanding and development of compact, short-pulsed fibre lasers built around the EDZF, we would like to reiterate that the original motivation behind the development of the EDZF was to develop an EDF with a high dopant concentration for compact EDFAs. Therefore, the EDZF possess the same optical characteristics as a conventional EDF.

In this chapter, the basic principles that define the optical behavior of EDZF is discussed. The chapter will focus on two primary aspects - the linear characteristics of the EDZF, covering the conventional performance parameters such as the ASE, gain and NF of the EDZF, as well as the non-linear characteristics of the fibre, in particular the FWM effect. The subsequent section will provide a background on the theoretical fundamentals that define the behavior of the erbium ions when incorporated into the host matrix, and subsequently the behavior of the EDZF.

3.2 *EDFA Theory*

The ability to amplify optical signals proved to be the key factor in making fibre optics the dominant means for long-range, high capacity communications in the modern world. While the amplification of optical signals was possible before through the use of electronic regenerators the limitations imposed by this technique, in particular the fact the dedicated regenerator was required for each transmission wavelength, made the simultaneous amplification of multiple signals very costly and thereby hindering optical systems from reaching their true potential. The advent of the EDFA in the late 1980s however changed this. EDFAs are broadband optical amplifiers that allow a single EDFA to simultaneously

amplify multiple optical signal, thus allowing high capacity optical communications systems to see worldwide deployment. Furthermore, the robustness and relatively compact form of the EDFA, as well as its versatility in the development of systems such as fibre lasers also proved highly attractive.

The inherent capabilities of the EDFA arise from the Er^{3+} ions that are integrated into the matrix of the silica host. Under exposure to incident light at a wavelength of 980 nm, the Er^{3+} ions are excited to higher energy levels, wherefrom these excited ions quickly relax to the lower $^9\text{I}_{11/2}$ level where they stay for about 10 ms. This intermediate level forms a metastable state, and the energy difference between the $^4\text{I}_{31/2}$ and the ground level of $^4\text{I}_{51/2}$ correspond to a wavelength of 1550 nm. Due to the Stark effect, each energy level is split into multiple levels, and thus a band of signals around 1550 nm can stimulate a broadband emission while the excited ions fall back to the ground state²³. By a remarkable coincidence, this wavelength falls within the third optical communications window where the attenuation in silica fibres is lowest and thus makes the EDFA the most suitable choice for amplification [53]. This, combined with the fact that the EDFA is essentially a fibre based device and therefore easily integrated into current optical communications infrastructure, made the amplifier the natural choice for most optical signal amplification applications.

3.2.1 Characteristics of Er^{3+} ions in a Silica Glass Matrix

Rare earth atoms can be divided into two groups, falling either under the category of lanthanides or actinides. These elements are most commonly found in their ionic form as bivalent or trivalent ions, and the element Erbium falls within this group, categorized as a trivalent lanthanide element with an ionic form of Er^{3+} . Trivalent lanthanides are a group of elements that have unparalleled importance in the development of active fibres, as laser oscillation in a glass host can only be observed in these ion groups [61].

Silica fibres are known to be a highly suitable host for Er^{3+} ions. Silica fibres are essentially glass, and therefore exists in a fusion cooled state without crystallizing. At the micro scale, the structure of glass is well defined and organized. However,

²³ This process is known as down-conversion, as the photons emitted are at a longer wavelength and therefore have lower photon energies. Up-conversion on the other hand occurs when the emitted photon is at a shorter wavelength, indicating that the photon energies are higher. This occurs when the excitation mechanisms involve more than one photon absorbed for each emitted photon.

moving towards the macro scale, it can be seen that the structure of a glass becomes completely random, asymmetric and aperiodic. The glass lattice is built around network former units made from tetrahedron SiO_4 molecules and are connected to each other by a bridging oxygen atom as shown in Figure 25.

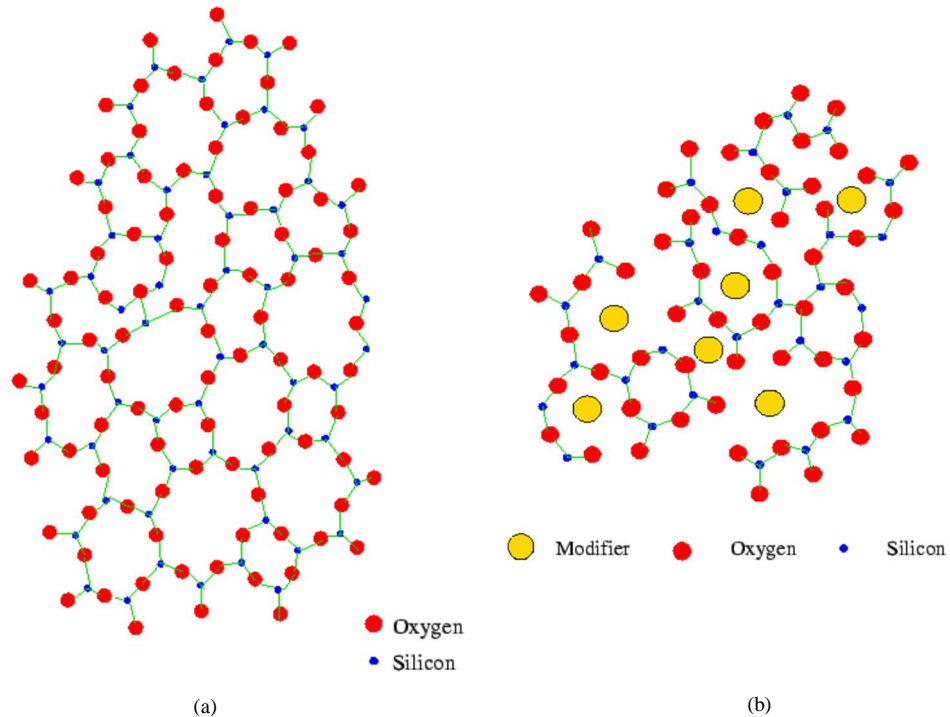


Figure 25²⁴: (a) Silicate glass structure based on $(\text{Si}^{4+}, \text{O}^{2-})$ network formers with no additional glass formers present. It can be seen that all ions are bridged, thus making it almost impossible to integrate new ions into the structure. (b) Silicate glass structure based on the same network formers, but now with alkali ions incorporated as network modifiers. It can be seen here that the bridging ions have now become non-bridging ions, making the addition of dopant ions significantly easier.

However, herein lies the problem – the bond by the bridging ions is very strong and cannot be easily broken, thus preventing the Er^{3+} ions from being easily incorporated into the host matrix. To overcome this barrier, the inclusion of certain glass modifiers becomes necessary, such as alkali and alkaline earths. These modifiers break the lattice and disrupt the network glass structure by causing the bridging ions to become non-bridging ions and subsequently allow Er^{3+} ions to be integrated within the silica matrix [62].

²⁴ Source: <http://www.cdeep.iitb.ac.in/nptel/Electrical%20&%20Comm%20Engg/Optical%20Communication/Mod-14/Slides>

3.2.2 Energy Levels of Er^{3+} Ions in Silica Host Matrix

Trivalent Er^{3+} ions are the active elements in the EDF, and are responsible for the optical characteristics of the fibre. The ability of the EDF to impart gain to the optical signals that traverse this fibre when it is active is due to the transitions of the electrons between the various energy levels of the Er^{3+} ion in its active state.

As with any active laser material, Er^{3+} ions are capable of stimulated absorption as well as stimulated and spontaneous emission [63]. Absorption occurs as incident photons traverse the length of the fibre doped with the active material, and are absorbed by the active ions by shifting the orbiting electrons from the lowest or most stable energy level, the ground state, to a higher energy level, known as the excited state. In the case of the Er^{3+} ion, the various energy levels and their relevant optical transitions are shown in Figure 26.

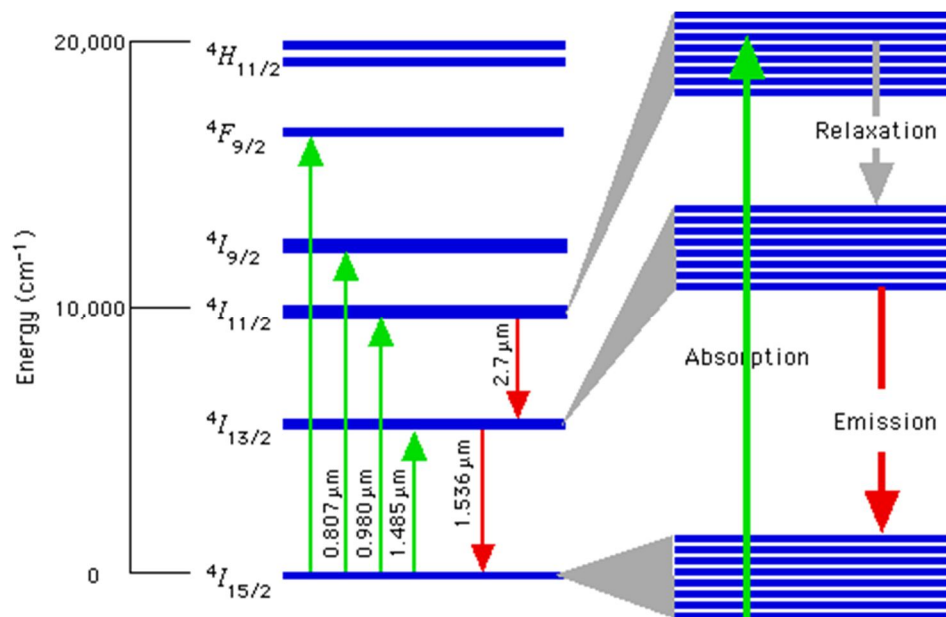


Figure 26²⁵: Partial energy diagram for the trivalent erbium ion.

25 Source: http://people.seas.harvard.edu/~jones/ap216/lectures/ls_2/ls2_u5/ls2_unit_5.html

For Er^{3+} ions, a three-level pumping system is formed, with the majority of the electrons orbiting the ion being located at the $^4\text{I}_{15/2}$ ground state²⁶ [10] at any given time. In the presence of a traversing photon however, particularly one whose wavelength corresponds to the energy levels required for excitation, excitation will occur and result in the electron being excited to the higher energy states. The energy state to which the photon is excited to is dependent on the wavelength of the incoming photon, whereby a photon at 980 nm will result in the electron transiting from $^4\text{I}_{15/2}$ to $^4\text{I}_{11/2}$, while a photon at 1480 nm will result in a transition from $^4\text{I}_{15/2}$ to $^4\text{I}_{13/2}$. Transitions are also possible at different wavelengths, such as 907 nm, which will give a transition to the $^4\text{I}_{9/2}$ level, but due to the relatively high energy needed and the overall inefficiency of this transition as well as transitions at wavelengths shorter than this, they are rarely observed.

When excited by photons at 980 nm, the electrons within the Er^{3+} ions enter what is known as a three-level system. This is because excited state at $^4\text{I}_{11/2}$ has a very short lifetime, of about only μs and will result in the electrons quickly decaying to the metastable level of $^4\text{I}_{13/2}$. This transition towards the lower, more stable energy state is rapid and non-radiative, meaning that the transition is not accompanied by any emissions. Instead, the energy released during this transition is in the form of mechanical vibrations in the fibre, which manifest as phonons [64]. The metastable state is more stable than the previous state, and as a result the electrons at this level have a longer lifetime, typically of 10 ms [65]. This permits a population inversion to take place, which is a necessary condition for lasing to occur. Photons at a wavelength of 1480 nm can also be absorbed by the electrons in the Er^{3+} ions, although this will only result in a transition to the $^4\text{I}_{13/2}$ state, making it a two-stage process which is less efficient than the three-stage process obtained under 980 nm pumping.

Transitions from the $^4\text{I}_{13/2}$ to $^4\text{I}_{15/2}$ levels on the other hand are accompanied by emissions, typically within the region of 1530 nm. These transitions are known as radiative transitions, and are responsible for the lasing and amplification capabilities of the EDFA. The frequencies at which these emissions occur are in accordance to Planck's Law [63], [66]. Two radiative emissions are possible. The first is spontaneous emission, and as the name suggests, occurs spontaneously as the electrons decay from the $^4\text{I}_{13/2}$ to $^4\text{I}_{15/2}$ levels. Spontaneous emissions usually occur at

²⁶ Also known as the relaxed state.

random times and at different wavelengths, creating a broad emission spectrum. Stimulated emission on the other hand requires the presence of an external photon, with a wavelength corresponding to the energy required to transit the ${}^4I_{13/2}$ to ${}^4I_{15/2}$ levels. As this photon traverses the EDF, it will ‘trigger’ the remaining electrons in the metastable state of ${}^4I_{13/2}$ to decay simultaneously, thus emitting a signal that is coherent in phase and wavelength. Both the upward and downward transitions are illustrated in Figure 26, with the green arrows illustrating upward, absorptive transitions, while the red arrows illustrate downward, radiative transitions. The grey arrow illustrates the downward, non-radiative transitions.

While both stimulated absorption and emission are desired characteristics of Er^{3+} ions in optical fibres, spontaneous emission is not, especially in amplifier and laser applications. This is because unlike stimulated emission, the photons emitted as a result of spontaneous emission propagate in random directions and as a result amplifies any noise present in the system. Furthermore, spontaneous emissions will also deplete a portion of the population in the ${}^4I_{13/2}$ metastable state, thus affecting slightly the performance of the EDF based amplifier or laser²⁷.

3.2.3 Er^{3+} Rate Equations

The transitions of electrons between the different energy levels of the Er^{3+} ions can be mathematically represented by rate equations. These equations will describe the governing mechanisms behind population changes during stimulated absorption, stimulated emission and spontaneous emission with respect to traversing photons from an incident field of light.

The transitions of electrons between the energy levels of the Er^{3+} ion can be represented by the three-level system as shown in Figure 27. The three energy levels are designated as 1, 2 and 3 with 1 being the ground state, 2 being the metastable state and 3 being the excited state. The transitions between the states are either absorptive or emissive in nature, and are represented by the notations R , W and A for the

²⁷ The reduction in performance is only at the initial point of lasing or amplification, before stimulated emission begins. As such, spontaneous emission occurs primarily when the external signal is absent, and once the lasing or amplification of a signal begins, the negative effects of spontaneous emissions are rarely seen. However, this is only valid for the case of CW systems. Pulse systems are highly susceptible to the effects of spontaneous emission, as the pulse creates multiple initial states, and can see the performance of the amplifier being affected.

pumping rates, stimulated emission rates and spontaneous decay rates respectively. The superscripts R and NR represent radiative and non-radiative transitions, while the subscripts 1, 2 and 3 each represent the transiting energy level, with the first subscript denoting the originating energy level, and the following subscript denoting the destination energy level.

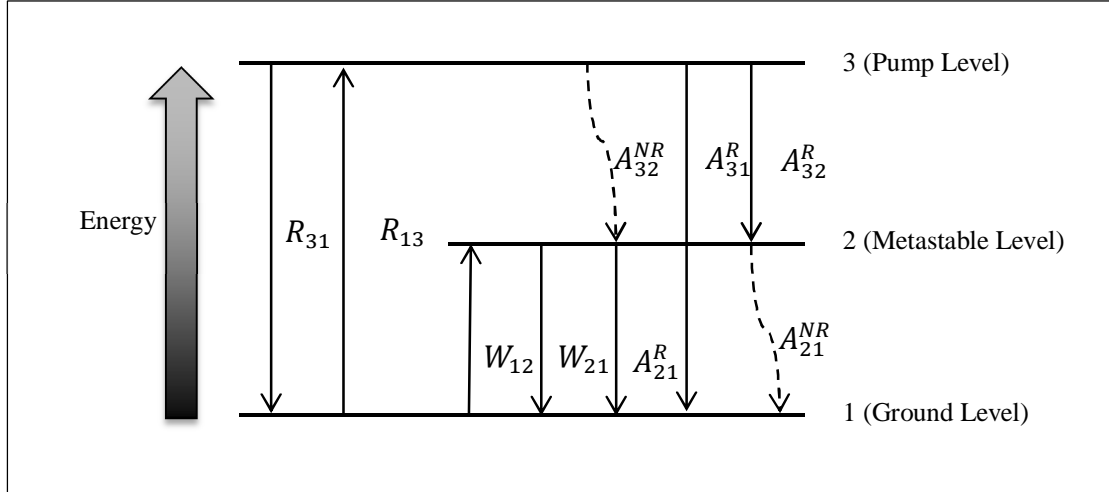


Figure 27: Energy level diagram corresponding to the pumping rates. Radiative and absorptive transitions are denoted by solid lines, while the dashed lines denotes non-radiate transitions

From the figure, it can be seen that nine transitions are possible. Pumping rate transitions take place between level 1 and 3 directly, bypassing level 2 to give an upward transition of R_{13} or a downward transition of R_{31} . Spontaneous decay can also occur directly between levels 1 and 3 and are radiative in nature. This transition is represented by A_{31}^R in Figure 27. Between levels 3 and 2 there are two possible transitions, namely A_{32}^{NR} , which is non-radiative in nature and A_{32}^R , which spontaneously emits as it decays. Between levels 1 and 2, four possible transitions can occur. Two of these transitions are stimulated emissions, represented by W_{12} and W_{21} , while the other two occur spontaneously, and are represented by A_{21}^R and A_{21}^{NR} .

In order to model the rate equations of the Er^{3+} ions, it is assumed that the spontaneous decay from level 3 is predominantly non-radiative, and is given by:

$$A_{32}^{NR} \geq A_3^R \dots\dots\dots(9)$$

where

$$A_3^R = A_{32}^R + A_{31}^R \dots\dots\dots(10)$$

In the same manner, the decay from the metastable level to the ground level is a combination of radiative and non-radiative decays, and is defined as:

$$A_2 = A_{21}^R + A_{21}^{NR} \dots\dots\dots(11)$$

whereby:

$$A_{21}^R = \frac{1}{\tau_2} \dots\dots\dots(12)$$

with τ being the fluorescence lifetime. The spontaneous decay from level 2 to 1 is predominately radiative, thus giving:

$$A_{21}^R \geq A_{21}^{NR} \dots\dots\dots(13)$$

The populations at levels 1, 2 and 3 can be denoted as N_1 , N_2 and N_3 . The atomic rate equations corresponding to these populations can be written as:

$$\frac{dN_1}{dt} = -R_{13}N_1 + R_{31}N_3 - W_{12}N_1 + W_{21}N_2 + A_{21}N_2 \dots\dots\dots(14)$$

$$\frac{dN_2}{dt} = W_{12}N_1 - W_{21}N_2 - A_{21}N_2 + A_{32}N_3 \dots\dots\dots(15)$$

$$\frac{dN_3}{dt} = R_{13}N_1 - R_{31}N_3 - A_{32}N_3 \dots\dots\dots(16)$$

The time derivatives in a steady-state situation are zero, thus giving:

$$\frac{dN_1}{dt} = \frac{dN_2}{dt} = \frac{dN_3}{dt} = 0 \dots\dots\dots (17)$$

As the transitions between the excited state and metastable states are very fast due to the high probability of these transitions occurring, thus N_3 is almost always very close to zero, with most of the population remaining at levels 1 and 2. In this regard, Equations 14 and 15 can be solved as follows:

$$N_1 = \rho \frac{1+W_{21}\tau}{1+R\tau+W_{12}\tau+W_{21}\tau} \dots\dots\dots (18)$$

$$N_2 = \rho \frac{R\tau+W_{12}\tau}{1+R\tau+W_{12}\tau+W_{21}\tau} \dots\dots\dots (19)$$

$$N_3 \approx 0 \dots\dots\dots (20)$$

with R being taken as R_{13} [63]. These population densities at each level are given as [67]:

$$\frac{\partial N_1}{\partial t} = A_{21}N_2 + W_{21}N_2 - W_{12}N_1 - RN_1 + R'N_3 \dots\dots\dots (21)$$

$$\frac{\partial N_2}{\partial t} = A_{32}N_3 - A_{21}N_2 - W_{21}N_2 + W_{12}N_1 \dots\dots\dots (22)$$

$$\frac{\partial N_3}{\partial t} = -A_{32}N_3 + RN_1 + R'N_3 \dots\dots\dots (23)$$

$$N_1 + N_2 + N_3 = N_T \dots\dots\dots (24)$$

whereby N_T is the total dopant concentration. Exposure of the Er^{3+} ions to incident light at 980 nm will result in multiple transitions occurring between the three levels. While it is possible to accurately represent the actual transitions taking place in a mathematical model, it is also very complex. However, certain conditions can be taken into account to build a model that is still accurate, albeit much less difficult. By taking into account the fact that transitions from the $^4\text{I}_{11/2}$ to $^4\text{I}_{13/2}$ levels are predominately non-radiative and those between the $^4\text{I}_{13/2}$ and $^4\text{I}_{15/2}$ levels are radiative in nature, equations 21 to 24 can now be simplified into just two equations:

$$A_{32}^{NR} \gg A_{32}^R + A_{31}^R \dots\dots\dots (25)$$

$$A_{21}^R \gg A_{21}^{NR} \dots\dots\dots (26)$$

As A_{32}^R is a very fast non-radiative transition, it can thus be assumed that the transition rate of A_{32}^R is much higher than the pump or stimulated emission rates, such that $A_{32}^R \gg R_{13,31}$. Therefore, the complex three-level system can now be essentially represented by the simpler two-level model.

As the time derivatives vanish in steady state conditions, the distribution of the excited electrons in the excited state is essentially a Boltzmann distribution. In this regard, the populations at the ground and excited levels can now be described as:

$$\begin{aligned} N_3 &= N_2 e^{\frac{-(E_3-E_2)}{kT}} \\ &\equiv \beta N_2 \dots\dots\dots (27) \end{aligned}$$

where

$$\beta = e^{\frac{-(E_3-E_2)}{kT}} \dots\dots\dots (28)$$

with E_3 being the energy at the excited state, and E_2 being the energy at the metastable state, k and T represent the Boltzmann constant and thermodynamic

temperature of the group of atoms, respectively. The inversion level, n can now be written as:

$$n = \frac{N_2}{N_2 - N_1} = \frac{(W_p + W_s)\tau}{W_p\tau(1-\beta)-1} \dots\dots\dots(29)$$

where W_p and W_s are the pump and signal wavelength powers. The lifetime of the metastable state is given as τ .

Equation 29 provides two crucial insights into the transition mechanisms that take place in the Er^{3+} ions when excited, which in turn explain the behavior of the EDFA. Firstly, it is plain to see that the inversion levels are heavily dependent on the pump and signal wavelength powers. Secondly, the β factor shows that pumping at 980 nm is more efficient than pumping at 1480 nm. This is because when excited by 980 nm pumping, the electrons orbiting the Er^{3+} are raised to the excited state level, but quickly decay to the metastable level as a result of the small lifetimes experienced at this level. The difference in terms of energy levels between the excited and metastable states is approximately 0.4 eV. Taking this energy difference into account, the obtained value of β becomes about 0.0. However, pumping the Er^{3+} ions at 1480 nm on the other hand cause thermalization²⁸ of the excited ions to occur at the within the metastable level itself and in turn increasing the value of β value to 0.4 [63]. The increase in the value of β can be seen in the inversion factor. When a strong pump power is introduced to an EDF, along with a small signal power such that $W_p\tau \gg 1$ and $W_s \sim 0$, pumping at 980 nm gives an inversion factor of almost 1. On the other hand, pumping at 1480 nm gives an inversion factor of 1.6, less efficient than that obtained at 980 nm pumping.

²⁸ Thermalization is used in place of non-radiative transitions as the energy released during the relaxation of the excited electrons is in the form of heat. In reality, thermalization and non-radiative relaxation transitions are one and the same.

As the optical properties of the Er^{3+} ions are essentially a function of the transitions between the various energy levels, thus the rate equations form the building blocks from which the subsequent behavior of the Er^{3+} ions can be understood. However, it must be taken into account that the factors that govern the behavior of the EDFA are not limited to those of the Er^{3+} ions specifically; even the host material can have a significant effect on the performance of the EDFA, particularly in terms of the absorption and emission cross sections. This will be described in detail in the next section.

3.2.4 *Absorption and Emission Cross Sections*

The absorption and emission cross sections of the EDFA depends tremendously on which particular host matrix in which Er^{3+} ions are suspended. This is because the spectral shape of the cross sections in the 1550 nm region, as well as the absolute magnitudes of the cross sections can vary with the host environment. An example of this is given in Figure 28 (a) and Figure 28 (b), which shows the absorption and emission cross sections of Er^{3+} ions near the 1550 nm region when suspended in an Al-Ge-Er-doped silica fibre matrix as well as the emission cross-sections obtained in other types of glass hosts.

It can be seen that in the silica glass host, the absorption and emission curves peak at about 1530 nm, which is typical for EDFAs at the region near 1550 nm [53]. However, in tellurite and fluoride glasses, different peak spectra are obtained. Although all three cross-sections peak at around 1530 nm, it is clearly visible that the magnitude of the peaks is vastly different. The emission cross-section of the Er^{3+} ions suspended in the tellurite fibre follows the basic shape as that of the Er^{3+} ions suspended in the silica fibre host, albeit at a much higher amplitude. In the fluoride fibre however, a different emission spectrum is observed, with a lower magnitude and an overall ‘smoother’ curve, as compared to the ‘steps’ seen in the emission spectra of the ions suspended in the tellurite and silica glass hosts.

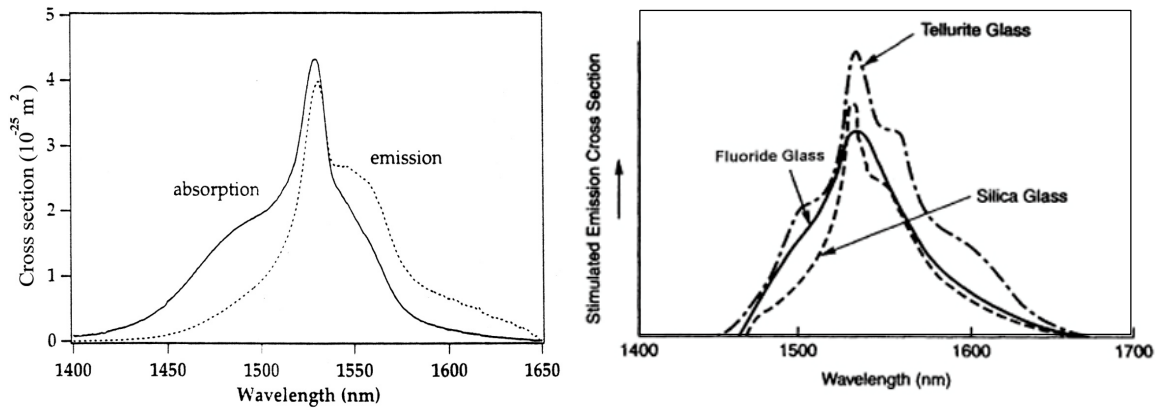


Figure 28: (a) Absorption and emission cross-sections of Er^{3+} ions suspended in an Al-Ge-Er based silica host matrix. The absorption and emission cross-sections peaks at 1530 nm, which is typical for Er^{3+} ions near the 1550 nm region. (b) Comparison of emission cross sections of Er^{3+} ions in silica, fluoride and tellurite glass hosts²⁹.

Obtaining the absorption cross sections of the Er^{3+} ions in the silica host is relatively straightforward, and is ascertained by simply normalizing the absorption measurements on a homogeneous bulk glass sample. However, the emission cross sections are much harder to obtain, and require approaches such as the calculation of the emission cross-sections from the absorption cross-sections, or by directly measuring the small signal gain in a short, uniformly inverted EDF. The absolute absorption cross-section values are obtained via measurement of the attenuation experienced by light propagating in the fibre, and dividing this value by the average erbium ion density and EDF overlap parameter at 1550 nm. The McCumber relationship then yields the emission cross section in terms of the absorption cross-section as:

$$\sigma^{(e)}(\nu) = \sigma^{(a)}(\nu) e^{\frac{(\varepsilon - h\nu)}{kT}} \dots\dots\dots(30)$$

where ε represents the mean energy of the $^4\text{I}_{13/2}$ to $^4\text{I}_{15/2}$ transition, $\sigma^{(e)}$ and $\sigma^{(a)}$ are the emission and absorption cross sections respectively. kT is the average thermal energy, while h is Plank's constant. The emission cross sections are obtained from the McCumber relationship whereby ε is 1535 nm, as shown in Figure 30. These

²⁹ Source: J. A. Harrington, *Infrared Fibres and Their Applications*, New Jersey: Pearson Education, Inc., 2004.

emission cross sections agree well with those obtained from the signal gain spectrum measured with this fibre [67].

3.2.5 ASE

The ASE is a product of spontaneous emission, and occurs when an EDF is subjected to a pump wavelength but no signal wavelengths are present. ASE is typically defined as a process where spontaneously emitted radiation or luminescence³⁰ emits from a fibre doped with rare-earth ions such as Er^{3+} or other rare earths under pumping, and is amplified to high power levels.

ASE is usually an unwanted effect as it has the tendency to limit the gain that can be achieved, typically in the order of 40–50 dB, as it ‘steals’ the photons that would otherwise participate in the stimulated emission process [67], [68]. Furthermore, ASE can prevent lasing at extreme wavelengths in certain laser designs, thereby limiting their operational capabilities. ASE is also a key contributor to the noise figure of a system, which is a measure of the excess noise introduced by the EDFA into a transmission. However, the ASE is not all that bad - in the case of fibre lasers, ASE is a desired effect and is used in conjunction with feedback and tuning mechanisms to form a laser resonator for a specific wavelength.

In a system with unsaturated gain, the output power of the ASE power is a function of the bandwidth, $\Delta\nu$ as well as the amplifier gain, G , as follows:

$$\begin{aligned} P_{ASE}^{\pm} &= n_{sp}^{\pm} h\nu_s \Delta\nu (G - 1) \\ &= n_{eq}^{\pm} h\nu_s \Delta\nu G \dots\dots\dots(31) \end{aligned}$$

where n_{sp}^{\pm} and n_{eq}^{\pm} are defined as the spontaneous emission factor and equivalent input noise, respectively. The superscript of \pm denotes whether the emitted spectrum is propagating in the positive (+) direction or negative (-) direction. Figure 29 shows the simulated ASE output for a typical EDF approximately 14 m long. The

³⁰ In this regard, ASE differs from luminescence in the sense that ASE is luminescence that has been amplified by the EDF. Furthermore, ASE is highly directional, occurring in the same direction as the propagating signal in the EDF. Luminescence on the other hand is not directional and can be observed in all directions from the EDF.

displacement from the point of origin³¹ is defined as z , while the length of the fibre is defined as L .

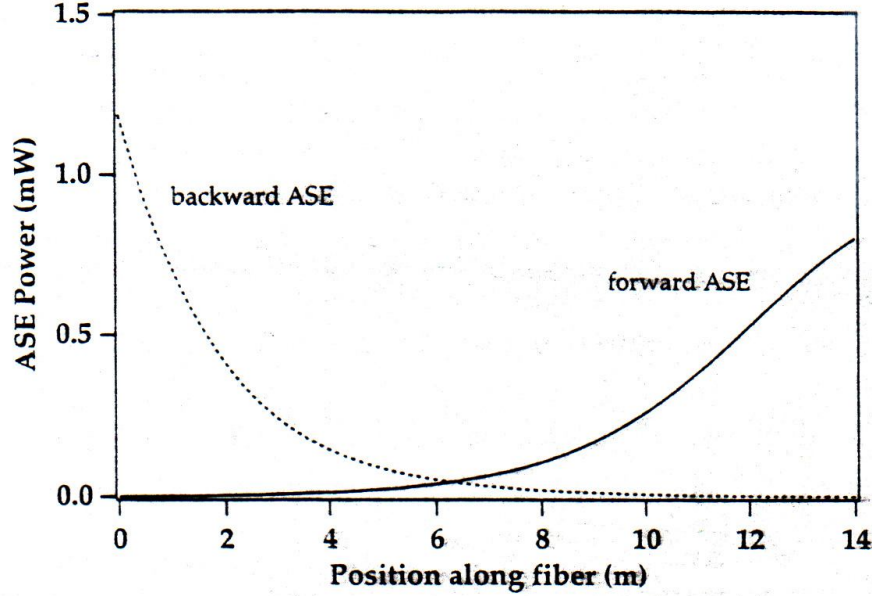


Figure 29: Total forward- and backward- propagating ASE power as a function of position along a 14 m length of an erbium-doped fibre pumped at 980 nm with 20 mW of power.

It is interesting to observe that the power emitted by the backward propagating ASE at $z = 0$ is higher than the forward propagating ASE that is emitted at $z = L$. This behavior is attributed to the location of the pump, which in the case of Figure 29 is at $z = 0$, as the ASE power is itself a function of its position along the EDF.

From Equation 31, it can be seen that the generation of the ASE noise power is equivalent to the amplification of n_{sp}^{\pm} or n_{eq}^{\pm} fictitious input photons. In the high gain regime and complete inversion limit, the equivalent noise input becomes $n_{sp}^{\pm} \approx n_{eq}^{\pm} \approx 1$, representing a single photon in bandwidth $\Delta\nu$. In this limit, the ASE power increases linearly with the gain. However, as the gain continues to increase, the stimulated emission by the ASE is enhanced to the point where it eventually begins to compete with the pumping rate. As a result, the inversion of the medium is reduced and the amplifier gain saturates in the absence of any input signal. This results in an almost proportional increase in ASE, as shown in Equation 31 and the effects of amplifier

³¹ The point of origin is the end of the fibre that is designated as the input end, or the end in which the pump wavelength will enter the EDF. In this manner, a forward propagation signal is a signal propagating from z to L , while a backward propagating signal is a signal propagating from L to z .

self-saturation by ASE cannot be entirely suppressed, even by increasing the pump input due to the corresponding increase in gain. However, in this regime the maximum gain eventually becomes limited by the effects of laser oscillation, which occurs when the amplifier gain is high enough to compensate for the return loss of any reflecting element in the path of the ASE signal. In this case, the ASE is reflected back and forth into the amplifier, which operates then as a laser [63].

As the ASE is the amplified luminescence of a fibre being pumped, therefore a gain threshold is necessary in order for the fibre to exhibit the ASE effect. The estimated gain required for the generation of ASE in an EDF is derived as in Equation 32 below:

$$h\nu\Delta\nu_e G = AI_{sat} \dots\dots\dots(32)$$

where A is the fibre core area, I_{sat} is the saturation intensity, G is the single pass gain required and $\Delta\nu_e$ is the emission bandwidth of the ASE spectrum. Rewriting Equation 32 as a function of G and A will yield:

$$I_{sat} = \frac{h\nu\Delta\nu_e G}{A} \dots\dots\dots(33)$$

The ASE spectrum can be observed in both the co-propagating (moving in the same direction with the pump signal) and counter-propagating (moving in the opposite direction of the pump signal) directions of the EDF.

3.2.6 Signal Gain

The ability of a rare-earth amplifier to amplify external signals traversing its length is the most important factor of an optical amplifier. This characteristic is known as the small signal gain, and is the fundamental parameter of an optical amplifier.

The small signal gain is defined as the increase in magnitude of an input signal that traverses through the amplifier. Gain can be shown as the ratio between the input signal and the output signal level, generally expressed in dB as in Equation 34 [67].

$$G \text{ (dB)} = 10 \log_{10} \left(\frac{P_{\text{signal}_{\text{out}}}}{P_{\text{signal}_{\text{in}}}} \right) \dots \dots \dots (34)$$

It must be noted that ASE is also produced during the amplification process, thereby rendering Equation 34 somewhat inaccurate. As the small signal gain is defined as the increase in the magnitude of *only* the small signal travelling through the fibre, thus the ASE power should be deducted from the total. As such, Equation 34 is now modified to give:

$$G \text{ (dB)} = 10 \log_{10} \left(\frac{P_{\text{signal}_{\text{out}}} - P_{\text{ASE}}}{P_{\text{signal}_{\text{in}}}} \right) \dots \dots \dots (35)$$

where $P_{\text{signal}_{\text{in}}}$, $P_{\text{signal}_{\text{out}}}$ and P_{ASE} are the signal input, signal output and ASE powers, respectively. Gain is represented by G , as in the previous sections.

As a result of the EDFA's ability to operate bi-directionally, predicting the gain can be complicated, more often than not requiring numerical techniques to obtain a solution. However, an alternative approach that is significantly simpler can be explored by understanding that the net amplifier gain can be represented by sum of individual 'slices' of gain along the length of the fibre. In this manner, the EDFA is not seen as a single device, but rather a compound device consisting of multiple amplifiers with an incremental length of Δz . This gives a net gain of, G as a function of all the gain elements, $g(z)$ as follows:

$$G = \exp \int_0^L g(z) dz \dots \dots \dots (36)$$

The incremental signal gain, $g(z)$ of a photon propagating along the EDF is given as:

$$g(z) = \Gamma_s [\sigma_{e,s} N_2(z) - \sigma_{a,s} N_1(z)] \dots \dots \dots (37)$$

where the subscript s is used to denote the signal wavelength. The overlap factor is given as Γ_s , while the stimulated emission and absorption cross-sections are given as

σ_e and σ_a respectively, while the ground-state population and metastable state population densities are given as N_1 and N_2 respectively. z is the distance in the EDF from the initial pump wavelength input, with the maximum value of z being L . Combining equations 36 and 37 now yields:

$$G = \exp \left(\int_0^L \{ \Gamma_s [\sigma_e N_2 - \sigma_a N_1] L \} dz \right) \dots\dots\dots 38$$

From Equation 38, it can be seen that the net gain is dependent on the average inversion level of erbium-ion population in the EDF, which in itself is a function of the power of the pump and signal wavelengths [68]. This agrees well with the general theories presented in the previous sections, and provides an accurate model of the gain characteristics of the EDF.

3.2.7 NF

One of the detrimental factors that influence the quality of an optical signal is noise. Optical noise is similar to electrical noise, and is highly undesirable as it interferes with the propagating signal, deteriorating its quality over time. In optical amplifiers, noise arises from spontaneous decays in the active medium, and do not really constitute a significant problem when only one or two optical amplifiers are present in the system. However, most real-world networks deploy hundreds of optical amplifiers, and it is here that noise becomes a problem; as the cumulative noise levels continues to build up over each amplifier iteration, it soon overcomes the propagating optical signal, essentially ‘drowning’ the signal in the background noise.

As optical amplifiers are predominantly used telecommunications applications, thus the noise performance of optical amplifiers has become a matter of critical importance. The noise performance in optical amplifiers is characterized by a measurable quantity known as the optical NF. The NF is a fundamental characteristic of the EDFA that quantifies the degradation of the Signal-to-Noise Ratio (SNR) after a signal has passed through the amplifier. Large NFs are detrimental to system performance as it results in poor received SNRs, increased jitter in soliton-based

systems as well as the accumulation of ASE in long-haul amplified links [63], [69], [70]. The NF of an optical amplifier will always be greater than one, due to the fact that the amplifier adds noise during the amplification process and the SNR at the output end (SNR_{out}) is always lower than at the SNR at the input end (SNR_{in}) [67]. The NF is typically given in terms of dB as a function of the input and output SNRs:

$$NF \text{ (dB)} = 10 \text{ Log } \left(\frac{SNR_{in}}{SNR_{out}} \right) \dots\dots\dots (39)$$

It is worthwhile to note that the SNR used in the definition of the NF is similar to the SNR experienced by electronic devices. In this regard, the output SNR is taken as the output of an ideal photodetector capable of converting each photon of incident light into electrical current. The input SNR on the other hand is defined as the SNR obtained from a shot-noise-limited source [71].

Another commonly used NF definition is the quantum-beat-noise-limited NF, or also known as the signal-spontaneous beat-noise-limited NF. This NF definition is typically used in modeling exercises as it is highly advantageous in simplifying measurement procedures. The signal-spontaneous beat-noise-limited NF is defined as [72]:

$$NF = \frac{2P_{ASE}}{Gh\nu} + \frac{1}{G} \dots\dots\dots (40)$$

where $h\nu$ is the photon energy and P_{ASE} is the ASE output density in the same polarization and wavelength as the propagating signal. In a typical EDFA setup, there are two propagating polarization modes, giving a total ASE power of:

$$P_{ASE} = 2n_{sp}h\nu(G - 1)B_0 \dots\dots\dots (41)$$

where B_0 is the optical bandwidth. Equation 41 can also be expressed as a function of the ASE spectral density alone, with the unit WHz^{-1} . This reduces the equation to:

$$P_{ASE} = 2n_{sp}h\nu(G - 1) \dots\dots\dots(42)$$

where the spontaneous emission factor, n_{sp} is given as [73]:

$$n_{sp} = \frac{\sigma_e N_2}{\sigma_e N_2 - \sigma_a N_1} \dots\dots\dots(43)$$

It is clearly evident from Equation 43 that n_{sp} is dependent on the populations of the ground and metastable levels, as well as the emission and absorption cross-sections of these levels, designated as σ_e and σ_a respectively. Both σ_e and σ_a are themselves a function of the wavelength of the propagating signal, λ , and thus can be described more accurately as $\sigma_e(\lambda)$ and $\sigma_a(\lambda)$. The lowest n_{sp} that can be obtained for a conventional EDF is at a wavelength of 980 nm, which gives a n_{sp} value of close to unity [74]. This represents a near perfect inversion scenario, with an almost complete population inversion from the ground to metastable levels. However, this is an ideal scenario; in reality, the population at the metastable state tends to decrease as the position on the fibre moves further and further away from light source as a result of the depletion of the pump power along with the effects of spontaneous emissions. As such, it is more accurate to represent the n_{sp} as an effective or integrated value instead [63].

It must be noted that the NF of the EDFA arises from two sources. The first source is the EDF itself, which generates noise when being pumped. The second source of noise is the electrical output of the photodetector, which converts the optical signal into an electrical signal. The noise generated from the EDF is the signal-spontaneous beat-noise-limited noise, and is represented by the first term in Equation 40. The noise generated from the photodetector on the other hand is the shot noise, and is represented by the second term of the same equation [75], [74], [76]. The signal-spontaneous beat-noise-limited noise arises from intensity fluctuations originating from the interactions between the signal wavelength and the generated

ASE. The shot-noise on the other hand originates from the uncertainty of time upon which the electrons or photons arrive at the detector, and is typically small enough when compared to the signal-spontaneous beat-noise-limited noise and can therefore be safely neglected. As such, Equation 40 can now be summarized as:

$$NF = \frac{2P_{ASE}}{Gh\nu} \dots\dots\dots(44)$$

This makes the overall computation of the NF easier.

In this section, the theoretical mechanisms which define the operation of the EDFA were examined. This background will provide an understanding into the actual operation of the EDZF, whose characterization will be the focus of the next section of this chapter.

3.3 *The EDZF as a Fibre Amplifier, Fibre Laser and Non-Linear Medium*

While the primary focus of this research is on the development of compact ultrafast fibre lasers, it must be remembered that the motivation that drove the development of the EDZF in the first place was to obtain a short but highly doped EDF that could be used to develop compact, high performance EDFAs.

In this section, the performance and application of the EDZF as a fibre amplifier and fibre laser will be examined. The ASE, gain and NF parameters of the EDZF based amplifier will be first measured, this will then be followed by an examination of the EDZF in generating an SLM output. The generation of the SLM output from the EDZF is a very important aspect of the development of the EDZF as a fibre laser, and is thus the focus of the section. Finally, the non-linear characteristics of the EDZF will also be explored, with a focus on the FWM effect in particular, due to its potential applications in a variety of applications such as multi-wavelength sources and wavelength converters.

3.3.1 ASE Characteristics of the EDZF

The ASE output of the EDZF is a crucial element of the fibre's performance. The ASE output will determine the operational limits of the EDZF, in terms of the levels of gain that can be achieved as well as the operational bandwidth of the developed EDFA.

Obtaining the ASE output requires only a simple setup, as shown in Figure 30:

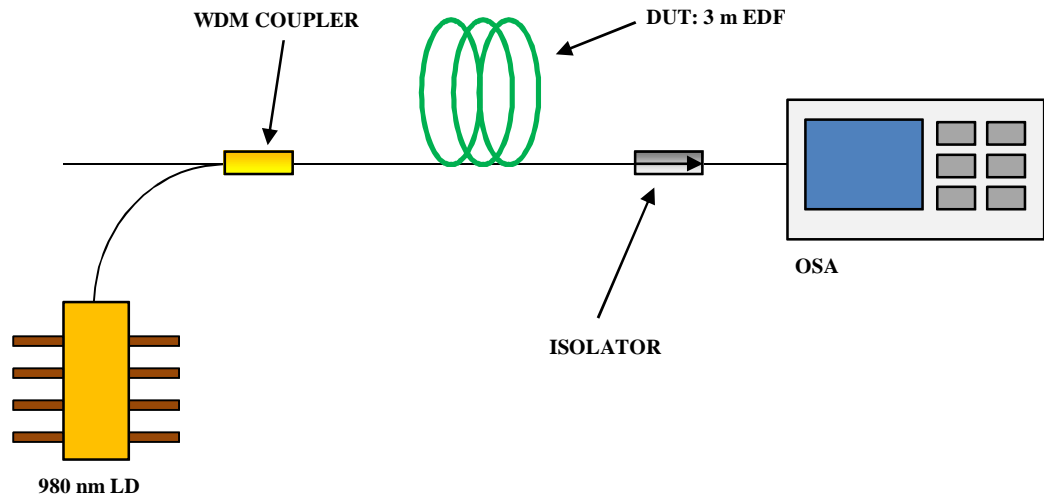


Figure 30: Experimental setup for ASE spectrum measurement and analysis with 3 m long EDF

The setup is similar to that of a simple EDFA, with the primary difference being the exclusion of an external signal. A 980 nm Laser Diode (LD) is used to pump a 3 m long Metrogain M-12 EDF, which has an Er^{3+} ion concentration of about 960 ppm. The EDF used has an absorption ratio of between 11 to 13 dBm at 980 nm, and Mode Field Diameters (MFDs) of 3.7 and 6.2 μm at wavelengths of 980 nm and 1550 nm, respectively. Physically, the fibre shares the same characteristics as a standard SMF-28 fibre, with a core of 90 μm and a cladding of 125 μm in [77]. The output of the LD is connected to the 980 nm port of a typical 980 / 1550 nm Wavelength Division Multiplexer (WDM), and the common output of the WDM is in turn connected to the EDF, which is the Device-Under-Test (DUT). The other end of the EDF is connected to an optical isolator, which serves to prevent any reflections from the end of the setup from interfering with the operation of the DUT, and thus affecting the output.

The output of the isolator is connected to a Yokogawa AQ3230 Optical Spectrum Analyzer (OSA) with a resolution of 0.02 nm and is used to analyze the output spectrum from the pumped EDF. The 1550 nm WDM is left unconnected, as it is not used for this particular experiment. The LD used in this work is a Lumics LU0977M200-2003F41A, capable of providing up to 200 mW of power at 977 nm and has an operation current rating of 343 mA, with the threshold for lasing occurring at 48.2 mA and kink-free lasing obtained at about 396 mA. The operational voltage for the LD is approximately 1.6 V.

The ASE obtained from the EDF under different pumping scenarios is shown in Figure 31.

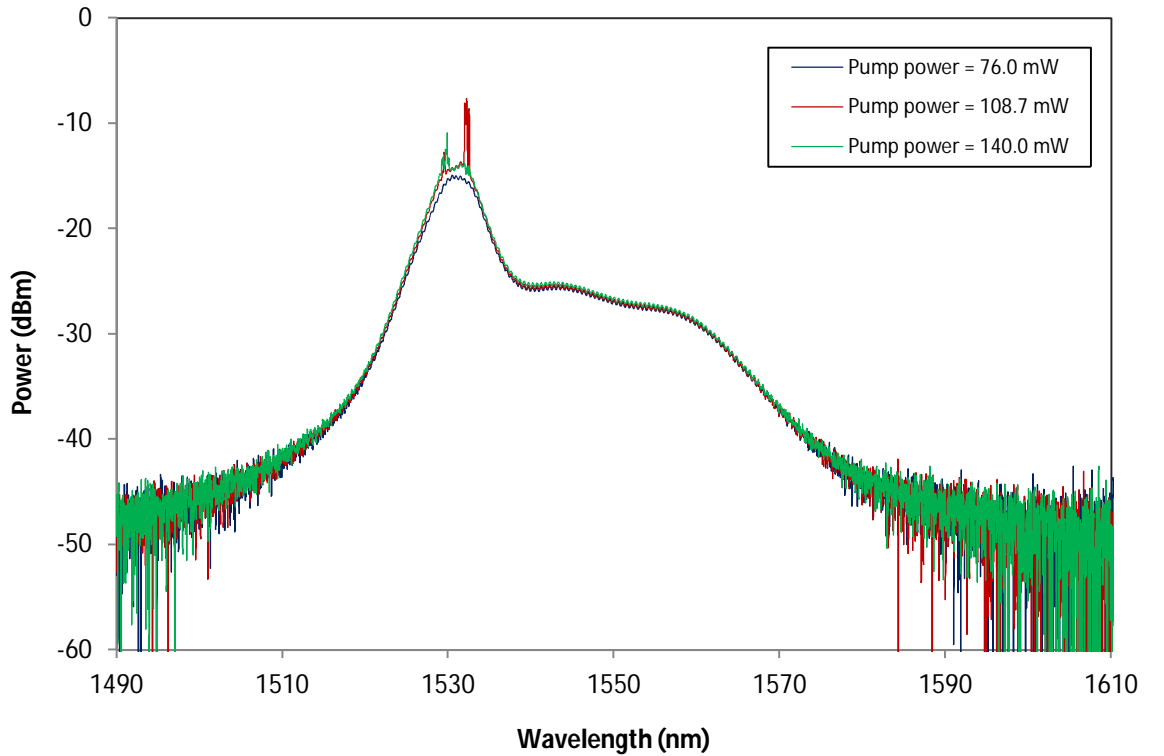


Figure 31: ASE spectrum from 1490 to 1610 nm from 3 m long EDF under various LD powers

It can be seen from the figure that in general, pumping the EDF at 76.0 mW, 108.7 mW and 140.0 mW yields an ASE spectrum that is relatively the same, with a low ASE output power of below -40.0 dBm at the shorter wavelength regions of 1510 nm and below. However, the output power picks up at about 1520 nm, rising quickly from below -40.0 dBm to a peak value of approximately -15.0 dBm at 1530 nm before dropping by about 10.0 dB near to 1540 nm. At this point, the output power

plateaus for a about 20 nm, before beginning to decrease again at 1560 nm and finally dropping to less than -40.0 dBm at a wavelength of 1570 nm. At the edges of the spectrum, below 1510 nm and above 1570 nm, the power of the spectrum is low enough that it is ‘drowned’ by the noise generated by the EDF. The ASE first becomes well defined at a pump power of 76.0 mW, which corresponds to an LD drive current of 150 mA. Increasing the LD drive current by another 50 mA yields an output power of 108.7 mW, while the maximum LD current of 250 mA allowed for this work provides an output power of 140.0 mW. It can be seen that under all three LD drive currents, the ASE output remains relatively unchanged, maintaining its spectral shape as well as relative power levels.

As the pump power is increased however, lasing lines at the peak region become more apparent. Figure 32 shows a more detailed view of the peak region, which permits the lasing lines to be better observed. At the lowest pump power of 76.0 mW, no lasing wavelengths or ‘spikes’ are seen in the spectrum, with the ASE at the 1530 nm region forming a smooth curve. As the output power is increased to 108.7 mW, signs of lasing begin to show, with a lasing wavelength at approximately 1530 nm, although it is not well defined. Further increasing the pump power to 140.0 mW sees the lasing wavelength become better defined, although now at a longer wavelength of 1532 nm. In both cases, the power of the wavelengths is substantial, with the lasing wavelength occurring when the pump power is 108.7 mW having a peak power of -12.0 dBm, while the lasing wavelength observed at the highest pump power has an even higher peak power of -8.6 dBm. However, this by no means translates to the presence of a usable wavelength; in both cases, the peak-to-floor³² ratio is minimal and ranges from about 1 dB to a maximum of approximately 4 dB, far too low for any practical use. These lasing wavelengths are attributed to dominant wavelengths being amplified slightly by the EDF under pumping conditions, as well as from reflections from the isolator, which can be overcome by incorporating small amounts of Index Matching Gel (IMG) into the setup.

³² The peak-to-floor ratio in this particular aspect is defined as the difference in power between the peak power of the lasing wavelength to the point where the ASE curve would be, if the lasing wavelength was not present.

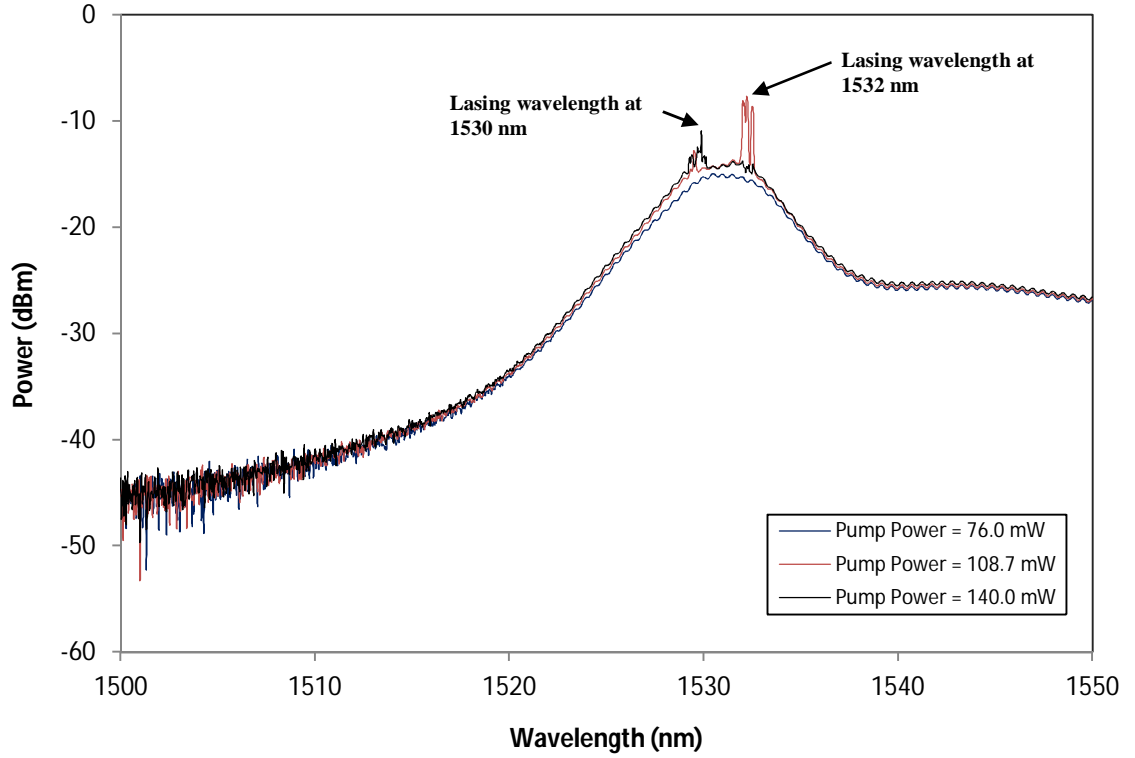


Figure 32: ASE spectrum from 1500 to 1550 nm from 3 m long EDF under various LD powers

The ASE spectra obtained for the 3 m long DUT under different pumping powers is typical for EDFs. In order to obtain the ASE output of the EDZF, only two minor changes in the setup of Figure 32 are necessary. The first change entails replacing the 3 m long EDF, which is the current DUT with a 3 m long EDZF. The second change is the insertion of another WDM coupler after the isolator, with the common port of the WDM coupler connected to the output of the isolator, while the 1550 nm port is connected to the OSA. The 980 nm port is left open so as to remove any excess 980 nm pump power for the system. This setup is shown in Figure 33:

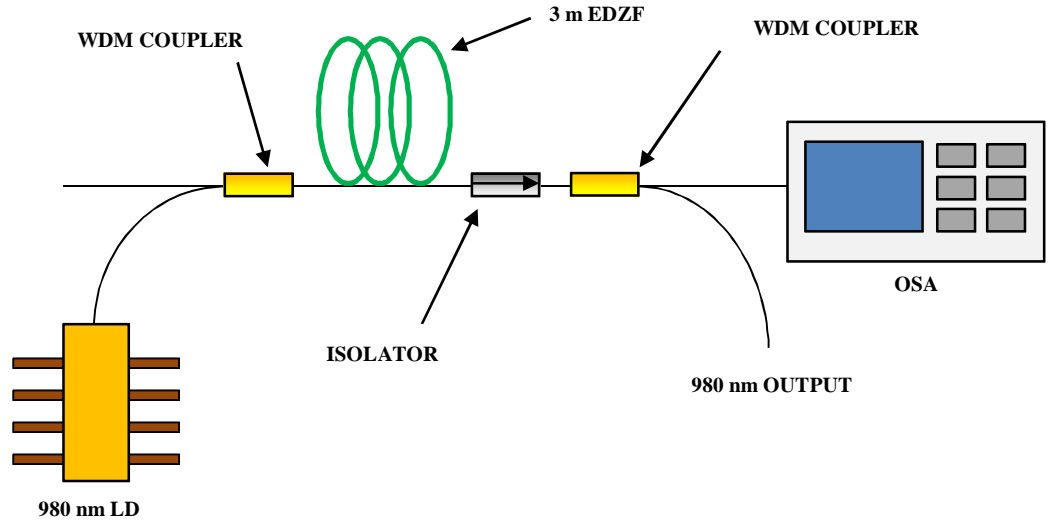


Figure 33: Experimental setup for ASE spectrum measurement and analysis with 3 m long EDZF

The EDZF used for the analysis of the ASE output characteristics is a ZEr-B type EDZF, with an Er^{3+} concentration of about 3880 ppm/wt. This EDZF has an absorption ratio of about 22.0 dB/m at 980 nm and approximately 53.0 dB/m at 1550 nm. The other parameters of the EDZF are similar to that of the EDF, including its physical characteristics. This is one of the key advantages of the EDZF, in that it allows a higher Er^{3+} dopant concentration to be realized while at the same time maintaining the ease of use that typical silica fibres enjoy. This was demonstrated first-hand in this particular experiment, whereby replacing the DUT was as simple as removing the EDF and splicing the EDZF in its place.

When pumped by the 980 LD under different pump powers, the EDZF generates ASE spectra of corresponding power as given in Figure 34.

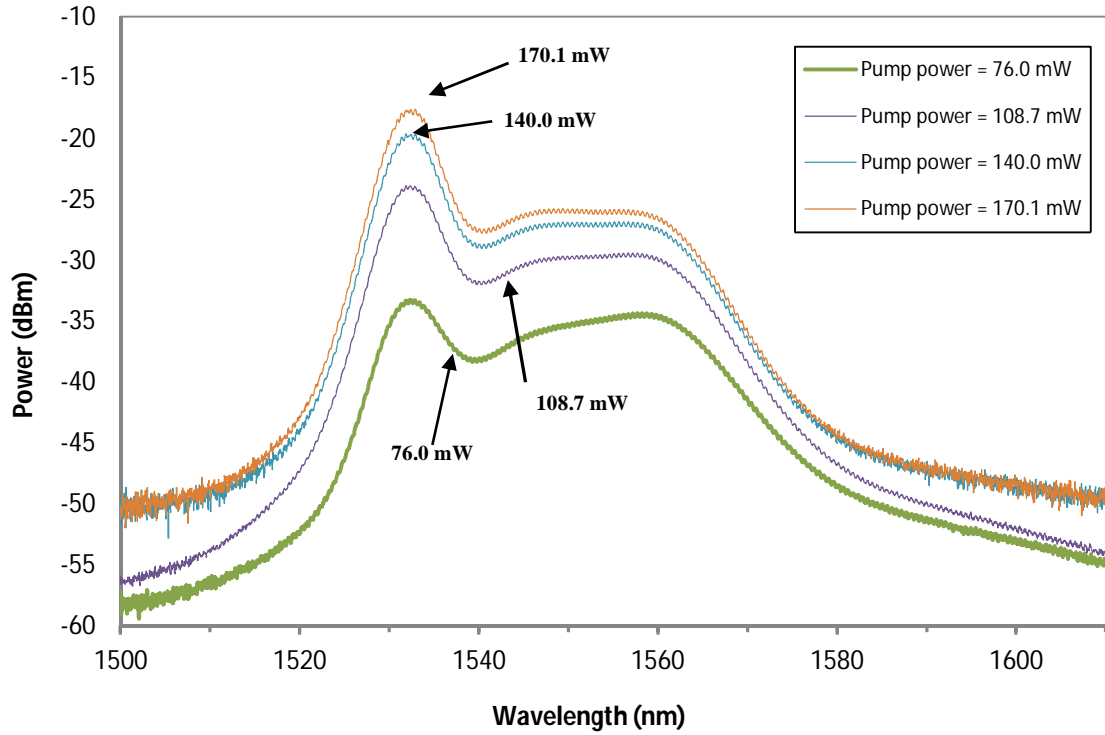


Figure 34: ASE spectrum from 1500 to 1610 nm from 3 m long EDZF under various LD powers

Even at a glance, it can be seen that the ASE generated by the EDZF is similar in many aspects to that obtained from a conventional EDF, rising to a peak region at 1530 nm followed by a short ‘plateau’ afterwards before dropping back again. However, the response of the EDZF to the increasing pump power is significantly different than that of the EDF. At a pump power of 76.0 mW, the spectrum obtained first peaks at 1530 nm with a power of about -33.0 dBm, before declining slightly and then rising again to the same value between 1553 nm and 1562 nm. Increasing the pump power to 108.7 mW sees the ASE spectrum also rising in power, with the 1530 nm peak now -24.2 dB and the plateau region flattening out at about -30.0 dBm. Further rises in the pump power to 140.0 mW and 170.1 mW show a similar change in the ASE spectrum as well, although not at the same magnitude as before. At the highest pump power, a peak power of -18.6 dBm is obtained at the 1530 nm region, while the plateau region gives an average power of -26.0 dBm. Lasing lines at the 1530 nm region are not observed under all pumping powers, indicating the possibility that the EDZF has yet to be fully pumped.

One of the key differences between the ASE spectra generated by the EDZF and the EDF is the region after the 1530 nm peak. In the ASE spectra originating from the EDF, the ASE power experiences a shallow decline after the peak region, before decreasing steeply. In the spectra obtained from the EDZF on the other hand, the ASE power remains relatively stable after the peak region, before declining. This is a very important characteristic, as it sets the operational boundaries of the EDZF. A comparative analysis of the ASE spectra obtained from the EDF and EDZF when pumped at 76.0 mW is given in Figure 35.

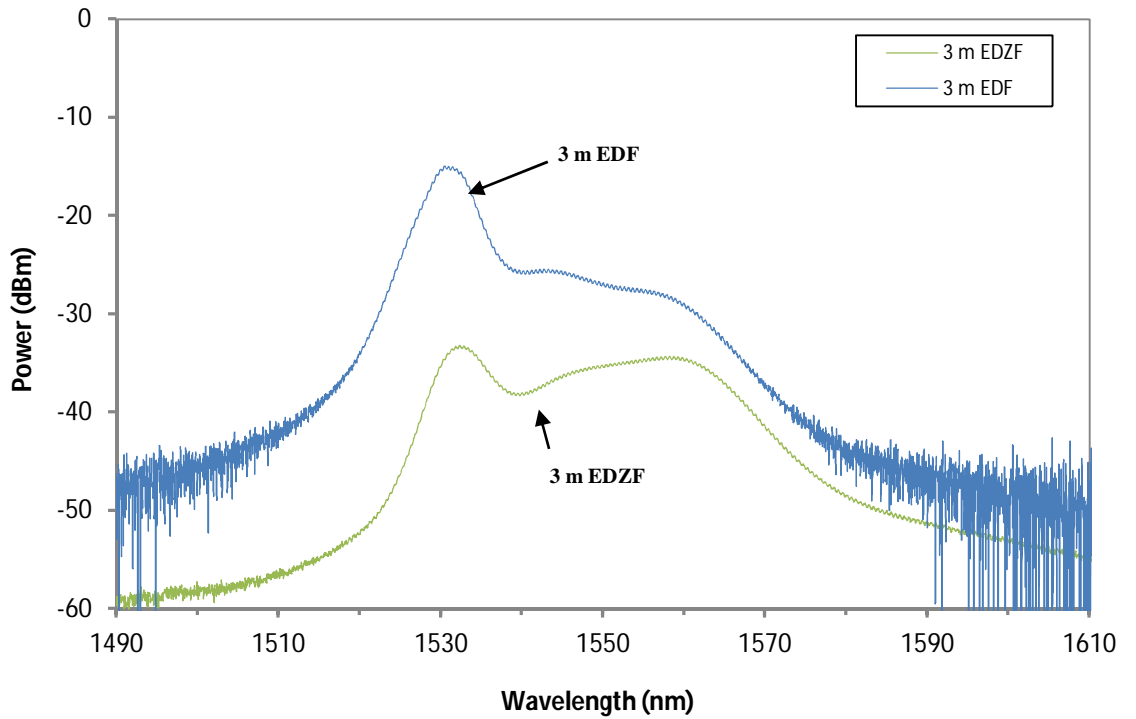


Figure 35: ASE spectrum from 1490 to 1610 nm from 3 m long EDZF and 3 m long EDF at pump power of 76.0 mW

The ASE spectrum generated by the EDF has a much higher power than that obtained from the EDZF, but this is to be expected as the significantly higher concentration of Er^{3+} ion in the EDZF would require a substantially higher pump power in order to create a population inversion similar to that in the EDF. Therefore, a relatively low pump power of 76.0 mW will result in an incomplete population inversion along the EDZF, with the initial part of the fibre being fully inverted while the middle to end portions of the fibre being only partially inverted at varying degrees. As a result of

this, the emissions generated at the initial part of the fibre where the population is fully inverted are absorbed by the portions of the fibre whose populations are only partially inverted, consequently lowering the overall power of the generated ASE spectrum.

While a glance of Figure 35 shows immediately the difference in the ASE output power, a closer inspection of the figure reveals another important characteristic of the EDZF. From the figure, it can be seen that in the region after the 1530 nm peak, the ASE power does not decrease but instead forms a plateau with a relatively flat power level. This is attributed to the high Er^{3+} dopant concentrations in the fibre, which essentially allows the parts of the fibre farthest from the pump source to amplify wavelengths that approach the L-band region of the third communications window. In other words, the high Er^{3+} dopant concentrations in the EDZF allow the 1550 nm ASE emitted in the forward parts of the fibre to be absorbed by the further portions of the fibre, which in turn promotes stimulated emissions in the wavelength region of 1560 nm. Figure 36 illustrates this mechanism.

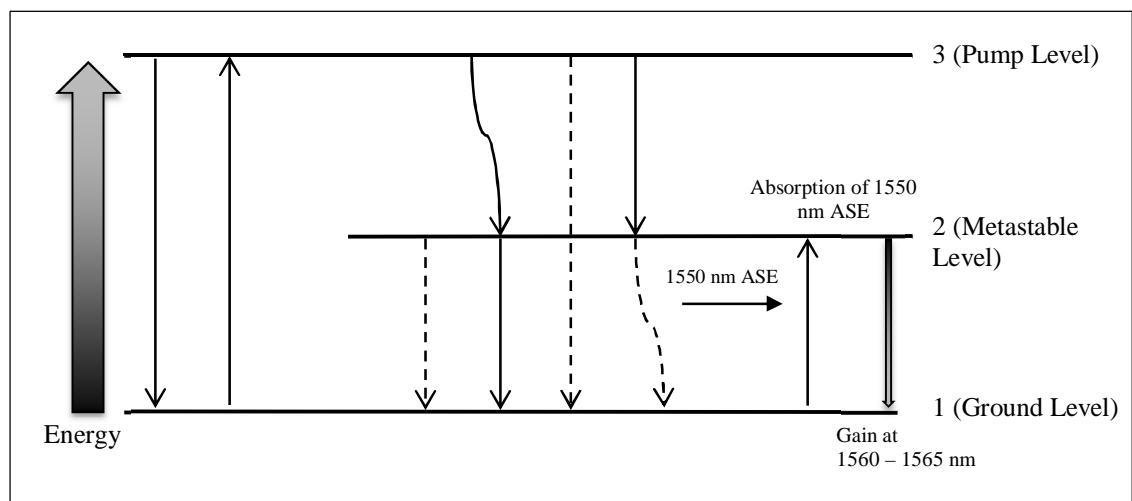


Figure 36: Energy level diagram showing absorption and emissions at wavelengths longer than the C-band region.

The amplification of wavelengths approaching the L-band region occurs when the primary pump power is not sufficient enough to create a population inversion at regions that are far away from the pump source due to the high dopant concentrations.

When this occurs, the Er^{3+} acts as a quasi-two-level system by absorbing photons at shorter wavelength short and re-emitting them as photons with longer wavelengths.

Increasing the 980 nm pump power on the EDF and EDZF has the effect of bringing the power of the ASE generated by the EDZF closer to average power levels of the EDF generated ASE. Figure 37 to Figure 39 compares the ASE spectra obtained from the 3 m EDZF and 3 m EDF at increasingly higher pump powers of 108.6 mW, 140.0 mW and 170.1 mW. It can be seen that on the whole, the average ASE power obtained from the 3 m EDF does not change significantly even as the pump power is increased, remaining at approximately -15.0 dBm at the 1530 nm region and slowly declining from -25.0 dBm to -27.0 dBm at a wavelength region from 1540 to 1560 nm. The excess energy from the pump manifests itself as lasing wavelengths in the 1530 nm region of the spectrum, but otherwise does not alter the shape or power of the spectrum.

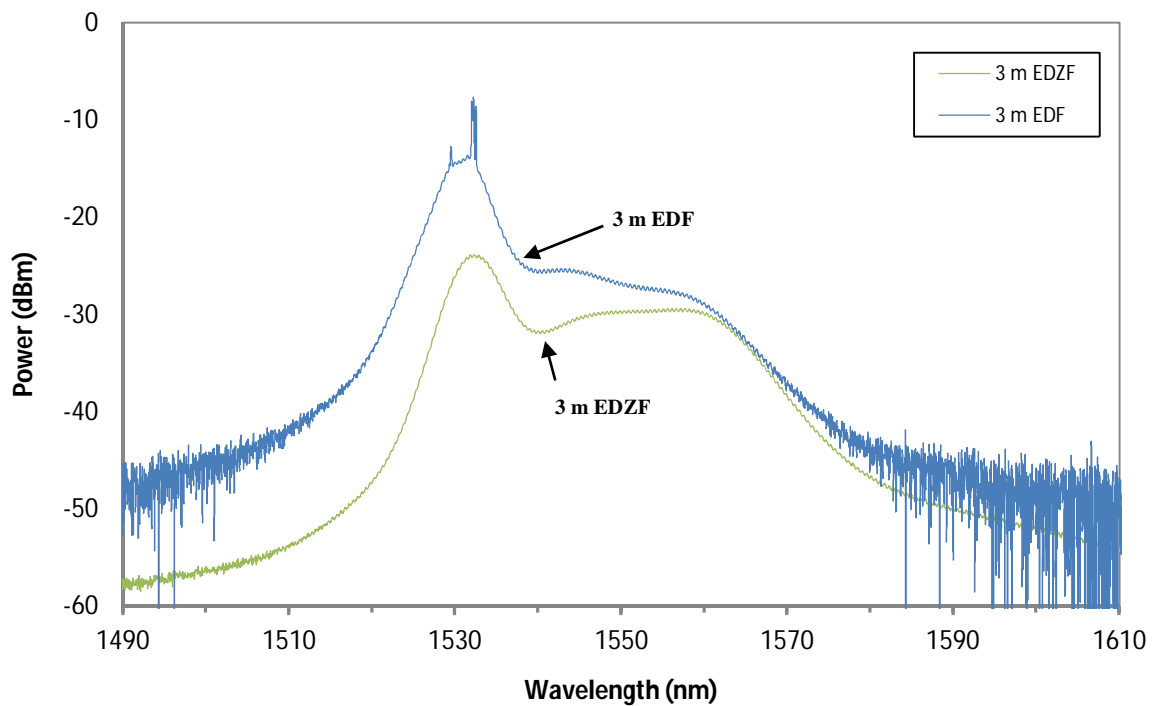


Figure 37: ASE spectrum from 1490 to 1610 nm from 3 m long EDZF and 3 m long EDF at pump power of 108.6 mW

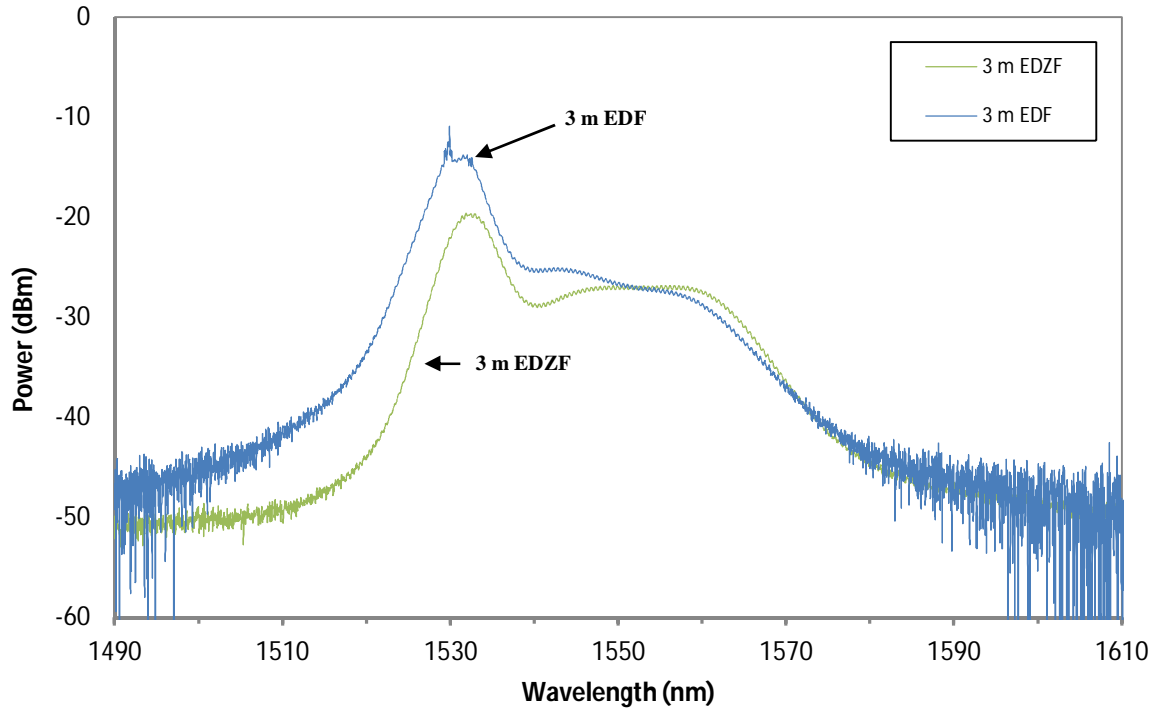


Figure 38: ASE spectrum from 1490 to 1610 nm from 3 m long EDZF and 3 m long EDF at pump power of 140.0 mW

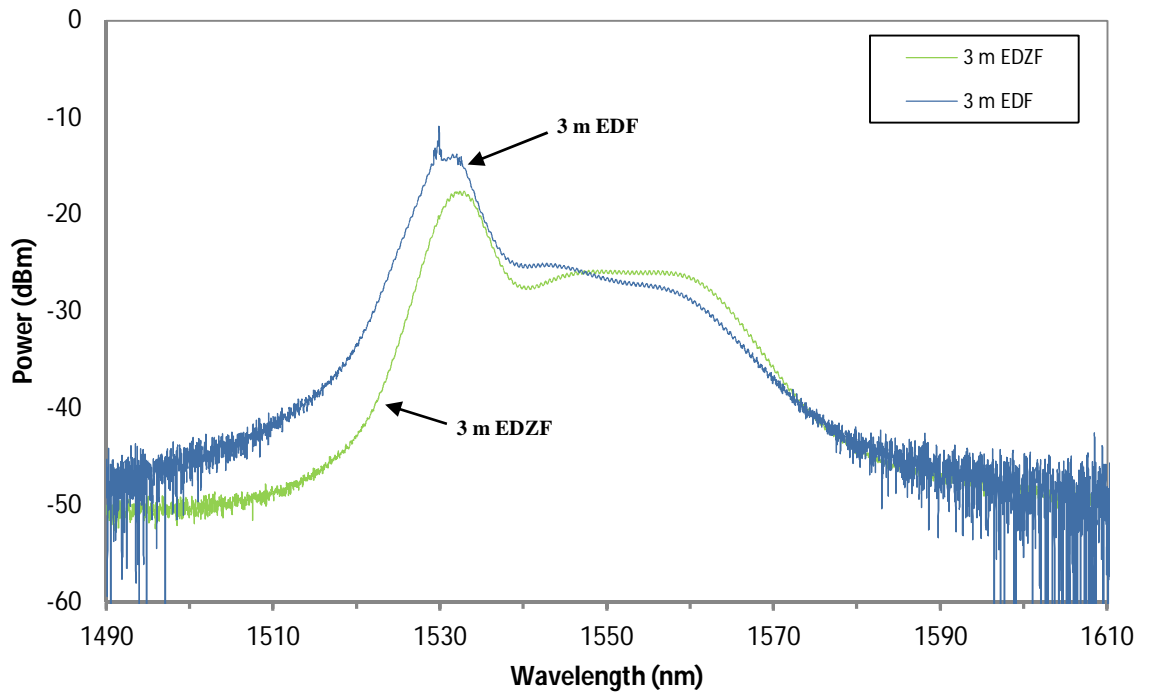


Figure 39: ASE spectrum from 1490 to 1610 nm from 3 m long EDZF and 3 m long EDF at pump power of 170.1 mW

In the case of the 3 m EDZF, increasing the pump power visibly increases the power level of the generated ASE spectrum, with the peak ASE power increasing from -33.6 dBm under a pump power of 76.0 mW to -24.9 dBm at a power of 108.7 mW. Further increases in the pump power to 140.0 mW and 170.1 mW yield ASE spectra with peak powers of -20.4 and -17.7 dBm, almost overlapping the ASE spectrum generated by the 3 m EDF under the same pumping conditions. It can be seen that at higher pump powers, a large increase in the pump power translates into only a small increase in the power of the ASE spectrum; this can be attributed to the EDZF approaching saturation, and it is thus predicted that further increases in the pump power will only yield minor, if not any change at all, in the power of the output spectrum.

An observation can be made in regards to the spectral curve of the ASE generated by the EDZF under different pumping powers. It can be seen that at the lowest pump power of 76.0 mW, both the 1530 nm peak and the following plateau have approximately the same power levels, averaging at -33.6 dBm. As the pump power is increased however, it is observed that the 1530 nm peak becomes more dominant, recording peak powers of -24.9, -20.4 and -17.7 dBm at pump powers of 108.7, 140.0 and 170.1 mW while the plateau region rises at a much slower rate, increasing from an average of -30.0 dBm to -28.0 dBm over the range of the same pump powers. This differs from that of the EDF, in which the region after the 1530 nm peak rises at about the same rate as the 1530 nm peak itself. The dominance of the 1530 nm peak region is attributed to the high dopant concentrations in the EDZF, whereby the initial part of the fibre will not fully undergo a population inversion under normal pumping conditions. As such, increasing the pump power will result in the energy being absorbed by the initial parts of the fibre, thus giving a higher 1530 nm peak power, but not allowing for the emissions from this region to be fully absorbed by the latter region of the EDZF, thus keeping the average power of the plateau region relatively constant in spite of the increased pump power.

As a matter of interest, the ASE spectrum obtained from the 3 m long is compared to that from a shorter EDZF, in this case a 2 m long EDZF. The spectrum is obtained by replacing the 3 m long EDZF as the DUT in Figure 33. The measurements for the 3 m long EDZF are then repeated with the new fibre as the DUT. The obtained spectra are shown in Figure 40 to Figure 43.

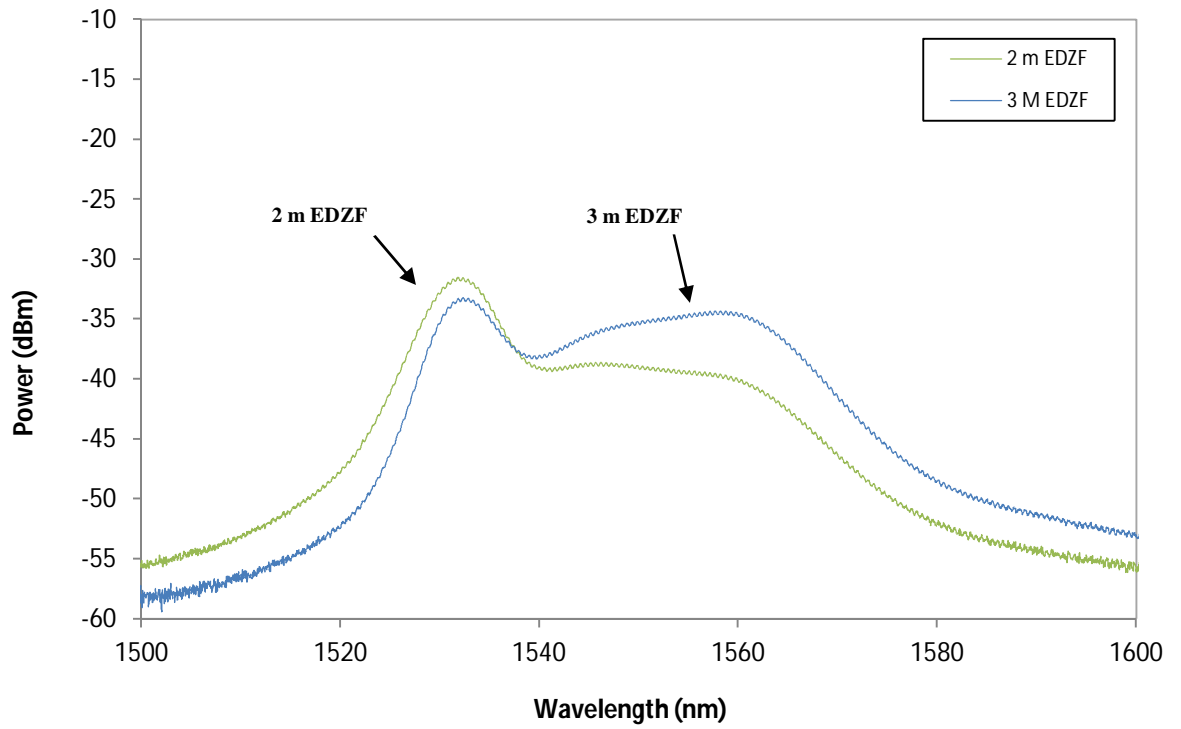


Figure 40: ASE spectrum from 1500 to 1600 nm from 2 m and 3 m long EDZF at pump power of 76.0 mW

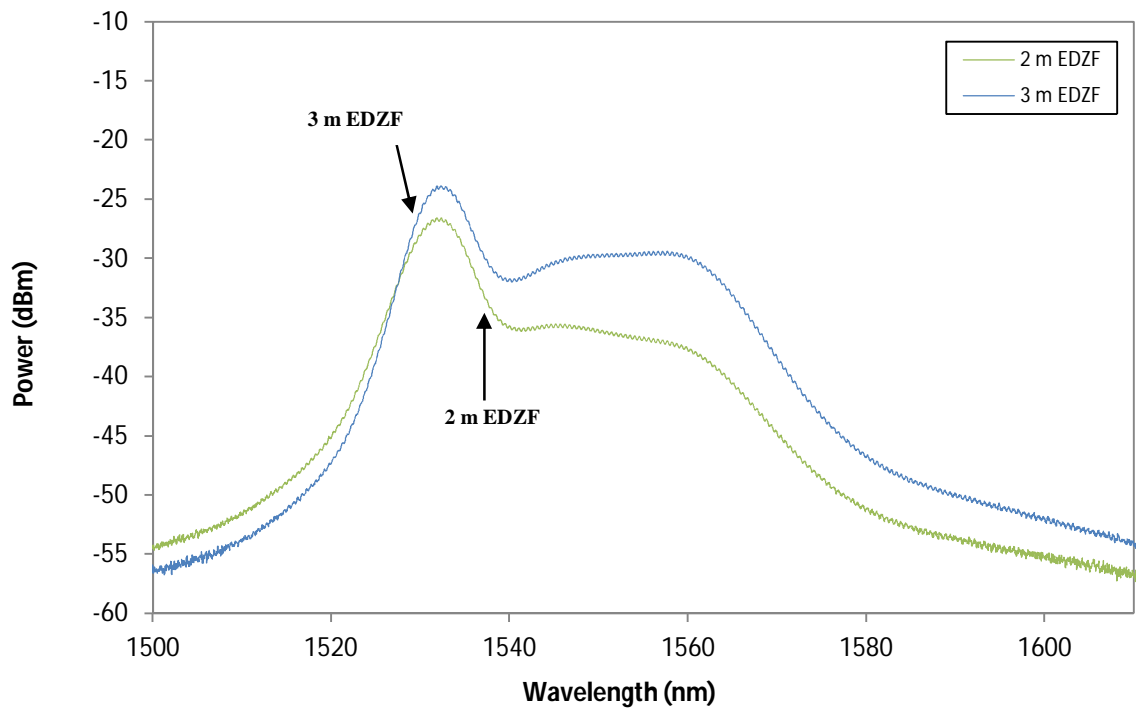


Figure 41: ASE spectrum from 1500 to 1600 nm from 2 m and 3 m long EDZF at pump power of 108.7 mW

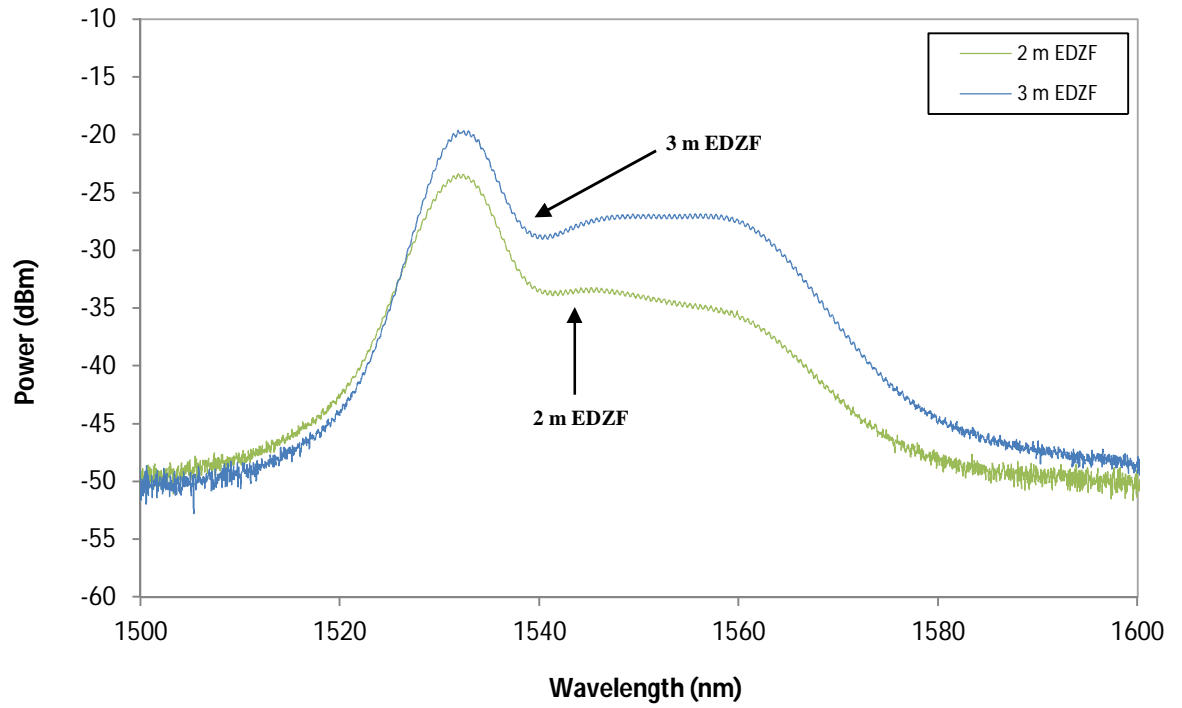


Figure 42: ASE spectrum from 1500 to 1600 nm from 2 m and 3 m long EDZF at pump power of 140.0 mW

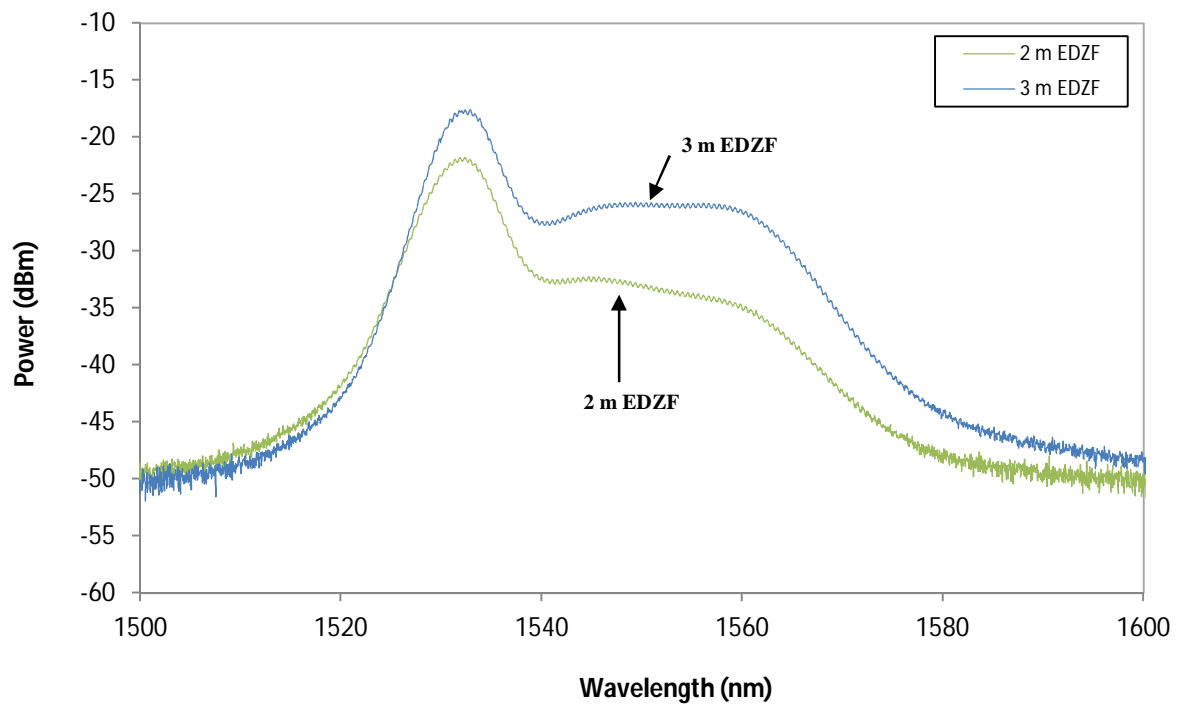


Figure 43: ASE spectrum from 1500 to 1600 nm from 2 m and 3 m long EDZF at pump power of 170.1 mW

It is interesting to note that spectrum of the ASE generated by the 2 m long EDZF is similar to that obtained from a normal EDF, with the power of the ASE spectrum experiencing a shallow decline after the 1530 nm peak, before dropping steeply as it nears 1560 nm. The ASE spectrum obtained from the 3 m EDZF on the other hand gives a flat plateau region after the 1530 nm peak up to 1560 nm, before the power levels drops sharply. The reason for this is again due to the higher concentration of Er^{3+} ions in the EDZF; naturally, the 3 m long EDZF would introduce a higher concentration of dopants into the system as compared to that of the 2 m long EDZF. Similarly to the behavior observed previously, the high dopant concentrations allow for the absorption of the ASE at the 1530 nm region and its re-emission at the longer wavelength region and effectively flattens the plateau region after the 1530 nm peak. The spectral curve of the 3 m long EDZF is as predicted, being of lower power than that of the 2 m EDZF at low pump powers, but quickly increasing as the pump power is raised. It can be seen that 2 m long EDZF is already saturated at a pump power of 76.0 mW, as the spectral curve barely changes in terms of power as the pump power is increased further.

This fact can be confirmed by measuring the excess 980 pump power, which will begin to rise once all the Er^{3+} ions in the active medium have been excited to the metastable level. Figure 44 shows the excess pump power for both the 2 m and 3 m long EDZFs as a function of the input pump power. It can be seen clearly from the figure that the 3 m long EDZF is far from saturated, with an excess pump of less than 0.5 mW at the highest input pump power of 170.0 mW. The 2 m long EDZF on the other hand shows a steady increase in the excess pump power above an input pump power of 41.0 mW, indicating that the EDZF has already reached saturation levels.

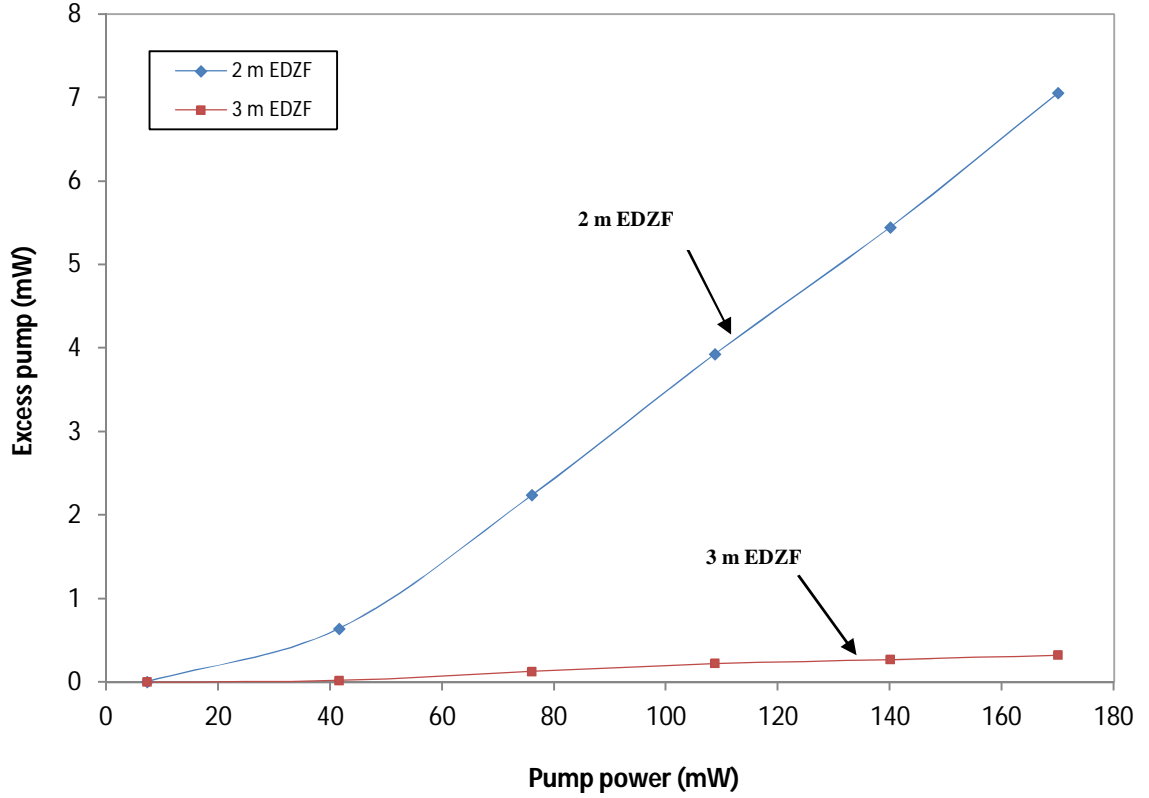


Figure 44: Excess 980 nm pump power as a function of the input 980 nm pump power for the 2 m and 3 m long EDZFs

This validates the spectral plots obtained in Figure 42 to Figure 44. The data also shows that further experimentation with the EDZF, such as gain and NF measurement as well as examinations of its non-linear characteristics are better conducted using the 3 m long EDZF, as the operational limits of the 2 m EDZF are reached too quickly.

3.3.2 Gain and NF Characteristics of the EDZF

The most crucial characteristic of the EDZF, and in fact the impetus of its development, is its ability to amplify propagating optical signals in a compact form factor. For this reason, the EDZFs gain and NF parameters are the most important aspects of its operation, and this will become the focus of this chapter.

The measurement of the gain and NF of the EDZF is done using the same setup as Figure 30, with the only difference to the setup now being the inclusion of an

external signal source in the form of a Tunable Laser Source (TLS). The modified setup is shown in Figure 45.

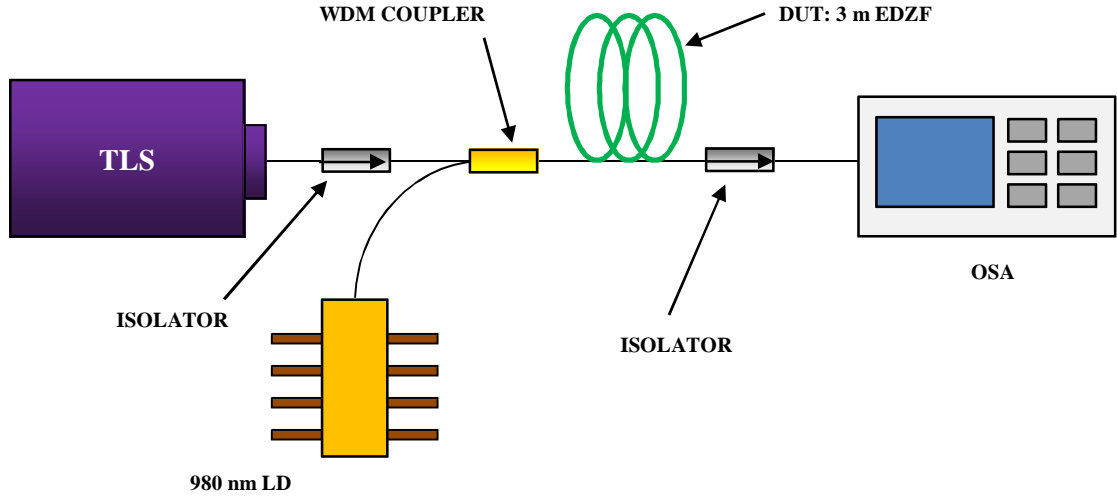


Figure 45: Experimental setup for gain and NF measurement of 3 m long EDZF

The external signal is generated from a Yokogawa AQ2200 TLS, which has an operational wavelength range of 1460 nm to 1640 nm. The signals generated by the TLS have a linewidth of 0.015 nm, with a maximum average output power of 12.8 dBm³³. An optical isolator is placed just after the output of the TLS to prevent any backward propagating signals from the DUT from reaching the TLS and possibly damaging it.

The gain and NF levels obtained by the EDZF based amplifier is similar to that of other amplifiers using highly-doped active media. The pump power of the system is kept at 170.1 mW, and two input signals at -30 dBm and 0 dBm are measured over a wavelength range of 1530 nm to 1590 nm, in 10 nm intervals. The -30 dBm signal represents a Low signal, or a low powered signal that is typically observed in optical transmission lines after a certain distance, due to the attenuation experienced by the signal. The 0 dBm signal on the other hand represents a saturated input signal, typically experienced near the source. These signals represent the different conditions under which the EDZF can be deployed, namely as an in-line

³³ It must be noted that the maximum output power of 12.8 dBm is not the highest power that can be obtained by the TLS, as it can be configured to deliver signals of higher power. In this work however the maximum power for the TLS is set at 12.8 dBm, for the purpose of preventing damage to the system as well as to avoid decreasing its operation lifespan.

amplifier, or as a booster amplifier. The gain performance of the EDZF as an amplifier is given in Figure 46.

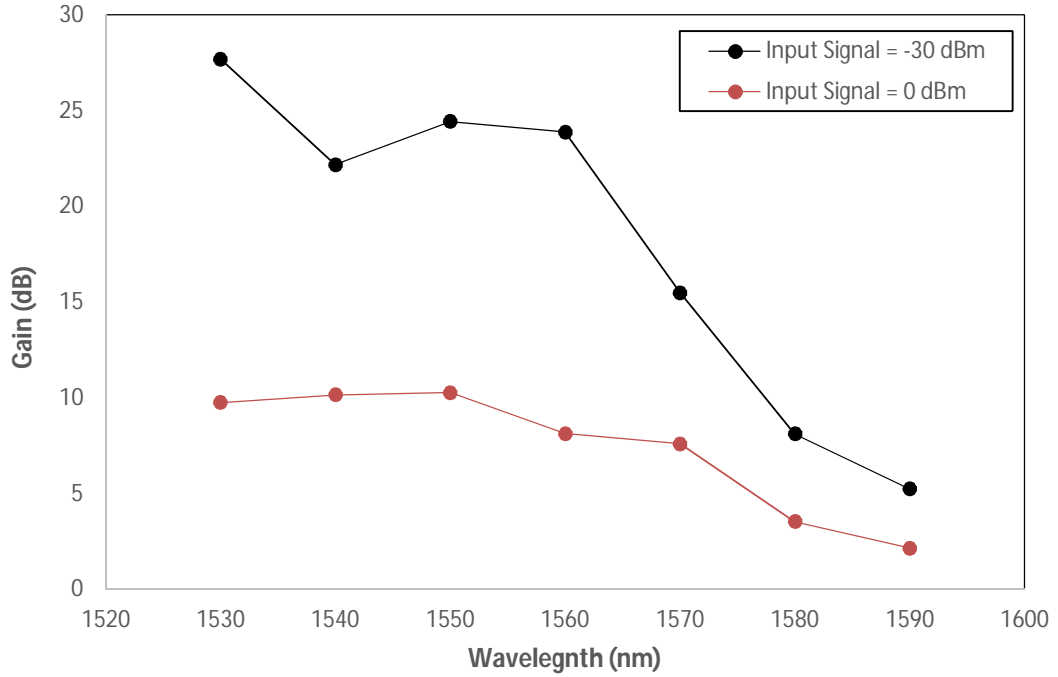


Figure 46: Gain of the EDZF imparted to Low (-30 dBm) signal and High (0 dBm) input signals.

It can be seen immediately from Figure 46 that the EDZF amplifier can impart very high gain levels, ranging from approximately 28.0 dB near the central region of 1530 nm, as well as a high gain level of between 22.0 to 25.0 dB at what would be the plateau region of the EDZF's ASE output. Outside of this region however, the gain begins to decline, as expected, and finally reaches a relatively low value of around 5.0 dB at 1590 nm. The same observation can also be made for the gain experienced by the High signal, with a relatively flat gain output of around 10.0 dB from 1530 nm to about 1570 nm, before the gain begins to drop to about 2.0 or 3.0 dB at 1590 nm.

However, the high gain levels imparted by the EDZF are also accompanied by relatively high NF levels. In the case of the 0 dBm input signal, the NF is initially recorded at high levels, approximately 14.1 dB before quickly dropping to 9.3 dB over a wavelength range of 1530 to 1550 nm. A subsequent increase in the input wavelength sees the NF decrease further, though not as steeply as before, reaching a value of 7.7 dB at 1580 nm. However, as the input wavelength continues to increase,

the NF begins to rise again, now increasing to 8.3 dB at 1590 nm. In the case of the -30 dBm input signal, a similar observation is made, with the initial high NF of 12.2 dB decreasing quickly to only 4.9 dB over a wavelength range of 1530 to 1550 nm. Subsequently increases in the input wavelength at this power see a further drop in the NF to 2.8 dB, before it rises slightly to approximately 3.9 dB at 1590 nm. The NF of the EDZF based amplifier, as a function of the wavelength, is given in Figure 47.

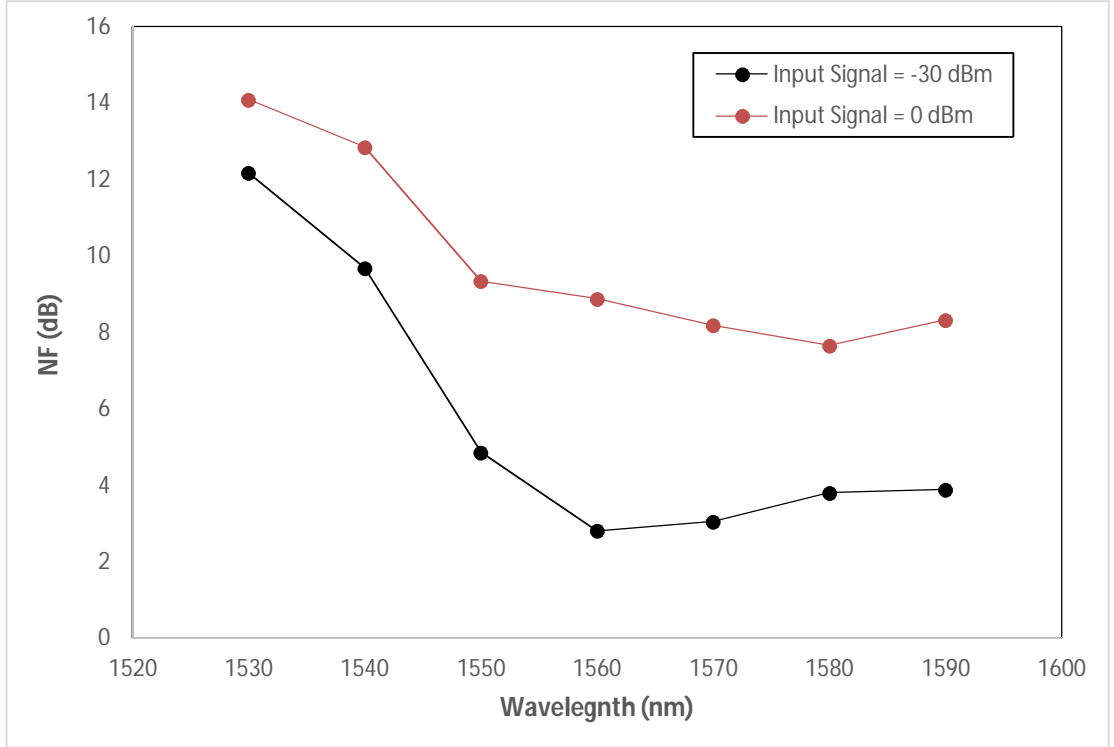


Figure 47: NF of the EDZF imparted to Low (-30 dBm) signal and High (0 dBm) input signals

The high NF levels can be attributed to the high ASE levels also encountered at this region. In fact, if one were to overlay the ASE spectrum against the gain and NF values obtained over the wavelength range, it would be seen that both the gain and NF follow a relatively similar pattern, with a peak value corresponding to the peak region of the ASE spectrum, followed by an almost constant region that where the plateau region of the ASE lies. This gives the EDZF some advantages, on particular the ability to provide almost constant gain over wavelength region, although at the cost of the high NF levels. The gain and NF values obtained in this work correspond to that previously obtained by M. C. Paul, et. al. in references [24] and [78].

3.3.3 *The EDZF as an SLM Fibre Laser*

Fibre lasers capable of generating a SLM output have recently become a key focus area in the development of fibre lasers. This is because these fibre lasers have multiple high potential applications such as dense optical communications systems, microwave and photonic generation and high-resolution optical spectroscopy [79], [80], [81], [82]. The SLM output is highly desired as it is able to provide a highly stable, continuous wave output where the oscillation of multiple densely spaced longitudinal modes has been prevented. Because of this, mode hopping is prevented between the side modes and central wavelength [83], giving a high quality output. In order to obtain the SLM output, many techniques and approaches have been tried, including the use of very short lasing cavities, Distributed Bragg Reflectors (DBRs) using two Fibre Bragg Gratings (FBGs) and also tunable fibre Fabry-Perot filters in a passive triple-ring cavity [84], [85]. These methods however are very complicated and necessitate fine tuning and adjustments in order to operate; while this may be acceptable in a controlled, laboratory setting, it is far from ideal for commercial use. It is possible to obtain the same effect in a Sagnac loop, which will function as a self-induced FBG filter to obtain the desired SLM output. This approach however requires a long EDF length, of about 15 m to work, making it costly and also bulky [86].

It is here that the EDZF plays a significant role. The high dopant concentrations in the fibre allow for a short cavity length to be realized, while the fact that the EDZF is based on a conventional silica host means that it can be easily connected to conventional fibre components. This is a significant advantage over other similar highly doped EDFs that are based on soft glasses, which cannot be easily integrated with silica fibre based components.

The setup of the proposed EDZF based SLM is shown in Figure 48. The SLM laser is configured in a ring cavity, with a short EDZF of only 0.5 m acting as the gain media. To ensure the SLM output is achieved, two saturable absorbers, SA1 and SA2 are also incorporated into the setup. The use of the short EDZF is intended primarily to ensure that the laser cavity length is kept as short as possible; due to the high dopant concentrations, the 0.5 m EDZF can provide the same performance as an EDF approximately 4 m long. This is a crucial factor in obtaining an SLM output as the power of the lasing wavelength should be adequately high, even if the cavity length is

shortened. The addition of SA1 and SA2 are to ensure the absorption of any stray side-modes, thus ensuring that only the central wavelength is allowed to propagate in the cavity.

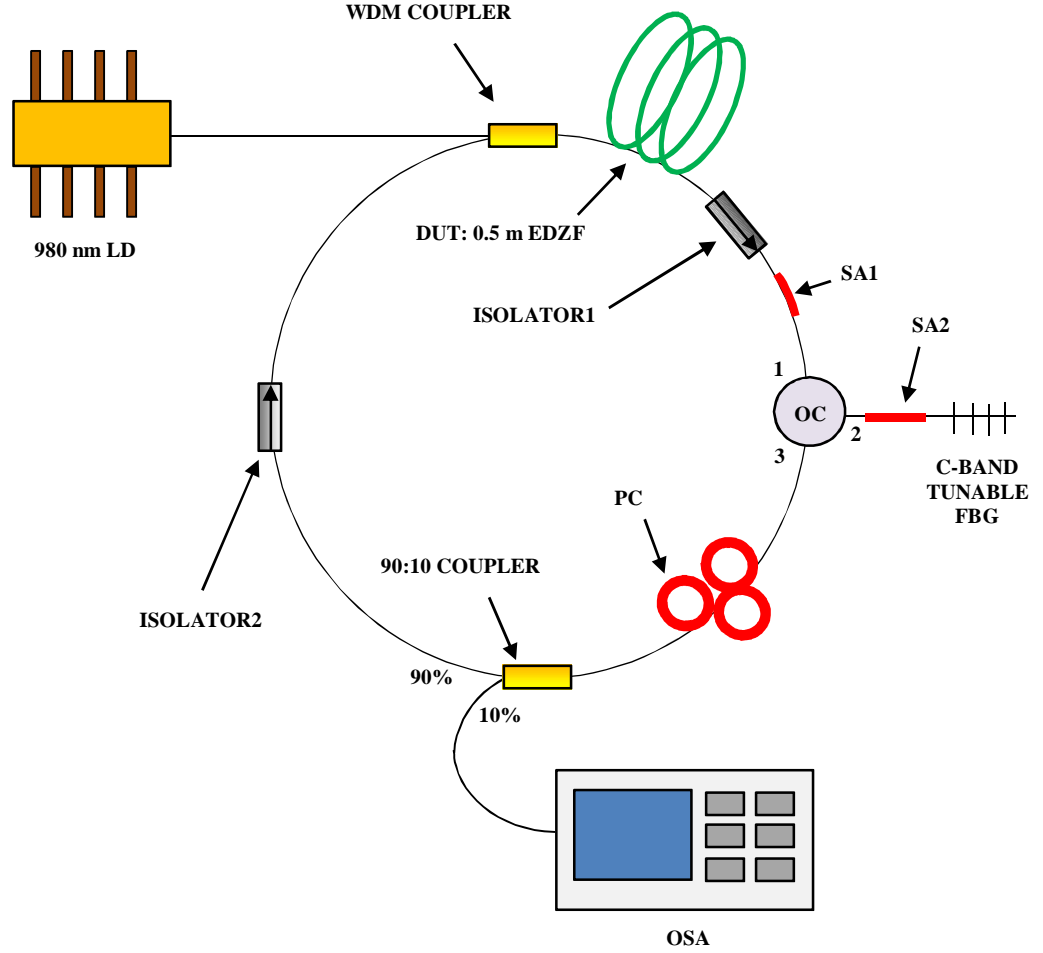


Figure 48: Experimental setup of the proposed SLM fibre laser

To take advantage of the longer operational bandwidth of the EDZF, a Tunable Fibre Bragg Grating (TBFG) operating in the C-band region is also added to the setup. This allows the wavelength of the SLM to be adjusted along the C-band region, thus giving the proposed setup a degree of customizability. The proposed SLM is pumped by a 980 nm LD with a maximum power of 80 mW, and the output from the LD is injected into the cavity through a 980/1550 nm WDM, with the common output of the WDM being connected to the 0.5 m long EDZF. The other end of the EDZF is connected to an optical isolator, designated Isolator 1 in Figure 48, which is in turn connected to SA1. SA1 is a short, 3 cm long conventional EDF, with an erbium ion

concentration of about 900 ppm/wt and an absorption rate of 5.0 dB/m at 1530 nm. The other end of SA1 is connected to Port 1 of the Optical Circulator (OC), with Port 2 of the OC being connected to SA2 and subsequently to the C-band TBFG. SA2 is made from the same EDF as SA1, with a length of 6 cm. Port 3 of the OC is connected to a Polarization Controller (PC), which serves as to adjust the polarization of the propagating wavelength and optimize the output power. The PC is then connected to a 90:10 tap coupler, which extracts 10% of the signal for further analysis, while the 90% port of the tap coupler is connected to another optical isolator, Isolator 2 that is in turn connected to the 1550 nm port of the WDM, thereby completing the laser cavity.

The TBFG used in this work is created by mounting a C-band FBG, which has a reflectivity of 99% and a bandwidth of 0.1 nm, onto a metal plate. The metal plate has one end fixed to an immovable stand; while the other end is fixed to a screw which when turned will impart pressure onto the metal plate, causing it to bend. The bending of the metal plate will in turn cause the polymer to stretch, and the FBG along with it. Thus, the FBG can be made to filter different wavelengths by simply adjusting the screw of the metal plate. Figure 49 shows the setup of the C-band TBFG.

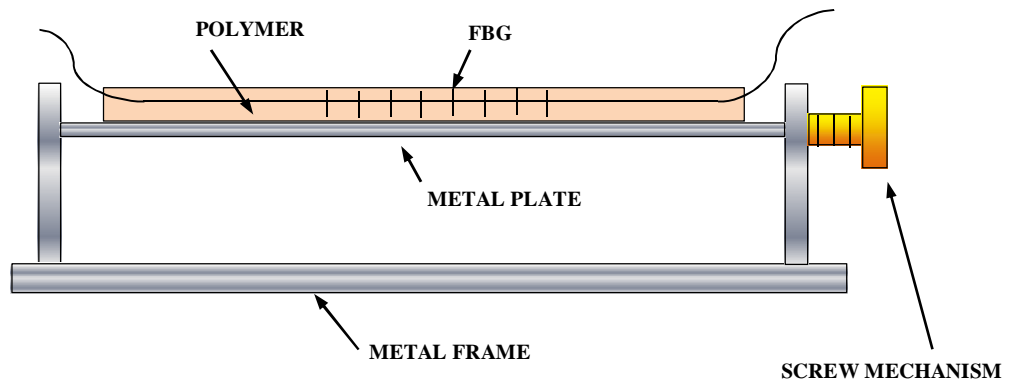


Figure 49: Setup of the C-band TBFG

Figure 50 shows the actual C-band TBFG mechanism.

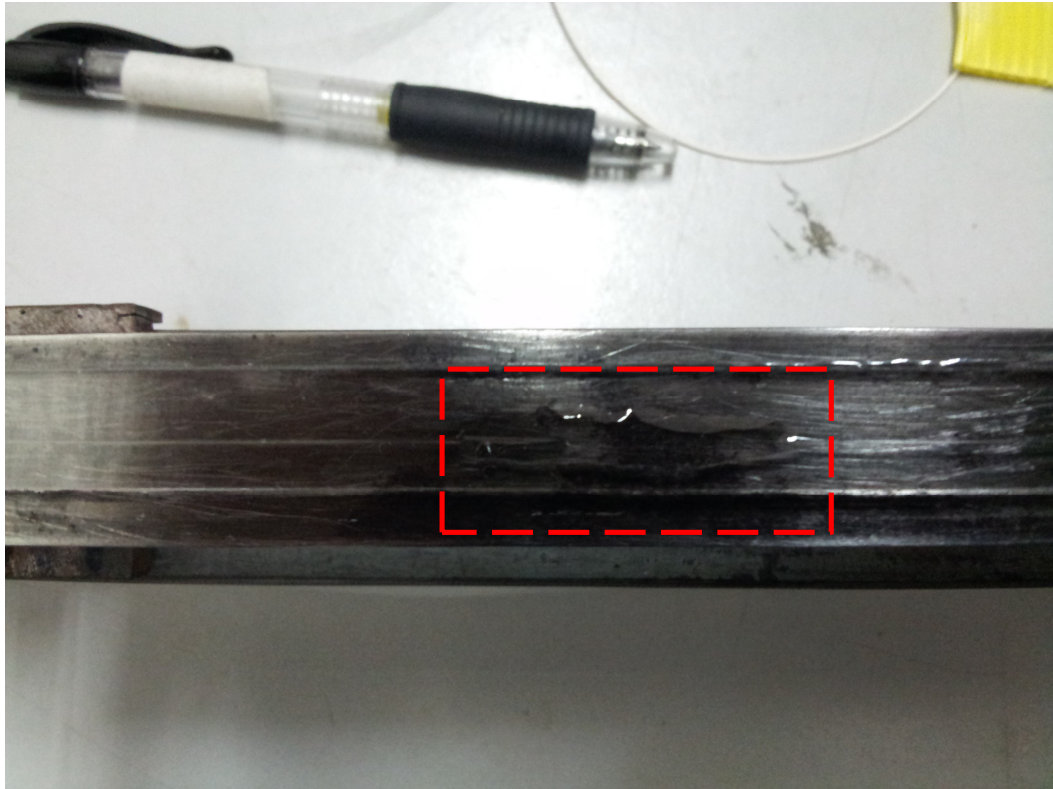


Figure 50: C-band TBFG. The TBFG itself is embedded in the polymer layer (*highlighted by the red box*), which serves as a medium to transfer the strain and compression experienced by the metal plate when it is bent, without damaging the C-band FBG itself.

The operation of the SLM fibre laser does not deviate from that of a conventional fibre laser with a wavelength selection mechanism. As the EDZF is pumped by the 980 nm LD, it generates an ASE spectrum which travels clockwise along the ring cavity until it encounters the OC. The OC directs the incoming spectrum towards the C-band TBFG, where the ASE will be filtered and reflect a single wavelength. This wavelength will now travel back towards the OC, where it re-enters the cavity from Ports 2 to 3 and will oscillate in the ring cavity, similar to a conventional fibre laser. The two saturable absorbers absorb any additional side modes and noise that may be generated in the ring cavity, thus giving an SLM output. Should the TBFG be altered, the process repeats itself from the beginning, with a new wavelength being filtered out. The total cavity length is 5.2 m, with a free spectral range of 3.9 MHz.

The tunability of the proposed fibre laser is shown in Figure 51. It is determined that the EDZF based SLM laser has a tuning range of approximately 11.2 nm from 1533.8 nm to 1545.0 nm with a peak wavelength around 1540.0 nm. The tuning of the output wavelength is done by bending a metal plate on which the C-band FBG is mounted onto [87]. The tuning range is not allowed to exceed 1533.8 nm or 1545.0 nm, as bending the metal plate this far will cause irreversible damage to the FBG due to excessive strain. The average SNR for the proposed laser is quite stable, with a value of more than 50 dB, while the output power for 5 wavelengths is above -10.0 dBm, with another two wavelengths having a power of above -15.0 dBm. It must be noted however that the output power at 1545 nm is lower than the power obtained at other wavelengths; this is because at this wavelength, the maximum strain is applied to the FBG, resulting in losses as the mechanical stretching become greater.

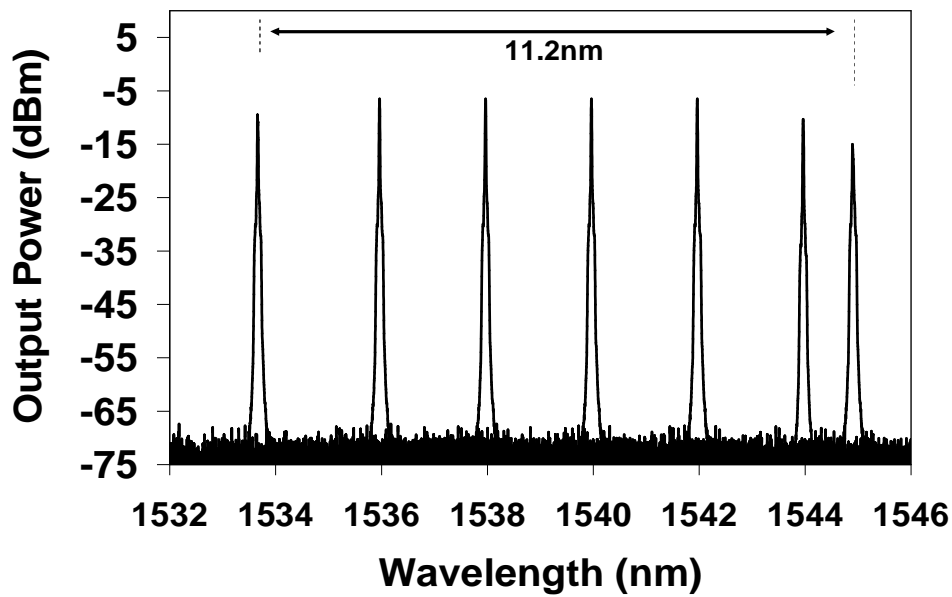


Figure 51: Tunability of the SLM fibre laser from 1533.8 nm to 1545.0 nm

Figure 52 (a) shows the Radio Frequency (RF) spectrum obtained from the fibre laser without the saturable absorbers present in the cavity, while Figure 52 (b) shows the output obtained by the same system, with the presence of the two saturable absorbers. The RF spectra are obtained by replacing the OSA with an Opto-Electronic (OE) converter and a Radio Frequency Sepctrum Analyzer (RF-SA). It can be seen that the beating noise peaks observed in the trace are densely spaced, indicating that the

modes allowed to propagate inside the cavity are the ones that fulfill the cavity length requirements for resonance by constructive interference of the different frequencies. However, in order to suppress these unwanted modes, the cavity length can be optimized and the saturable absorbers added to the system so that only the mode with the highest power (which is the desired mode) is allowed to oscillate in the laser cavity. It can be seen clearly that the incorporation of the saturable absorbers absorbs all of the undesirable modes and allows only one longitudinal mode to oscillate in the system. The inset of Figure 52 (b) further validates that the proposed laser operates in the single longitudinal mode.

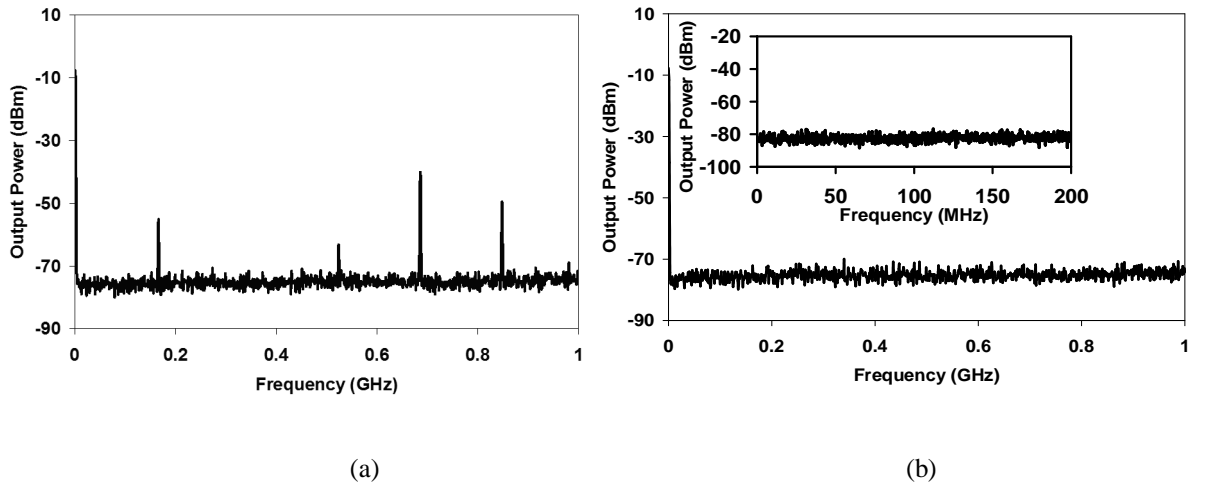


Figure 52: Frequency spectra of the SLM fibre laser obtained using an RF-SA (a) before the addition of the saturable absorbers and (b) with SA1 and SA2 present in the laser cavity

The output of the EDZF based SLM laser is highly stable, with almost no fluctuations in power or wavelength. This is shown in Figure 53, with the system set to generate an output at 1540 nm. The output of the system is measured over a period of two and a half hours in 10-minute intervals, and during this period almost no fluctuations are observed in either the power or wavelength of the laser's output.

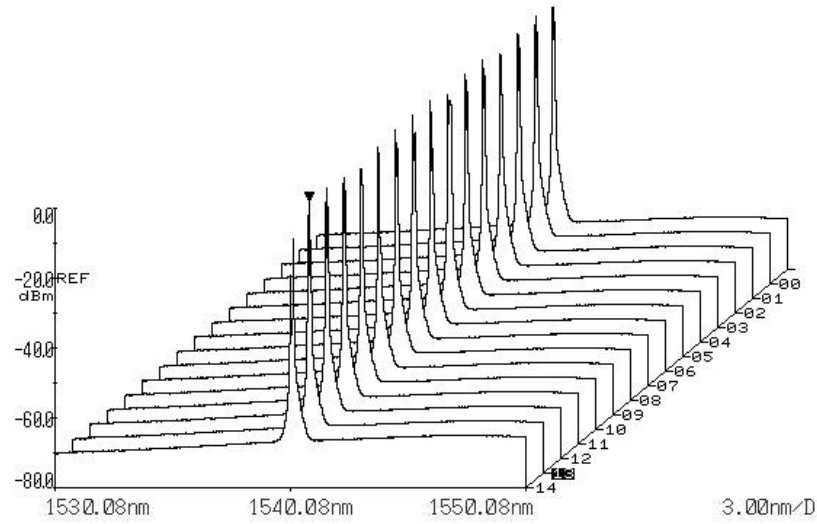
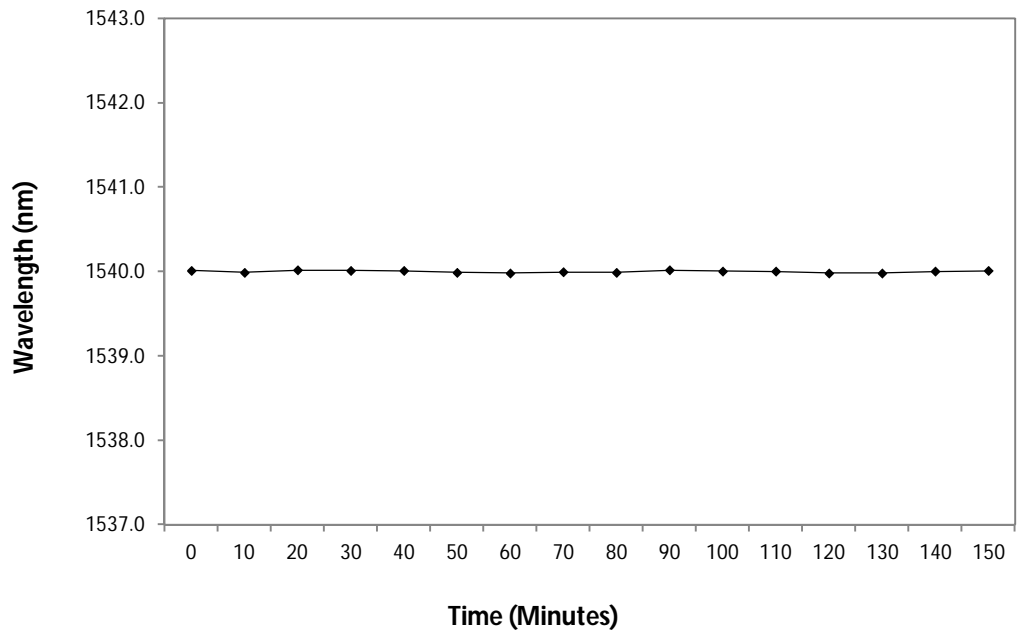


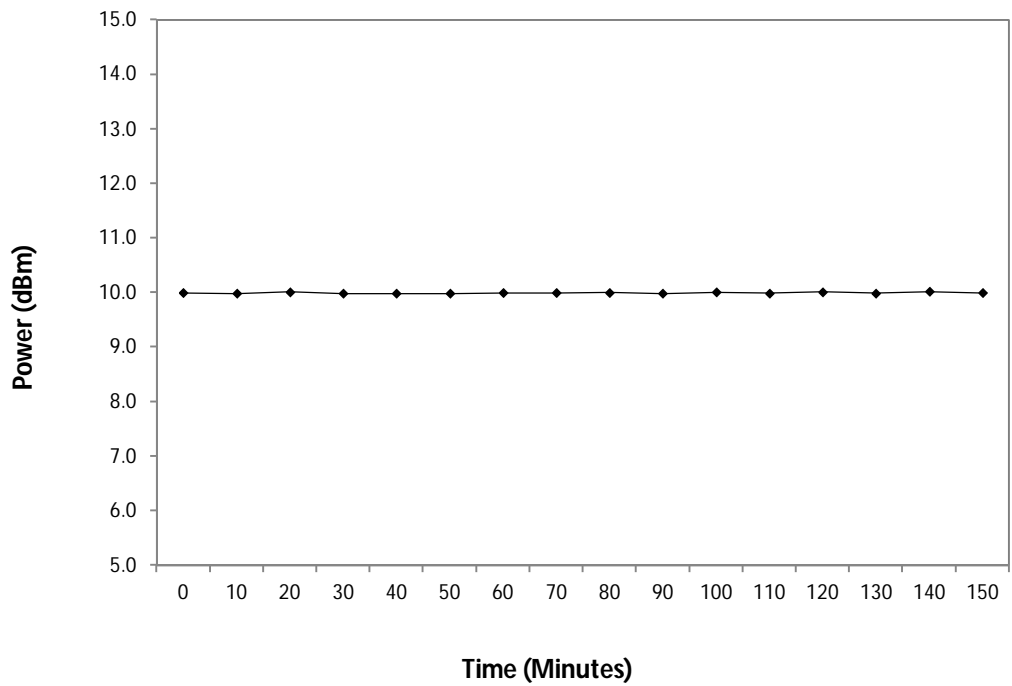
Figure 53: 3-dimensional plot of the EDZF based SLM fibre laser's output power and wavelength against time. The measurements are taken at 10 minute intervals over a period of two and a half hours.

A clearer representation of the data in Figure 53 is given in Figure 54. It can be seen clearly that both the wavelength and power of the SLM laser remains steady over the entire test period, thereby validating the stability of the system.

The other important measurement of the output of the SLM is the linewidth of the measurement. In this experiment, the self-heterodyne linewidth measurement technique is used to measure the linewidth of the generated output, using the setup as shown in Figure 55. For this technique, the output of the SLM fibre laser is divided into two arms of about equal power using a 3 dB coupler. One output of the coupler is connected to a 500 m long SMF, which functions as a delay line, and is in turn is connected to a PC to form the upper arm as shown in Figure 55. The other output of the 3 dB coupler is connected to an Acousto-Optic Modulator (AOM) operating at 80 MHz, and forms the lower arm of the setup. The signals propagating from both arms are then recombined using another 3 dB coupler, with the output of the coupler now connected to a RF-SA.



(a)



(b)

Figure 54: (a) plot of output wavelength over time, (b) plot of output power against time.

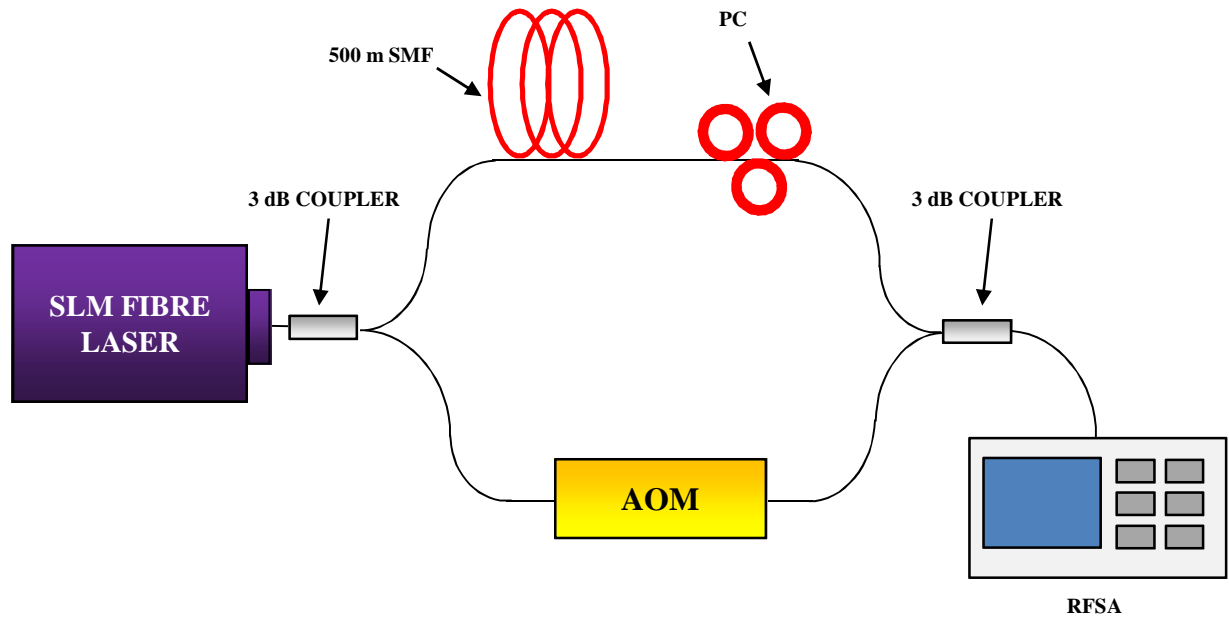


Figure 55: Setup of the self-heterodyne linewidth measurement technique

Figure 56 shows the linewidth measurement obtained for the proposed SLM. From the figure, the linewidth measurement clearly shows that the linewidth of the SLM is about 0.2 MHz.

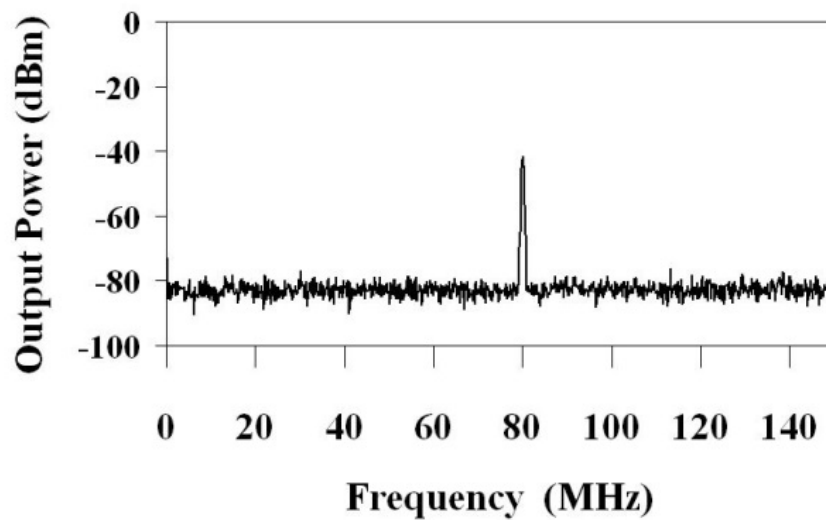


Figure 56: Linewidth measurement of the output from the SLM fibre laser

The proposed tunable, wavelength-swept SLM laser can have many important applications such as in the area of high-resolution spectroscopy, WDM communications technology and also as sources for test and measurement equipment. The advantage of this system is that it makes use of the EDZF, which allows high erbium concentrations, and therefore a short cavity length to be realized and thus creating a compact, cost-effective and rugged platform with a highly stable output. It is also prudent to note that this is the first time, to the knowledge of the research team, of the application of the EDZF as the primary gain media for obtaining an SLM output.

3.3.4 The EDZF as a Non-Linear Gain Medium

One of the interesting characteristics of the EDZF is its non-linear properties. Although non-linear interactions in silica optical fibres are typically observed only when high intensity signals propagate through them the presence of additional materials, such as ZrO₂ micro-crystallites in the core region of the EDZF, allow these interactions to occur at lower signal intensities.

In most cases, non-linear effects are detrimental towards the performance of optical systems, as they affect the quality of the propagating signals. The effects of non-linear optical phenomena are especially prevalent in WDM systems, where many closely-spaced signals propagate along the fibre simultaneously. The interactions of these signals will generate high optical intensities in the fibre, thus forcing engineers and system designers to limit the power of the input signals to prevent these non-linear effects from manifesting. For instance, in a 128 channel, 10 GB system the power of each launched signal must be limited to around – 5.0 dBm, with a total combined launch power of 16.0 dBm. Any higher than this, and non-linear effects start to manifest, and significantly degrade the performance of the system [88], [89]. However, non-linear optical phenomena are beginning to find substantial potential for a variety of applications in optical fibre systems, especially in the development of all-optical systems [90], [91], [92] such as wavelength converters, multiplexing and demultiplexing and also optical monitoring and switching. In this section, the non-linear characteristics of the EDZF will be explored, with attention being paid to the FWM

effect. The reason for this is that of most of the non-linear phenomena that can be generated in a fibre, the FWM effect in particular has a high potential for real-world applications as a wavelength converter.

Optical non-linear phenomena can be divided into two general categories. The first category of non-linear phenomena are those that arise from scattering, such as Stimulated Brillouin Scattering (SBS) and Stimulated Raman Scattering (SRS). The second group of non-linear phenomena arises from changes in the refractive index of the fibre, and typically results in effects such as Self Phase Modulation (SPM), Cross Phased Modulation (XPM), Modulation Instability (MI) and the desired effect of interest, the FWM effect. The effects from both categories arise from the modification of the optical response of the material by a large optical field [90], [93], and can be represented as:

$$P = \epsilon_0 \chi^{(1)} \cdot E_j + \epsilon_0 \chi^{(2)} : E_j E_k + \epsilon_0 \chi^{(3)} \cdot E_j E_k E_l + \dots \quad (45)$$

where P is the electrical polarization, and E_j , E_k , and E_l represent the electric field intensities. Equation 45 can also be refined further as:

$$P_i = \epsilon_0 \sum_{j=1}^3 \chi_{ij}^{(1)} \cdot E_j + \epsilon_0 \sum_{j=1}^3 \sum_{k=1}^3 \chi_{ijk}^{(2)} \chi^{(2)} \cdot E_j E_k + \epsilon_0 \sum_{j=1}^3 \sum_{k=1}^3 \sum_{l=1}^3 \chi_{ijkl}^{(3)} \cdot E_j E_k E_l + \dots \quad (46)$$

with ϵ_0 being the vacuum permittivity and $\chi^{(n)}$ being the n^{th} order susceptibility, with a tensor of rank $n+1$. The second-order susceptibility of an optical fibre is always zero, due to optical isotropy, on the condition that the glass is in no way perturbed. Once perturbed, the susceptibilities start to play an effect, with the real parts of the susceptibility being associated with the changes to the index of refraction while the imaginary part is associated with the phase delay of the material.

The non-linear effects that manifest in optical fibres can also be divided into two general categories; Type I or Type II [90], [94]. Type I non-linear effects encompass non-linear effects that arise from scattering, namely SBS and SRS effects, while Type II effects encompass those that arise from changes induced in the refractive index of the fibre due to the high intensity signals. These effects include

modulation effects, in the form of SPM or XPM, or the generation of new propagating wavelengths and parametric processes such as MI and FWM. The SPM, XPM and FWM effects share a common mathematical origin [90], and by considering the interactions of two propagating wavelengths, the total electric field can be written as:

$$E(r, t) = \frac{1}{3} [E_1 \exp(-i\omega_1 t) + E_2 \exp(-i\omega_2 t)] + c \dots \dots \dots (47)$$

Inserting equation 46 into 47 now gives a number of P_i terms. $P_i(\omega_1) \propto (|E_1|^2 + 2|E_2|^2)E_1$ and $P_i(\omega_2) \propto (|E_2|^2 + 2|E_1|^2)E_2$ both contain SPM as the first term in each, and XPM in the second term. Additionally the P_i terms, $P_i(2\omega_1 - \omega_2) \propto E_1^2 E_2^*$ and $P_i(2\omega_2 - \omega_1) \propto E_2^2 E_1^*$ represent the FWM terms. In this work however, the interest in the EDZF's non-linear characteristics is focused exclusively on the FWM effect, as this particular non-linear phenomena can be used for specialty applications such as wavelength conversion to occur, which has highly potential in commercial systems.

The FWM process is a nonlinear process that involves the recombination of signals with different frequencies. In this regards, photons from one or more signals with different wavelengths are annihilated, and new photons are generated at different frequencies. The original signals are typically known as the pumps, while the new frequencies are known as the signals and the idlers. The pump frequencies can be represented by ω_1 and ω_2 respectively, while the frequencies of the generated signals and idlers are designated as ω_3 and ω_4 respectively. The net energy and momentum of the system remains conserved, regardless of the different frequencies of the photons [90]. As the photon energy and momentum for a photon with a frequency of ω can be given as $\hbar\omega$ and $\beta\omega$, thus the conservation relations can take the form of:

$$\omega_1 + \omega_2 = \omega_3 + \omega_4, \quad \beta(\omega_1) + \beta(\omega_2) = \beta(\omega_3) + \beta(\omega_4) \dots \dots \dots (48)$$

where β is the propagation constant as a function of frequency. For degenerate FWM, $\omega_1 = \omega_2$. As all these wave vectors propagate in the same direction, thus only the magnitude of these vectors is shown in Equation 48. The second half of Equation 48 is also of particular importance, as $\beta(\omega_j)$ is responsible for the phase shift

experienced by the i^{th} wave. Thus, the second half of the equation is also known as the phase matching condition [93].

The actual mechanism in which the new frequencies are generated can be illustrated by considering the bound electrons inside the non-linear media, which in this case would be the EDZF. When input signals of high intensity propagate in the fibre, the bound electrons will be forced to oscillate, in most cases almost instantaneously and at any frequency. As the electrons are still confined to their original atoms, they respond to the applied electromagnetic field by emitting secondary waves at both the original frequencies, which constitutes a linear response, as well as at two new frequencies, which constitute a third-order non-linear response [90]. The signal and idler frequencies, ω_3 and ω_4 are generated at frequencies corresponding to:

$$\omega_3 = 2\omega_1 - \omega_2, \text{ and } \omega_4 = 2\omega_2 - \omega_1 \dots \dots \dots (49)$$

The above case is known as non-degenerate FWM, whereby four different frequency components interact with each other. It is also possible to encounter degenerate FWM, which occurs when two of the four frequency components overlap. In this scenario, the pump wavelength will act as an amplifier source; thus for two photons taken from the pump wavelength, one is added to the signal wavelength, while the other is added to the idler which appears on the side of the pump wavelength opposite to the signal [95]. The FWM effect can also be explained by the coupled differential equations for the propagating amplitudes, and including the phase mismatches that occur due to XPM and SPM [94]. The formula derived by Hill A et. al. [96], which was subsequently modified by Shibata et. al. [97] to incorporate the phase-mismatch dependent efficiency is able to predict well the occurrence and characteristics of the FWM effect in the fibre.

In addition to generating new wavelengths, the FWM process can also be used to derive the non-linear coefficient of a fibre. This is done by taking advantage of the fact that the FWM effect is dependent on the non-linear coefficient of a fibre. Determining the non-linear coefficient can be done by using the relationship:

$$\gamma = \sqrt{\frac{P_{FWM}}{\eta P_s P_p^2 e^{-\alpha L} L_{eff}^2}} \dots\dots\dots (50)$$

where P_{FWM} is the FWM output power, P_s is the input signal power, P_p is the input pump power, L is the fibre length and α is the attenuation coefficient of the fibre. L_{eff} is the effective length of the fibre, and is given as:

$$L_{eff} = \frac{1 - e^{-\alpha L}}{\alpha} \dots\dots\dots (51)$$

The normalized FWM efficiency, η , can be given as:

$$\eta = \frac{\alpha^2}{\alpha^2 + \Delta\beta^2} \left[1 + \frac{2e^{-\alpha L}(1 - \cos(\Delta\beta L))}{(1 - e^{-\alpha L})^2} \right] \dots\dots\dots (52)$$

where $\Delta\beta$ is the phase mismatch, and is defined as:

$$\Delta\beta = \frac{2\pi\lambda^2}{c} D \cdot \Delta f^2 \dots\dots\dots (53)$$

The dispersion parameter, D , is given as:

$$D = \frac{-2\pi c}{\lambda^2} \beta^2 \dots\dots\dots (54)$$

with β^2 being the group velocity dispersion parameter. From Equation 54, it can be seen that P_{FWM} is at its minima when $\Delta\beta \frac{L}{2} = k\pi$, with k being an integer. As such, the phase mismatch occurs at every $\frac{2\pi}{\Delta\beta}$ m in the fibre when the two signals are propagating. Alternatively, the P_{FWM} minima can also be determined as a product of the channel spacing:

$$\Delta f_k = \sqrt{\frac{kc}{\lambda^2 DL}} \dots\dots\dots (55)$$

The analysis of the P_{FWM} minima can be used to analyse the dispersion of the optical fibre, as the magnitude of the non-linearity coefficient only shifts at this point. The non-linearity coefficient itself can be determined from the total fibre attenuation. The setup for obtaining the non-linearity coefficient is the same as that required for generating the FWM effect, and requires only two laser sources and an EDZF of proper length. The channel spacing upon which the first P_{FWM} minima is reached is needed for the calculation of the dispersion in the fibre, which is given as:

$$D = \frac{c}{\lambda^2 \Delta f^2 L} \dots\dots\dots (56)$$

Using Equations 50 to 55, the theoretical FWM power can now be estimated as:

$$P_{FWM} = \eta \gamma P_s P_p^2 e^{-\alpha L} L_{eff}^2 \dots\dots\dots (57)$$

γ can be determined by bi-directional measurements of the FWM power, while the chromatic dispersion is determined by wavelength detuning of the FWM Power Conversion Efficiency (PCE). Both measurements use the same experimental setup as given by the schematic in Figure 57³⁴. Two Yokogawa AQ2200 TLS units are used to generate the pump and signal sources. The TLS generating the pump wavelength, P_p is designated TLS1, while the TLS generating the signal wavelength, P_s is designated TLS2. Both TLS1 and TLS2 have tuning ranges from 1460 nm to 1640 nm and linewidths of 0.015 nm. P_p is fixed at a wavelength of 1560 nm and an average output power of 12.8 dBm, while P_s is varied from 1552 nm to 1557 nm at an average power level of 10.8 dBm.

³⁴ Measurement and analysis of the FWM effect was carried out with the assistance Ms. Noor Azura Awang, who at that time was specializing in the FWM effect in exotic optical fibers.

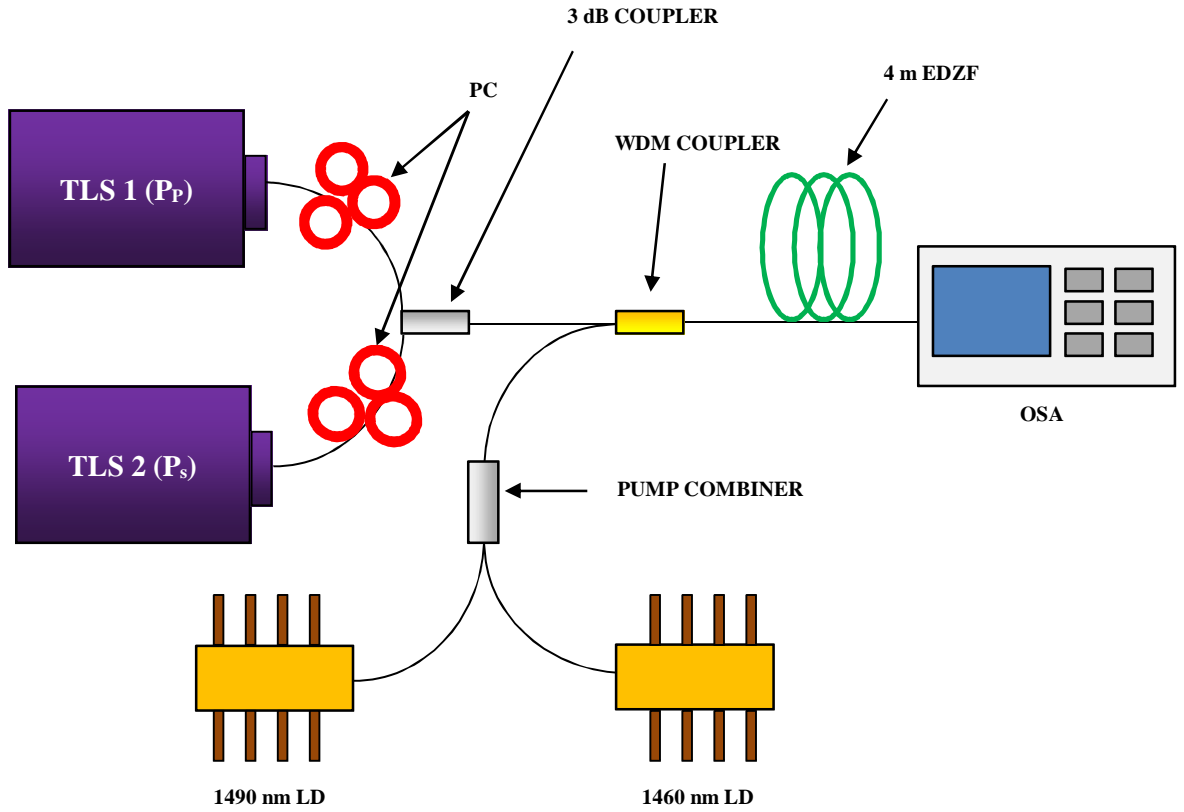


Figure 57: Experimental setup for non-linear coefficient measurement.

A PC is placed after TLS1 and TLS2 to optimize the control the polarization of the generated signals in order to obtain the maximum FWM efficiency. Both P_p and P_s are combined using a 3 dB coupler and channeled towards the WDM coupler. Two LDs, one operating at 1460 nm and the other at 1490 nm, are used as pump sources and combined with a pump combiner before being channeled to the second input of the WDM coupler. The LDs are used to pump the EDZF at just enough power to excite the Er^{3+} ions so that the EDZF becomes transparent to the P_p and P_s signals. This is necessary, as the EDZF sample incorporates both Er_2O_3 ions and any incoming signal will be either absorbed or amplified if the Er^{3+} ions have not yet been suppressed, thus disrupting the experiment. The EDZF sample tested is a 4 m long ZEr-B fibre with an Er^{3+} ion concentration of 3880 ppm, as well as a core refractive index value of 1.466 and an effective area of $87 \mu\text{m}^2$. The ZEr-B has propagation loss, α of 0.68 dB/m, which has been previously determined by the cut-back method. These values are necessary in determining the non-linearity coefficient of the fibre. A

Yokogawa AQ3230 OSA with 0.02 nm resolution bandwidth completes the experimental setup, and is used to obtain and analyse the generated FWM spectrum.

The power of idlers generated as a result of the interaction of the pump and signal beams propagating in the fibre are dependent on the wavelength of the pump and input signal. In this work, P_p and P_s are detuned by 0.4 nm, and set at powers of +15 dBm and +13 dBm, respectively. The output from the TLS is optimized by careful adjustment of the PCs. The output power from the ZEr-B, P_{FWM} against different signal wavelengths is given in Figure 58.

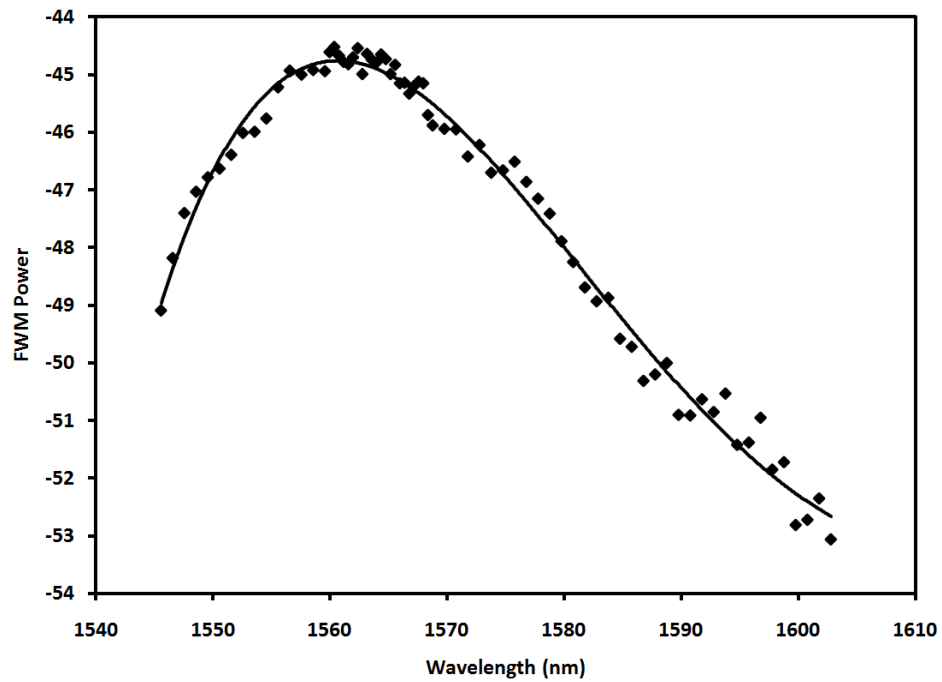


Figure 58: Obtained P_{FWM} at different signal wavelengths and fixed pump wavelength³⁵.

It is immediately visible from the figure that P_{FWM} increases from a low value of -48 dBm, at a pump wavelength of 1545 nm to a peak power of -45 dBm at 1558 nm. The power of the converted signal remains relatively unchanged as P_s increases from 1558 nm to 1565 nm, with only minor fluctuations of approximately 0.5 dB observed. Above 1565 nm however, the power begins to decrease rapidly as the signal wavelength continues to move towards the longer-wavelength region. The reason for this lies in the gain profile of the EDZF; at a wavelength of 1560 nm, the gain

35 Figure modified from that in H. Ahmad, M. C. Paul, N. A. Awang, S. W. Harun, M. Pal and K. Thambiratnam, "Four-Wave-Mixing in Zirconia-Yttria-Aluminum Erbium," *J. Europ. Opt. Soc. Rap. Public.*, vol. 7, pp. 12011-1 - 12011-8, 2012.

spectrum of the ZEr-B is the highest. Based on this, it can be inferred that setting the pump signal to 1560 nm will ensure that the generated FWM signal will fall in flat region. This value is used in the measurement of the nonlinearity coefficient of ZEr-B.

Figure 59 shows the spectrum with of the generated idler wavelengths, along with the pump and signal wavelengths. The spectrum shown is obtained from the OSA with a 25.0 dB fixed attenuator attached. The attenuator serves to protect the OSA from spikes in the signal which could potentially damage it. The pump wavelength is left constant at 1560 nm and a power of -9.9 dBm while the signal wavelengths are varied from 1560 nm to 1564 nm in steps of 1 nm, with the power being maintained at -10.5 dBm. From the figure, two sidebands, C_1 and S_2 , are generated by the interaction of the pump and signal wavelengths in the EDZF. In order to generate the first set of idlers, the pump wavelength is kept constant at 1560 nm, while the signal wavelength is tuned to 1561 nm. Two idlers are formed, with C_1 observed at 1559 nm and S_2 observed at 1562 nm, corresponding to a shift in the wavelength by about 1 nm from the pump and signal wavelengths. Increasing the signal wavelength to 1562 nm gives a corresponding shift in the idlers of 2 nm on either side, with C_1 now at 1558 nm and S_2 observed at 1564 nm. This pattern remains true as the signal wavelength increases until 1564 nm, with C_1 shifting accordingly to 1555 nm and S_2 shifting towards 1570 nm. It is prudent to note that as the signal wavelength increases, the power of the generated sidebands drops; this is attributed to the signal wavelength moving away from the peak region of the EDZF's gain spectrum. The channel spacing obtained in Figure 59 is essential in determining the fibre non-linear coefficient, dispersion and dispersion slope of the EDZF, which is seen in the following results.

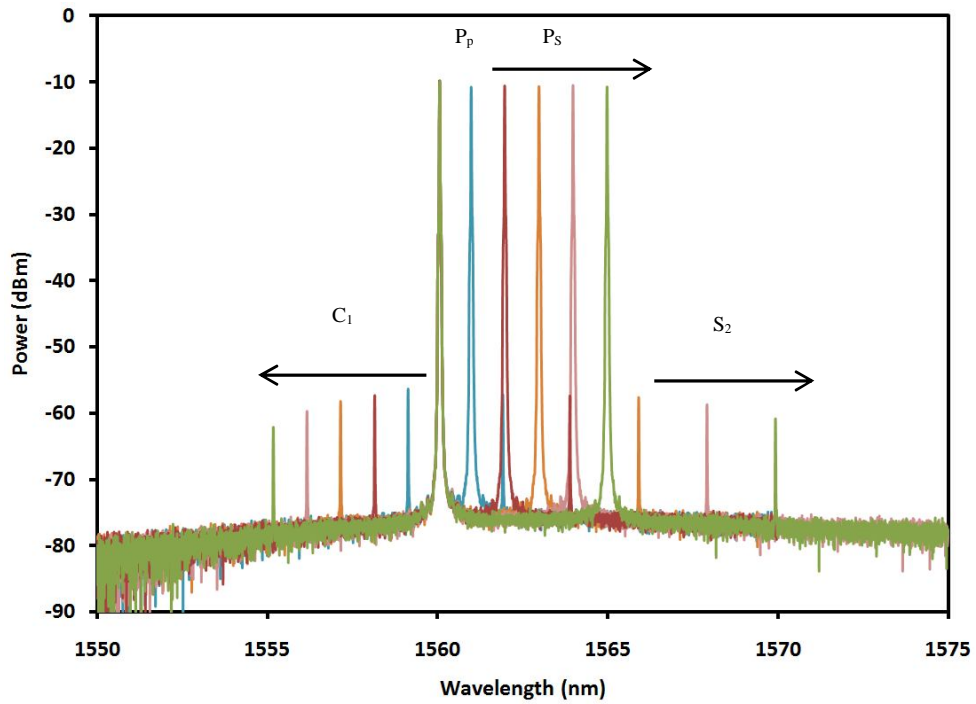


Figure 59: The typical output spectra at P_p and P_s , as well as the generated idlers C_1 and S_2 , with P_p kept constant at 1560 nm and P_s varied from 1552 nm – 1567 nm. C_1 wavelengths are obtained by the equation $\omega_3 = 2\omega_1 - \omega_2$, while S_2 wavelengths are obtained from the formula $\omega_4 = 2\omega_2 - \omega_1$ ³⁶.

Figure 60 shows the power of the converted signal, S_2 against the wavelength of the input signal. As was the case previously, the pump is left constant 1560 nm, while the signal wavelength is varied from 1550 nm to 1557 nm with a frequency spacing of 0.2 nm, or approximately 22.7 GHz. To ensure that the maximum power is obtained for the converted signal, the two PCs are adjusted to optimize the output power. As can be observed from the figure, the power of the converted signal is initially low at about -58 dBm. However, as the signal wavelength increases, so does the power of the converted signal, reaching a power of approximately -45 dBm at a wavelength of 1557 nm. Above this wavelength, further increases in the input signal wavelength do not result in any change to the converted signal power, and the experimental results augur well with the theoretical predictions for EDZF.

³⁶ Figure modified from that in H. Ahmad, M. C. Paul, N. A. Awang, S. W. Harun, M. Pal and K. Thambiratnam, "Four-Wave-Mixing in Zirconia-Yttria-Aluminum Erbium," *J. Europ. Opt. Soc. Rap. Public.*, vol. 7, pp. 12011-1 - 12011-8, 2012.



Figure 60: FWM conversion efficiency versus wavelength detuning³⁷.

The analysis of the P_{FWM} as a function of channel spacing can be used to estimate the fibre chromatic dispersion and dispersion slope. Figure 61 shows the normalized FWM efficiency against the input signal frequency, and it can be seen that as the channel spacing is increased from 30 GHz to 400 GHz, the FWM conversion efficiency remains relatively the same, with fluctuations of about 0.5 units. However, above 400 GHz, the FWM efficiency begins to drop, reaching almost 0 at a channel spacing of 1000 GHz. The initial high FWM efficiency can be attributed to the channel spacing being narrow, thus allowing for a larger transfer of energy from the pump and signal wavelengths to the generated idlers. These measurements auger well with the theoretical predictions for the EDZF fibre, and from Equation 54 and Figure 61, a chromatic dispersion and slope dispersion value of 28.45 ps/nm.km and 3.63 ps/nm².km respectively is obtained for the fibre. Taking the signal power, pump power, converted power and the normalized FWM efficiency, the nonlinear coefficient of the EDZF can be estimated using Equations 51 to 53, giving a nonlinear coefficient value of 14 W⁻¹km⁻¹. Figure 62 shows the variation of the non-linear coefficient against the channel spacing.

³⁷ Figure modified from that in H. Ahmad, M. C. Paul, N. A. Awang, S. W. Harun, M. Pal and K. Thambiratnam, "Four-Wave-Mixing in Zirconia-Yttria-Aluminum Erbium," *J. Europ. Opt. Soc. Rap. Public.*, vol. 7, pp. 12011-1 - 12011-8, 2012.

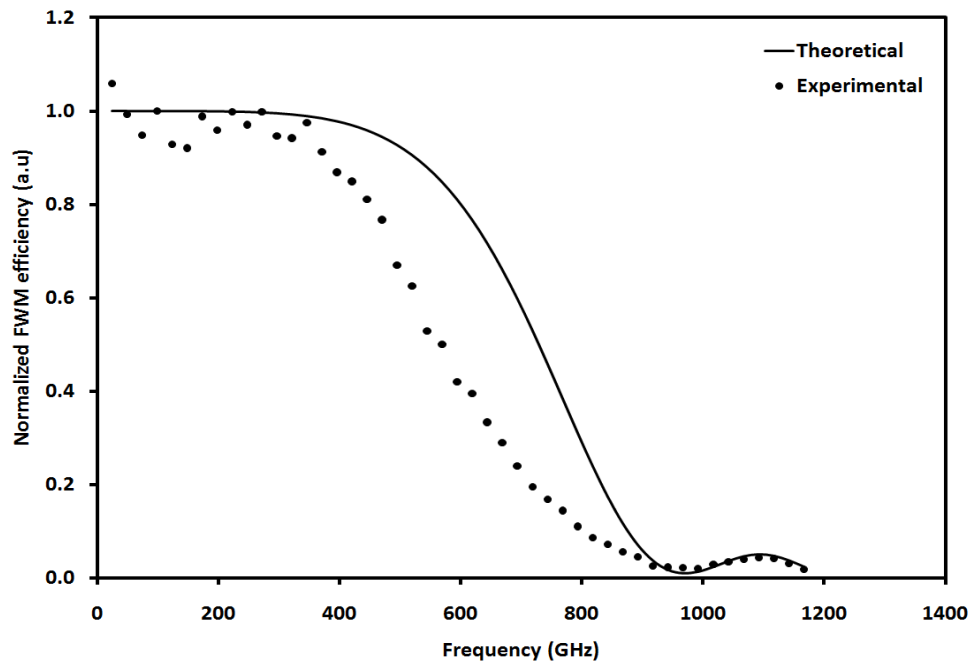


Figure 61: Normalized FWM efficiency against the input signal frequency³⁸.

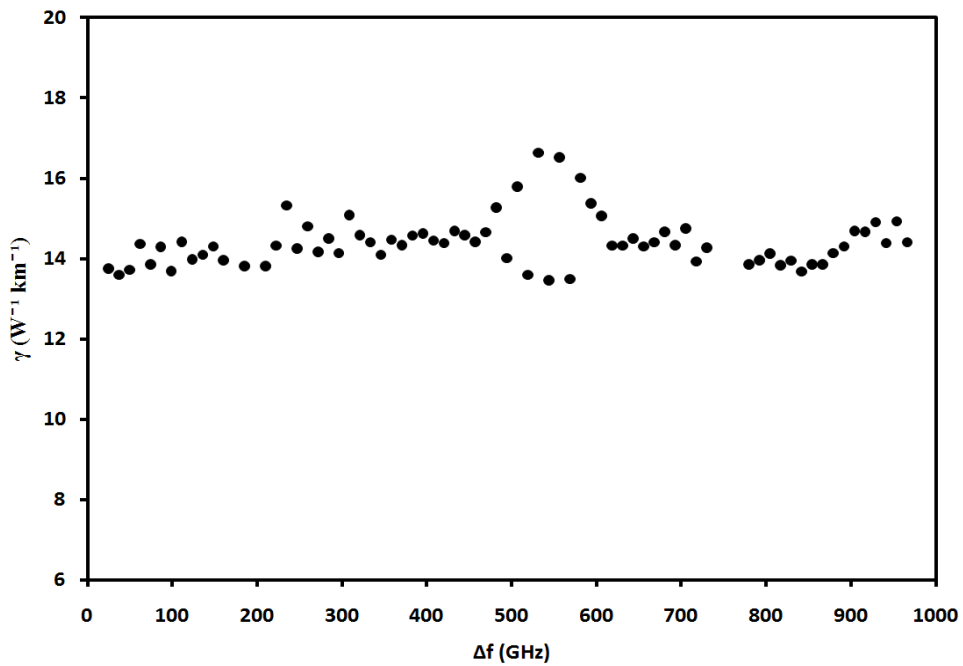


Figure 62: Nonlinear coefficients with varying the frequency spacing³⁹.

38 Figure modified from that in H. Ahmad, M. C. Paul, N. A. Awang, S. W. Harun, M. Pal and K. Thambiratnam, "Four-Wave-Mixing in Zirconia-Yttria-Aluminum Erbium," *J. Europ. Opt. Soc. Rap. Public.*, vol. 7, pp. 12011-1 - 12011-8, 2012.

39 Figure modified from that in H. Ahmad, M. C. Paul, N. A. Awang, S. W. Harun, M. Pal and K. Thambiratnam, "Four-Wave-Mixing in Zirconia-Yttria-Aluminum Erbium," *J. Europ. Opt. Soc. Rap. Public.*, vol. 7, pp. 12011-1 - 12011-8, 2012.

From the figure, it is determined that the non-linear coefficient remains constant at almost all channel spacing values, with the only variation of significance observed within the channel spacing regions of 500 to 600 GHz. As such, the developed EDZFs can be used for a variety of applications such as wavelength conversion and wavelength generation.

3.4 *Summary and Conclusion*

In this chapter, the various optical properties of the EDZF are investigated. This chapter begins with a detailed examination into the theoretical background of the EDF. Subsequently, the rate equations that are used to model these transitions are discussed, followed by a derivation of the equations that govern the ASE, gain and noise figure of the EDFA.

The chapter examines the ASE characteristics of the EDZF. The work is carried out with a 3 m long EDZF, which has a dopant concentration in excess of 3880 ppm/wt with an absorption ratio of about 22.0 dB/m at 980 nm and approximately 53.0 dB/m at 1550 nm. A conventional EDF of the same length is also examined under the same conditions, and the resulting spectra compared. The conventional EDF used has an Er^{3+} ion concentration of about 960 ppm and absorption ratio of between 11 to 13 dBm at 980 nm. The spectral shape of the EDZF's ASE output differs substantially from that of a conventional EDF, rising to a peak region at 1530 nm followed by a short 'plateau' afterwards before dropping back again. At the highest pump power, a peak power of -18.6 dBm is obtained at the 1530 nm region, while the plateau region gives an average power of -26.0 dBm. This is a very important characteristic, as it sets the operational boundaries of the EDZF and gives it a longer operating bandwidth as compared to the EDF. This is attributed to the high Er^{3+} dopant concentrations in the fibre, which essentially allows the EDZF to act as an L-band amplifier. Additionally, the 1530 nm peak becomes more dominant at higher pump powers, recording peak powers of -24.9, -20.4 and -17.7 dBm at pump powers of 108.7, 140.0 and 170.1 mW while the plateau region remains rises at a much slower rate, increasing from an average of -30.0 dBm to -28.0 dBm over the

range of the same pump powers. This is further confirmed by comparing the ASE from a 3 m long EDZF to that of a 2 m long EDZF that is pumped under the same conditions. Observation of the spectra obtained indicates that the shorter EDZF acts more like a conventional EDF, instead of its expected behavior when observing longer EDZF lengths.

As a gain medium, the EDZF exhibits characteristics that are typical of a highly doped EDF. For a -30 dBm signal, the EDZF-based EDFA is able to provide high gain of approximately 28.0 dB near the central region of 1530 nm in addition to a substantial gain of between 22.0 to 25.0 dB at the plateau region of the EDZF's ASE output. A relatively high NF is also observed, approximately 12.2 dB at 1530 nm before decreasing to around 2.8 dB at the 1550 nm wavelength region. At longer wavelengths though, the NF increases again, reaching 3.9 dB at 1590 nm. A 0 dBm input signal on the other hand experiences lower gains, averaging between 7.0 to 10.0 dB over a range of 1530 nm to 1570 nm and lower gains of 2.0 to 3.0 dB at longer wavelengths. In this configuration, the EDFA acts instead as a booster amplifier. The NF of experienced by the signal in this scenario is also higher, at approximately 14.1 dB before dropping to 7.7 dB at 1580 nm and subsequently rising slightly to 8.3 dB at 1590 nm.

As a fibre laser, the ability of the EDZF to act as the gain medium for an SLM laser is examined. This is because the high dopant concentrations in the fibre allow for a short cavity length to be realized, a necessary requirement for the SLM, while at the same time being highly compatible with conventional optical fibres due to the fact that the EDZF is based on a conventional silica host. As an SLM fibre laser, a 0.5 m long EDZF with a dopant concentration of 3880 ppm/wt and absorption rate of about 21.0 dB/m at 980 nm serves as the gain medium. Due to the high dopant concentrations, the 0.5 m EDZF can provide the same performance as an EDF approximately 4 m long, thus significantly reducing the cavity length. Two short EDFs, approximately 3 cm and 6 cm long are also inserted in the cavity to act as saturable absorbers. The EDFs used are conventional EDFs, with an erbium ion concentration of about 900 ppm/wt and absorption rates of 5.0 dB/m at 1530 nm. A tunable C-band FBG provides the tuning mechanism. The SLM output of the laser has a tunable range of 11.2 nm, from 1533.8 nm to 1545.0 nm, as well as an average SNR of more than 50 dB with an output power of above -8.9 dBm. The output of the system is measured over a period of two and a half hours in 10-minute intervals, and

during this period almost no fluctuations are observed in either the power or wavelength of the laser's output. Measurement with an RF-SA provides positive indication that the oscillation is in the single mode as the beating noise peaks observed in the trace are densely spaced, while measurements of the linewidth provide a value of about 0.2 MHz for the SLM output.

Another interesting characteristic of the EDZF is its non-linear properties. Although non-linear interactions in silica optical fibres are typically observed only when high intensity signals propagate through them, the presence of the ZrO₂ micro-crystallites in the core region of the EDZF allow these interactions to occur at lower signal intensities. The most predominant, and useful non-linear effect that can be generated by the EDZF is the FWM effect, due to its multiple uses as wavelength sources and also in wavelength conversion. In investigating the FWM effect, a 4 m long EDZF is used to determine the non-linear characteristics of the fabricated fibre. FWM power levels of approximately -45 dBm are obtained at a wavelength of around 1565 nm, auguring well with the theoretical predicted values. Adjusting the pump and single wavelengths will also cause the idlers to shift in accordance with the theoretically predicted models. The EDZF has a non-linear coefficient of $14 \text{ W}^{-1}\text{km}^{-1}$ along with chromatic and dispersion slopes of 28.45 ps/nm.km and $3.63 \text{ ps/nm}^2.\text{km}$ that are well in accordance to the theoretical values.

It can be concluded that the EDZF does indeed succeed in meeting one of its main objectives, which is to develop an EDF with a high-dopant concentration without sacrificing the compatibility and strength of the SMF. The high dopant concentration of the EDZF allow for high gain levels to be obtained from compact EDFAs and also plays an important role in the development of SLM based fibre lasers, whereby the cavity length should be as short as possible. In both cases, the benefit of the silica host is evident - the fibre amplifiers and lasers are easily setup using conventional fibre components, thus demonstrating the real-world application prospects for the EDZF. The presence of the Zr³⁺ rich microcrystalline structures in the matrix of the silica host also allows for interesting non-linear phenomena to be observed, in particular the FWM effect, which has tremendous practical applications such as wavelength conversion.

The application of the EDZF as the gain medium for passive fast and ultra-fast pulsed lasers is of significant importance and is a key objective in this work. This is described in detail in the next chapter.

4. GENERATION OF FAST AND ULTRA-FAST PULSES USING PASSIVE SATURABLE ABSORBERS AND THE ZIRCONIA–YTTRIA–ALUMINO SILICATE GLASS-BASED ERBIUM-DOPED FIBRE

4.1 Introduction

The development of compact fibre lasers with short, high energy pulsed outputs has recently become the focus of significant research efforts due to the multitude of applications they have. While there are many ways of generating a high energy pulsed output, the most common methods used to obtain high energy ultra-fast pulses from fibre lasers are Q-switching and mode-locking, although the method chosen depend very much on the application of the fibre laser. Mode-locked pulses are typically desired when ultra-fast pulses of typically less than 1 ns are desired, such as in optical communications [98]. Q-switched pulses on the other hand are desired when pulses need not be very short, or in cases where long pulses would be of better advantage, such as in sensing, range-finding and medicine [99], [100], [101], [102]. Furthermore, Q-switched pulses have high pulse energies and do not require the delicate balancing of cavity losses required for mode-locking.

In this chapter, the generation of fast and ultra-fast pulses from an EDZF based fibre laser will be discussed. Although these pulses can be generated from both active and passive modulation, this chapter will focus specifically on passive saturable absorbers formed from either graphene or carbon nanotubes layers. This is in-line with the overall scope of this work – to develop an ultrafast pulse laser using the EDZF as a compact, highly doped linear gain medium together with graphene and carbon nanotube saturable absorbers. In this regard, the following sections of this chapter will focus on the optical characteristics and behavior of graphene and carbon nanotubes, with a particular focus on their applications as saturable absorbers. This will then be followed by the application of these saturable absorbers to first obtain Q-switched pulses from an EDZF fibre laser, and subsequently mode-locked pulses from the same laser configuration.

4.2 *Pulse Generation in Fibre Lasers*

The generation of pulsed laser outputs is not new, and had in fact been demonstrated as early as the mid-1960's. During this time, Q-switching and mode-locking techniques were applied to He-Ne and dye lasers [103], [104] and almost a decade later, sub-picosecond mode-locked pulses with pulse energies of around 3 nJ and peak powers in the range of 4 kW could be obtained from dye lasers [105], [106]. The advent of the pulse in these early years would be a crucial factor in that would spur the growth of the laser until now, as the output of the lasers could now be pulsed to carry information along an optical fibre, or to generate high energy pulses for a variety of applications from manufacturing to medicine [35], [34], [33].

However, pulsed laser systems have long been dominated by bulk lasers. The current preferred source for ultra-fast, high powered pulses remains the Ti:Sapphire laser, with commercial Ti:Sapphire lasers capable of pulses 100 fs long at repetition rates of up to 80 MHz, as well as pulse energies and peak powers of up to 15 nJ and between 1 to 3 W. In fact, pulses as fast as 12 fs have been achieved by Ti:Sapphire lasers [107], [108], [109]. However, Ti:Sapphire lasers, and for that matter most, if not all pulsed lasers based on bulk laser systems suffer from a number of limitations. These lasers are complex to build and operate, and in many cases very costly. Bulk lasers are also highly sensitive, requiring precise alignment of their optical components as well as substantial cooling and maintenance to ensure they are able to provide an optimal output. Still, with all these requirements fulfilled, many bulk lasers are unable to reach their theoretically predicted output efficiencies – the Ti:Sapphire laser for example rarely exceeds an output efficiency of 20.0% [110].

In addressing these shortcomings, the fibre laser is fast being seen as a viable solution for generating both fast and ultrafast pulses with substantial energy outputs, while at the same time ensuring low cost and complexity. Pulsed outputs from a fibre laser can be either mode-locked or Q-switched. Mode-locking of the fibre laser is typically carried out when ultra-fast pulses shorter than 1 ns are desired, such as in optical communications [98]. Q-switching on the other hand is used when a longer pulse is necessary, such as those used for sensing and range-finding, or in applications where ultra-fast pulses are not necessarily needed [99], [100], [101], [102]. Both approaches have their advantages and disadvantages – mode-locking generates very fast pulses, but at relatively low energy levels while at the same time requiring delicate cavity loss balancing in order to be achieved. Q-switching on the other hand generates slower pulses, but with higher pulse energies and without the requirement of

complex cavity design modifications and adjustments. Thus, the choice of a mode-locked pulse or a Q-switched pulse would depend entirely on the application desired.

4.2.1 *Q-Switched Fibre Lasers*

Q-switching is a mode of laser operation designed to elicit a high powered beam from a laser in the form of a pulse. The process is known as Q-switching as the quality factor, Q of the fibre laser is altered when the technique is applied.

The Q-switching technique works by storing energy from the pump source in the laser medium when the Q factor is still low, to prevent the emission of a laser beam. This is because although the energy and gain in the active medium is high, the cavity losses are also kept high, thus prohibiting lasing and subsequently building up the population inversion to a level far above the threshold required for normal lasing actions. The time by which the energy is stored can be given as τ_f , which is the lifetime of the upper laser transition level. When a high Q factor is restored to the system, the stored energy is now released in the form of a very short pulse of light, and as a result of the high gain levels created by the energy stored in the system, the excess excitations are discharged in a very short time and the peak power of the resulting pulse is of many magnitudes higher than that which could be obtained by a longer pulse from the same laser. The general sequence of a Q-switched pulse is shown in Figure 63, which shows the lamp current, resonator cavity loss, population inversion and photon flux of the Q-switched laser as a function of time. The time at which the high cavity losses are removed from the laser cavity is marked as 0, with t_0 being the point in which the Q-switched pulse begins. Δt_p is the duration of the Q-switched pulse.

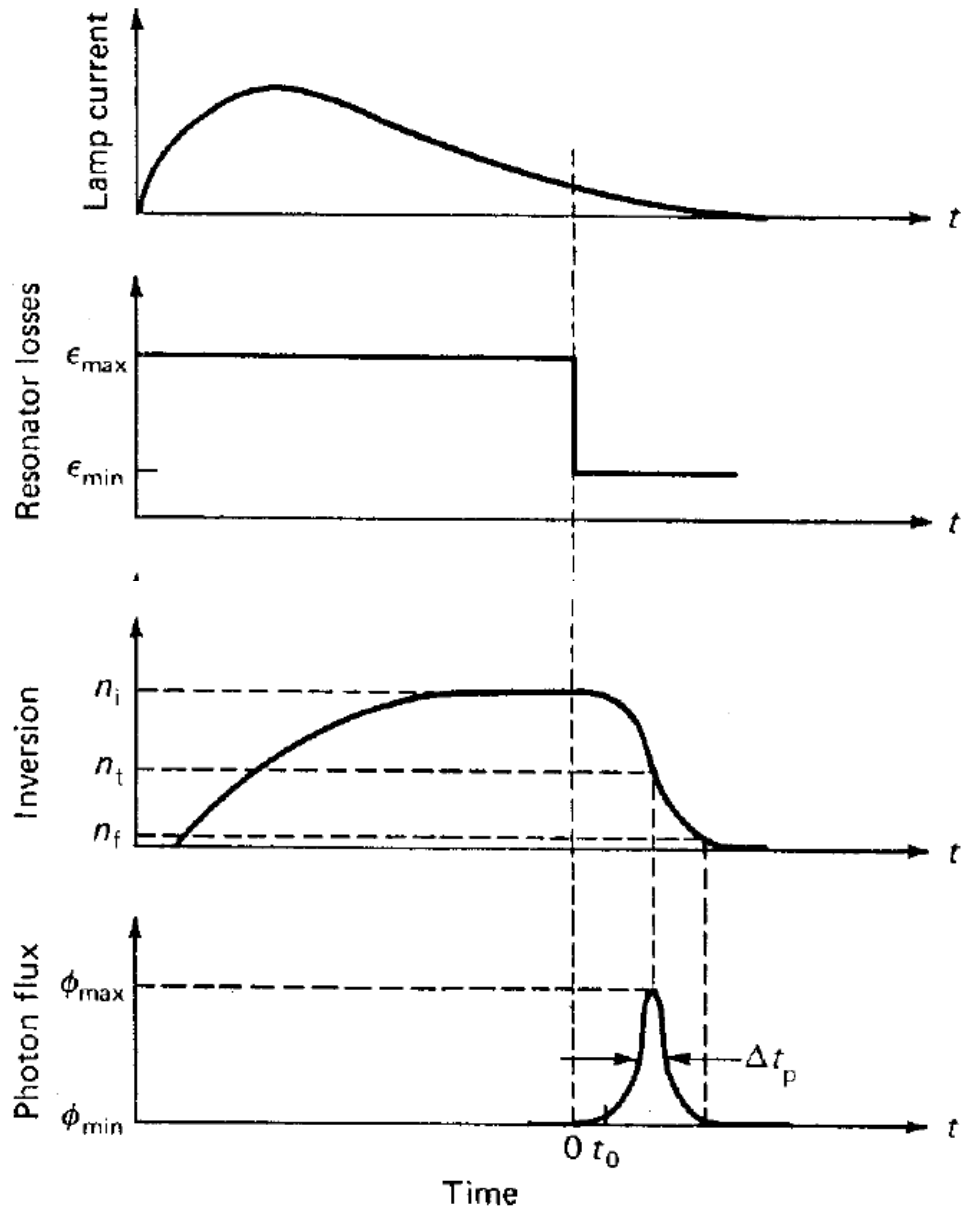


Figure 63⁴⁰: Generation of the Q-switched pulse as a function of the lamp current, resonator loss, population inversion and photon flux levels against time.

Figure 64 shows the Q-switching mechanism in a conventional laser resonator cavity, from the initial build-up, to sustaining the population inversion and finally the release of energy from the cavity.

⁴⁰ Source: W. Koechner, M. Bass, Solid-State Lasers: A Graduate Text, Springer, New York, 2003

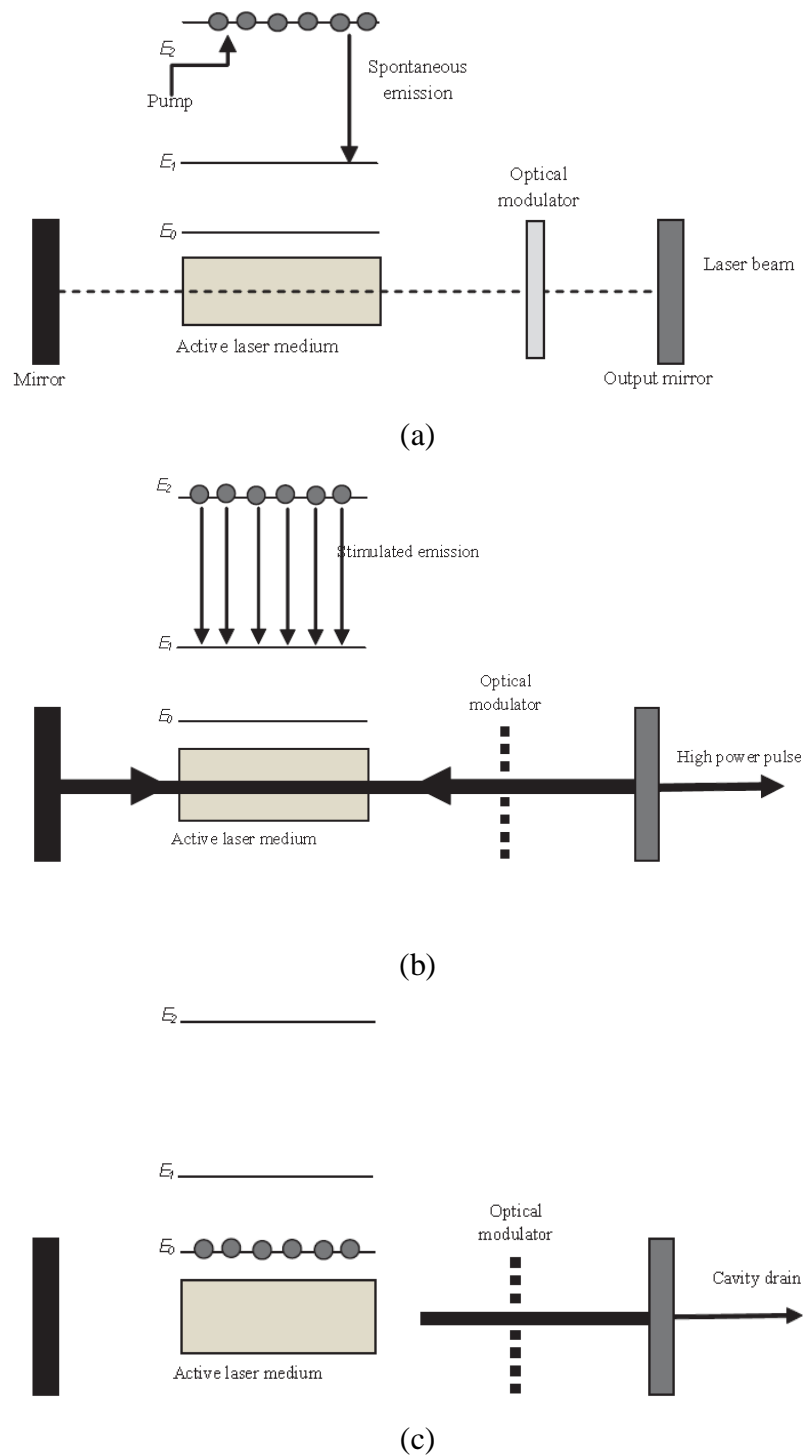


Figure 64⁴¹: Different stages of Q-switching (a) population inversion build-up, (b) sustainment of complete population inversion and (c) release of energy, resulting in excited population dropping back to the ground level and a release of energy in the form of a high energy pulse. Note that the above described system is for a bulk laser, however the same operating principles also apply to a Q-switched fibre laser.

⁴¹ Source: T. Ennejah, R. Attia, Mode-Locked Fibre Lasers, Current Developments in Optical Fibre Technology, InTech Open, 2013

The rate equations that define the Q-switching process can be given as:

$$\frac{d\phi}{dt} = \frac{\phi}{t_r} [2\sigma_{es}N_2L - \ln\left(\frac{1}{R}\right) - L'] \dots\dots\dots(58)$$

and

$$\frac{dN_2}{dt} = -\Gamma c_o \sigma_{es} \phi N_2 \dots\dots\dots(59)$$

where ϕ is the intracavity photon density, σ_{es} is gain medium's emission cross-section and N_2 is the excited population in the gain medium. L and R represent the length of the gain medium and the reflectivity of the output couplers respectively, while L' denotes the round trip dissipative loss. The inversion reduction factor, Γ , is 1 for four level systems and 2 for three level systems. Finally, the round cavity trip time, t_r is given as $\frac{2L_o}{c_o}$, with L_o being the optical cavity length and c_o being the speed of light in a vacuum. As t_r is proportionally dependent on the cavity length, thus a short as possible cavity length will result in a low t_r , which will in turn give a larger $\frac{d\phi}{dt}$ value as it is inversely proportional to the round cavity trip time. In this regard, a compact but highly doped EDF, such as the EDZF, will be able to generate a significantly high power laser output.

The laser output pulse energy can be given as:

$$E = \frac{h\nu A}{2\sigma_{es}\Gamma} \ln\left(\frac{1}{R}\right) \ln\left(\frac{N_2'}{N_2''}\right) \dots\dots\dots(60)$$

where A is the effective beam area and N_2' is the initial population inversion density. The final population inversion density is given as N_2'' . Using a Lagrange multiplier approach, the optimum reflectivity of the cavity can be obtained as [111], [112]:

$$R_{opt} = \exp\left[L' \frac{\ln z + 1 - z}{\ln z}\right] \dots\dots\dots(61)$$

where z is the ratio of the initial round trip gain of the cavity over the dissipative losses in the same cavity. z can be written as:

$$z = \frac{2\sigma_{es}N_2'L}{L'} = \frac{N_2'}{N_2''} \dots\dots\dots(62)$$

while the maximum output energy under the condition of R_{opt} can be described by the equation:

$$E_{max} = \frac{Ah\nu L'}{2\sigma_{es}\Gamma} (z - 1 - \ln z) \dots\dots\dots(63)$$

The threshold level for an optimally Q-switched laser is:

$$N_t = \frac{L'}{2\sigma_{es}L} \left[\frac{z-1}{\ln z} \right] \dots\dots\dots(64)$$

Where N_t is the inversion density threshold. The maximum power of the Q-switched pulse, P_{max} , and its Full-Width at Half Maximum (FWHM), t_p duration are given as:

$$P_{max} = \frac{Ah\nu L'^2}{2\sigma_{es}\Gamma t_r} \left[\frac{\ln z + 1 - z}{\ln z} \right] \left\{ z - \left[\frac{z-1}{\ln z} \right] \left[1 + \ln z \left(\frac{z \ln z}{z-1} \right) \right] \right\} \dots\dots\dots(65)$$

$$t_p = \frac{t_r}{L'} \left\{ \left[\frac{\ln z}{z} \right] \left[\frac{1}{1 - \left(\frac{z-1}{\ln z} \right) \left[1 + \ln z \left(\frac{z \ln z}{z-1} \right) \right]} \right] \right\} \dots\dots\dots(66)$$

The Q-switching of the laser output can be realized either actively or passively. In order to achieve active Q-switching, an active control element is needed, such as an AOM or an Electro-Optic Modulator (EOM). Passive Q-Switching on the other hand can be realized by a number of techniques, with the most common of these being the use of saturable absorbers. Both active and passive Q-switching have their

own advantages – active Q-switching allows easy control of the pulse repetition rates and pulse widths while passive Q-switching on the other hand allows for a cheaper and simpler setup, as well as providing a significantly stable output, but without the benefits of control as seen in active modulation. Therefore, the choice of active or passive Q-switching would be a consideration that must be taken into account when designing a Q-switched fibre laser.

4.2.2 *Mode-Locked Fibre Lasers*

Another method of generating pulses from a laser system is through mode-locking. Mode-locking, as the name would suggest, entails the locking of multiple axial modes in a resonator cavity. In this manner, a pulsed output can be generated by forcing coherence between the different modes.

Mode-locking of a laser output was first demonstrated by Hargrove et. al. [103] by applying an acousto-optic modulator to a He-Ne laser, while Harris et. al. [113] reported the first Frequency Modulated (FM) mode-locked laser around the same time. However, early work on mode-locking was focused exclusively on bulk laser systems, and it would be almost a decade later that the first mode-locked fibre laser was demonstrated by Ippen, Shank and Dienes in 1972 [114]. Mode-locked fibres offer a significant advantage over similar bulk laser systems due to their compact size and relatively easier construction, foregoing the complex and precise alignments needed by the optics of bulk systems. This early work would be followed by the development of mode-locked soliton lasers and subsequently FM and Amplitude Modulated (AM) mode-locked fibre lasers [115], [116], [117], [118]. The following years would also see a massive expansion in the field of mode-locked fibre lasers, with the development of passively mode-locked fibre lasers based on NPR and SESAMs allowing for the design of self-starting and stable mode-locked fibre lasers [119], [120], [121].

In mode locking, frequencies oscillating in the resonator that have lower losses than gains are designated longitudinal modes. These modes achieve additional gain with each additional pass through the active gain medium, with a separation of

$$\Delta f = \frac{v}{2L} \dots\dots\dots(67)$$

in the case of a linear cavity, or

$$\Delta f = \frac{v}{L} \dots\dots\dots(68)$$

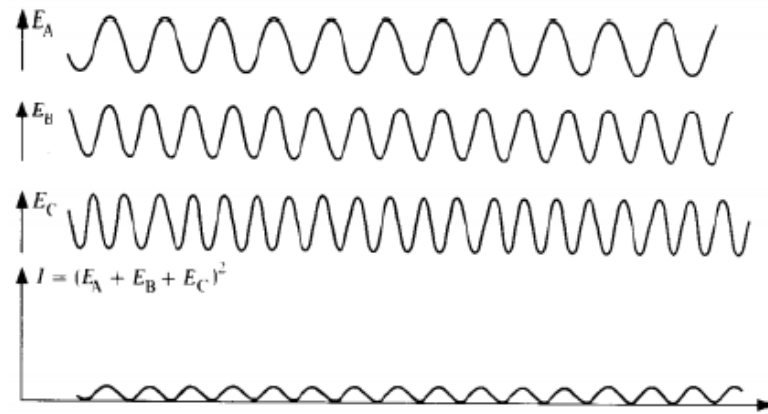
in the case of a ring cavity. The notations used for equations 67 and 68 are as per convention, with Δf being the separation of the modes in the frequency domain, v being the speed of light in the fibre and L being the cavity length. v can also be expressed as $\frac{c}{n}$, where c is the speed of light in a vacuum, while n is the refractive index of the fibre. To avoid confusion between the notations for frequency and the speed of light in the fibre, the frequency in this case is denoted by f , as opposed to the more traditionally used ν . When these modes are allowed to oscillate independently in the fibre or laser cavity, the lasing output generated is emitted continuously. However, should there be a fixed phase shift be present between these oscillating modes, the independent modes now become phase-locked, resulting in the emission of a pulse train, as shown in Figure 65.

The total optical field in the cavity is given by:

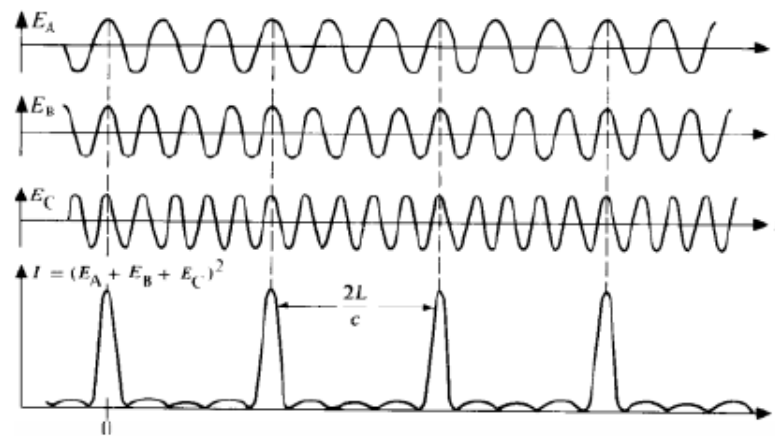
$$E(t) = \sum_{m=-M}^M E_m \exp(i\phi_m - i\omega_m t) \dots\dots\dots(69)$$

where the amplitude, phase and frequency of the m^{th} mode among $N = 2M + 1$ modes is given as E_m , Ψ_m and ω_m respectively. Mode locking begins when the longitudinal modes in the gain bandwidth are synchronized, and relative phase differences of neighboring modes, Ψ , is constant at a value of $\Psi = \Psi_m - \Psi_{m-1}$. The total intensity can be obtained by modifying Equation 73, thus giving [270]:

$$|E(t)|^2 = \frac{[\sin^2[(2M+1)\pi\Delta f t + \frac{\Psi}{2}]]}{\sin^2(\pi\Delta f t + \frac{\Psi}{2})} E_o^2 \dots\dots\dots(70)$$



(a)



(b)

Figure 65⁴²: Mechanism of mode-locking: (a) the output signal of the laser when the modes oscillate independently of each other, resulting in a CW output, and (b) output when there is a fixed phase shift, locking the mode together and generating a mode-locked output pulse.

From this, it can be seen that the mode-locked pulse train occurs at a repetition period of $\frac{2L}{c} = \frac{1}{\Delta f}$, with Δf being the difference in the frequency of the longitudinal modes equal to the cavity round-trip time. As a result of this, the optical spectrum of the mode-locked pulse train consists of discrete lines with a constant spacing equal to the pulse repetition rate. The pulse width of the mode-locked pulses can be given as:

⁴² Source: T. Ennejah, R. Attia, Mode-Locked Fibre Lasers, Current Developments in Optical Fibre Technology, InTech Open, 2013

$$\tau_P = \frac{T}{N} = \frac{1}{N\Delta f} = \frac{\lambda_0^2}{2c\delta\lambda} \dots\dots\dots(71)$$

The phase locked modes, N are connected to the stimulated emission bandwidth, $\delta\lambda$ by the relation $N = 4L \frac{\delta\lambda}{(\lambda_0)^2}$. It can be seen from these relationships that as the spectral width broadens, the width of the generated pulses becomes shorter. This behavior is a result of the relationship between the time and frequency domains, and can be described by Fourier transforms. The FWHM of the pulse in terms of time, $E(t)$ and the bandwidth of the frequency evolution of the electric field, $E(w)$ depends only on the pulse shape. The magnitudes of the FWHM product for a perfectly mode-locked Gaussian pulse is 0.441, while similar values for hyperbolic secant, Lorentzian and exponential pulse forms are 0.315, 0.142 and 0.140, respectively [122].

The generation of Q-switched and mode-locked pulses can be done by either active or passive means, with each technique providing various advantages and disadvantages. In this work however, the passive generation of these pulses using saturable absorbers, in particular those based on graphene or SWCNTs will become the focus. This is in-line with the overall objective of this research, which is to develop very compact and cost-effective Q-switched and mode-locked fibre lasers based on the EDZF. Thus, while this section provided some background on Q-switching and mode-locking, the next section will now focus on the mechanisms that allow graphene and SWCNT based saturable absorbers to generate these pulses.

4.3 Saturable Absorbers

Saturable absorbers can be considered among the earliest methods of creating passively Q-switched and mode-locked laser pulses. Early saturable absorbers typically consisted of organic dyes that absorbed lasing wavelengths, and became more and more transparent as the intensity of light increases. At high enough intensity levels, the material ‘saturates’ or ‘bleaches’ resulting in a high transmission output.

Saturable absorbers can be used to generate both Q-switched and mode-locked pulses. In passive Q-switching applications, saturable absorber initially exhibits high absorption properties at the lasing wavelength, preventing laser oscillation in the cavity. However, as the gain in the cavity increases during a pump pulse and exceeds the round-trip losses, the saturable absorber becomes transparent, and at high transmission levels will ‘bleach’, allowing the release of the built-up energy as a high-powered laser pulse. The process then repeats itself, thus generating a pulse train. For bulk lasers, organic dyes or doped crystals are typically used, while in fibre lasers SESAMs [40], [123] are usually preferred as saturable absorbers. As the passively generated Q-switched pulses are triggered by the laser radiation itself, it therefore requires no external trigger such as a high voltage, fast electro-optic driver, or radio frequency signal generator, thus allowing the system to be remarkably smaller, robust and cheaper than actively Q-switched lasers. However, this advantage is also a disadvantage – the lack of a precision external trigger limits control over the pulse generated, while the exclusion of the external modulator results in the obtained pulses being of lower pulses.

Early saturable absorbers were originally based on different organic dyes, in the form of either a dye dissolved in an organic solution or impregnated in thin films of cellulose acetate. However, these saturable absorbers were limited in their operation though due to the degradation of the light sensitive organic dye over time and exposure, and the low thermal limits of plastic materials. These shortcomings were overcome with the emergence of crystals doped with absorbing ions or containing color centers, which provided significant improvements and durability over the then conventional saturable absorber. The first of these new materials to be used as saturable absorbers for passive Q-switching was the $F_2^-:LiF$ color center crystal, although more modern crystal based saturable absorbers are based on $Cr^{4+}:YAG$ crystals.

The behavior of saturable absorber that allows it to act as a Q-switching medium, and later on a mode-locking medium, can be explained by observing a simplified model of the energy levels in the material that forms the saturable absorber as given in Figure 66:

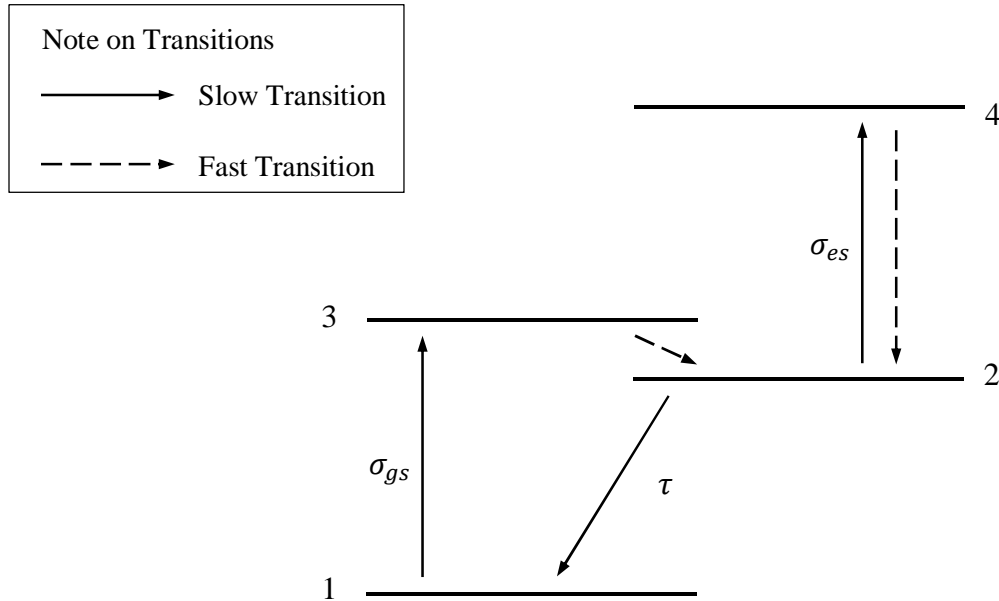


Figure 66: Energy levels of a saturable absorber under excited state absorption. σ_{gs} is the ground state absorption coefficient, while σ_{es} is the absorption coefficient of the excited state. τ is the excited state lifetime

The solution to the rate equations of the saturable absorber are intensity dependent, and are given as [124]:

$$\alpha_o(E) = \frac{\alpha_o}{1 + \frac{E_i}{E_s}} \dots\dots\dots(72)$$

where α_o is the small-signal absorption coefficient and E_s is the saturation intensity. E_s can be represented by the equation:

$$E_s = \frac{h\nu}{\sigma_{gs}} \dots\dots\dots(73)$$

with σ_{gs} being the absorption coefficient for the transitions between levels 1 and 3. E_i is the initial intensity. In order to serve as a material suitable for generating a Q-switched pulse, the ground absorption state of the material has to be large, while at the same time the lifetime of the upper state (2), has to be long enough to allow the ground state to be almost completely depleted by the pump laser. As such, a saturable absorber will look opaque to a propagating

laser signal until the photon flux is large enough to cause the ground level to depopulate. Once the upper state is sufficiently populated, the material will then become transparent to laser radiation, similar to a conventional three-level laser that has been adequately pumped to generate a zero inversion level.

The small signal transmission of the saturable absorber is given as:

$$T_0 = \exp(-\alpha_0 t_s) = \exp(-n_g \sigma_{gs} t_s) \dots\dots\dots(74)$$

t_s is the thickness of the saturable absorber material and n_g is the ground state intensity. This equation however is more suitable when applied to crystal based or thick saturable absorbers, as new and novel saturable absorbers such as graphene or carbon nanotubes are very thin, making t_s almost zero. However, it is important to note that the general behavior of saturable absorbers follows this model, regardless of their thickness or material. In order to solve differential equations for population density and photon flux, the Frantz-Nodvik equation can be applied [125]. This gives the energy of the transmission, T_i as a function of the input intensity as follows:

$$T_i = \frac{E_i}{E_s} \ln[1 + (e^{\frac{E_i}{E_s}} - 1) T_0] \dots\dots\dots(75)$$

Equation 75 can be reduced to $T_i = T_0$ when $E_i < E_s$, and $T_i = 1$ when $E_i > E_s$. Saturable absorbers were also the only mode of achieving mode-locked pulses from a laser system before the advent of additive-pulse mode-locking. Mode-locking by a saturable absorber can be easily understood by considering a fast saturable absorber whose absorption changes on the time-scale of a pulse width. As the pulse propagates through the absorber, the edges or ‘wings’ of the pulse experience mode loss that the central part of the pulse, thus shortening the pulse during its passage through the absorber, and hence creating the mode-locked pulse.

Passive mode-locking in fibre lasers can be achieved either using either fast or slow saturable absorbers. Traditional saturable absorbers, such as the SESAM, are typically defined as slow saturable absorbers, while new materials such as graphene and carbon nanotubes have high potential for application as fast saturable absorbers. The modulation of a saturable absorber can be given in the form of its transmission through the absorber:

$$s(t) = \frac{s_0}{1 + \frac{I(t)}{I_{sat}}} \dots\dots\dots(76)$$

where s_0 is the unsaturated loss, typically <1 , $I(t)$ is the dependent intensity and I_{sat} is the saturation intensity. Under a condition of weak saturation, Equation 76 can be reduced to:

$$s(t) = s_0 - s_0 \left(\frac{I(t)}{I_{sat}} \right) \dots\dots\dots(77)$$

The power of the mode is given by the intensity of the pulse multiplied by the effective area of the mode, A_{eff} . Normalizing the mode amplitude to the power such that $\alpha(t)^2 = \text{power}$, the transmission can now be written as:

$$s(t) = s_0 - \frac{s_0 \alpha(t)^2}{I_{sat} A_{eff}} \equiv s_0 - Y \alpha(t)^2 \dots\dots\dots(78)$$

In this equation, Y is the self-amplitude modulation coefficient. The master equation for a fast saturable absorber for mode-locking can now be obtained by introducing the saturable loss into the equation and removing the active modulation term. Incorporating the unsaturated loss, s_0 into the loss coefficient gives:

$$\frac{1}{T_R} \frac{\partial}{\partial T} \alpha = (g - l) \alpha + \frac{g}{\Omega_g^2} \frac{\partial^2}{\partial t^2} \alpha + Y(\alpha^2) \alpha \dots\dots\dots(79)$$

This gives a solution in the form of a simple hyperbolic secant:

$$\alpha_0 = A_0 \text{sech}\left(\frac{t}{T}\right) \dots\dots\dots(80)$$

It is interesting to note that the same models that define saturable absorption in materials such as dyes can also be applied to semiconductor materials with a p-n junction [126]. Above the threshold value, the p-n junction produces gain with relaxation times of the order of 100 ps. Below this threshold value however, it provides saturable absorption with roughly the same relaxation time. As a result of this, the principle of mode-locking of dye-lasers to

semiconductor lasers consisting of two junctions, driven by currents above and below threshold.

Traditional saturable absorbers were made from liquid dyes or achieved by Kerr-Lens mode-locking. Recently however, graphene and carbon nanotubes, both allotropes of carbon, have shown extensive potential for use as saturable absorbers. Saturable absorbers formed from these materials are highly advantageous as they perform on par with conventional absorbers such as SESAMs, but at a fraction of the size and cost. Therefore, graphene and carbon nanotube based saturable absorbers will have significant applications in the development of compact, cost-effective and robust Q-switched and mode-locked fibre lasers.

4.3.1 Graphene as a Passive Saturable Absorber

Graphite is an allotrope of carbon, and the most common form of carbon found in nature⁴³. Typically, natural carbon can be found in three principal forms, namely crystalline flake graphite⁴⁴, amorphous graphite and lump graphite. Crystalline flake graphite can be found as isolated, flat particles with hexagonal edges, or with irregular or angular if the particles are damaged. Amorphous graphite on the other hand is typically found fine particles, while lump graphite is found in fissures and veins.

However, it is not graphite that becomes the interest of most research today, but rather the base units of carbon that make up graphite: graphene. Graphene consists of monoatomic carbon layers arranged in a hexagonal lattice and has been studied since 1947, although with not as much devotion as many other fields. However, the practical isolation of graphene using by the exfoliation of highly-ordered pyrolytic graphite [127] has seen a significant shift in research dynamics towards studying graphene and its applications, particularly its optical characteristics. Due to its planar nature, graphene can be taken to be the structural base of other forms of graphite. In this manner, graphene would form a 2-D material, while an SWCNT can be taken as a quasi-1-D object created by rolling a graphene ribbon into a cylinder. Graphite can be taken as a 3-D formation of graphene layers, stacked one on top of the other. Graphene even form the basis of other complex carbon allotropes, such as fullerenes

⁴³ The other allotrope of carbon are diamonds, although these are very rare in nature and do not possess the same electrical and optical properties as graphite.

⁴⁴ Also known as flake graphite

or carbon nanocones. The various forms that graphene can take are shown in Figure 67.

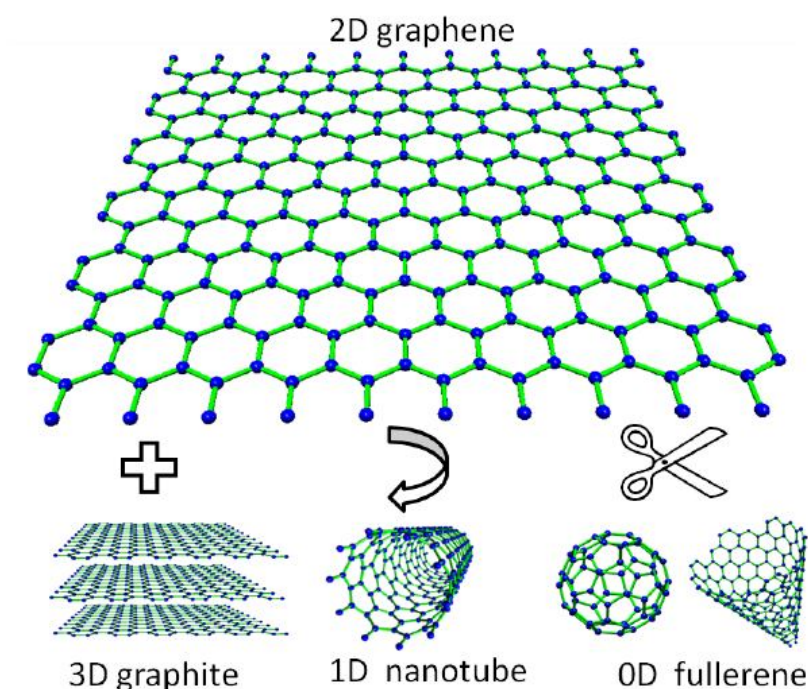


Figure 67⁴⁵: 2-D graphene as the structural base for other carbon structures graphite (3D); SWCNTs (1D);and fullerene (buckyballs) (0D)

The carbon atoms in graphene are arranged in a two-dimensional hexagonal crystal lattice, with the primitive graphene cell containing a carbon atom at each of two sublattice sites. Each atom in the sub-lattice is separated by a bond length of $d = 1.42 \text{ \AA}$, with a bond distance of 2.46 \AA to the next nearest neighbor. The outer shell of carbon atoms holds 4 electrons, with 3 of these electrons forming thig σ -bonds with neighboring atoms by sp^2 hybridization of the atomic orbitals. The fourth electron forms a weak $\pi(\pi^*)$ – bond, and it is this bond that gives graphene its unusual electronic band gap structures. Figure 68 shows the strong and weak σ – and π – bonds in graphene.

⁴⁵ Source: Petr Obraztsov: Non-Linear Optical Phenomena in Graphene Based Materials, Dissertations in Forestry and Natural Sciences

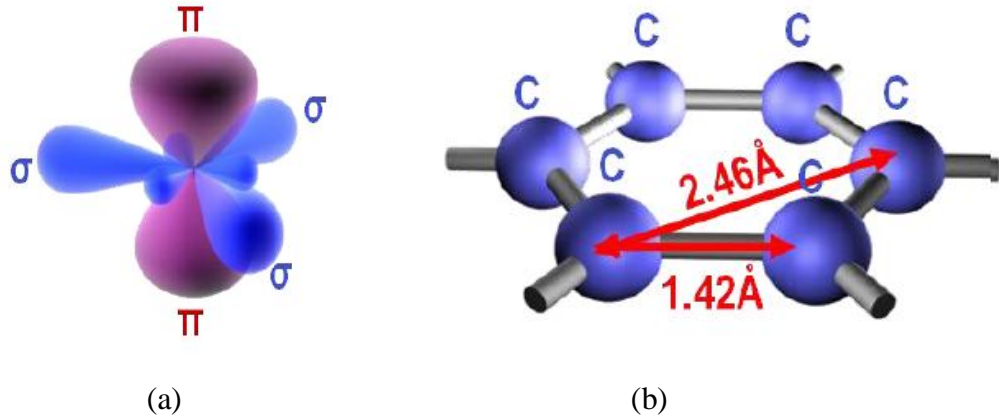


Figure 68⁴⁶: (a) Schematic representation of strong and weak σ – and π – bonds in graphene, and (b) the atomic structure of graphene.

In a tight-binding approximation, the dispersion of the valance and conduction bands can be given by the equation:

$$E(k_x k_y) = \pm \gamma_0 \sqrt{1 + 4 \cos\left(\frac{\sqrt{3}}{2} k_x \alpha\right) \cos\left(\frac{1}{2} k_x \alpha\right) + 4 \cos^2\left(\frac{1}{2} k_y \alpha\right)} \dots (81)$$

where $k = (k_x k_y)$ is the 2D electone wave-vector measured from the Γ point. This is the center of the graphene Brillouin zone, which is shown in Figure 68 along with the calculated electron dispersion for the first Brillouin zone. The ‘+’ and ‘-’ notations in Equation 85 correspond to the electrons and holes respectively in the valance and conduction bands. The nearest-neighbor hopping energy, γ_0 is approximately 3 eV, while the lattice constant α is approximately 2.46 Å. Figure 69 shows the first Brillouin Zone in graphene, as well as the electron dispersion calculated for the first Brillouin Zone in graphene.

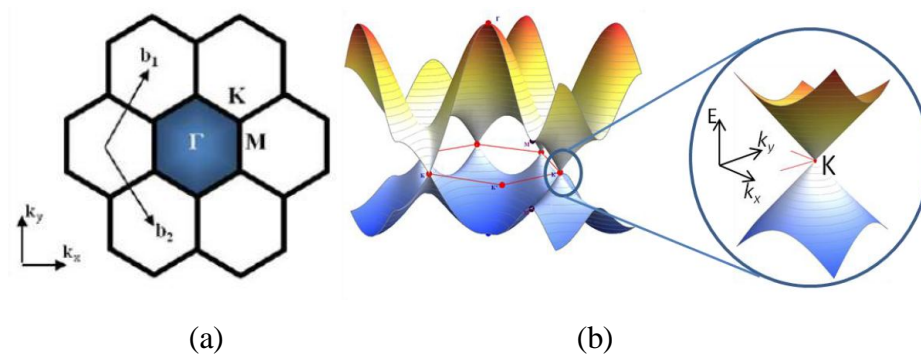


Figure 69⁴⁷: (a) The first Brillouin Zone in graphene, and (b) The electron dispersion calculated for the first Brillouin Zone in graphene

The upper and lower parts of Figure 69 (a) are the conduction and the valence bands respectively, and the optical properties of graphene are determined by band structure at the fringe of Brillouin Zone; in other words, the K and K' respectively. At these points, a cone-shape is formed by the meeting of the top of the valence band and bottom of the conduction band, with the Fermi energy $E_F = 0$. Therefore, the dispersion of the electron and holes at the K(K') point can be given by the Dirac equation:

$$E(k) = \pm \hbar v_F |k| \dots\dots\dots(82)$$

with $v_F = \sqrt{\frac{3\gamma_0 a}{2\hbar}}$, approximating to 10^6 ms^{-1} . This is the Fermi velocity in graphene, and thus the dispersion of electrons in graphene near the K and K' points are a linear function of the wave-vector k .

In both the infrared and visible spectral ranges, the optical properties of graphene are influenced by the electrons in the K and K' points of the Brillouin Zone. As a result of the lack of the bandgap and linear dispersion of electrons in atomic structure of graphene, thus photons at any energies or wavelengths can be absorbed. In this manner, as long as the electrons at the center of the Brillouin Zone do not play any role in the absorption of light, the absorption coefficient of graphene remains constant and independent of any material parameters over a wide spectral range. Both

⁴⁷ Source: Petr Obraztsov: Non-Linear Optical Phenomena in Graphene Based Materials, Dissertations in Forestry and Natural Sciences

experimental and theoretical studies [128], [129] have shown that a single layer of graphene is capable of absorbing $\pi\alpha \approx 2,3\%$ of incident photons, with α in this case being the fine structure constant and given by the equation:

$$\alpha = \frac{e^2}{hc} = \frac{1}{137} \dots\dots\dots(83)$$

This absorption coefficient scales proportionally to the number of stacked graphene layers, and as a result of this, the absorption spectra will allow for an estimation of the number of graphene layers present in a multiple layer sample.

In this work, the graphene based saturable absorber is formed by optically depositing graphene flakes onto the face of a fibre ferrule. The schematic of the optical deposition system is shown in Figure 70. The main component of the optical deposition system is a Yokogawa AQ2200 TLS, which is connected to Port 1 of an OC. Port 3 of the OC is connected to an ILX Lightwave 6810 Optical Power Meter (OPM) which functions to measure the reflected power from the graphene layer during the deposition process. To create the saturable absorber, an SMF-28 patchcord, with FC/PC terminations is prepared and designated as FP2. One end of FP2 is connected to Port 2 of the OC while the other end is left unconnected, as graphene layer will be deposited on this fibre ferrule. To begin the deposition of the graphene layer, the unconnected end of FP1 is immersed in the aqueous solution containing the graphene flakes and the TLS is activated. The graphene flakes are obtained from Graphene Research Ltd suspended in an N-MethylPyrrolidone (NMP) solution, with an average particle size of 550 nm and average flake thickness of 0.35 nm. The power of the TLS signal is set at 11 dBm and the TLS is made to transmit the signal through FP1 for about 3 minutes. As a result of optical thermophoresis, a thick layer of graphene will form on the surface of the ferrule [100]. After the 3 minute period, the laser is deactivated, and FP2 is now connected to FP1 using an FC/PC fibre adaptor. The laser is activated again for approximately 3 minutes, and during this period a portion of the graphene layer deposited on the ferrule of FP1 will now be transferred to FP2. The system is then deactivated, and FP2 is removed and cleaned, before being reconnected to FP1. The process of activating the laser and cleaning FP2 is repeated until the reflected power, measured by the OPM, is measured to be about 4.1% of the transmitted power. This reflection of 4.1% is a result of the reflection of the laser

signal from the graphene layer, which is approximately 0.1% [43] and also from Fresnel reflection from the unconnected ferrule of FP2, which accounts for about 4.0%. Once this situation is achieved, the saturable absorber has been formed.

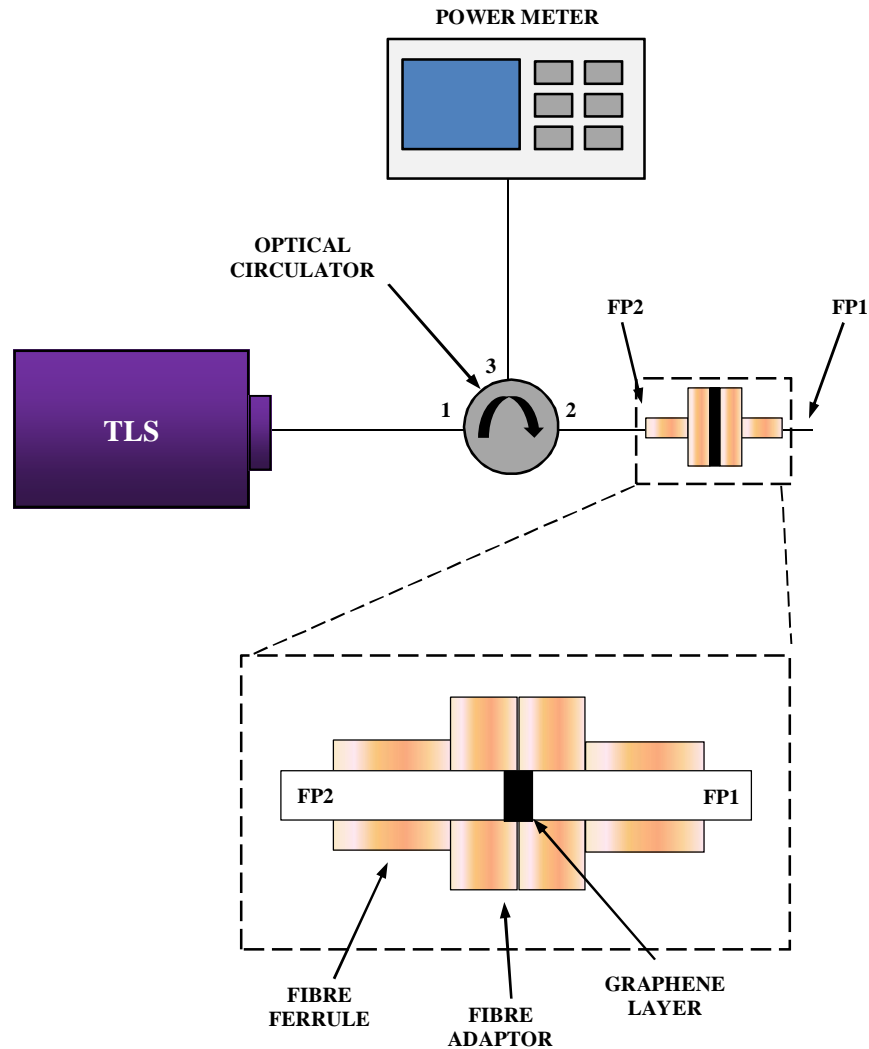


Figure 70: Setup for optical deposition of graphene layer to form the saturable absorber

An examination of the deposited graphene layer is done scanning the face of FP1⁴⁸ using a Renishaw InVia Raman spectrometer at 532 nm (2.33 eV) over a period of 10s with a grating value of 1800 lines/mm. The depth of field and incident power is set at 1 μm and 5 mW, respectively. A Charge Coupled Device (CCD) with a 100 \times objective lens and numerical aperture of 0.8 is used together with the Raman

⁴⁸ For the purpose of analyzing the deposited graphene layer, FP1 is disconnected from FP2, but both fibre ferrules are not cleaned – once the analysis is complete, they are reconnected for use in further experiments.

spectrometer, giving the system a spot size of 0.5 μm . The obtained Raman spectrum from the graphene layer is shown in Figure 71. It can be seen that the spectrum exhibits two intensity peaks at 1597 cm^{-1} and 2684 cm^{-1} . These peaks validate the presence of the graphene layer, with the peak at 1597 cm^{-1} corresponding closely to the expected G peak for graphene, which is usually at 1580 cm^{-1} , while the second peak at 2684 cm^{-1} corresponds closely to the 2D peak for graphene, which is typically obtained at 2700 cm^{-1} [130], [131]. It is also worthwhile to note that the ratio of G to 2D does not exceed 1. This indicates that a nearly single layer of graphene has been obtained on the fibre ferrule, with the actual number of layers being probably 2 or 3⁴⁹. On the other hand, if the ratio of G to 2D was more than 1, this would be indicative of multiple layers of graphene being deposited on the fibre ferrule.

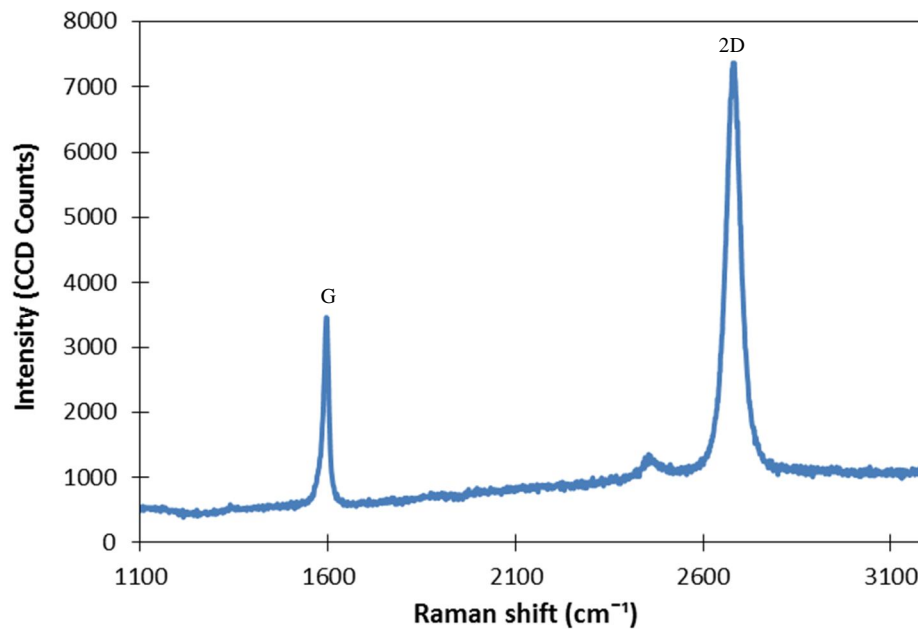


Figure 71: Raman spectrum of the deposited graphene layer on the face of the fibre ferrule.

The spot image of the graphene layer, which complements the Raman spectra is given in Figure 72 (a). The image of the graphene layer on the face of the fibre ferrule, as seen using the fibre scope, is given in Figure 72 (b).

⁴⁹ Due to the unavailability of equipment, the actual thickness of the graphene layers cannot be determined accurately. However, analysis of the obtained spectroscopy results allows for the assumption of an almost single layer to be present on the face of the fibre ferrule.

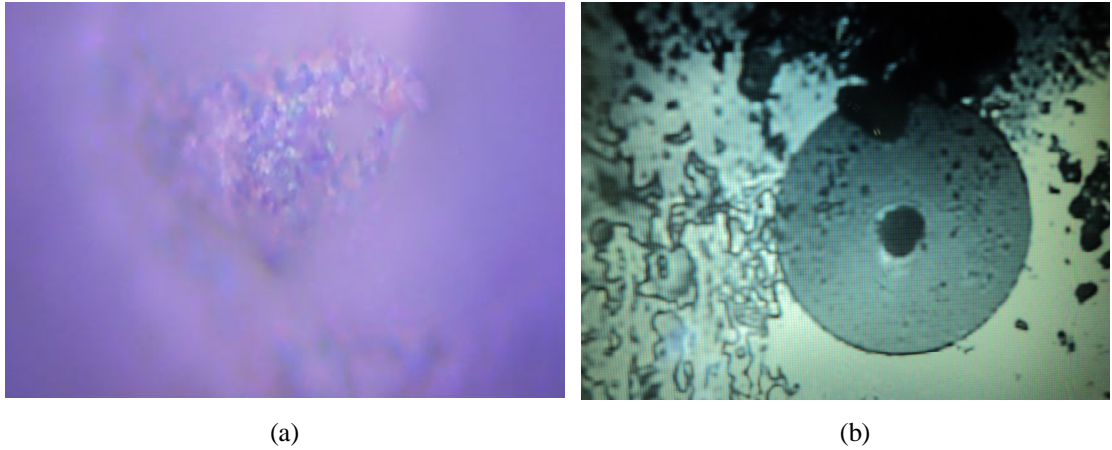


Figure 72: (a) The spot image of the graphene layer, and (b) the face of the fibre ferrule as observed using an optical fibre scope. The graphene layer on the fibre ferrule is visible as the black parts over what would be the core of the fibre. The oily residue, at the left hand and the edges of the image are the leftover traces of the NMP solution.

The graphene based saturable absorber is now ready for use in the generation of fast and ultra-fast pulses from an EDZF based fibre laser. This will be the focus of the following sections of this chapter.

4.3.2 Carbon Nanotubes as a Passive Saturable Absorber

In addition to the graphene, CNTs have also garnered significant interest as a possible saturable absorber that could, in theory, outperform SESAMs. CNTs, like graphene, is another allotrope of carbon and consists of a carbon honeycomb sheet of sp^2 bonded carbon atoms. SWCNTs are of particular interest, as they can be formed by essentially ‘rolling-up’ a graphene sheet – thus they would share the same optical characteristics and properties of graphene.

SWCNTs typically have a diameter of between 1 nm and 2 nm, and are essentially quasi-one-dimensional structures. The formation of the SWCNT from graphene can be classified by two commonly used indices: n and m . An example of how a graphene sheet can be ‘rolled’ into a SWCNT is shown in Figure 74, along the primitive vectors a_1 and a_2 .

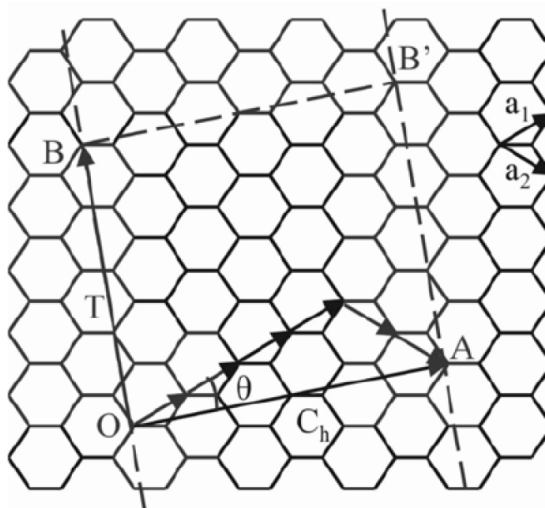


Figure 73⁵⁰: ‘Rolling’ of SWCNT from a sheet of graphene

The chiral vector of the SWCNT is given by the equation:

$$C_h = na_1 + ma_2 \dots\dots\dots(84)$$

Knowledge of the chiral vector is important, as the length of the chiral vector will become the circumferences of the SWCNT tube. Subsequently, the diameter of the tube can be calculated employing the equation:

$$d = \frac{a}{\pi} \sqrt{n^2 + nm + m^2} \dots\dots\dots(85)$$

where $a = 2.46 \text{ \AA}$ in accordance to the structure of graphene, and $n \geq m$. There are two varying conditions – if $m = 0$, then the SWCNTs have a ‘zig-zag’ formation. On the other hand, if $n = m$, then the SWCNTs are said to be in an ‘armchair’ configuration. In all other cases, they are referred to as being chiral. This is an important factor, as the diameter of the SWCNTs will determine its chiral vector, which in turn determines whether it carries the properties and characteristics of semiconductors or metals. The different chiral vectors creates periodicities in the electronic wave-function, manifests itself as delta-shaped peaks known as Van Hove singularities [132], [133]. As a result of this, the SWCNTs only absorb photons with

energies equivalent to those allowed by the transition energy of its particular chiral vector [134], [135]. Since a saturable absorber fabricated from SWCNTs would contain SWCNTs of different chiral vectors and diameters, thus the optical absorption spectrum would also contain several resonances with the overall absorption line width corresponds to the diameter distribution of SWCNTs in the saturable absorber layer [135]. This is in contrast to graphene, which has a zero bandgap and therefore behaves like a semi-metal, absorbing light at all wavelengths. However, as SWCNTs are formed from graphene, both are bound by the Pauli blocking principle and can therefore be used as saturable absorbers.

Another important characteristic of SWCNTs is the high exciton binding energy, which approximates 300 meV. Excitons are bound electron-hole pairs that are able to move along the crystalline matrix and transfer energy. The relatively high exciton binding energies in SWCNTs creates additional energy states, which are also known as exciton states in the band structure of the SWCNT, appearing as additional absorption lines. The inherent abilities of SWCNTs as saturable absorbers have allowed their use in multiple configurations [136], [137], [138] and for operational wavelengths ranging from 1 μm to 2 μm [139]. SWCNTs have also been a key enabler in the development of various mode-locking operating regimes such as stretched-pulse mode-locking [140] and dissipative solitons [141].

The SWCNT saturable absorber is fabricated by simply housing the nanotubes in a host material. This is a significant advantage over graphene, which requires complex fabrication process – in this regard, SWCNTs can be simply mixed with the host material and applied directly to the surface of the fibre ferrule. Traditionally, Polyvinyl Alcohol (PVA) is used as a host material for the SWCNTs, and the saturable absorber is made by simply depositing the SWCNTs into the PVA host. In this work, a new host material, Polyethylene Oxide (PEO) is explored for its potential and performance as a host material. PEO has a lower melting point PVA and also disperses very easily in water, making the fabrication process easier while at the same time having no adverse effects on the performance of the SWCNTs as saturable absorbers [142].

The saturable absorber is formed by sandwiching a SWCNT/PEO composite in between two fibre ferrules, much like the approach taken for the graphene based saturable absorber. The SWCNTs used are 99% pure and is procured from Cheap Tubes Inc, with lengths of between 3 to 30 μm and average diameters of between 1 to

2 nm. The PEO solution has an average molecular weight of 1×10^6 g/mol while Sodium Dodecyl Sulfate (SDS), which is used to disperse the SWCNTs, has an average molecular weight of 288.38 g/mol. These chemicals are obtained from Sigma-Aldrich, and are used to fabricate the SWCNT/PEO composite. In the fabrication of the saturable absorber, the SWCNT is soaked in a 1% SDS solution before being ultrasonically dispersed at 50 W for a period of 30 minutes. This forms a composite by solution casting which is then mixed with the PEO, before the entire solution is simply dropped onto the face of the fibre ferrule and allowing it to dry in air for 24 hours. Figure 74 (a) shows the SWCNT/PEO layer that has formed on the face of the fibre ferrule taken under 20 times magnification. The mixture formed is also analyzed using Raman spectroscopy to validate the presence of the SWCNTs. The obtained spectrum of the Raman shifts are given in Figure 74 (b), and it can be seen that the spectrum obtained is highly similar to that obtained by Dresselhaus et. al. [143], with the *G*, *D*, and *G'* peaks at 1598 cm^{-1} , 1362 cm^{-1} and 2684 cm^{-1} , indicating the presence of the SWCNTs.

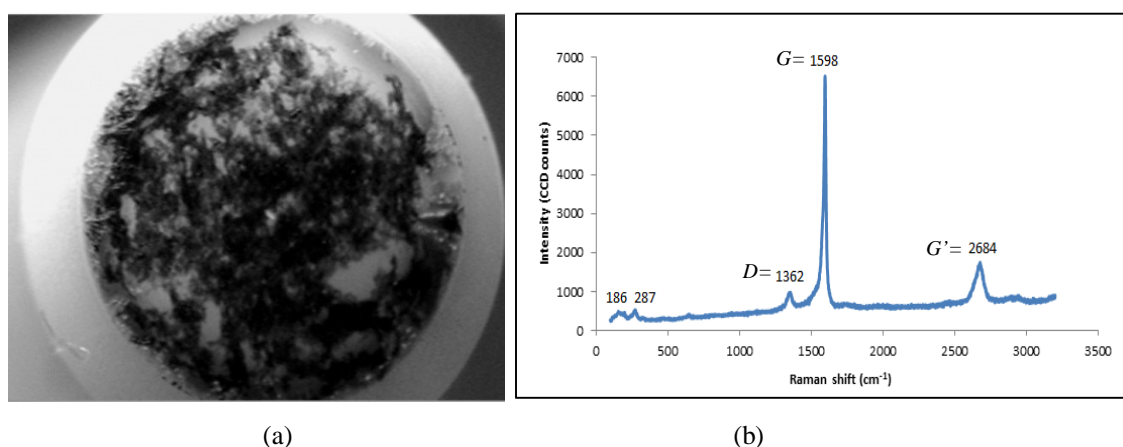


Figure 74: (a) SWCNT/PEO saturable absorber on the face of the fibre ferrule, and (b) the Raman spectroscopy confirming the presence of the SWCNTs⁵¹.

The two additional peaks at 186 cm^{-1} and 287 cm^{-1} are the radial breathing modes, which correspond to the nanotube diameter and occur at low wavenumbers [144]. Thus, a saturable absorber can be formed easily using SWCNTs and a suitable host material.

⁵¹Figure adapted from H. Ahmad, A.Z. Zulkifli, K. Thambiratnam and S.W. Harun "Q-switched Zr-EDF laser using single-walled CNT/PEO polymer composite as a saturable absorber," *Opt. Mater.*, vol. 35, pp. 347-352, 2013.

The next sections will now discuss the applications of the developed graphene and SWCNT based saturable absorbers in fast and ultra-fast EDZF based fibre lasers.

4.4 The EDZF as an Passively Pulsed Fibre Laser

One of the key interests of the EDZF is its compact size and high dopant levels, which allow it to maintain a compact form factor while still providing a significantly high output. This is especially useful in applications such as mode-locking and Q-switching, where low cavity losses arising from compact cavities and shorter optical resonator lengths will allow for better performance.

In this section, the design and performance of the fast and ultra-fast EDZF lasers using passive saturable absorbers are examined. Both the SWCNT and graphene based saturable absorbers will be used to achieve the pulsed output, where possible. The fibre lasers are designed in a ring configuration both to ensure it's simple setup and also to reduce, as much as possible, cavity losses that may arise from the introduction of extra fibre lengths and fibre components.

4.4.1 The EDZF as a Passively Q-Switched Fibre Laser

The configuration of the proposed Q-switched EDZF laser using a SWCNT/PEO composite as a saturable absorber is shown in Figure 75. The laser consists of two primary components; the EDZF, which is the gain medium, and also the SWCNT/PEO based saturable absorber, which is responsible for generating the Q-switched pulses. The EDZF used is 3 m long of highly doped Zr-EDF, with a dopant concentration of about 3880 ppm/wt as the gain medium, with an absorption coefficient of 22.0 dB/m at 980 nm. The EDZF is pumped by a 980 nm pump laser diode through a 980 / 1550 nm WDM, with the common port connected to one end of the EDZF. The open end of the EDZF is then connected to Port 1 of the OC, with Port 2 of the OC connected to an FBG with a centre wavelength of 1550 nm and a

reflectivity of approximately 98.9%. The 3 dB bandwidth of the FBG is 0.24 nm. Port 3 of the OC reconnects to the laser cavity, joining the 70:30 coupler via its common port. The 70% port connected to one end of the ferrule assembly containing the SWCNT/PEO composite saturable absorber. The other end the saturable absorber is then connected to the 1550 nm port of the WDM to complete the ring cavity. The 30% port of the tap coupler is connected to a 3 dB coupler, which splits the tapped signal into two equal portions. One portion is directed to the Yokogawa AQ3230 OSA which has a resolution of 0.02 nm while the other output is connected to a LeCroy 352A oscilloscope together with an OE converter.

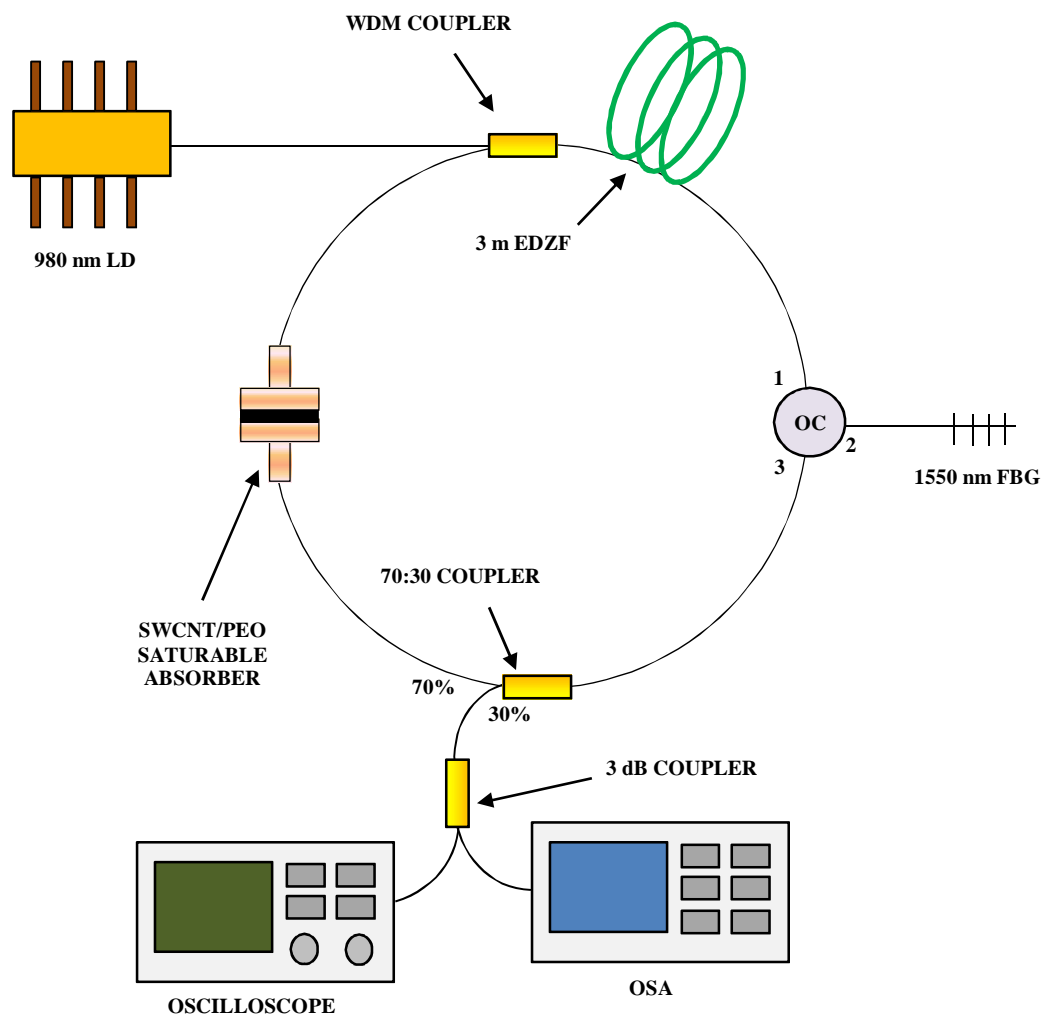


Figure 75: Q-switched EDZF fibre laser with SWCNT/PEO based saturable absorber

In order to generate the desired pump output, the pump power is slowly increased until it reaches its maximum value of 141.80 mW. The ASE generated at both ends of the EDZF will travel in a clockwise direction because of the OC placed in the optical cavity before encountering the FBG. The FBG will allow a particular wavelength of interest to oscillate in the cavity, and this selection can be tuned applying strain or temperature to the FBG mechanism. The filtered wavelength is reflected by the FBG into the cavity through the OC, where it now encounters the 70:30 coupler. The propagating wavelength emitted by the 70% port now travels to the SWCNT/PEO based SA, where the Q-switched pulses are generated and then travel to the WDM. From here, the generated pulse will continue to propagate in the laser cavity, thus forming the fibre laser. The portion of the propagating signal extracted by the 30% port will be used for the analysis of the optical and pulse properties of the signal.

The repetition rates and widths of the pulses generated are shown in Figure 76 for different pump powers. It can be seen that at a pump power of 95.1 mW, which is near to the threshold region, a train of pulses with a repetition rate of 3.77 kHz and pulse width of 25.6 μ s is obtained. This is shown in Figure 76 (a). The pulses generated at this pump power do show slight fluctuations from peak-to-peak, but as the pump power is increased to 110.3 mW, the locations becomes much less. Increasing the pump power to 110.3 mW also increases the repetition rate of the generated pulse train to 7.88 kHz, with a corresponding pulse width of approximately 9.5 μ s as shown in Figure 76 (b). At the highest pump power of 141.8 mW, the pulses generated have a repetition rate of approximately 14.20 kHz, with a pulse width of 8.6 μ s only a slight difference from the pulse width obtained at a pump power of 110.3 mW. The pulses are also very stable, and show very little peak-to-peak fluctuations.

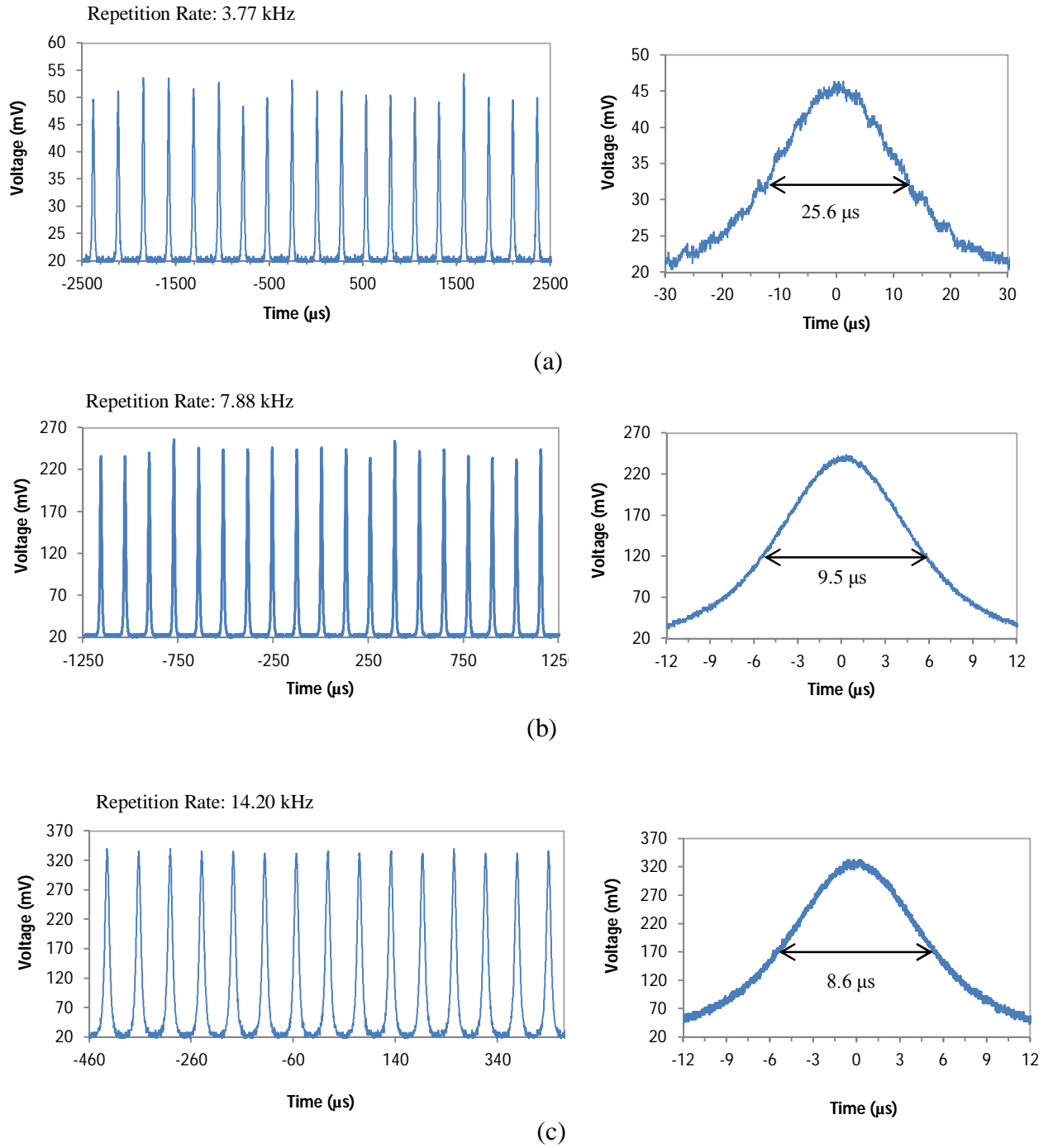


Figure 76: Repetition rate and pulse width at pump powers of (a) 95.1 mW, (b) 110.3 mW and (c) 141.8 mW⁵².

⁵² Figure adapted from H. Ahmad, A.Z. Zulkifli, K. Thambiratnam and S.W. Harun "Q-switched Zr-EDF laser using single-walled CNT/PEO polymer composite as a saturable absorber," *Opt. Mater.*, vol. 35, pp. 347-352, 2013.

Figure 77 shows the pulse repetition rate and the pulse width as a function of the pump power to the EDZF.

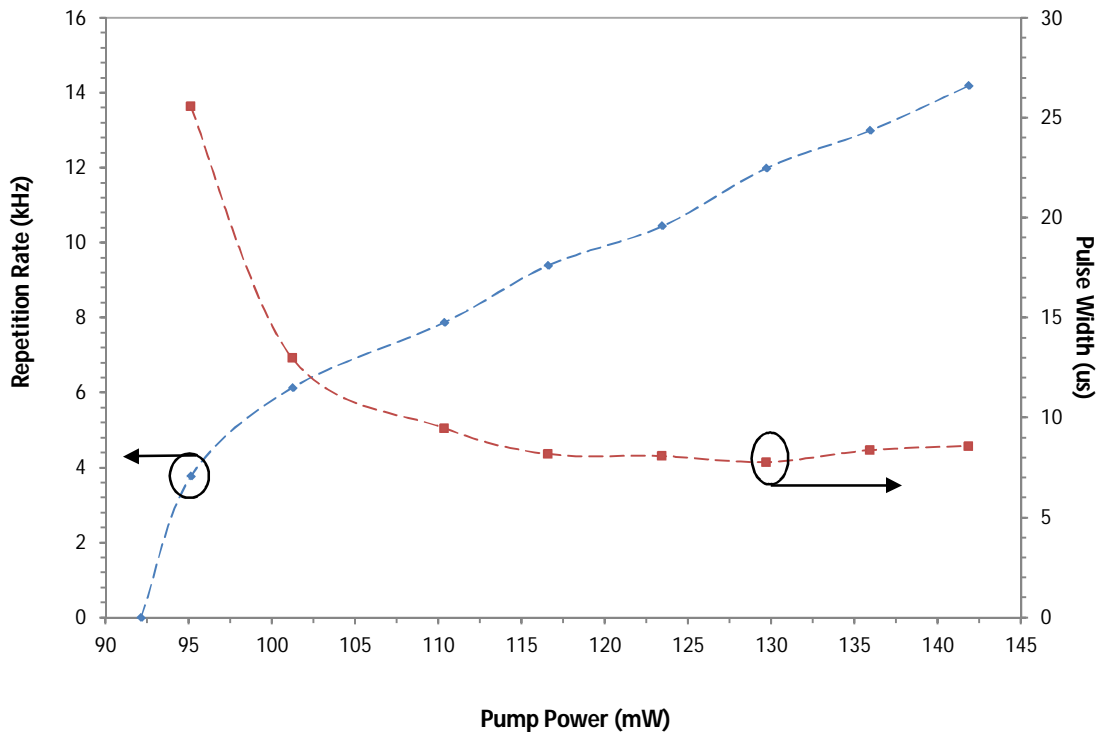


Figure 77: Pulse Repetition Rate (kHz) and Pulse Width (μs) as a function of the pump power⁵³.

It can be seen that the repetition rate grows predictably with the increase in the pump power, giving a maximum repetition rate 14.20 kHz at a pump power of 141.8 mW while the overall slope of the repetition rate plot is approximately 0.25 kHz/mW. It can also be inferred from the figure that the threshold value for obtaining the pulse train is a pump power of between 92.5 to 95.0 mW of the output power from the pump laser. The plot of Figure 77 clearly shows that tuning the pump power will allow for the repetition rate to be varied.

Analysis of the pulse width shows that it initially decreases with the pump power, followed by a period of only minimal change as the pump powers is increased from 110.3 mW to the maximum pump power of 141.8 mW. The decay pattern is almost exponential, with the pulse width being 25.6 μs being at around the threshold value, and decreasing to 8.6 μs at the highest pump power. At the higher pump powers, the minor changes in the pulse width, along with linear changes in the

⁵³ Figure adapted from H. Ahmad, A.Z. Zulkifli, K. Thambiratnam and S.W. Harun "Q-switched Zr-EDF laser using single-walled CNT/PEO polymer composite as a saturable absorber," *Opt. Mater.*, vol. 35, pp. 347-352, 2013.

repetition rate both indicate that the SWCNT/PEO saturable absorber is operating in an almost saturated condition.

Figure 78 shows the average output power and pulse energy of the EDZF laser with the SWCNT/PEO saturable absorber⁵⁴.

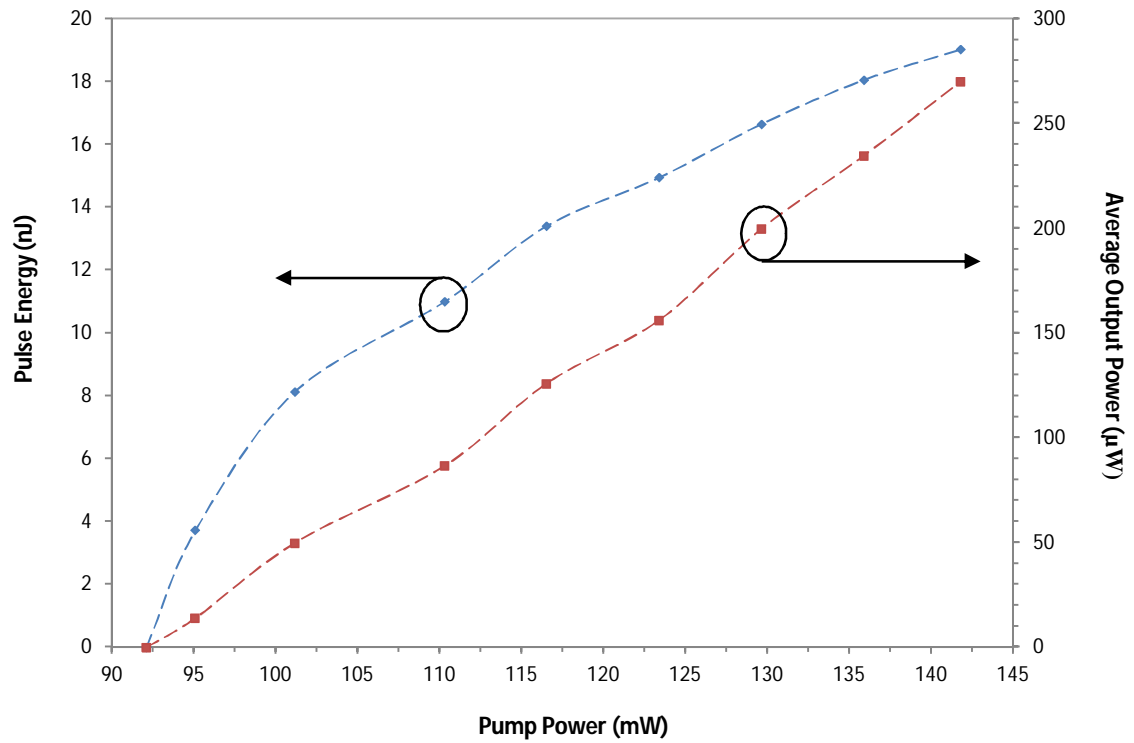


Figure 78: Pulse energy (nJ) and average output power (μW) as a function of the pump power.

It can clearly be seen from the figure that the average output power of the laser increases almost linearly against the pump power, giving an average output power of 270.0 μW at a maximum pump power of 141.8 mW. The change of the average output power against the pump power is mainly linear, giving a slope of 5.48 μW/mW. The figure also shows that the pulse energy increases with the pump power, although steeply in the initial stages with a slope value of about 0.66 nJ/mW, before becoming slightly shallower above a pump power value of 101.2 mW with a slope of approximately 0.27 nJ/mW. At the highest pump power of 141.8 mW the maximum pulse energy of 19.02 nJ is obtained.

⁵⁴ Figure adapted from H. Ahmad, A.Z. Zulkifli, K. Thambiratnam and S.W. Harun "Q-switched Zr-EDF laser using single-walled CNT/PEO polymer composite as a saturable absorber," *Opt. Mater.*, vol. 35, pp. 347-352, 2013.

The graphene based saturable absorber can also be used to generate a Q-switched output from the EDZF. In this regard, the setup of Figure 75 is modified slightly, with the new setup being shown in Figure 79.

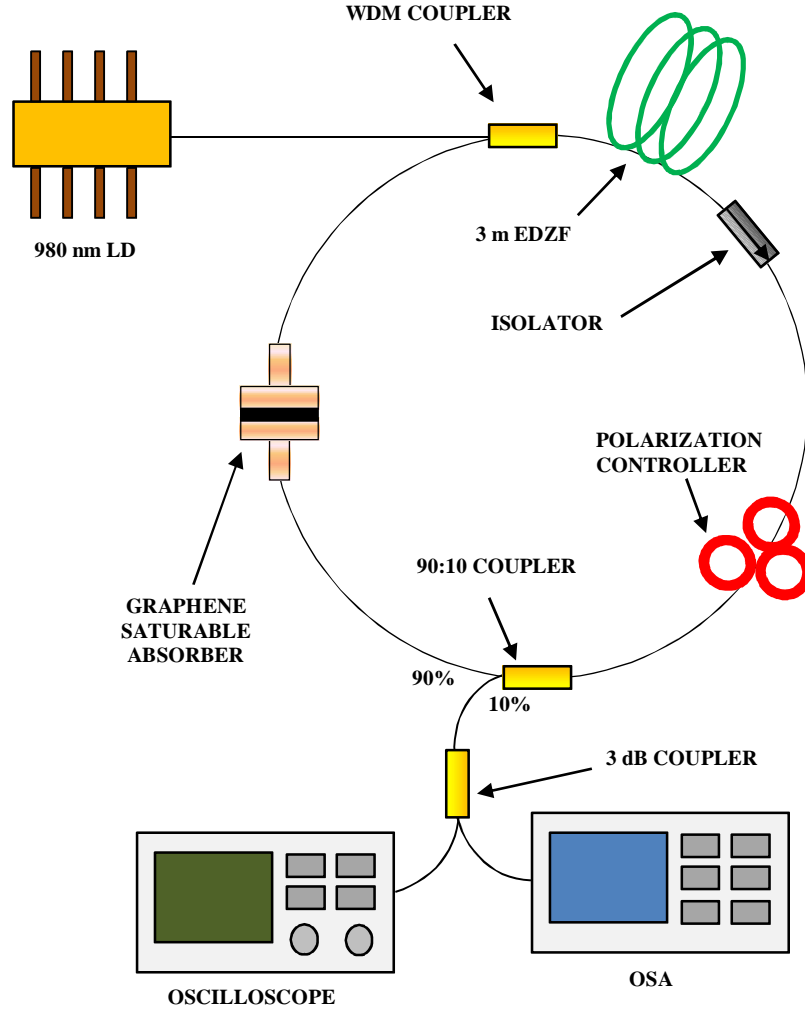


Figure 79: Q-switched EDZF fibre laser with graphene based saturable absorber

The major change in the setup would be the replacement of the SWCNT/PEO based saturable absorber with a graphene based saturable absorber. At the same time, the 1550 nm FBG along with the OC is removed, while a PC is added to the setup. The reason for this is to take advantage of the large bandwidth in which the graphene based saturable absorber can operate in; thus it would be interesting to see the laser operate without any wavelength locking mechanism. The ratio of the tap coupler has also been changed from 70:30 to 90:10, so as to allow the laser to operate more

efficiently. The other components and operating parameters of the setup are kept consistent with that in the setup of Figure 75.

The optical spectrum of the pulses generated by Q-switched EDZF laser incorporating the graphene based saturable absorber is shown in Figure 80.

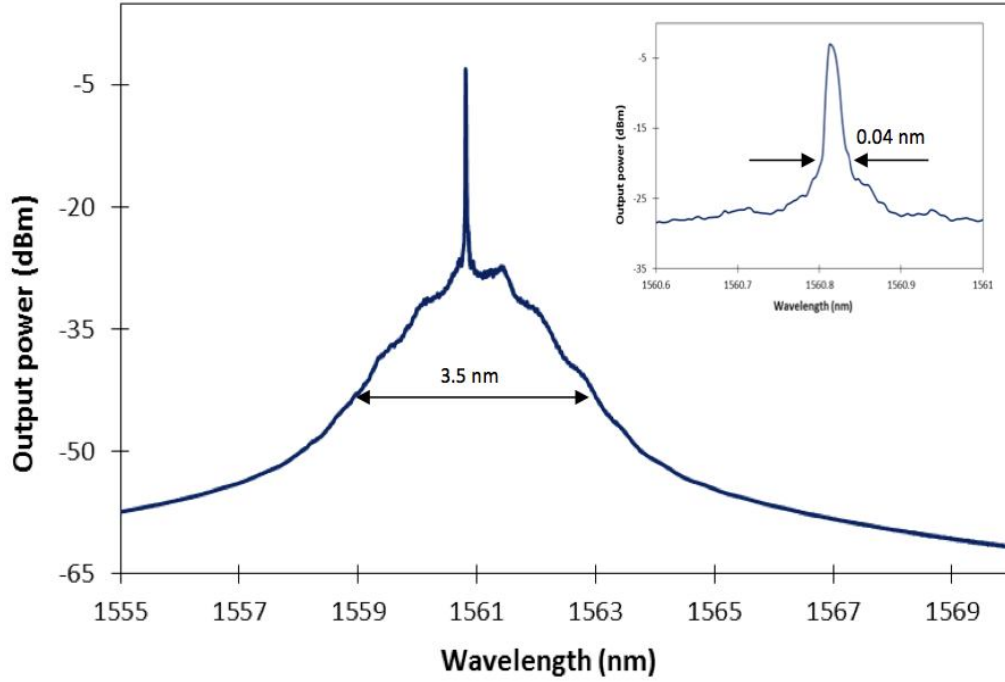


Figure 80: Optical spectrum of Q-switched pulses from the EDZF laser incorporating a graphene based saturable absorber⁵⁵.

The spectrum is taken at a pump power of about 100 mW, and shows that the obtained pulse has a wide laser bandwidth, spanning from 1559.2 nm to 1562.7 nm at a power of -40 dBm. This gives the pulse a bandwidth of approximately 3.5 nm, which can be attributed to multimode oscillations and cavity perturbations [94]. The laser pulse peaks at 1560.8 nm, with a peak power of about -3.1 dBm and a linewidth of about 0.04 at -20 dBm. Figure 81 shows the output pulse train of the laser at the same pump power. A pulse train with a repetition rate of 50.1 kHz is observed with the intensity of the peaks almost constant at 15 mV, indicating that the output of the laser is very stable.

⁵⁵ Image adapted from K. Thambiratnam, H. Ahmad, , F. D. Muhammad, M. Z. Zulkifli, A. Z. Zulkifli, M. C. Paul and S. W. Harun, "Q-Switching and Mode-Locking in Highly-Doped Zr₂O₃-Al₂O₃-Er₂O₃ Doped Fibre Lasers using Graphene as a Saturable Absorber," IEEE J. Select. Topics in Quant. Electron., vol. 20, pp. 1100108, 2013.

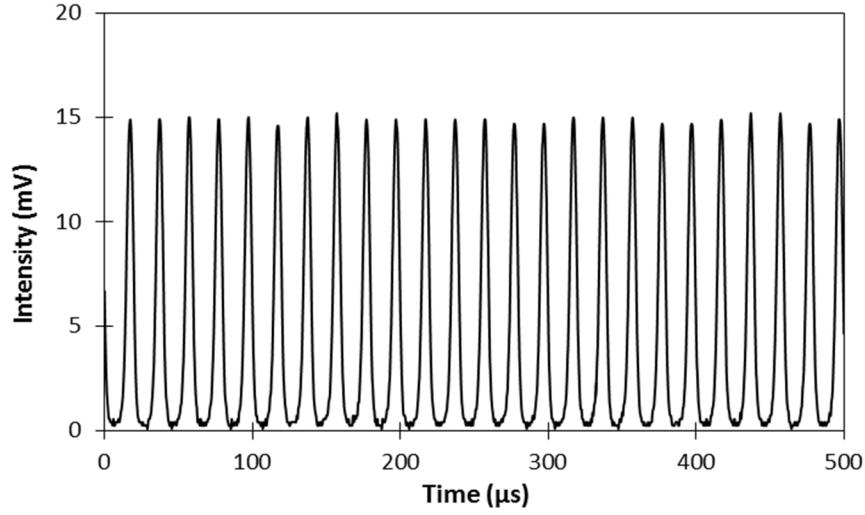


Figure 81: Output pulse train of the Q-switched pulses from the EDZF laser incorporating a graphene based saturable absorber⁵⁶.

The average output power against the pump power of the graphene based Q-switched EDZF laser is given in Figure 82.

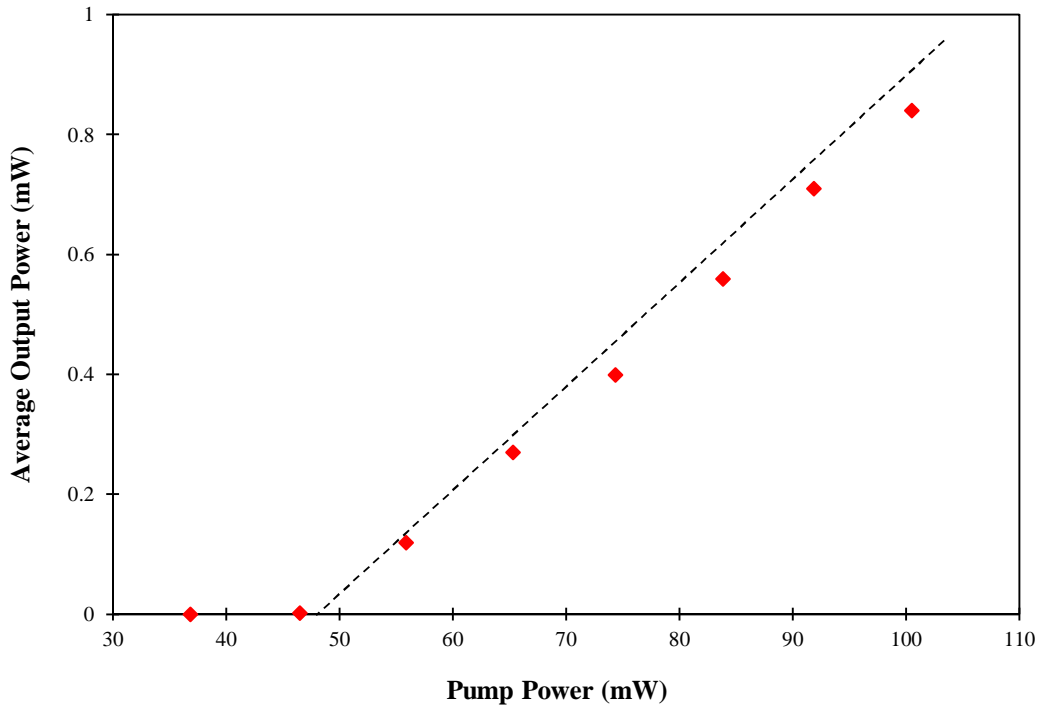


Figure 82: Average output power against the pump power⁵⁷

56 Image adapted from K. Thambiratnam, H. Ahmad, , F. D. Muhammad, M. Z. Zulkifli, A. Z. Zulkifli, M. C. Paul and S. W. Harun, "Q-Switching and Mode-Locking in Highly-Doped $\text{Zr}_2\text{O}_3\text{-Al}_2\text{O}_3\text{-Er}_2\text{O}_3$ Doped Fibre Lasers using Graphene as a Saturable Absorber," IEEE J. Select. Topics in Quant. Electron., vol. 20, pp. 1100108, 2013.

57 Image adapted from K. Thambiratnam, H. Ahmad, , F. D. Muhammad, M. Z. Zulkifli, A. Z. Zulkifli, M. C. Paul and S. W. Harun, "Q-Switching and Mode-Locking in Highly-Doped $\text{Zr}_2\text{O}_3\text{-Al}_2\text{O}_3\text{-Er}_2\text{O}_3$ Doped Fibre Lasers using Graphene as a Saturable Absorber," IEEE J. Select. Topics in Quant. Electron., vol. 20, pp. 1100108, 2013.

From the plot of the graph, it is quite clear that above a pump power of 50 mW, the average output power of the fibre laser rises almost linearly in accordance with the increase in the pump power. The change in the average output power amounts to an increment of about 0.15 mW for every 10 mW rise in the pump power. The maximum average output power that can be obtained in this setup is approximately 0.9 mW, which is obtained at a pump power of 100 mW. Due to the relatively fragile nature of the graphene layer used to form the saturable absorber, higher pump powers are not tested to prevent the graphene layer from being damaged. However, extrapolating the graph of Figure 82 will give an average output power of about 1.4 mW at a pump power of 141.8 mW. Furthermore, extrapolating the linear response of the laser allows a lasing threshold for this setup to be estimated, which in this case would be about 48 mW, with the Q-switching threshold determined to be at 56 mW.

The repetition rates and widths of the pulses obtained from the graphene-based Q-switched EDZF laser against different pump powers is given Figure 83. It can be seen that the repetition rate increases almost linearly against the rise in the pump power, increasing from 21.3 kHz at a pump power of 56 mW to a maximum to a maximum repetition rate of 50.1 kHz at 100 mW. The average change in the repetition rate is between 3 to 7 kHz for every additional 10 mW of pump power. higher repetition rates could be achieved in theory, however the pump power is not allowed to exceed 100 mW to prevent the graphene layer from being damaged. The pulse width decreases as the pump power increases, with an overall drop in the pulse width from 11.1 μ s to 4.6 μ s as the pump power changes from 56 mW to 100 mW. This is to be expected, and in fact the plot of the pulse width against the pump power forms an exponential decay. It is expected that higher repetition rates can be obtained with higher pump powers, however these pump powers are not explored due to the worry of inflicting damage onto the graphene layers due to the high intensity of light.

The pulse energy and pulse peak power of the EDZF's laser output is shown in Figure 84. The pulse energy rises steeply from 5.6 nJ to 13.4 nJ as the pump power increases from approximately 56 mW to 74 mW, but this pump power, the increase in the pump energy becomes slower, rising from 15.3 nJ at a pump power of 84 mW to only 16.8 nJ at the highest pump power of 100 mW.

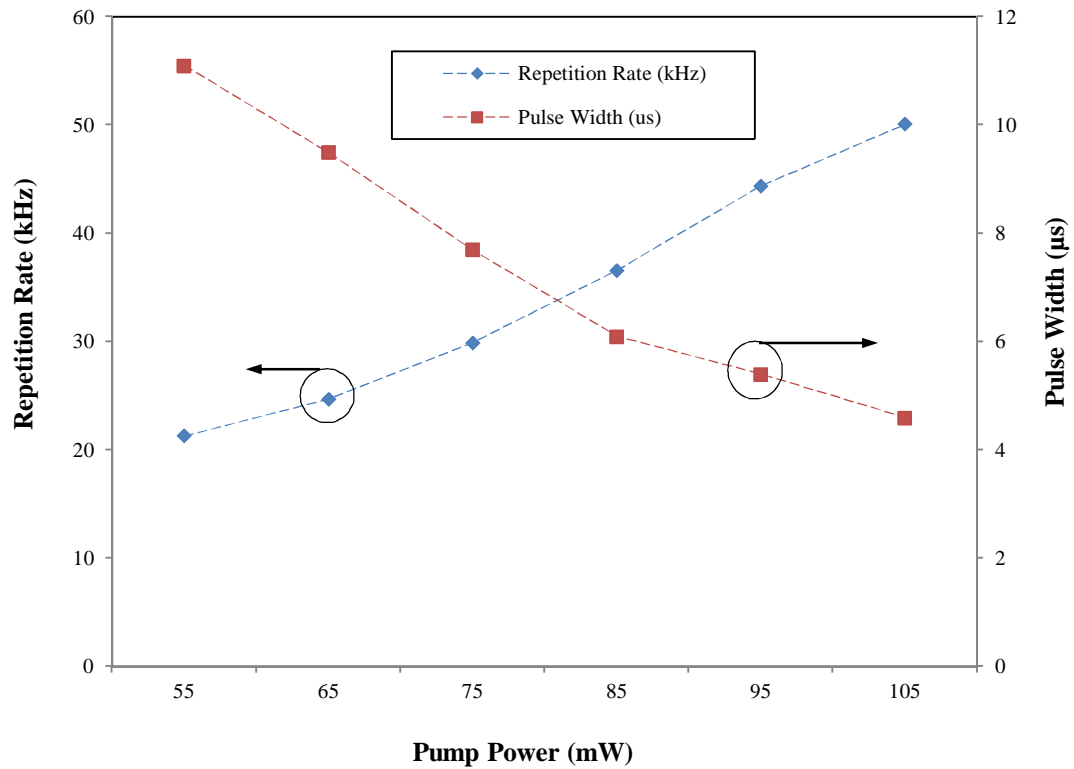


Figure 83: Pulse repetition rate and pulse width against the pump power⁵⁸

⁵⁸ Image adapted from K. Thambiratnam, H. Ahmad, F. D. Muhammad, M. Z. Zulkifli, A. Z. Zulkifli, M. C. Paul and S. W. Harun, "Q-Switching and Mode-Locking in Highly-Doped $\text{Zr}_2\text{O}_3\text{-Al}_2\text{O}_3\text{-Er}_2\text{O}_3$ Doped Fibre Lasers using Graphene as a Saturable Absorber," IEEE J. Select. Topics in Quant. Electron., vol. 20, pp. 1100108, 2013.

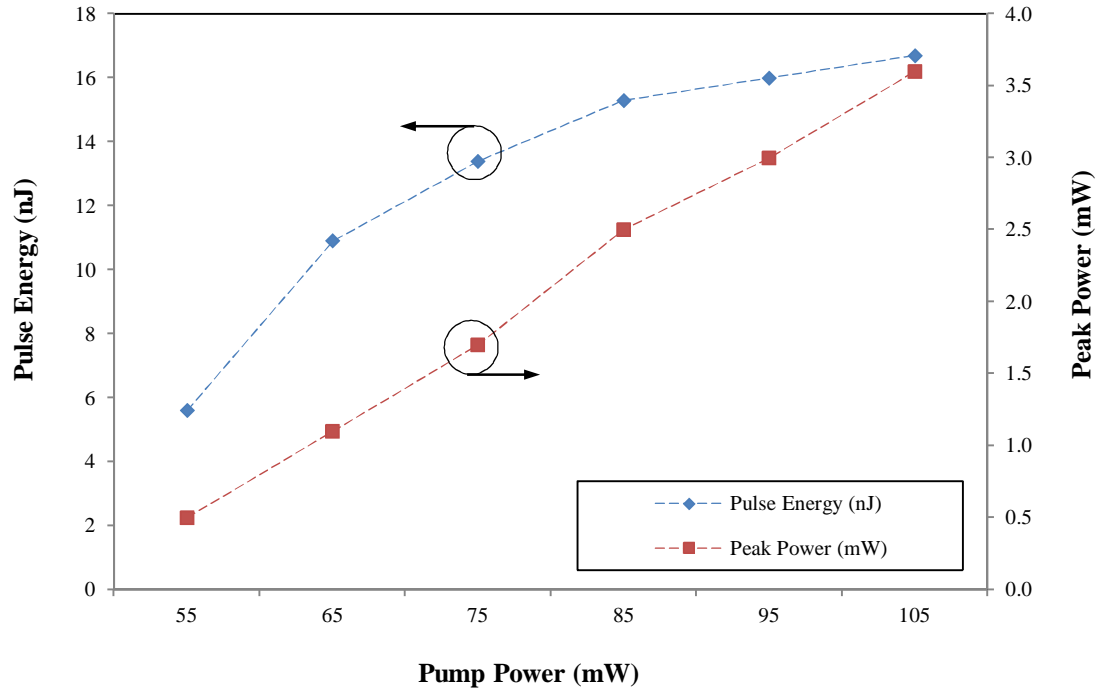


Figure 84: Pulse energy and peak power against the pump power⁵⁹

In the case of the peak power, it is observed to increase linearly with the pump power, from a minimum value of 0.5 mW and a maximum value of 3.6 mW as the pump power is changed from 56 mW to 100 mW. This gives an increment rate of about 0.6 mW in the peak power of the system for every 10 mW increase in the pump power.

Thus it can be seen that the EDZF is able to generate fast laser pulses in the form of a Q-switched optical output, using both the graphene and SWCNT based saturable absorbers. The next section will now see if it is possible to obtain ultra-fast pulses, in the form of a mode-locked output from the EDZF based fibre laser, using the graphene and SWCNT saturable absorbers.

⁵⁹ Image adapted from K. Thambiratnam, H. Ahmad, F. D. Muhammad, M. Z. Zulkifli, A. Z. Zulkifli, M. C. Paul and S. W. Harun, "Q-Switching and Mode-Locking in Highly-Doped $\text{Zr}_2\text{O}_3\text{-Al}_2\text{O}_3\text{-Er}_2\text{O}_3$ Doped Fibre Lasers using Graphene as a Saturable Absorber," IEEE J. Select. Topics in Quant. Electron., vol. 20, pp. 1100108, 2013.

4.4.2 The EDZF as a Passively Mode-Locked Fibre Laser

In order to create a mode-locked EDZF laser, the same base setup as in Figure 79 is used, with only a single modification being made to the setup in the form of an 8 m long SMF being included into the setup in between the saturable absorber and the 1550 nm port of the WDM. The modified setup is given in Figure 85.

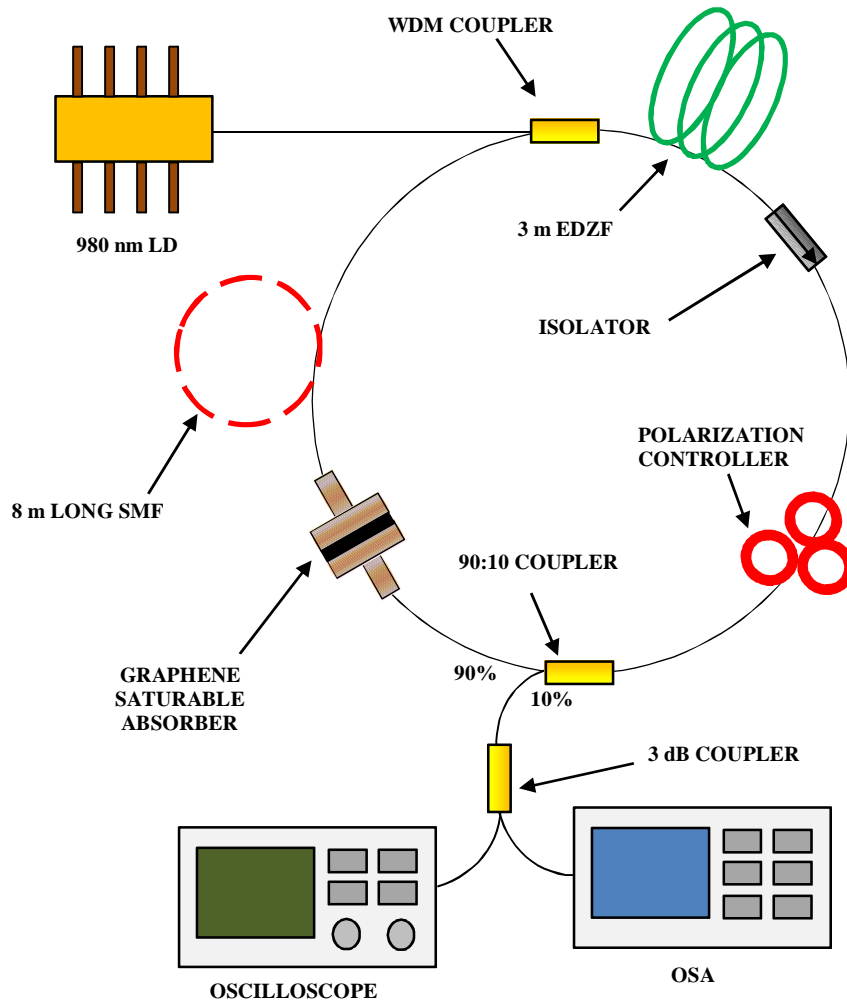


Figure 85: Mode-locked EDZF fibre laser with graphene based saturable absorber

The inclusion of the 8 m long SMF is to change the Group Velocity Dispersion (GVD) of the laser cavity. As the EDZF has a dispersion coefficient of $+28.45 \text{ ps} \cdot \text{nm}^{-1} \cdot \text{km}^{-1}$, thus the GVD coefficient of the cavity as in Figure 79 would be approximately $-36.86 \text{ ps}^2/\text{km}$. The 8 m long SMF has a dispersion coefficient of $+17 \text{ ps} \cdot \text{nm}^{-1} \cdot \text{km}^{-1}$,

giving it a GVD coefficient of $-22.02 \text{ ps}^2\text{.km}$. Therefore, by including the SMF into the setup, the GVD for the entire cavity now becomes -0.294 ps^2 , taking into account the remaining SMF lengths in the cavity as well. This puts the cavity in the anomalous dispersion region, and allows the laser to operate in a soliton mode-locking regime. For the additional measurement of the mode-locked time characteristics, an Alnair HAC-200 auto-correlator is also used in the setup, while the spectrum of the output pulses in frequency domain is measured using an Anritsu MS2683A RFSA.

During the initial operation of the mode-locked laser, soliton mode-locking behavior had been observed at a threshold pump power of 90 mW. As a result of this, all subsequent measurements are taken at a pump power of 100 mW for the mode-locked fibre laser. Figure 86 shows the optical spectrum of the mode-locked pulses, spanning from 1545 to 1580 nm with a 3 dB bandwidth of 3.6 nm. The central wavelength of the pulse lies at approximately 1563.0 nm with multiple Kelly's sidebands observed, thereby confirming that the system is operating in the soliton regime. The formation of the Kelly's sidebands is attributed to the periodical perturbation of the intracavity [145], which confirms the attainment of the anomalous dispersion, soliton-like mode locking operation. No crease patterns or CW lasing peaks are observed at the midpoint or for that matter at any other part of the output spectrum, further validating the fact that the laser is operating in the mode-locking regime. This is a highly desirable scenario, as CW components will carry an adverse effect on the stability of the mode-locked pulses [146]. At this power, the mode-locked pulses have an average output power of 1.6 mW, with a pulse energy of 23.1 pJ and peak power of 31.6 W. The pulse repetition rate is 69.3 MHz, corresponding to a pulse spacing of approximately 14.5 ns in the pulse train.

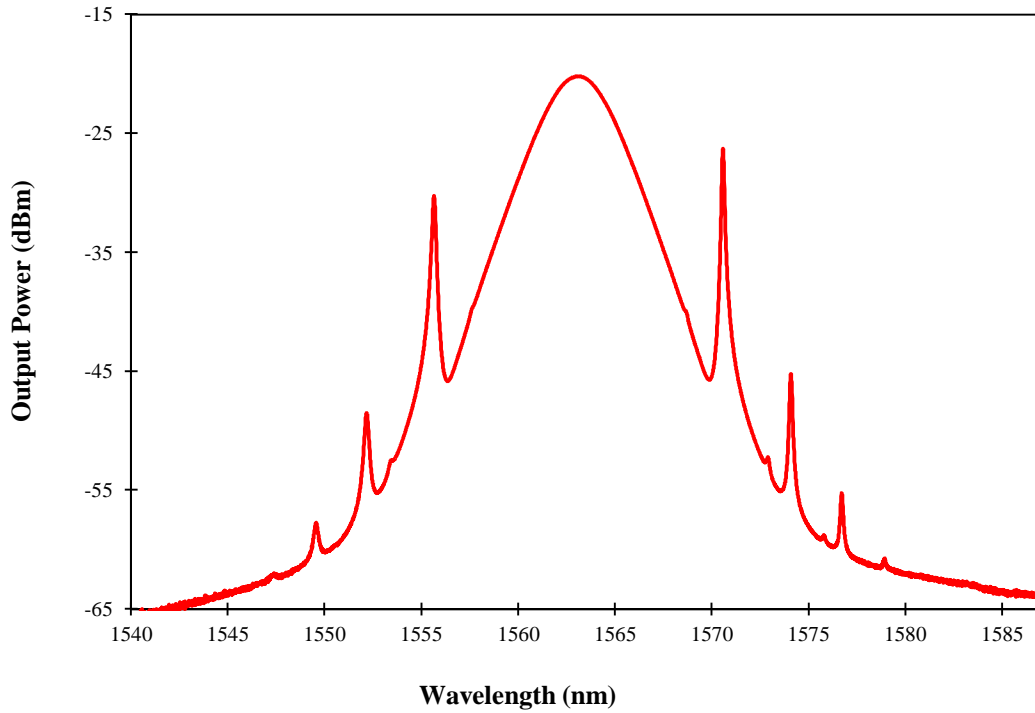


Figure 86: Optical spectrum of the EDZF mode-locked fibre laser at a pump power of 100 mW using the graphene based saturable absorber⁶⁰.

Figure 87 shows the autocorrelation trace of the second harmonic generation, which has an estimated pulse duration of 730 fs at the FWHM point. The autocorrelation trace shows that the experimentally obtained values agrees well with the theoretical sech² fitting, with no pulse breaking or pulse pair generation. A time-bandwidth product of 0.32 is obtained from the product of the 3 dB bandwidth, which amounts to 3.6 nm or 0.44 THz and the FWHM of the pulse. Although the obtained value is slightly higher than the transform limit of 0.315, this is to be expected as it would be highly unlikely that the system will be able to generate pulses that match exactly the transform limit.

⁶⁰ Image adapted from K. Thambiratnam, H. Ahmad, , F. D. Muhammad, M. Z. Zulkifli, A. Z. Zulkifli, M. C. Paul and S. W. Harun, "Q-Switching and Mode-Locking in Highly-Doped Zr₂O₃-Al₂O₃-Er₂O₃ Doped Fibre Lasers using Graphene as a Saturable Absorber," IEEE J. Select. Topics in Quant. Electron., vol. 20, pp. 1100108, 2013.

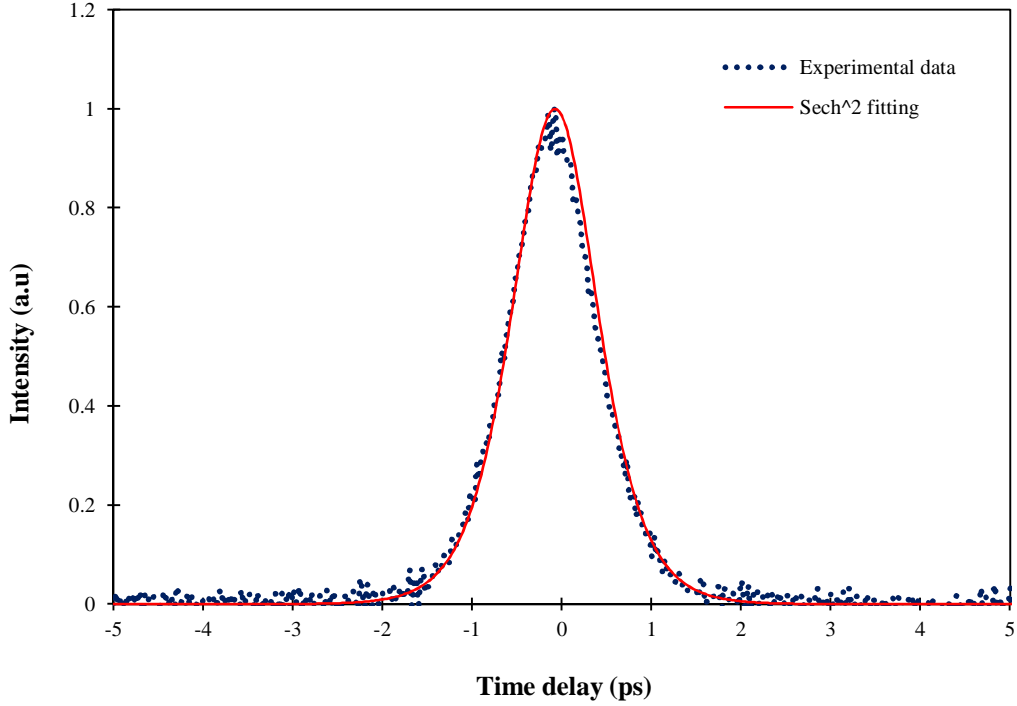


Figure 87: Autocorrelation trace of the mode-locked pulses, obtained from the mode-locked EDZF using the graphene based saturable absorber, against with sech^2 fitting⁶¹.

Figure 88 shows the mode-locked laser spectrum in the frequency domain, obtained from the RFSA. The output pulse is observed over a 1 GHz-span RF spectrum, and is seen to be highly stable with no fluctuations arising from Q-switching. This can be deduced from the evenly spaced frequency interval in the RF spectrum that is that shows no spectral modulation [147]. It can also be seen that due to the absence of low-repetition-rate modulations in the output pulse train that result in relaxation oscillations, the laser is now operating in CW mode locking laser oscillation [148], [149]. The RF repetition rate of the pulse is approximately 69.3 MHz, again agreeing well with the measurements obtained from the oscilloscope.

Figure 89 shows the fundamental harmonic frequency of the mode-locked laser output. The frequency obtained corresponds to 69.3 MHz as measured with an 80 kHz frequency span and a resolution of 300 Hz, and indicates that the mode-locked laser works in its fundamental regime, with the estimated peak-to-pedestal ratio being about 37 dB.

⁶¹ Image adapted from K. Thambiratnam, H. Ahmad, , F. D. Muhammad, M. Z. Zulkifli, A. Z. Zulkifli, M. C. Paul and S. W. Harun, "Q-Switching and Mode-Locking in Highly-Doped $\text{Zr}_2\text{O}_3\text{-Al}_2\text{O}_3\text{-Er}_2\text{O}_3$ Doped Fibre Lasers using Graphene as a Saturable Absorber," IEEE J. Select. Topics in Quant. Electron., vol. 20, pp. 1100108, 2013.

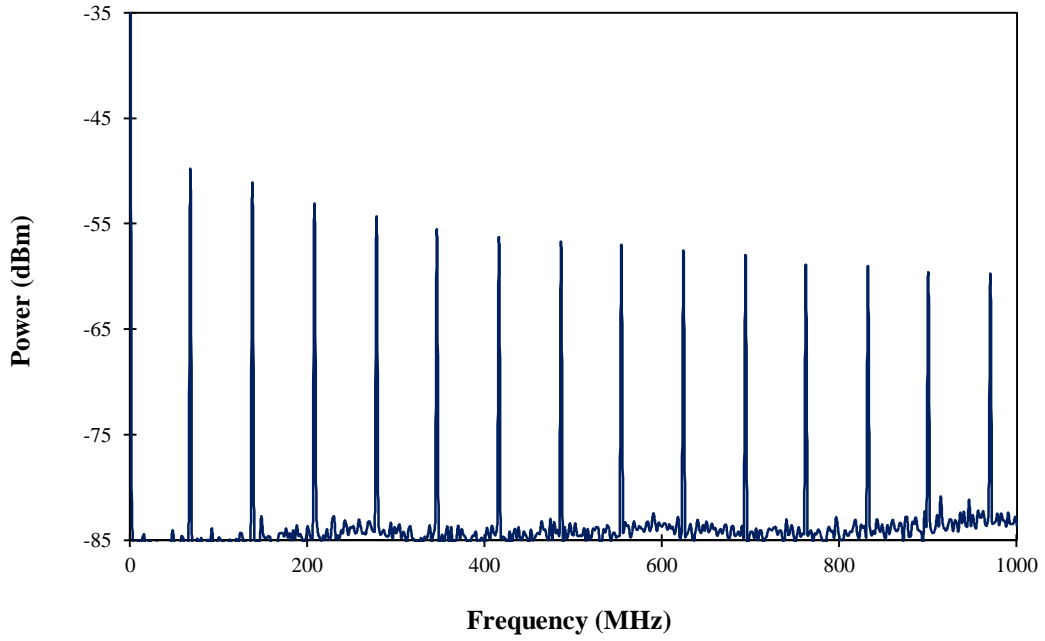


Figure 88: RF spectrum of the mode-locked pulse obtained from the mode-locked EDZF with the graphene based saturable absorber, taken at a 1 GHz span⁶².

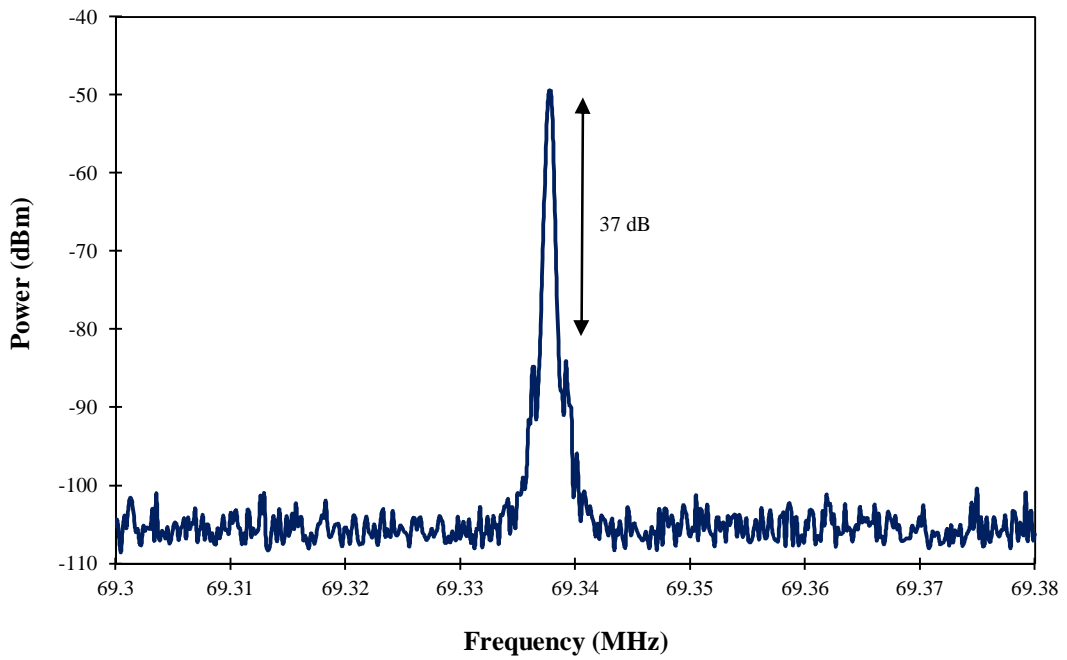


Figure 89: RF spectrum at the fundamental repetition rate of 69.3 MHz with an 80 kHz frequency span and resolution of 300 Hz⁶³.

62 Image adapted from K. Thambiratnam, H. Ahmad, , F. D. Muhammad, M. Z. Zulkifli, A. Z. Zulkifli, M. C. Paul and S. W. Harun, "Q-Switching and Mode-Locking in Highly-Doped $\text{Zr}_2\text{O}_3\text{-Al}_2\text{O}_3\text{-Er}_2\text{O}_3$ Doped Fibre Lasers using Graphene as a Saturable Absorber," IEEE J. Select. Topics in Quant. Electron., vol. 20, pp. 1100108, 2013.

63 Image adapted from K. Thambiratnam, H. Ahmad, , F. D. Muhammad, M. Z. Zulkifli, A. Z. Zulkifli, M. C. Paul and S. W. Harun, "Q-Switching and Mode-Locking in Highly-Doped $\text{Zr}_2\text{O}_3\text{-Al}_2\text{O}_3\text{-Er}_2\text{O}_3$ Doped Fibre Lasers using Graphene as a Saturable Absorber," IEEE J. Select. Topics in Quant. Electron., vol. 20, pp. 1100108, 2013.

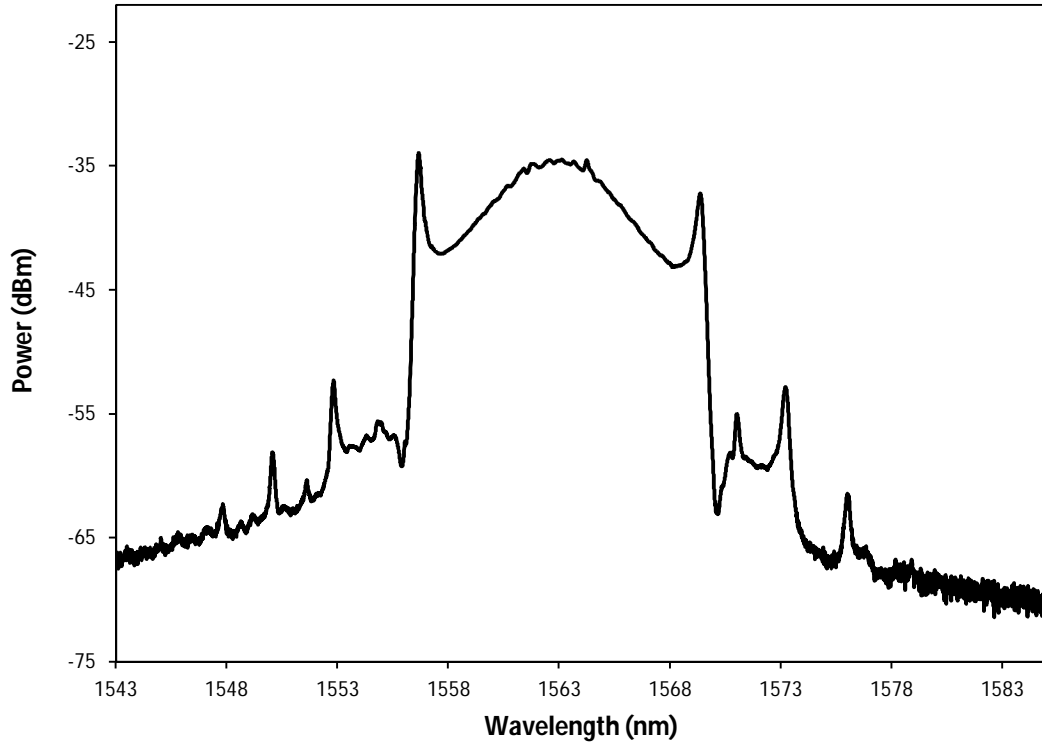


Figure 90: Optical spectrum of the EDZF mode-locked fibre laser at a pump power of 100 mW using the SWCNT/PEO based saturable absorber⁶⁴.

The output has a central wavelength of 1562.67 nm, and it is worthwhile to observe that unlike the mode-locked pulses obtained from the system when the graphene based saturable absorber is employed these mode-locked pulses do exhibit some perturbations in the midpoint region, thus indicating that the generated pulses are relatively less stable. The average output power of the system is measured to be 180 μ W, with a repetition rate of 17.74 MHz and a peak power of 14.09 W. The pulse energy of the system is 0.01 nJ.

The autocorrelation trace of the second harmonic generation for the mode-locked pulses obtained when using the SWCNT/PEO based saturable absorber is shown in Figure 91.

⁶⁴ Image adapted from K. Thambiratnam, H. Ahmad, , F. D. Muhammad, M. Z. Zulkifli, A. Z. Zulkifli, M. C. Paul and S. W. Harun, "Q-Switching and Mode-Locking in Highly-Doped Zr_2O_3 - Al_2O_3 - Er_2O_3 Doped Fibre Lasers using Graphene as a Saturable Absorber," IEEE J. Select. Topics in Quant. Electron., vol. 20, pp. 1100108, 2013.

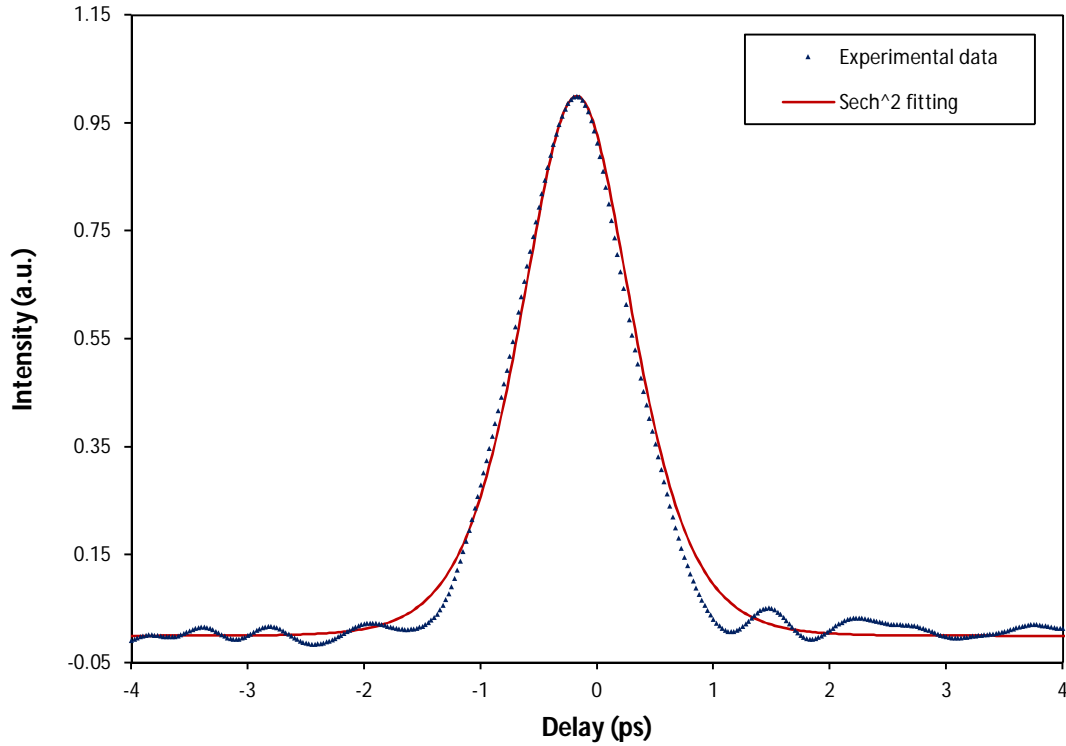


Figure 91: Autocorrelation trace of the mode-locked pulses, obtained from the mode-locked EDZF using the graphene based saturable absorber, against with sech^2 fitting⁶⁵.

Similar to the mode-locked EDZF based fibre laser which employed the graphene based saturable absorber, the estimated pulse duration obtained by the system incorporating the SWCNT/PEO based saturable absorber is approximately 720 fs at the FWHM point. The autocorrelation trace indicates that the experimentally obtained values augur well with the theoretical sech^2 fitting, and no pulse breaking or pulse pair generation is observed. A time-bandwidth product of 0.48 is obtained from the product of the 3 dB bandwidth, which is higher than the expected transform limit of 0.315, although this comes as no surprise as it is not likely that system will be able to generate pulses matching the transform limit exactly.

The spectrum of the mode-locked pulses in the frequency domain, as obtained by the RFSA, is shown in Figure 92.

⁶⁵ Image adapted from K. Thambiratnam, H. Ahmad, , F. D. Muhammad, M. Z. Zulkifli, A. Z. Zulkifli, M. C. Paul and S. W. Harun, "Q-Switching and Mode-Locking in Highly-Doped Zr_2O_3 - Al_2O_3 - Er_2O_3 Doped Fibre Lasers using Graphene as a Saturable Absorber," IEEE J. Select. Topics in Quant. Electron., vol. 20, pp. 1100108, 2013.

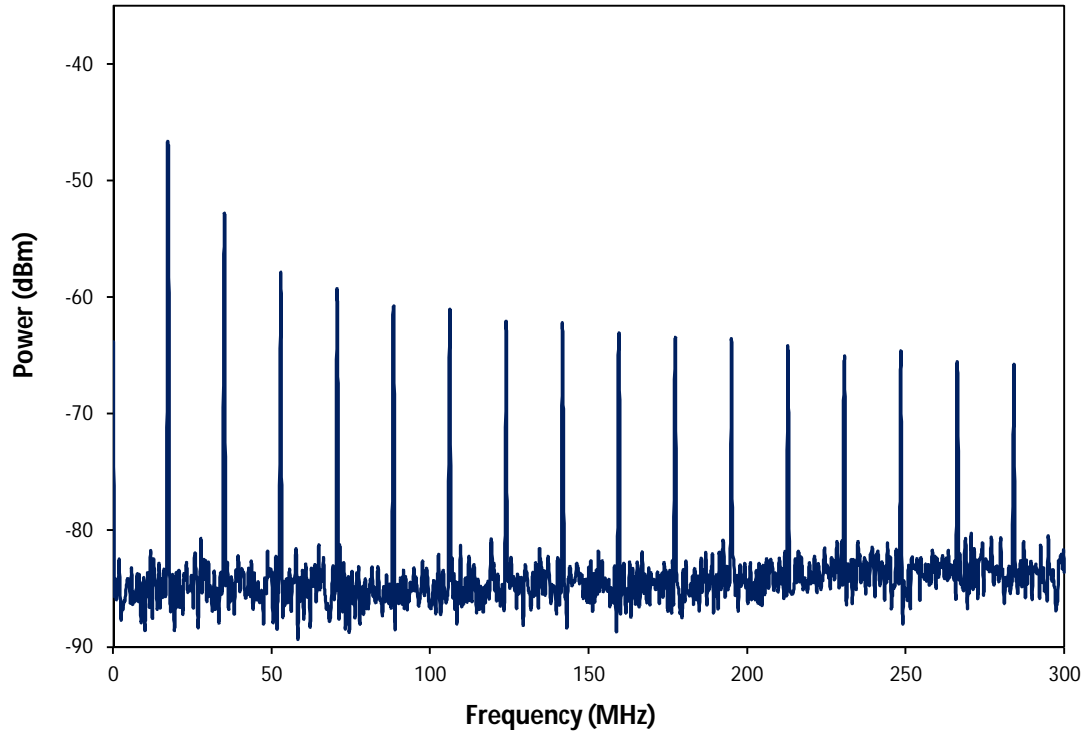


Figure 92: RF spectrum of the mode-locked pulse obtained from the mode-locked EDZF with the SWCNT/PEO based saturable absorber, taken at a 300 GHz span. The fundamental harmonic frequency is 17.74 MHz⁶⁶.

It can be seen that the mode-locked spectrum is stable, with no fluctuations caused by Q-switching as the frequency spacing is even. Furthermore, the lack of low-repetition-rate modulations in the output pulse train indicates that the laser is now operating as a CW mode-locked laser. From the RFSA, the repetition rate of the pulses is determined to be 17.74 MHz, and this agrees with measurement of the pulse as obtained using an oscilloscope.

Figure 93 shows the fundamental harmonic frequency of the mode-locked laser output, which corresponds to a frequency of 17.74 MHz. The fundamental harmonic frequency is obtained over a 60 kHz span with an estimated peak-to-pedestal ratio being about 35 dB. This is only slight lower than the peak-to-pedestal ratio of 37 dB obtained when the system is configured using the graphene based saturable absorber.

⁶⁶ Image adapted from K. Thambiratnam, H. Ahmad, F. D. Muhammad, M. Z. Zulkifli, A. Z. Zulkifli, M. C. Paul and S. W. Harun, "Q-Switching and Mode-Locking in Highly-Doped $\text{Zr}_2\text{O}_3\text{-Al}_2\text{O}_3\text{-Er}_2\text{O}_3$ Doped Fibre Lasers using Graphene as a Saturable Absorber," IEEE J. Select. Topics in Quant. Electron., vol. 20, pp. 1100108, 2013.

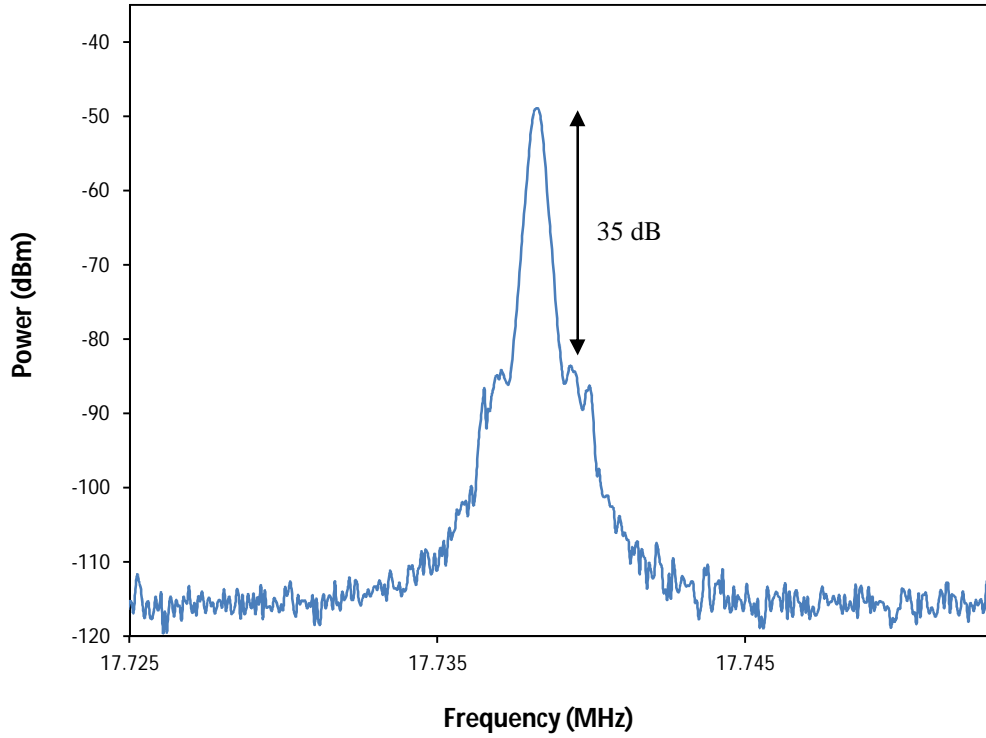


Figure 93: RF spectrum at the fundamental repetition rate of 17.74 MHz with an 60 kHz frequency span and resolution of 300 Hz⁶⁷.

In both cases, the generated pulses are stable and consistent, thereby allowing the EDZF based mode-locked fibre laser a multitude of uses and practical real-world applications.

4.5 Summary and Conclusion

In generating the fast and ultrafast pulses, the EDZF is configured to as a fibre laser working in conjunction with passive saturable absorbers formed from graphene or SWCNTs.

The formation of the saturable absorbers is described, with both saturable absorbers being formed by different means. The graphene based saturable absorber is formed by the optical deposition technique, using graphene flakes are obtained from Graphene Research Ltd suspended in an NMP solution. The flakes have an average particle size of 550 nm and

⁶⁷ Image adapted from K. Thambiratnam, H. Ahmad, , F. D. Muhammad, M. Z. Zulkifli, A. Z. Zulkifli, M. C. Paul and S. W. Harun, "Q-Switching and Mode-Locking in Highly-Doped Zr₂O₃-Al₂O₃-Er₂O₃ Doped Fibre Lasers using Graphene as a Saturable Absorber," IEEE J. Select. Topics in Quant. Electron., vol. 20, pp. 1100108, 2013.

average flake thickness of 0.35 nm. Taking advantage of the optical thermophoresis effect, the graphene layer is formed by first dipping a fibre ferrule in the aqueous solution containing the graphene flakes, before connecting it to another fibre ferrule and exposing the ferrules to an intense laser signal. After a period of time, the ferrules are disconnected and one cleaned, before being reconnected and the process repeated. The graphene based saturable absorber can be assumed to be formed once a reflected power of about 4.1% of the transmitted power is obtained, with the graphene layer reflecting approximately 0.1% of the signal and Fresnel reflection accounting for the remaining 4.0% of the reflected signal. Examination of the deposited graphene layer with a Renishaw InVia Raman spectrometer at 532 nm (2.33 eV) over a period of 10s with a grating value of 1800 lines/mm gives two intensity peaks at 1597 cm^{-1} and 2684 cm^{-1} . These peaks confirm the presence of the graphene layer, with the peak at 1597 cm^{-1} corresponding closely to the expected 1580 cm^{-1} G peak for graphene, while the peak at 2684 cm^{-1} corresponds closely to the 2700 cm^{-1} 2D peak for graphene. Furthermore, the ratio of G to 2D does not exceed 1 indicating that a nearly single layer of graphene has been obtained on the fibre ferrule, with the actual number of layers being probably 2 or 3.

The SWCNT saturable absorber on the other hand is more easily fabricated and can be accomplished by simply hosting the nanotubes in a suitable host material. Typically, PVA is the preferred choice for a host material but in this research a new host material, PEO, is used to form the SWCNT saturable absorber. PEO has a number of advantages over PVA, such as a lower melting point and also easy dispersion in water, making the fabrication process easier while at the same time having no adverse effects on the performance of the SWCNTs as saturable absorbers. The saturable absorber itself is formed by sandwiching a SWCNT/PEO composite in between two fibre ferrules. The SWCNTs used are 99% pure with lengths of between 3 to 30 μm and average diameters of between 1 to 2 nm and are procured from Cheap Tubes Inc. The PEO solution has an average molecular weight of 1×10^6 g/mol while the SDS solution that is used to disperse the SWCNTs has an average molecular weight of 288.38 g/mol. The SWCNT is soaked in a 1% SDS solution before being ultrasonically dispersed at 50 W for a period of 30 minutes and is then mixed with the PEO before the entire solution is simply dropped onto the face of the fibre ferrule and allowing it to dry in air for 24 hours. Analysis by Raman spectroscopy shows G, D, and G' peaks at 1598 cm^{-1} , 1362 cm^{-1} and 2684 cm^{-1} , indicating the presence of the SWCNTs in the saturable absorber. Two RBM peaks at 186 cm^{-1} and 287 cm^{-1} are also observed.

As a Q-switched laser capable of generating fast pulses, a 3 m long EDZF lasers with an active ion concentration of approximately 3880 ppm/wt is used as the gain medium and the SWCNT/PEO composite saturable absorber as the Q-switching mechanism. The Q-switched pulse train is obtained above a threshold pump power of 92.5 to 95.0 mW, and at the maximum pump power of 141.8 mW a repetition rate of 14.20 kHz is obtained, with a corresponding pulse width of 8.6 μ s. The average output power of the fibre laser is 270.0 μ W at 141.8 mW, and the maximum pulse energy obtained is 19.02 nJ. Using the graphene based saturable absorber on the other hand gives Q-switched pulses with a pulse width of 4.6 μ s and a pulse energy and pulse peak power of 16.8 nJ and 3.6 mW respectively. The repetition rate of the Q-switched pulses is approximately 50.1 kHz, with a lasing threshold of 48 mW, and a Q-switching threshold of 56 mW.

When operating in the mode-locking regime using the graphene based saturable absorber, the EDZF fibre laser has a mode-locking threshold of 90 mW, with the generated pulses having an average output power, pulse energy and peak power of approximately 1.6 mW, 23.1 pJ and 31.6 W respectively as well as a pulse width of 730 fs. The repetition rate of the pulses is 69.3 MHz, corresponding to a channel spacing of 14.5 ns in the pulse train with a central wavelength of about 1563.0 nm. Replacing the graphene based saturable absorber with one formed from a SWCNT/PEO composite now allows the EDZF based mode-locked laser to generate pulses with a central wavelength of 1562.7 nm, although the obtained spectrum indicates the presence of some perturbations in the midpoint region. The mode-locked laser has an average output power of 180 μ W, with a repetition rate and peak power of 17.74 MHz and 14.09 W respectively as well as a pulse energy of 0.01 nJ. The estimated pulse duration is approximately 720 fs at the FWHM point, with a time-bandwidth product of 0.48. Examination of the pulses using an RFSA confirms the repetition rate of the pulses to be 17.74 MHz, with an estimated peak-to-pedestal ratio of 35 dB. In all cases, the generated pulses are stable and consistent, and allow them to be deployed with a high degree of confidence and reliability in multiple practical applications.

5. SUMMARY AND CONCLUSION

5.1 *Introduction*

In this chapter, a summary of the findings and results of this work is presented, as well as the conclusions that can be drawn from the outcomes of this work. The next section will provide a summary of the findings of this research, which will be matched to the objectives set out in Chapter 1.

5.2 *Summary*

The first chapter details the background of the work, beginning with a brief history on the history of optical communications, followed by a short overview of the factors and events that drove the development of the EDFA. Subsequently, the chapter examined the impetus that would result in the creation of the EDZF, and the role it will play in the development of compact fast and ultra-fast fibre lasers. In this chapter also the three objectives of this research are defined, these being:

1. revisiting the EDZF fabrication process,
2. examine the behavior of the active ions in the EDZF when exposed to pump wavelengths, and
3. employing the EDZF as a gain medium for compact fast and ultrafast pulse lasers using graphene and SWCNT based saturable absorbers.

Each subsequent chapter is arranged in such a way as to address one of these key objectives, with the following chapter addressing the fabrication of the EDZF.

5.2.1 *Revisiting the EDZF Fabrication Process*

The first objective, which is to revisit the fabrication process of the EDZF, is addressed in Chapter 2. The fabrication process begins with the selection of a suitable material to act as the host. The selected hollow tube is cleaned and then mounted on a glass lathe, where it will undergo the MCVD process. In this process, the gases O_2 , N_2 and CCl_2F_2 are fed through $SiCl_4$, $GeCl_4$ & $POCl_3$ solutions via a bubbler to create SiO_2 , GeO_2 & P_2O_5 gases. These gases are heated so that they oxidize, and form sub-micron particles. These particles, also known as soot, are deposited in the same direction as the reactant flow that contains the $SiCl_4$, $GeCl_4$, $POCl_3$ vapors. An oxy-hydrogen burner maintains a temperature of between $1350 - 1400^\circ C$. A dopant control program is used to adjust the NA values to within the range of 0.15-0.25 with a core diameter of between $5.0-6.0\ \mu m$, with the relative density of the soot layer estimated on the basis of RE concentration ranging between 0.30 to 0.50. The glass tube, together with its porous layer, now undergoes solution doping, where the various dopants are incorporated into the glass structure in the form of an alcoholic-water mixture at a ratio of 1:5. The main solutions introduced are $ErCl_3 \cdot 6H_2O$ at between 0.005 M to 0.010 M and $ZrOCl_2 \cdot 8H_2O$ and $AlCl_3 \cdot 6H_2O$ complexes between 0.1 M to 1.0 M. Small amounts of Y_2O_3 and P_2O_5 are also added to serve as nucleating agents. The tube is allowed to soak in the solution for about 1 hour to allow the saturation of the developed pores before allowing N_2 gas to flow through the tube for approximately 15-30 minutes at room temperature to remove the ethanol solvent. Once this is complete, the tube is now oxidized at $800^\circ C$ to $1000^\circ C$ in presence of excess O_2 for converting the halide or nitrate salts present in the pores into their corresponding oxides. Subsequently, the substrate now undergoes dehydration using a careful combination of temperature, $Cl_2:O_2$ ratio and selected time period, before finally undergoing a sintering process at a temperature of between 1400 to $1600^\circ C$. Once the sintering process is complete, tube is collapsed to form the preform, which is then drawn to form the fibre. The drawn fibre is coated with Desolite DP-1004 resin as the primary coating as well as Desolite DS-2015 resin as the secondary coating to provide physical protection to the fibre. The drying of the resins is done by a UV curing oven, and finally the fibres are wound on a precision spooling machine.

The drawn fibres are now studied for their morphology. Two fibres are drawn, ZEr-A and ZEr-B, with different dopant concentrations. Visual inspection of both fibres' lateral surfaces shows a smooth polymer layer with no bubbles or other deformities present in the polymer coating. Examination of both fibres under microscopic view shows both EDZFs have a very distinct core with a diameter of approximately 10 μm . The core region morphology of selected ZEr-A and ZEr-B preform samples developed without any thermal treatment or annealing is studied using FEGSEM, and the obtained results show that the micro-crystallite structures in the ZEr-B fibre have better defined boundaries than those in the ZEr-A fibre, owing to the higher ZrO_2 ion concentrations in the ZEr-B fibre. The presence of the ZrO_2 rich micro-crystallites is further confirmed by TEM scanning, with XRD analysis of the preform samples shows a small diffraction peak at a 2θ value of about 30° , indicating the formation of tetragonal ZrO_2 in the host matrix. An EPMA analysis of the preform samples shows that both samples have an almost similar level of Al_2O_3 dopants, at about 0.24-0.25 mole% but also indicate clearly that the ZEr-B preform has significantly higher ZrO_2 and Er_2O_3 dopant concentrations, at approximately 2.21 mole% and 0.155 mole% respectively, as compared to concentrations of only 0.65 mole% and 0.225 mole% for the same dopants in the ZEr-A fibre. The spectral characterization of the ZEr-A fibre shows a peak at 980 nm with a loss of about 16.5 dB/m as well as a second peak at 1550 nm with a spectral attenuation of around 27.5 dB/m. Similarly, the ZEr-B fibre sample also shows two attenuation peaks, the first occurring at 980 nm with a loss of about 22.0 dB/m while the second occurring at 1550 nm with a loss of around 53.0 dB/m. Both fibres also show a peak at 800 nm, with spectral attenuations of 6.0 and 8.0 dB/m for the ZEr-A and ZEr-B fibres respectively. The ZEr-A and ZEr-B fibres show somewhat similar fluorescence life-times of 10.93 and 10.86 ms respectively, with the slightly shorter lifetime of the ZEr-B fibre being attributed to the higher dopant concentrations of that fibre. This is an important point, as it indicates that the concentration-quenching phenomenon is strongly reduced through an increase in the ZrO_2 doping levels. Examination of the refractive index profile of the ZEr-B, as well as the ZEr-A fibres gives a standard W-profile that is to be expected of the optical fibre.

5.2.2 *Examining the Behavior of the Active Ions in the EDZF when Exposed to Pump Wavelengths*

Chapter 3 discusses the various optical properties of the fibre. A detailed foray into the theoretical background of the EDF is undertaken, with a particular focus on the behavior of the erbium ions as the active gain medium. The energy levels of the erbium ions are examined, as well as the various electron transitions between the energy levels and their resulting emissions. The rate equations that are used to model these transitions are also discussed, followed by a derivation of the equations that govern the ASE, gain and noise figure of the EDFA. The chapter then looks into the ASE characteristics of the EDZF, which in itself is an important aspect of this work as it will determine the operational limits of the EDZF, particularly the operational bandwidth of the developed amplifier. The EDZF used for this aspect is 3 m long, with a dopant concentration in excess of 3880 ppm/wt with an absorption ratio of about 22.0 dB/m at 980 nm and approximately 53.0 dB/m at 1550 nm. For comparison purposes, a Metrogain M-12 EDF, which has an Er^{3+} ion concentration of about 960 ppm and absorption ratio of between 11 to 13 dBm at 980 nm is also tested under the same conditions. A crucial point to observe is the spectral shape of the EDZF's ASE output differs substantially from that of a conventional EDF, rising to a peak region at 1530 nm followed by a short 'plateau' afterwards before dropping back again. The ASE spectra originating from the EDF declines in power slightly after the peak region before decreasing steeply. The ASE spectra of the EDZF on the other hand remains relatively stable after the peak region, before beginning to decline. This is a very important characteristic, as it sets the operational boundaries of the EDZF and gives it a longer operating bandwidth as compared to the EDF. This can be attributed to the high Er^{3+} dopant concentrations in the fibre, which allows the parts of the fibre farthest from the pump source to absorb the ASE generated by the initial sections of the fibre, in the same manner as an L-band amplifier. Also, at higher pump powers, the 1530 nm peak becomes more dominant in the spectral curve of the EDZF, recording peak powers of -24.9, -20.4 and -17.7 dBm at pump powers of 108.7, 140.0 and 170.1 mW while the plateau region remains rises at a much slower rate, increasing from an average of -30.0 dBm to -28.0 dBm over the range of the same pump powers. This fact is further confirmed by comparing the ASE from a 3 m long

EDZF to that of a 2 m long EDZF that is pumped under the same conditions which shows that the shorter EDZF acts more like a conventional EDF, as opposed to following the spectra generated by the longer EDZF.

As an amplifier, the gain and NF levels observed are similar to that of other amplifiers based on highly-doped active media. The EDZF amplifier is able to impart very high gains of approximately 28.0 dB near the central region of 1530 nm, as well as a high gain level of between 22.0 to 25.0 dB at the plateau region of the EDZF's ASE output, before reaching a lower value of around 5.0 dB at 1590 nm for a -30 dBm input signal. The same observation can also be made for the gain experienced by a 0 dBm input signal, with a relatively flat gain of 10.0 dB from 1530 nm to about 1570 nm, before it begins to drop to about 2.0 or 3.0 dB at 1590 nm. The NF of the EDZF is also high, reaching 14.1 dB before quickly dropping to 9.3 dB over a wavelength range of 1530 to 1550 nm for a 0 dBm input signal. For a -30 dBm signal on the other hand, the initially high NF of 12.2 dB decreases quickly to only 4.9 dB over a wavelength range of 1530 to 1550 nm. In both cases, maintaining the power but increasing the wavelength of the input signal results in a further drop in the NF, but also results in the gain decreasing as well. The high NF levels are attributed to the high ASE levels at this wavelength region, and superimposing the two spectra reveals that both the gain and NF generally follow the same spectral shape as the ASE. Based on the gain and NF spectra, it can be seen that an EDZF based amplifier would have some advantages over conventional EDFAs, especially in its ability to impart high gain as well as a relatively flat gain region.

The application of the EDZF as the gain medium for an SLM laser is then examined. The reason for this experiment is that the high dopant concentrations in the EDZF allow for a short cavity length to be realized, which is a necessary requirement for the development of SLM lasers. As such, the EDZF can be used as a compact gain medium that is at the same time highly compatible with conventional optical fibres as it is based on a conventional silica host. As an SLM fibre laser, an EDZF approximately 0.5 m long with a dopant concentration of 3880 ppm/wt serves as the gain medium for SLM fibre laser. Due to the high dopant concentrations, the 0.5 m EDZF can provide the same performance as a EDF approximately 4 m long, thus significantly reducing the cavity length. A 980 nm laser diode is used as the pump source, while two short EDFs 3 cm and 6 cm long inserted in the cavity to act as saturable absorbers. The EDFs used are conventional EDFs, with an erbium ion

concentration of about 900 ppm/wt and an absorption rates of 5.0 dB/m at 1530 nm. A tunable C-band FBG fabricated by embedding a C-band FBG, which has a reflectivity of 99% and a bandwidth of 0.1 nm, onto a polymer layer on a metal plate provides the tuning mechanism. The SLM output of the laser has a tunable range of 11.2 nm, from 1533.8 nm to 1545.0 nm, as well as an average SNR of more than 50 dB with an output power of above -8.9 dBm. The output of the system is measured over a period of two and a half hours in 10-minute intervals, and shows almost no fluctuations are observed in either the power or wavelength of the laser's output. Measurement with an RF-SA provides positive indication that the oscillation is in the single mode as the beating noise peaks observed in the trace are densely spaced, while measurements of the linewidth provide a value of about 0.2 MHz for the SLM output.

Another interesting characteristic of the EDZF is its non-linear properties. This is because the presence of the ZrO_2 micro-crystallites in the core region of the EDZF would allow for non-linear interactions to occur at lower signal intensities. In investigating the non-linear characteristics of the EDZF, the FWM effect in particular is chosen, due to its potential applications. The fundamental principles and theoretical models that define the operation generation of the FWM effect are first described and subsequently, a 4 m long EDZF is used to determine the non-linear characteristics of the fabricated fibre. In generating the FWM output, FWM power levels of approximately -45 dBm at obtained at a wavelength of around 1565 nm, auguring well with the theoretical predicted values. Adjusting the pump and single wavelengths will also cause the idlers to shift in accordance with the theoretically predicted models. The EDZF shows a non-linear coefficient of $14 \text{ W}^{-1}\text{km}^{-1}$ along with chromatic and dispersion slopes of 28.45 ps/nm.km and $3.63 \text{ ps/nm}^2.\text{km}$ that are well in accordance to the theoretical values.

5.2.3 Employing the EDZF as a Gain Medium for Compact Fast and Ultrafast Pulse Lasers using Graphene and SWCNT based Saturable Absorbers.

This final major chapter of this work, Chapter 4 examines the application of the EDZF in fast and ultra-fast pulsed fibre lasers. The EDZF will be used in conjunction with passive saturable absorbers formed from graphene and SWCNTs,

and will be operated in both the Q-switched and mode-locked regimes. The chapter begins in the same manner as the previous two, with an in-depth analysis on the physics behind Q-switching and mode-locking, followed by an overview of saturable absorption. The chapter then moves onward to discuss the characteristics of graphene and carbon nanotubes, and their role in the fabrication of saturable absorbers for use in passive Q-switching and mode-locking applications.

Although graphene and SWCNTs are carbon allotropes, and therefore derived from the same base material, the means in which they are formed into saturable absorbers are different. In the case of the graphene based saturable absorber, the optical deposition technique is used, with the base material being graphene flakes with an average particle size of 550 nm and thickness of 0.35 nm, suspended in an NMP solution. Using this technique, a fibre ferrule is dipped into an aqueous solution containing the graphene flakes, before it is connected to another fibre ferrule and exposed to an intense laser signal to take advantage of the optical thermophoresis effect. This will deposit the graphene flakes onto the face of the fibre ferrule, and after a period of time, the ferrules are disconnected and one cleaned before being reconnected and the process repeated. The saturable absorber layer can be assumed to have formed once a reflected power of about 4.1% of the transmitted power is obtained. A Renishaw InVia Raman spectrometer operating at 532 nm (2.33 eV) is used to inspect the formed graphene layer, and the presence of peaks at 1597 cm^{-1} and 2684 cm^{-1} correspond to the expected G and 2D peaks for graphene respectively. A nearly single layer of graphene can be assumed to have formed, as the ratio of G to 2D does not exceed 1. The SWCNT saturable absorber on the other hand is much easier to fabricate, using PEO as a host material. Although PVA is traditionally used as a host for SWCNTs, PEO offers a number of significant advantages, including lower melting point and also easy dispersion in water, thereby making the overall fabrication process easier. The SWCNT/PEO saturable absorber is formed from SWCNTs used being 99% pure with lengths of between 3 to 30 μm and average diameters of between 1 to 2 nm incorporated into the PEO host, and then sandwiched between two fibre ferrules. The PEO solution used has an average molecular weight of $1 \times 10^6\text{ g/mol}$, and the SWCNTs are soaked in a 1% SDS solution before being ultrasonically dispersed at 50 W for a period of 30 minutes and then mixed with the PEO. The entire solution is then simply dropped onto the face of the fibre ferrule and

allowed to dry in air for 24 hours. Analysis by Raman spectroscopy shows indicates the presence of the SWCNTs in the composite with peaks at 1598 cm^{-1} , 1362 cm^{-1} and 2684 cm^{-1} , corresponding to the G, D, and G' peaks. Two RBM peaks are also observed at 186 cm^{-1} and 287 cm^{-1} .

The EDZF based Q-switched laser uses a 3 m long EDZF lasers with an active ion concentration of approximately 3880 ppm/wt as the gain medium and the SWCNT/PEO composite saturable absorber as the Q-switching mechanism. In this configuration, a Q-switched pulse train is obtained above a threshold pump power of about 95.0 mW, with a repetition rate of 14.20 kHz and pulse width of 8.6 μs obtained at a maximum pump power of 141.8 mW. At this pump power, the average output power of the fibre laser is 270.0 μW and the maximum pulse energy obtained is 19.02 nJ. Configuring the EDZF based Q-switched laser with a graphene based saturable absorber on the other hand gives Q-switched pulses with a pulse width of 4.6 μs as well as pulse energy, pulse peak power and repetition rate of 16.8 nJ, 3.6 mW and 50.1 kHz respectively. The lasing threshold of the Q-switched laser is approximately 48 mW, with a Q-switching threshold of 56 mW. When operating in the mode-locking regime, the EDZF based laser, with a graphene based saturable absorber has a mode-locking threshold of 90 mW. The generated pulses have an average output power of 1.6 mW, with a pulse energy and peak power of approximately 23.1 pJ and 31.6 W respectively. The measured pulse width is 730 fs. The output pulses of the laser have a repetition rate of 69.3 MHz, which corresponds to a channel spacing of 14.5 ns in the pulse train with a central wavelength of about 1563.0 nm. Replacing the graphene based saturable absorber with the SWCNT/PEO composite based saturable absorber now allows the mode-locked laser to generate pulses with a repetition rate and peak power of 17.74 MHz and 14.09 W at a central wavelength of 1562.7 nm, with a pulse energy of 0.01 nJ. Unlike the mode-locked pulses obtained using the graphene based saturable absorber, the output obtained when using the SWCNT/PEO saturable absorber indicates some perturbations near the central region, although the overall output is stable. The mode-locked laser has an average output power of 180 μW , with an estimated pulse duration of approximately 720 fs at the FWHM point as well as a time-bandwidth product of 0.48. Examination of the pulses using an RFSA confirms a repetition rate 17.74 MHz, with an estimated peak-to-pedestal ratio of 35 dB. In all cases, the generated pulses are stable and consistent, and allow them to be

deployed with a high degree of confidence and reliability in multiple practical applications.

5.3 Conclusion

In conclusion, the research work has been able to achieve its primary objectives; to obtain an in-depth understanding of the fabrication process of the EDZF, to examine the performance of the EDZF as a fibre amplifier, fibre laser and as the medium for generating non-linear optical phenomena as well as to use the EDZF in conjunction with graphene and SWCNT based saturable absorbers to create compact, passively mode-locked and Q-switched fibre lasers. Therefore, this research was successfully undertaken and completed.

During this work, a significant portion of research findings had been translated into publications, which have been accepted by journals indexed in the ISI Web of Knowledge. These publications detail research findings, related either directly or indirectly to this work, and have been included in Appendix 2.

REFERENCES

- [1] I. Fang, A History of Mass Communication: Six Information Revolutions, Newton: Focal Press, 1997.
- [2] N. C. Beese , "Light Sources for Optical Communication," *Infrared Phys.*, vol. 1, pp. 5-16, 1961.
- [3] K. O. Kao and G. A. Hockam, "Dielectric-Fibre Surface Waveguides for Optical Frequencies," *IEE Proc.*, vol. 133, no. 7, pp. 1151-1158, 1996.
- [4] T. Miya, Y. Terunima, T. Hosaka and T. Miyashita, "Ultimate Low-Loss Single Mode Fibre at 1550 nm," *Electron. Lett.*, vol. 15, pp. 106-108, 1979.
- [5] G. E. Keiser, Optical Fibre Communication, 2nd Ed., New York: McGraw Hill, 1991.
- [6] R. Ramaswami, Optical Networks: A Practical Perspective, 3rd ed., San Francisco, California: Morgan Kaufmann, 2009.
- [7] D. Cotter and A. D. Ellis, "Asynchronous Digital Optical Regeneration and Networks," *J. Lightwav. Technol.*, vol. 16, pp. 2068-2080, 1998.
- [8] S. Abbot, "Review of 20 Years of Undersea Optical Fibre Transmission System Development and Deployment since TAT-8," in *Optical Communication, 2008, ECOC 2008 34th European Conference on*, 1998.
- [9] K. Rottwitt and J. H. Povlsen, "Analysing the Fundamental Properties of Raman Amplifiers in Optical Fibres," *J. Lightwav. Technol.*, vol. 23, pp. 3597-3613, 2005.
- [10] J. H. Lee, Y. M. CHang, Y. G. Han, H. Chung, S. H. Kim and S. B. Lee, "A Detailed Experimental Study on Single Pump Raman/EDFA Hybrid Amplifiers: Static, Dynamic, and System Performance Comparison," *J. Lighthav. Technol.*, vol. 23, p. 3848, 2005.
- [11] P. Doussiere, A. Jourdan, G. Soulage, P. Garabedian, T. Fillion, E. Derouin and D. Leclerc, "Clamped Gain Travelling Wave Semiconductor Optical Amplifier for Wavelength Division Multiplexing Applications," in *Semiconductor Laser Conference, 1994, 14th IEEE International*, 1994.
- [12] K. Morito, "Output-Level Control of Semiconductor Optical Amplifier by External Light Injection," *J. Lightwav. Technol.*, vol. 18, pp. 4332-4341, 2005.

- [13] J. M. Chavez Boggio, P. Dainese, F. Karlsson and H. L. Fragnito, "Broad-Band 88% Efficient Two-Pump Fibre Optical Parametric Amplifier," *Photon. Technol. Lett.*, vol. 15, pp. 1528-1530, 2003.
- [14] G. E. Keiser, "A Review of WDM Technology and Applications," *Opt. Fibre Technol.*, vol. 5, pp. 3-39, 1999.
- [15] R. J. Mears, L. Reekie, I. M. Jauncey and D. N. Payne, "Low-noise Erbium-doped fibre amplifier at 1.54 μ m," *Electron. Lett.*, vol. 23, pp. 1026-1028, 1987.
- [16] Y. Ohishi, A. Mori, M. Yamada, H. Ono, Y. Nishida and K. Oikawa, "Gain Characteristics of Tellurite-Based Erbium-Doped Fibre Amplifiers for 1.5- μ m Broadband Amplification," *Opt. Lett.*, vol. 23, p. 274, 1998.
- [17] A. Cucinotta, F. Poli and S. Selleri, "Design of Erbium-Doped Triangular Photonic-Crystal-Fibre-Based Amplifiers," *Photon. Technol. Lett.*, vol. 16, p. 2027, 2004.
- [18] S. Aozasa, H. Masuda and M. Shimizu, "S-band Thulium-Doped Fibre Amplifier Employing High Thulium Concentration Doping Technique," *J. Lightwav. Technol.*, vol. 24, pp. 3842-3848, 2006.
- [19] S. W. Harun, N. Tamchek, S. Shahi and H. Ahmad, "L-band Amplification and Multi-Wavelength Lasing with Bismuth-Based Erbium Doped Fibre," *Prog. Electromagn. Res. C.*, vol. 6, pp. 1-12, 2009.
- [20] S. D. Emami, P. Hajireza, F. Abd-Rahman, H. A. Abdul-Rahsid, H. Ahmad and S. W. Harun, "Wide-Band Hybrid Amplifier Operating in S-Band Region," *Prog. Electromagn. Res. C.*, vol. 102, pp. 301-313, 2010.
- [21] E. Snoeks, P. G. Kik and A. Polman, "Concentration Quenching in Erbium Implanted Alkali Silicate Glass," *Opt. Mater.*, vol. 5, p. 159, 1996.
- [22] D. M. Gill, L. McCaughan and J. C. Wright, "Spectroscopic Site Determinations in Erbium-Doped Lithium Niobate," *Phys. Rev. B*, vol. 53, p. 2334, 1996.
- [23] H. Ahmad, M. C. Paul, N. A. Awang, S. W. Harun, M. Pal and K. Thambiratnam, "Four-Wave-Mixing in Zirconia-Yttria-Aluminum Erbium," *J. Europ. Opt. Soc. Rap. Public.*, vol. 7, pp. 12011-1 - 12011-8, 2012.

- [24] M. C. Paul, S. W. Harun, N. A. D. Huri, A. Hamzah, S. Das, M. Pal, S. K. Bhadra, H. Ahmad, S. Yoo, M. P. Kalita, A. J. Boyland and J. K. Sahu, "Performance comparison of Zr-based and Bi-based erbium-doped fibre amplifiers," *Opt. Lett.*, vol. 35, pp. 2882-2884, 2010.
- [25] M. C. Paul, S. K. Bhadra, S. Das, Y. Seongwoo, M. P. Kalita, A. J. Boyland and J. K. Sahu, "Study of Multichannel Amplification in Erbium-Doped Zirconia-Yttria-Alumino-Silicate Fibre," *J. Lightwavav. Technol.*, vol. 29, pp. 2109-2115, 15 July 2011.
- [26] J. R. Armitage, "Spectral Dependence of the Small-Signal Gain around 1.5 μ m in Erbium Doped Silica Fibre Amplifiers," *J. Quantum Electron.*, vol. 26, pp. 423-425, 1990.
- [27] B. Pedersen, A. Bjarklev, J. H. Povlsen, K. Dybal and C. C. Larsen, "The design of erbium-doped fibre amplifiers," *J. Lightwav. Technol.*, vol. 9, pp. 1105-1112, 1991.
- [28] J. Yang, S. Dai, Y. Zhou, L. Wen, L. Hu and Z. Jiang, "Spectroscopic Properties and Thermal Stability of Erbium-Doped Bismuth-Based Glass for Optical Amplifier," *App. Phys*, vol. 93, pp. 977-983, 2003.
- [29] P. Peterka, B. Faure, W. Blanc, M. Karasek and B. Dussardier, "Theoretical Modelling of S-band Thulium-Doped Silica Fibre Amplifiers," *Opt. and Quant. Electron.*, vol. 36, pp. 201-212, 2004.
- [30] K. Kikuchi and C. Lorattanasane, "Design of Highly Efficient Four-Wave-Mixing Devices using Optical Fibres," *Photon. Technol. Lett.*, vol. 6, pp. 992-994, 1994.
- [31] O. Aso, A. Shin-Ichi, T. Yagi, M. Tadakuma, Y. Suzuki and S. Namiki, "Broadband Four-Wave Mixing Generation in Short Optical Fibres," *Electron. Lett.*, vol. 36, pp. 709-711, 2000.
- [32] J. Clowes, "Next Generation Light Sources for Biomedical Applications," *Opt. Photonics News*, vol. 3, pp. 36-38, 2011.
- [33] L. Shah and M. E. Fermann, "High Power Femtosecond Fibre Chirped Pulse Amplification System for High Speed Micromachining," *J. Las. Micro/Nanoengineering*, vol. 1, pp. 176-180, 2006.
- [34] H. Ohta, S. Nogiwa, N. A. Oda and H. Chiba, "Highly Sensitive Optical Sampling System using Timing-Jitter-Reduced Gain-Switched Optical Pulse," *Electronics Letters*, vol. 33, no. 25, pp. 2142-2143, 1997.

- [35] T. R. Schibli, K. Minoshima, F. L. Hong, H. Inaba, A. Onae, H. Matsumoto, I. Hartl and M. E. Fermann, "Frequency Metrology with a Turnkey All-Fibre System," *Opt. Lett.*, vol. 29, pp. 2467-2469, 2004.
- [36] M. Seitz, R. Ell, U. Morgner, T. R. Schibli, F. X. Kartner, M. J. Lederer and B. Braum, "All Optical Active Mode-locking with Non-Linear Semiconductor Modulator," *Opt. Lett.*, vol. 27, pp. 2209-2211, 2004.
- [37] K. Kieu and M. Mansuripur, "Active Q-switching of a Fibre Laser with a Microsphere Resonator," *Opt. Lett.*, vol. 31, pp. 3568- 3570, 2006.
- [38] Y. M. Chang , J. Lee, Y. M. Jhon and J. H. Lee, "Active Q-Switching in an Erbium-Doped Fibre Laser using an Ultrafast Silicon-Based Variable optical Attenuator," *Opt. Expr.*, vol. 19, no. 27, pp. 26911-26916, 2011.
- [39] E. A. Kuzin, B. I. Escamilla, D. E. Garcia-Gomez and J. W. Haus, "Fibre Laser Mode Locked by a Sagnac Interferometer with Non-Linear Polarization Rotation," *Opt. Lett.*, vol. 26, pp. 1559-1561, 2001.
- [40] O. Okhotnikov, A. Grudinin and M. Pessa, "Ultra-fast fibre laser systems based on SESAM technology: New horizons and applications," *New J. Phys.*, vol. 6, p. 177, 2004.
- [41] G. Steinmeyer, D. H. Sutter, L. Gallmann, N. Matuschek and U. Keller, "Frontiers in ultrashort pulse generation: Pushing the limits in linear and nonlinear optics," *Science*, vol. 286, pp. 1507-1512, 1999.
- [42] Z. Sun, T. Hasan, F. Torrisi, D. Popa, G. Privitera, F. Wang, F. Bonaccorso, D. M. Baski and A. C. Ferrari, "Graphene Mode-Locked Ultrafast Laser," *ACS Nano*, vol. 4, pp. 803-810, 2010.
- [43] F. Bonaccorso, Z. Sun, T. Hasan and A. C. Ferrari, "Graphene Photonics and Optoelectronics," *Nat. Photon.*, vol. 4, pp. 611-622, 2010.
- [44] L. P. Davila, S. H. Risbud and J. F. Shackelford, "Quartz and Silicas," in *Ceramic and Glass Materials: Structure, Properties and Processing*, J. F. Shackelford and R. H. Doremus, Eds., New York, Springer, 2008, pp. 71-80.
- [45] Y. Waseda and K. Sugiyama, "Structural Characterization of Oxide Materials by the Anomalous X-Ray Scattering Method," *Bulletin on the Institute of Chemical Research, Kyoto University*, vol. 72, pp. 286-304, 1994.

- [46] M. C. Teich and B. E. A. Saleh, Fibre Optics, in Fundamentals of Photonics, New York, New York: John Wiley & Sons, Inc., 2001.
- [47] J. M. Senior, Optical Fibre Communications: Principles and Practice, New Jersey: Pearson Education, 2009.
- [48] W. H. Zachariasen, "The Atomic Arrangement of Glass," *J. Amer. Chem. Soc.*, vol. 54, pp. 3841-3851, 1932.
- [49] J. Laegsgaard, "Dissolution of Rare-Earth Clusters in SiO₂ by Al Codoping: A Microscopic Model," *Phys. Rev. B*, vol. 65, pp. 174114-1, 2002.
- [50] P. Barua, E. H. Sekiya, K. Saito and A. J. Ikushima, "Influences of Yb³⁺ Ion Concentration on the Spectroscopic Properties of Silica Glass," *J. Non-Cryst. Solids.*, vol. 354, pp. 4760-4764, 2008.
- [51] K. Arai, H. Namikawa, K. Kumata, T. Honda, Y. Ishii and T. Handa, "Aluminum or Phosphorous Co-Doping Effects on the Fluorescence and Structural Properties of Neodymium-Doped Silica Glass," *J. Appl. Phys.*, vol. 59, pp. 3430-3436, 1986.
- [52] K. Oh and U.-C. Paek, Silica Optical Fibre Technology for Devices and Components: Design, Fabrication, and International Standards, Hoboken, New York: John Wiley & Sons, 2012.
- [53] H. J. Dutton, IBM Redbook: Understanding Optical Communications, IBM, 1998.
- [54] J. B. MacChesney, P. B. O'Conner and H. M. Presby, "A New Technique for the Preparation of Low-Loss and Graded-Index Optical Fibres," *IEEE Proc.*, vol. 62, no. 9, pp. 1280-1281, 1974.
- [55] P. C. Schultz, "Fabrication of Optical Waveguides by the Outside Vapor Deposition Process," *Proc. IEEE*, vol. 8, pp. 1187-1190, 1980.
- [56] T. Izawa and N. Inagaki, "Materials and Processes for Fibre Preform Fabrication - Vapor-Phase Axial Deposition," *IEEE Proc.*, vol. 68, pp. 1184-1187, 1980.
- [57] P. Geittner, P. B. O'Conner and H. M. Presby, "A New Technique for the Preparation of Low-Loss and Graded Index Optical Fibres," *Proc. IEEE*, vol. 62, pp. 1280-1281, 1974.
- [58] S. Ungar, Fibre Optics: Theory and Applications, New York: John Wiley & Sons, 1990.

- [59] V. Majer, J. Sedlbauer and R. H. Wood, "Calculation of standard thermodynamic properties of aqueous electrolytes and nonelectrolytes," in *Aqueous Systems at Elevated Temperatures and Pressures*, Elsevier, 2004, pp. 99-147.
- [60] C. Zhao, O. Richard, H. Bender, M. Caymax, S. De Gendt, M. Heyns, E. Young, G. Roebben, O. Van der Biest and S. Haukka, "Miscibility of amorphous $\text{ZrO}_2\text{-Al}_2\text{O}_3$ binary alloy," *Appl. Phys. Lett.*, vol. 80, pp. 2374-2376, 4 September 2002.
- [61] M. J. Weber, "Lanthanide and Actinide Chemistry and Spectroscopy," in *Lanthanide and Actinide Lasers*, Washington, American Chemical Society, 1980, pp. 275-311.
- [62] S. L. L. Rao, G. Ramadevudu, M. Shareefuddin, A. Hameed, M. N. Charry and M. L. Rao, "Optical Properties of Alkaline Earth Borate Glasses," *Int. J. Eng., Sci. and Technol.*, vol. 4, pp. 25-35, 2012.
- [63] E. Desurvire, *Erbium-doped Fibre Amplifiers Principles and Applications*, New York: John Wiley & Sons, Inc., 1994.
- [64] D. A. Chapman, "Erbium-doped Fibre Amplifiers: The Latest Revolution in Optical Communications," *Electron. Commun. Eng.*, vol. 6, pp. 59-67, 1994.
- [65] A. Ghatak, *Optics*, New Dehli: Tata McGraw-Hill Publishing Company Ltd, 2008.
- [66] B. Xia, D. Pudo and L. R. Chen, "Comparison of the Static and Dynamic Properties of Single- and Double-Pass Partially Gain-Clamped Two-Stage L-Band EDFAs," *Photon. Technol. Lett.*, vol. 15, pp. 519-521, 2003.
- [67] P. C. Becker, N. A. Olsson and J. R. Simpson, *Erbium-Doped Fibre Amplifiers: Fundamentals and Technology*, San Diego: Academic Press, 1997.
- [68] D. Derickson, *Fibre Optic Test and Measurement*, New Jersey: Prentice-Hall, 1998.
- [69] G.-I. Kweon, "Noise Figure of Optical Ampli," *J. Kor. Phys. Soc.*, vol. 41, pp. 617-628, 2002.
- [70] C. R. Giles and E. Desurvire, "Propagation of Signal and Noise in Concatenated Erbium-Doped Fibre Optical Amplifiers," *J. Lightwav. Technol.*, vol. 9, pp. 147-154, 1991.
- [71] M. J. F. Digonnet, *Rare-Earth-Doped Fibre Lasers and Amplifiers*, 2nd Ed., New York: Marcel Dekker, 2001.

- [72] S. W. Harun, P. Poopalan and H. Ahmad, "Gain Enhancement in L-Band EDFA through a Double-Pass Technique," *Photon. Technol. Lett.*, vol. 14, pp. 296-297, 2002.
- [73] D. K. Mynbaev and L. L. Scheiner, *Fibre Optic Communications Technology*, New Jersey: Prentice-Hall, 2000.
- [74] R. I. Laming and D. N. Payne, "Noise Characteristics of Erbium-Doped Fibre Amplifier Pumped at 980nm," *Photon. Technol. Lett.*, vol. 2, pp. 418-421, 1990.
- [75] H. Masuda, K. Aida and K. Nakagawa, "Noise Figure Monitoring of a Cascaded In-Line Erbium Doped Fibre Amplifier," *Photon. Technol. Lett.*, vol. 5, pp. 1436-1438, 1993.
- [76] M. Yamada, M. Shimizu, M. Okayasu, T. Takeshita, M. Horiguchi, Y. Tachikawa and E. Sugita, "Noise Characteristics of Er³⁺-Doped Fibre Amplifier Pumped by 0.98 and 1.48 μ m Laser Diodes," *Photon. Technol. Lett.*, vol. 2, pp. 205-207, 1990.
- [77] Fibrecore Ltd., *Metrogain M12 Datasheet*, Fibrecore Ltd..
- [78] M. C. Paul, S. W. Harun, N. A. D. Huri, A. Hamzah, S. Das, M. Pal, S. K. Bhadra, H. Ahmad, S. Yoo, M. P. Kalita, A. J. Boyland and J. K. Sahu, "Wideband EDFA Based on Erbium Doped Crystalline Zirconia Yttria Alumino Silicate Fibre," *J. Lightwav. Technol.*, vol. 28, pp. 2919-2924, 2011.
- [79] C.-. C. Lee, Y.-. K. Chen and S. K. Liaw, "A Wavelength-Switchable Single-Longitudinal-Mode Fibre Laser with Passive Multiple Ring Cavity and its Applications for Video Transmission," *Opt. Lett.*, vol. 5, pp. 358-360, 1998.
- [80] F. Bos, "Versatile High-Power Single-Longitudinal-Mode Pulsed Dye Laser," *Appl. Opt.*, vol. 10, pp. 1886-1890, 1981.
- [81] T. T. Basiev, A. G. Papashvilli, V. V. Federov, S. V. Vassiliev and W. Gellermann, "Single-Longitudinal-Mode Pulsed LiF: Color-Center Laser for High Resolution Spectroscopy," *Las. Phys.*, vol. 14, pp. 23-29, 2004.
- [82] S. Baunel, O. Brox, J. Kreissl, G. Sahin and B. Sartorius, "Optical Microwave Source," *Electron. Lett.*, vol. 7, pp. 334-335, 2002.
- [83] J. Zhang, C.-. Y. Yue, G. W. Schim, W. R. L. Cements and J. W. Y. Lit, "Stable Single-Mode Compound Ring Erbium-Doped Fibre Laser," *J. Lightwav. Technol.*, vol. 14, pp. 104-109, 1996.

- [84] W. Liu, M. Jiang, D. Chen and S. He, "Dual-Wavelength Single-Longitudinal-Mode Polarization-Maintaining Fibre Laser and Its Application in Microwave Generation," *J. Lightwav. Technol.*, vol. 20, pp. 4455-4459, 2009.
- [85] C. H. Yeh, T. T. Huang, H. C. Chien, C. H. Ko and S. Chi, "Tunable S-band Erbium Doped Triple-Ring Laser with Single-Longitudinal-Mode Operation," *Opt. Expr.*, vol. 2, pp. 382-386, 2007.
- [86] K. Zhang and J. U. Kang, "C-band Wavelength-Swept, Single-Longitudinal-Mode Erbium-Doped Fibre Ring Laser," *Opt. Expr.*, vol. 16, pp. 14173-14179, 2008.
- [87] S. S. Chong, H. Ahmad, M. Z. Zulkifli, A. A. Latif, W. Y. Chong and S. W. Harun, "Synchronous Tunable Wavelength Spacing Dual-Wavelength SOA Fibre Ring laser using Fibre Bragg Grating Pair in a Hybrid Tuning Package," *Opt. Comm.*, vol. 285, pp. 1326-1330, 2012.
- [88] L. G. L. Wagenar, M. L. Povinelli, A. G. Green, P.P. Mitra, J. B. Stark and P. B. Littlewood, "The effect of propagating nonlinearities on the information capacity of WDM optical fibre systems: Cross-phase modulation and four-wave-mixing," *Physica, D*, vol. 189, pp. 81-99, 15 Feb 2004.
- [89] M. Wu and W. I. Way, "Fibre nonlinearity limitations in ultra-dense WDM systems," *J. Lightwav. Technol.*, vol. 22, pp. 1483-1498, Jun 2004.
- [90] J. Toulouse, "Optical Nonlinearities in Fibres: Review, Recent Examples, and Systems Applications," *J. Lightwav. Technol.*, vol. 23, pp. 3625-3641, Nov 2005.
- [91] B. B. Tiwari, V. Prakash, V. Tripathi and N. Malaviya, "Nonlinear effects in optical fibre transmission system," *IETE Technol. Rev.*, vol. 16, pp. 461-479, Sep-Dec 1999.
- [92] E.-. H. Lee, K. H. Kim and H. K. Lee, "Nonlinear effects in optical fibre: Advantages and disadvantages for high capacity all-optical communication application," *Opt. and Quant. Electron.*, vol. 34, pp. 1167-1174, Dec 2002.
- [93] R. Boyd, *Non Linear Optics*, San Diego, California: Academic Press, 1992.
- [94] G. P. Agrawal, *Nonlinear Fibre Optics*, 2nd ed., New York: Academic Press, 1995, pp. 322-324.
- [95] R. L. Carmen, R. Y. Chiao and P. L. Kelley, "Observation of Degenerate Stimulated Four-Photon Interaction and Four-Wave Parametric Amplification," *Phys. Rev. Lett.*, vol. 17, no. 26, pp. 1281-1283, 1966.

- [96] K. O. Hill, D. C. Johnson, B. S. Kawasaki and R. I. MacDonald, "CW Three-Wave Mixing in Single-Mode Fibres," *J. Appl. Phys.*, vol. 49, pp. 5098-5106, 1978.
- [97] N. Shibata, R. P. Braun and R. G. Warrts, "Phase-Mismatch Dependence of Efficiency of Wave Generation through Four-Wave Mixing in a Singlemode Fibre," *J. Quant. Electron.*, Vols. QE-23, pp. 1205-1211, 1987.
- [98] D. Popa, Z. Sun, T. Hasan, F. Torrisi, F. Wang and A. C. Ferrari, "Graphene Q-switched, tunable fibre laser," *Appl. Phys. Lett.*, vol. 98, p. 073106, 2011.
- [99] R. J. Williams, N. Janovic, G. D. Marshall and M. J. Whitford, "All-optical, actively Q-switched fibre laser," *Opt. Expr.*, vol. 18, pp. 7714-7723, 2010.
- [100] W. -J. Cao, H. -Y. Wang, A. -P. Luo, Z. -C. Luo and W. -C. Xu, "Graphene-based, 50 nm wide-band tunable passively Q-switched fibre laser," *Las. Phys. Lett.*, vol. 9, pp. 54-58, 2011.
- [101] M. L. Siniaeva, M. N. Siniavsky, V. P. Pashinin, A. A. Mamedov, V. I. Konov and V. V. Kononenko, "Laser ablation of dental materials using a microsecond Nd:YAG laser," *Las. Phys.*, vol. 19, pp. 1056-1060, 2009.
- [102] H. Shangguan, L. W. Casperson, A. Shearin and S. A. Prahl, "Drug Delivery with Microsecond Laser Pulses into Gelatin," *Appl. Opt.*, vol. 35, pp. 3347-3357, 1996.
- [103] L. E. Hargrove, R. L. Fork and M. A. Pollack, "Locking of He-Ne laser modes induced by synchronizing intracavity modulation," *Appl. Phys. Lett.*, vol. 5, pp. 4-5, 1 July 1964.
- [104] A. J. DeMaria, W. H. Glenn, M. J. Brienza and M. E. Mack, "Picosecond laser pulses," *Proceedings of the IEEE*, vol. 57, pp. 2-25, Jan 1969.
- [105] C. V. Shank and E. P. Ippen, "Subpicosecond kilowatt pulses from a mode locked cw dye laser," *Appl. Phys. Lett.*, vol. 24, pp. 373-375, 1974.
- [106] W. T. Silvfast, "Selected papers on fundamentals of lasers," *SPIE Milestone Series*, vol. MS 70, pp. 509-511, 1993.
- [107] J. C. Diels and W. Rudolph, *Ultrashort Laser Pulse Phenomena*, Massachusetts: Academic Press, 2006.
- [108] M. T. Asaki, C. P. Huang, D. Garvey , J. Zhou, H. Kapteyn and M. M. Murnane, "Generation of 11 fs pulses from a self-mode locked Ti:Sapphire laser," *Opt. Lett.*, vol. 18, pp. 977-979, 1993.

- [109] A. Stingl, C. Spielmann, F. Krausz and R. Szipocs, "Generation of 11 fs pulses from a Ti:Sapphire laser without the use of prisms," *Opt. Lett.*, vol. 19, pp. 204-206, 1994.
- [110] J. Dawson, M. Messerly and J. An, "Fibre Laser Replacement for Short Pulse Ti:Sapphire Oscillators – Scalable Mode Locking to Record Pulse Energies," Lawrence Livermore National Laboratories, Livermore, 2006.
- [111] J. J. Degnan, "Theory of the optimally coupled Q-switched laser," *J. Quant. Electron.*, vol. 25, p. 1890–1901, 1989.
- [112] R. Courant and D. Hilbert, *Methods of Mathematical Physics*, New York: Interscience, 1953..
- [113] S. Harris and R. Targ, "FM Oscillation of the He-Ne Laser," *Applied Physics Letters*, vol. 5, no. 10, pp. 202-205, 1964.
- [114] E. Ippen, C. Shank and A. Dienes, "Passive Mode Locking of the CW Dye Laser," *Applied Physics Letters*, vol. 21, no. 8, pp. 348-350, 1972.
- [115] L. F. Mollenauer and R. H. Stolen, "The Soliton Laser," *Optics Letters*, vol. 9, no. 1, pp. 13-15, 1984.
- [116] G. Geister and R. Ulrich, "Neodymium-Fibre Laser with Integrated-Optic Mode Locker," *Optics Communications*, vol. 68, no. 3, pp. 187-189, 1988.
- [117] M. I. Dzhibladze, Z. G. Ésiashvili, E. S. Teplitskiĭ, S. K. Isaev and V. R. Sagaradze, "Mode Locking in a Fibre Laser," *Soviet Journal of Quantum Electronics*, vol. 13, no. 2, p. 245, 1983.
- [118] J. Kafka, T. Baer and D. E. Hall, "Mode-Locked Erbium-Doped Fibre Laser with Soliton Pulse Shaping," *Optics Letters*, vol. 14, no. 22, pp. 1269-1271, 1988.
- [119] M. Hofer, M. Ober, F. Haberl and M. Fermann, "Characterization of Ultrashort Pulse Formation in Passively Mode-Locked Fibre Lasers," *Quantum Electronics, IEEE J. of*, vol. 28, no. 3, pp. 720-728, 1992.
- [120] U. Keller, D. Miller, G. Boyd, T. Chiu, F. Ferguson and M. Asom, "Solid-State Low-Loss Intracavity Saturable Absorber for Nd: YLF Lasers: an Antiresonant Semiconductor Fabry–Perot Saturable Absorber," *Optics Letters*, vol. 17, no. 7, pp. 505-507, 1992.
- [121] K. Tamura, H. Haus and E. Ippen, "Self-Starting Additive Pulse Mode-Locked Erbium Fibre Ring Laser," *Electronics Letters*, vol. 28, no. 24, pp. 2226-2228, 1992.

- [122] C. Hirlimann, "Pulsed Optics," in *Femtosecond Laser Pulses: Principles and Experiments*, C. Rullière, Ed., New York, New York: Springer, 2005, pp. 25-56.
- [123] T. Hakulinen and O. G. Okhotnikov, "8 ns Fibre Laser Q-Switched by the Resonant Saturable Absorber Mirror," *Opt. Lett.*, vol. 21, pp. 204-209, 2007.
- [124] R. L. Fork, B. I. Greene and C. V. Shank, "Generation of Optical Pulses Shorter than 0.1 psec by Colliding Pulse Mode-Locking," *Appl. Phys. Lett.*, vol. 38, pp. 617-619, 1981.
- [125] Y. Kalisky, A. Ben-Amar Baranga, Y. Shimony and M. R. Kokta, "Cr⁴⁺ Doped Garnets: Novel Laser Materials and Non-Linear Saturable Absorbers," *Opt. Mater.*, vol. 8, pp. 129-134, 1997.
- [126] H. A. Haus, "Mode-Locking of lasers," *IEEE Select. Topics in Quant. Electron.*, vol. 6, pp. 1173-1185, 2000.
- [127] K. S. Novoselov, A. K. Geim, S. V. Morozov, D. Jiang, Y. Zhang, S. V. Dubonos, I. V. Grigorieva and A. A. Firsov, "Electric Field Effect in Atomically Thin Carbon Films," *Science*, vol. 306, pp. 666-669, 2004.
- [128] R. R. Nair, P. Blake, A. N. Grigorenko, K. S. Novoselov, T. J. Booth, T. Stauber, N. M. R. Peres and A. K. Geim, "Fine Structure Constant Defines Visual Transparency of Graphene," *Science*, vol. 298, pp. 2361-2366, 2002.
- [129] A. B. Kuzmenko, E. v. Heumen, F. Carbone and D. v. d. Marel, "Universal Optical Conductance of Graphite," *Phys. Rev. Lett.*, vol. 100, pp. 117401-117405, 2008.
- [130] A. C. Ferrari, J. C. Meyer, V. Scardaci, C. Casiraghi, M. Lazzeri, F. Mauri, S. Piscanec, D. Jiang, K. S. Novoselov, S. Roth and A. K. Geim, "Raman Spectrum of Graphene and Graphene Layers," *Phys. Rev. Lett.*, vol. 97, p. 4, 2006.
- [131] D. Graf, F. Molitor, K. Ensslin, C. Stampfer, A. Jungen, C. Hierold and L. Wirtz, "Spatially Resolved Raman Spectroscopy of Single and Few Layer Graphene," *Nano Lett.*, vol. 7, pp. 238-242, 2007.
- [132] R. Saito, G. Dresselhaus and M. S. Dresselhaus, "Physical Properties of Carbon Nanotubes," *Imperial College Press, London*, vol. 272, 1993.
- [133] R. Saito, G. Dresselhaus and M. S. Dresselhaus, "Triagonal Warping Effect of Carbon Nanotubes," *Phys. Rev. B*, vol. 61, pp. 2981-2990, 2000.

- [134] H. Kataura, Y. Kumazawa, Y. Maniwa and I. Umeza, "Optical Properties of Single-Wall Carbon Nanotubes," *Synt. Met.*, vol. 103, pp. 2555-2558, 1999.
- [135] S. M. Bachilo, M. S. Strano, C. Kittrell, R. H. Hauge, R. E. Smalley and R. B. Weisman, "Structure-Assigned Optical Spectra of Single-Walled Carbon Nanotubes," *Science*, vol. 298, pp. 2361-2366, 2002.
- [136] A. G. Rozhin, Y. Sakakibara, S. Namiki, M. Tokumoto, H. Kataura and Y. Achiba, "Sub-200-fs pulsed erbium-doped fibre laser using a carbon nanotube-polyvinylalcohol mode locker," *Appl. Phys. Lett.*, vol. 88, no. 5, pp. 051118-1 - 051118-3, 2006.
- [137] W. B. Cho, J. H. Yim, S. Y. Choi, S. Lee, U. Griebner, V. Petrov and F. Rotermund, "Mode-locked self-starting Cr:forsterite laser using a single-walled carbon nanotube saturable absorber," *Opt. Lett.*, vol. 33, pp. 2449-2451, 2008.
- [138] S. Y. Set, H. Yaguchi, M. Jablonski, Y. Tanaka, Y. Sakakibara, A. G. Rozhin, M. Tokumoto, H. Kataura, Y. Achiba and K. Kikuchi, "A Noise Suppressing Saturable Absorber at 1550nm Based on Carbon Nanotube Technology," in *Optical Fibre Communication Conference: Novel Signal Processing Devices (FL)*, Atlanta, 2003.
- [139] K. Cheng, S. Z. Zhao, K. J. Yang, G. Q. Li, G. Zhang, L. H. Zheng, F. Wu, L. B. Su and J. Xu, "540 nm diode-pumped passively Nd:SSO/KTP green laser with a single-walled carbon nanotube saturable absorber," *Las. Phys. Lett.*, vol. 10, p. 055807, 2013.
- [140] Z. Sun, T. Hasan, F. Wang, A. G. Rozhin, I. H. White and A. C. Ferrari, "Ultrafast Stretched-Pulse Fibre Laser Mode-Locked by Carbon Nanotubes," *Nano Res.*, vol. 3, pp. 404-411, 2010.
- [141] J. H. Im, S. Y. Choi, F. Rotermund and D.-I. Yeom, "All-fibre Er-doped dissipative soliton laser based on evanescent field interaction with carbon nanotube saturable absorber," *Opt. Expr.*, vol. 18, pp. 22141-22146, 2010.
- [142] M. Park, H. Kim, J. P. Youngblood, S. W. Han, E. Verplogen and A. J. Hart, "Excellent dispersion of MWCNTs in PEO polymer achieved through a simple and potentially cost-effective evaporation casting," *Nanotechnology*, vol. 22, p. 415703, 2011.
- [143] M. S. Dresselhaus, G. Dresselhaus, R. Saito and A. Jorio, "Raman spectroscopy of carbon nanotubes," *Phys. Rep.*, vol. 409, pp. 47-99, 2005.
- [144] A. Jorio, G. Dresselhaus and M. S. Dresselhaus, *Carbon Nanotubes: Advanced Topics in the Synthesis, Structure, Properties and Applications*, New York: Springer, 2008.

- [145] M. L. Dennis and I. N. Duling, "Experimental study of sideband generation in femtosecond fibre laser," *IEEE Quant. Electron.*, vol. 30, pp. 1469-1477, 1994.
- [146] G. Sobon, J. Sotor and K. M. Abramski, "All-polarization maintaining femtosecond Er-doped fibre laser mode-locked by graphene saturable absorber," *Las. Phys. Lett.*, vol. 9, pp. 581-586, 2012.
- [147] C. Honninger, R. Paschotta, F. M. Genoud, M. Moser and U. Keller, "Q-switching stability limits of continuous wave passive mode locking," *J. Optic. Soc. of Amer. B*, vol. 16, pp. 45-56, 1999.
- [148] F. Wang, A. G. Rozhin, V. Scardaci, Z. Sun, F. Hennrich, I. H. White, W. I. Milne and A. C. Ferrari, "Wideband-tuneable, nano-tube mode-locked fibre laser," *Nat. Nanotechnol.*, vol. 3, pp. 738-742, 2008.
- [149] U. Keller, K. J. Weingarten, F. X. Kartner, D. Kopf, B. Braun, I. D. Jung, R. Fluck, C. Honninger, N. Matuschek and J. Ausderau, "Semiconductor saturable absorber mirrors (SESAMs) for femtosecond to nanosecond pulse generation in solid-state lasers," *IEEE J. Select. Topics Quant. Electron.*, vol. 2, pp. 435-453, 1996.
- [150] M. Wasfi, "Optical Fibre Amplifiers – Review," *International Journal of Communications Networks and Information Security*, vol. 1, pp. 42-47, 2009.
- [151] S. Christensen, G. Frith and B. Samson, "Developments in thulium-doped fibre lasers offer higher powers," 11 July 2008. [Online]. Available: <http://spie.org/x26003.xml>.
- [152] J. A. Harrington, *Infrared Fibres and Their Applications*, New Jersey: Pearson Education, Inc., 2004.
- [153] J. Clowes, "Next generation light sources for biomedical applications," *Opt. Photonics News*, vol. 3, pp. 36-38, 2008.
- [154] Y. Jeong, A. J. Boyland, J. K. Sahu, S. Chung, J. Nilsson and D. N. Payne, "Multi-kilowatt Single-mode Ytterbium-doped Large-core Fibre Laser," *J. Opt. Soc. of Kor.*, vol. 13, pp. 416-422, 2009.
- [155] S. Jiang, B.-. C. Hwang, T. Luo, K. Seneschal, F. Smektala, S. Honkanen, J. Lucas and N. Peyghambarian, "Net Gain of 15.5 dB from a 5.1 cm-Long Er³⁺-Doped Phosphate Glass Fibre," in *Optical Fibre Communications Conference Proceedings (IEEE)*, 2000.

- [156] H. Ohta, S. Nogiwa, N. A. Oda and H. Chiba, "Highly sensitive optical sampling system using timing-jitter-reduced gain-switched optical pulse," *Electron. Lett.*, vol. 33, pp. 2142-2143, 1997.
- [157] J. Swiderski, A. Zajac, P. Konieczny and M. Skorczakowski, "Numerical model of a Q-switched double-clad fibre laser," *Opt. Expr.*, vol. 12, pp. 3554-3559, 2004.
- [158] D. R. Zimmerman and L. H. Spiekman, "Amplifiers for the Masses: EDFA, EDWA, and SOA Amplets for Metro and Access Applications," *J. Lightwav. Technol.*, vol. 22, pp. 63-70, 2004.

APPENDIX 1

Appendix Table 1 provides the optical losses induced by various transition metal impurities in optical silica fibres.

Appendix Table 1: Optical losses induced in silica optical fibres by transition metal impurities

Impurity	Peak Absorption Wavelength (nm)	Optical Loss (dB/km) per Part per Billion
Cr^{3+}	625	1.60
Co^{2+}	685	0.10
Cu^{2+}	850	1.10
Fe^{2+}	1100	0.68
Fe^{3+}	400	0.15
Ni^{2+}	650	0.10
Mn^{3+}	460	0.20
V^{4+}	725	2.70

APPENDIX 2

The following are the publications that have resulted from this work.

Book Chapters

1. Chapter 2: Nano-Engineered Glass-Based Erbium Doped Optical Fibers for Study of Multi-Channel Amplification and Four-Wave Mixing Phenomena, M. C. Paul, M. Pal, K. Thambiratnam, S. W. Harun, N. A. Awang, S. Das, S. K. Badhra, H. Ahmad and J. K. Sahu. Rare Earths: New Research (Chemistry Research and Applications: Materials Science and Technologies) (Zhaosen Liu (Editor)) Nova Science Publishers Inc. (1 July 2013, Hauppauge, New York, No. of pages: 289, ISBN-10: 162618996X).

Publications in ISI Journals

1. H. Ahmad, K. Thambiratnam, N. A. Awang, M. H. Jemangin, and S. W. Harun, "Stable Zirconia-Erbium Doped Multiwavelength Fibre Laser by Precise Control of Polarization States," *Las. Phys. Lett.*, vol. 22, pp. 982-985, 2012.
2. H. Ahmad, M. C. Paul, N. A. Awang, S. W. Harun, M. Pal and K. Thambiratnam, "Four-Wave-Mixing in Zirconia-Yttria-Aluminum Erbium," *J. Europ. Opt. Soc. Rap. Public.*, vol. 7, pp. 12011-1 - 12011-8, 2012.
3. H. Ahmad, N. A. Awang, M. Z. Zulkifli, K. Thambiratnam, M.C. Paul, S. Das, and S.W. Harun, "Supercontinuum from Zr-EDF using Zr-EDF mode-locked fibre laser," *Las. Phys. Lett.*, vol. 9, pp. 44-49, 2012.
4. H. Ahmad, K. Thambiratnam, N. A. Awang, Z. A. Ghani and S.W. Harun, "Four-wave mixing in zirconia-erbium doped fibre – a comparison between ring and linear cavities," *Las. Phys. Lett.*, vol. 9, pp. 819-825, 2012.

5. H. Ahmad, K. Thambiratnam, M. C. Paul, A. Z. Zulkifli, Z. A. Ghani, and S. W. Harun, "Fabrication and application of zirconia-erbium doped fibres," *Opt. Mat. Expr.*, vol. 2, pp. 1690-1701, 2012.
6. H. Ahmad, A.Z. Zulkifli, K. Thambiratnam and S.W. Harun "Q-switched Zr-EDF laser using single-walled CNT/PEO polymer composite as a saturable absorber," *Opt. Mater.*, vol. 35, pp. 347-352, 2013.
7. K. Thambiratnam, H. Ahmad, , F. D. Muhammad, M. Z. Zulkifli, A. Z. Zulkifli, M. C. Paul and S. W. Harun, "Q-Switching and Mode-Locking in Highly-Doped $\text{Zr}_2\text{O}_3\text{-Al}_2\text{O}_3\text{-Er}_2\text{O}_3$ Doped Fibre Lasers using Graphene as a Saturable Absorber," *IEEE J. Select. Topics in Quant. Electron.*, vol. 20, pp. 1100108, 2013.

Proceedings / Presentations in National and International Conferences

1. H. Ahmad, K. Thambiratnam and S. W. Harun, Fabrication of Nano-Engineered Zirconia Yttria Aluminosilicate Glass Co-doped with Erbium and its Applications, 9th International Symposium on Modern Optics and Its Applications (ISMOA 2013), 24 Jun 2013 to 27 Jun 2013, Indonesian Optical Society (InOs) Physics of Magnetism and Photonics Group Institut Teknologi Bandung (International)
2. A. Zarif, H. Ahmad, K. Thambiratnam, M. C. Paul and S. W. Harun, Four-wave Mixing Effect in Zirconia-erbium Doped Fibers, International Conference on Materials for Advanced Technologies (ICMAT2013), 30 June 2013 to 5 July 2013, Materials Research Society (MRS) Singapore (International).
3. A. Z. Zulkifli, K. Thambiratnam, F. Ahmad, H. Ahmad and S. W. Harun, Single Walled CNT / PEO based Saturable Absorber with Zr-EDF for Passively Q- Switched Pulse Laser Generation, 7th Asia-Oceania Top University League on Engineering (AOTULE 2012) Student Conference, 24th to 25th November 2012, University of Malaya, Kuala Lumpur, Malaysia (Local).

Stable Zirconia–Erbium Doped Multiwavelength Fiber Laser by Precise Control of Polarization States¹

H. Ahmad^a, K. Thambiratnam^a, N. A. Awang^a, M. H. Jemangin^a, and S. W. Harun^b

^a Photonics Laboratory, Department of Physics, University of Malaya,
50603 Kuala Lumpur, Malaysia

^b Department of Electrical Engineering, Faculty of Engineering, University of Malaya,
50603 Kuala Lumpur Malaysia

e-mail: harith@um.edu.my

Received December 3, 2011; in final form, December 15, 2011; published online April 3, 2012

Abstract—A compact zirconium–erbium doped fiber (Zr-EDF) based multiwavelength fiber laser (MWFL) with stable output comb is proposed and demonstrated. The MWFL utilizes a 3 m long Zr-EDF with an erbium concentration of 3000 ppm and pumped by a 1480 nm laser diode (LD) as the active gain medium. A fiber based multimode polarization controller (PC) is used to precisely control the polarization states of the oscillating modes in the MWFL, distributing the total energy of the system among the lasing wavelengths in order to overcome the mode-suppression and mode-competition that arises from homogenous line broadening. The MWFL is capable of generating up to four lasing wavelengths with average peak powers of 0.08 dBm in the extended L-band of 1600 nm. The lasing wavelengths have a 3-dB linewidth of 0.1 and an extinction ratio of 40 dB as well as highly stable, with minimal fluctuations of less than 0.6 dB observed in the peak powers of the lasing wavelengths over a period of 1 h. The proposed system allows for the realization of a compact, cost-effective and stable erbium based MWFL capable of operating at room temperature.

DOI: 10.1134/S1054660X12050015

1. INTRODUCTION

Multiwavelength fiber lasers (MWFLs) have been the focus of substantial efforts to develop cost-effective signal sources which are compatible to existing optical fibers for a multitude of applications such as dense wavelength division multiplexing (DWDM) and optical sensor systems [1–3]. MWFLs have been explored and developed using a variety of gain media including erbium-doped fibers (EDFs) [1, 4], bismuth-doped fibers (BDFs) [5, 6] and semiconductor optical amplifiers (SOAs) [7]. Of these approaches, EDF-based MWFLs have demonstrated the highest potential for further development due their significant advantages such as low threshold power, high power conversion efficiency and compatibility with existing optical communications infrastructure as compared to other gain media [8].

However, erbium ions exhibit strong homogeneous line broadening and cross-saturation gain at room temperatures, leading to mode competition and unstable multiwavelength operation. Various techniques have been put forward to overcome this problem, including cooling the EDF in liquid nitrogen [9] or using specially designed twin-core EDFs [10]. Whilst these methods are able to overcome the mode competition and unstable multiwavelength operation EDF based MWFLs, the complexity and cost of these approaches far outweighs the benefits gained. A signif-

icantly simpler approach towards overcoming the mode suppression and mode competition in the EDF based MWFL is to precisely controlling the polarization states of the lasing wavelengths in the laser cavity [11] using a standard polarization controller (PC). This method allows for the interchange of energy between the lasing wavelengths so as to create a stabilized multiwavelength comb with uniform peak powers [11].

In this work, a compact EDF-based MWFL is demonstrated using a highly doped zirconia-erbium-doped fiber (Zr-EDF). The Zr-EDF is fabricated from a zirconia–yttria–aluminum (Zr–Al–Y) co-doped silica fiber as a ternary glass host and doped with a high erbium ion concentration of 3000 ppm [12, 13], allowing for the realization of a short-length linear gain medium with a performance comparable to that of conventional EDFs. The Zr-EDF also exhibits non-linear properties and can be used for a variety of applications such as supercontinuum generation [14], however in this work the focus of the Zr-EDF is exclusively as the linear gain medium for the proposed compact MWFL, and is used in conjunction with a PC to control the polarization states of the lasing wavelengths to provide a stable and flat output.

2. EXPERIMENTAL SETUP

The proposed MWFL consists of a 3 m long Zr-EDF in a ring configuration as shown in Fig. 1 below.

¹ The article is published in the original.

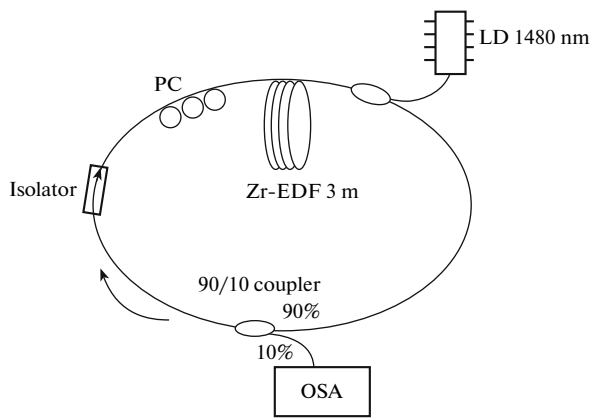


Fig. 1. Experimental setup of the proposed Zr-EDF based MWFL.

The 3 m long Zr-EDF used has a nonlinear coefficient of $7.2 \text{ W}^{-1} \text{ km}^{-1}$ and a nonlinear refractive index of $1.54 \times 10^{-19} \text{ m}^2/\text{W}$. It has an erbium concentration of 3000 ppm as well as a pump absorption rate of 14.5 dB/m at 978 nm and an effective area of the fiber is $87 \mu\text{m}^2$.

The Zr-EDF is pumped in a counter-propagating configuration by a 1480 nm laser diode (LD) coupled to the Zr-EDF using a 1480/1550 nm wavelength division multiplexer (WDM). A Polarization Controller (PC) is used to control the birefringence in the ring cavity so that the power of the output laser can be controlled and optimized, and is connected to the input of the Zr-EDF through an optical isolator with an insertion loss of 0.5 dB and an isolation of 55 dBm. The addition of the optical isolator is crucial towards

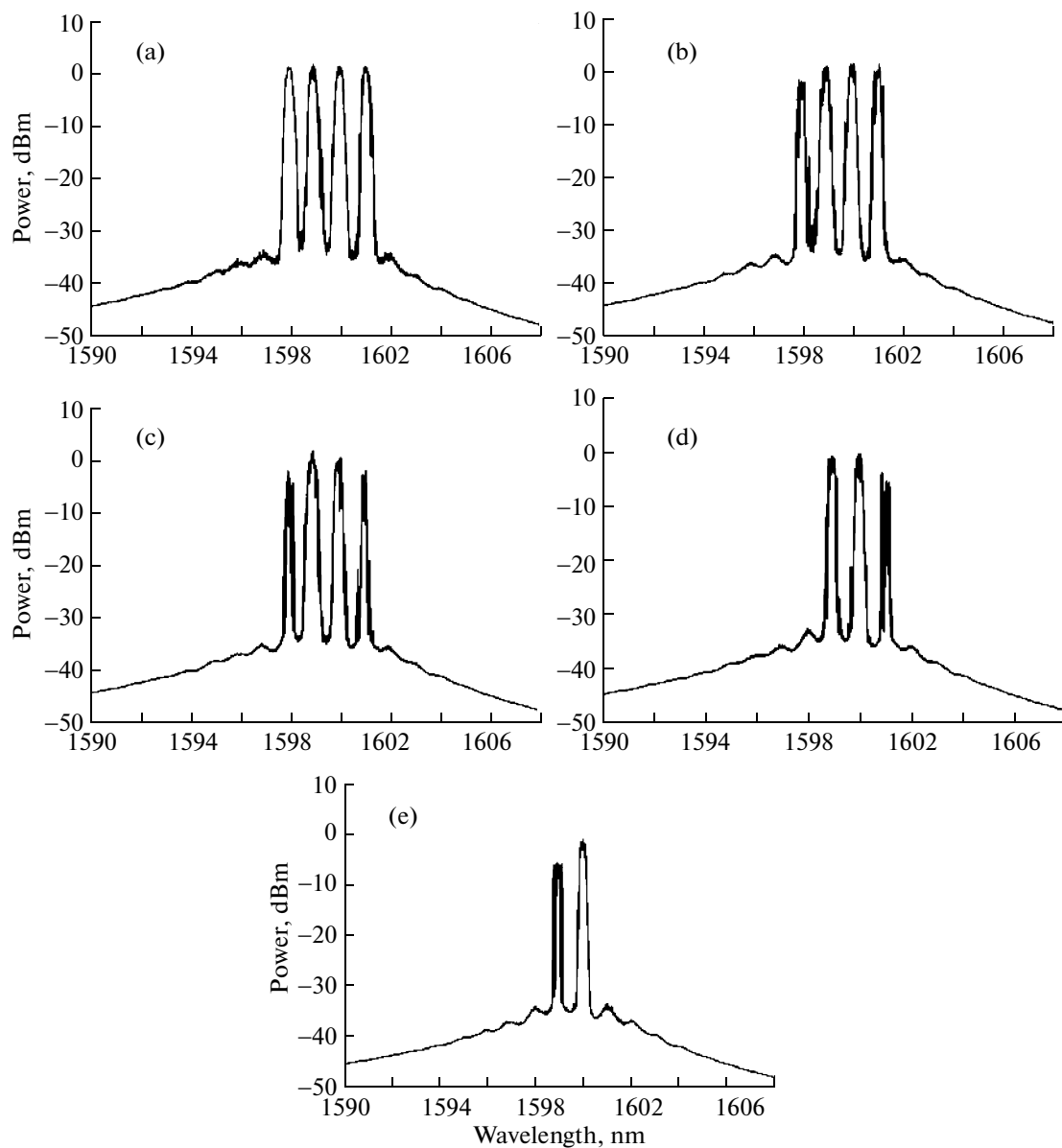


Fig. 2. Power spectra at the output of the fiber at pump power of (a) 84, (b) 71, (c) 59, (d) 46, and (e) 33 mW.

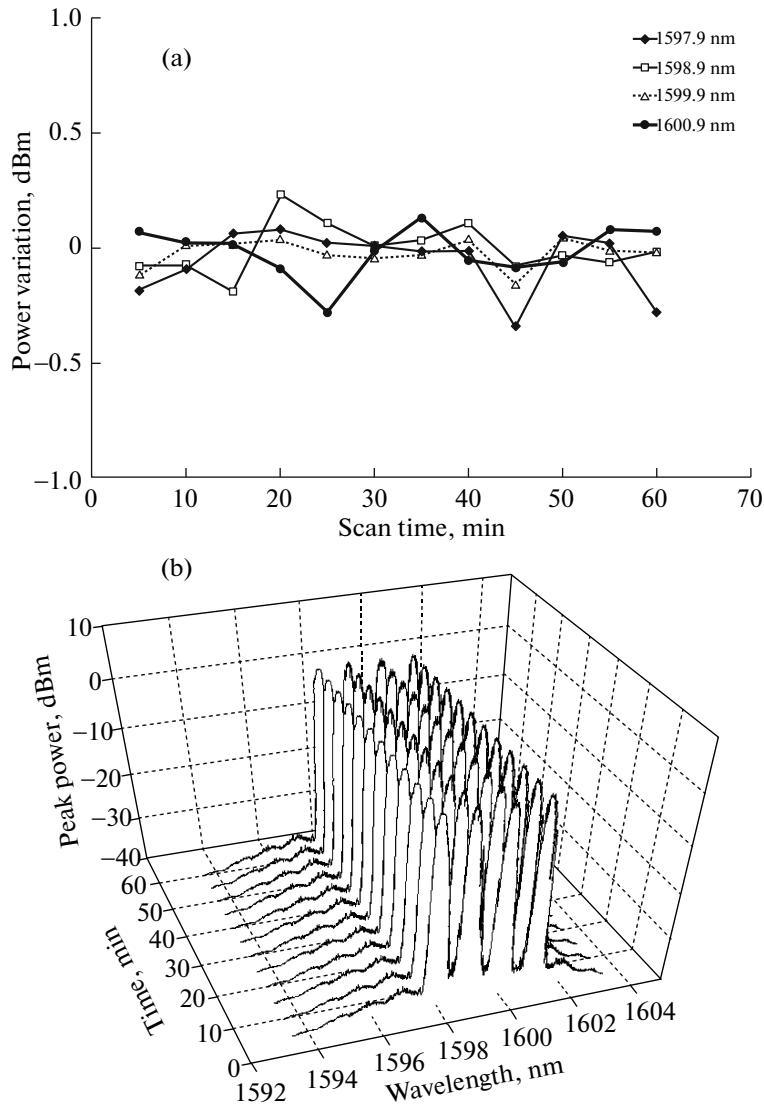


Fig. 3. (a) Repeatedly-measured output power of the quad-wavelength. (b) Repeated scanning spectrum, of the proposed multi-wavelength per minute within 1 h.

ensuring the unidirectional operation of the laser. A portion of the laser output is extracted by the 10% port of a 90 : 10 coupler and routed to an optical spectrum analyzer (OSA) with a resolution of 0.02 nm for further analysis.

3. RESULTS AND DISCUSSION

Figure 3 shows the output spectrum of the MWDL obtained at different 1480 nm LD pump powers of 84, 71, 59, 46, and 33 mW. At the highest pump power, 4 lasing wavelengths are obtained from the MWFL at approximately 1597.9, 1598.9, 1599.9, and 1600.9 nm. It can be observed that the lasing wavelengths have an almost uniform channel spacing of 1.0 nm, and an average peak power of 0.08 dBm. The generated MWFL spectrum falls in the 1600 nm region, which

constitutes the extended L-band region. The extension of the amplification bandwidth into this region, as opposed to falling within the expected C-band of 1550 nm is attributed to the suppression of excited-state absorption (ESA) and the lower cavity losses in this region [15, 16]. In typical EDF based MWFL configurations, mode-suppression and mode-competition will limit the number of lasing wavelengths present in the laser cavity of a homogenous gain medium such as the Zr-EDF [17]. However, using a multi-mode PC to change the polarization of the spatial modes in the lasing cavity allows for an interchanging of energy between the lasing modes, thereby distributing the energy evenly over several wavelengths [11]. The actual mechanism which allows for the interchange of energy is still not understood fully, and therefore it highly difficult to provide a definite

expression of the transmission functions that describe this interchange of energy. However, it is known that by controlling the polarization states, the power of the lasing wavelengths, the channel spacing between them and even the number of generated wavelengths can be controlled.

As the pump power is decreased to 71 mW, the wavelengths generated also begin to show less uniformity in power. A further reduction in the pump power to 59 mW results in the generated wavelengths showing even less uniformity in power. At a pump power of 46 mW, it can be seen that the MWFL can no longer sustain 4 lasing wavelengths, with only 3 lasing wavelengths observed. Finally, at the lowest pump power of 36 mW, only two lasing wavelengths are observed. In this regard, it can be inferred that by adjusting the PC, the energy distribution between the polarization states is adjusted such that although fewer lasing wavelengths are generated, a significantly high power level can still be maintained. The lasing wavelengths also show a uniform 3 dB bandwidth of 0.1 nm, and an extinction ratio of 40 dB at the highest pump power of 84 mW.

In addition to the generation of a multiwavelength output with a relatively uniform peak power and channel spacing, adjusting the polarization states in the ring cavity also increases the stability of the generated multiwavelength comb over time. Figure 3a shows the power fluctuation at of the multiwavelength comb at the maximum pump power of 84 mW, whilst Fig. 3b shows the repeated scan of the multiwavelength comb over a period of 1 h. From Fig. 3a, it can be seen that the output power of the generated wavelengths is very stable against time, with minimal fluctuations of less than 0.6 dB observed in the peak powers of the lasing wavelengths over a period of 1 hour. This is unlike the typical performance of EDF-based MWFLs, which are prone to suffer power instabilities arising from the cross-saturation gain of signals with different wavelengths. The same inference can also be made from Fig. 3b which shows the spectrum of the multiwavelength comb over a period of 1 hour, with the additional observation that the wavelengths of the output comb do not drift and the spacing between the lasing wavelengths remains constant as well. These results demonstrate a compact and stable EDF based MWFL capable of operating at room temperature.

4. CONCLUSIONS

A compact and stable EDF-based MWFL is demonstrated using a 3 m long highly doped Zr-EDF pumped by a 1480 nm LD and a PC to control the polarization states of the lasing wavelengths in the ring

laser cavity. The proposed MWFL is capable of generating up to four lasing wavelengths with average peak powers of 0.08 dBm in the region of the extended L-band of 1600 nm at a pump power of 84 mW. The generated wavelengths also have a 3-dB linewidth of 0.1 nm and an extinction ratio of 40 dB. The output of the MWFL is stable against time, with minimal fluctuations of less than 0.6 dB observed in the peak powers of the lasing wavelengths over a period of 1 h. The proposed setup allows the realization of a compact, cost-effective and stable EDF-based MWFL capable of operating at room temperature.

REFERENCES

1. N. Park and P. F. Wysocki, *IEEE Photon. Technol. Lett.* **8**, 1459 (1996).
2. D. Chen, *Laser Phys. Lett.* **4**, 437 (2007).
3. H. Ahmad, M. Z. Zulkifli, A. A. Latif, K. Thambiratnam, and S. W. Harun, *Laser Phys.* **19**, 2188 (2009).
4. J. Suna, J. Qiub, and D. Huanga, *Optics Comm.* **182**, 193 (2000).
5. H. Ahmad, M. Z. Zulkifli, K. Thambiratnam, S. F. Latif, and S. W. Harun, *Laser Phys. Lett.* **6**, 380 (2009).
6. S. W. Harun, R. Parvizi, S. Shahi, and H. Ahmad, *IEEE Photon. J.* **1**, 254 (2009).
7. H. Ahmad, K. Thambiratnam, A. H. Sulaiman, N. Tamchek, and S. Harun, *Laser Phys. Lett.* **5**, 726 (2008).
8. K. K. Qureshi, H. Y. Tam, W. H. Chung, and P. K. Wai, *IEEE Photon. Technol. Lett.* **17**, 1611 (2005).
9. S. Yamashita and K. Hotate, *Electron. Lett.* **32**, 1298 (1996).
10. R. I. Laming, J. D. Minelly, L. Dong, and M. N. Zervas, *Electron. Lett.* **29**, 509 (1993).
11. Z. Li, C. Lou, and Y. Gao, *Int. J. of Infr. and Millimeter Waves* **20**, 1487 (1999).
12. M. C. Paul, S. W. Harun, N. A. D. Huri, A. Hamzah, S. Das, M. Pal, S. K. Bhadra, H. Ahmad, S. Yoo, M. P. Kalita, A. J. Boyland, and J. K. Sahu, *J. of Light-wave Technol.* **28**, 2919 (2010).
13. M. Pal, M. C. Paul, S. K. Bhadra, S. Das, Y. Seongwoo, M. P. Kalita, A. J. Boyland, and J. K. Sahu, *J. of Light-wave Technol.* **29**, 2109 (2011).
14. H. Ahmad, N. A. Awang, M. Z. Zulkifli, K. Thambiratnam, M. C. Paul, S. Das, and S. W. Harun, *Laser Phys. Lett.* **9**, 44 (2012).
15. N. A. D. Huri, A. Hamzah, H. Arof, H. Ahmad, and S. W. Harun, *Laser Phys.* **21**, 202 (2011).
16. A. Hamzah, M. C. Paul, S. W. Harun, N. A. D. Huri, A. Lokman, M. Pal, S. Das, S. K. Bhadra, H. Ahmad, S. Yoo, M. P. Kalita, A. J. Boyland, and J. K. Sahu, *Laser Phys.* **21**, 176 (2011).
17. R. J. Mears, L. Reekie, I. M. Jauncey, and D. N. Payne, *Electron. Lett.* **23**, 1026 (1987).

Four-Wave-Mixing in Zirconia-Yttria-Aluminum Erbium Codoped Silica Fiber

H. Ahmad
harith@um.edu.my

Photonics Research Centre, Physics Department, University of Malaya, 50603 Kuala Lumpur, Malaysia

M. C. Paul

Fiber Optics and Photonics Division, Central Glass & Ceramic Research Institute-CSIR, Kolkata, India

N. A. Awang

Faculty of Science, Technology and Human Development, Universiti Tun Hussein Onn Malaysia, 86400 Batu Pahat, Johor

S. W. Harun

Department of Electrical Engineering, Faculty of Engineering, University of Malaya, 50603 Kuala Lumpur Malaysia

M. Pal

Fiber Optics and Photonics Division, Central Glass & Ceramic Research Institute-CSIR, Kolkata, India

K. Thambiratnam

Photonics Research Centre, Physics Department, University of Malaya, 50603 Kuala Lumpur, Malaysia

The generation and characterization of the Four-Wave-Mixing (FWM) effect in an Erbium Doped Zirconia-Yttria-Alumino Silicate Fiber (EDZF) is described. The EDZF is fabricated from a conventional silica preform by Modified Chemical Vapour Deposition (MCVD) and also solution doping to add glass modifiers and nucleating agents, with the resulting preform annealed and drawn into a fiber strand with a $125 \pm 0.5 \mu\text{m}$ diameter. A 4 m long EDZF, ZEr-B with a propagation loss of 0.68 dB/m and an erbium concentration of 3000 ppm is used to investigate the FWM effect. The FWM power levels are measured to be approximately -45 dBm at a region of 1565 nm and show good agreement with the theoretical predicted values. A non-linear coefficient of $14 \text{ W}^{-1}\text{km}^{-1}$ is also measured, along with chromatic and slope dispersion values of 28.45 ps/nm.km and 3.63 ps/nm².km, which agree with the predicted values. The fabricated ZEr-B fibre has many potential applications utilizing the FWM effect, including the generation of multi-wavelength outputs.

[DOI: <http://dx.doi.org/10.2971/jeos.2012.12011>]

Keywords: Zirconia-Erbium doped fiber, non-linear optical phenomena, four-wave-mixing

1 INTRODUCTION

Fiber Optical Amplifiers (FOAs) are a key component in realizing the deployment of long range, high-speed and large capacity communication networks [1, 2]. FOAs are able to effectively counter the attenuation and distortion of multiple signals travelling in optical transmission fibers at the same time [2] and have been widely used in Dense Wavelength Division Multiplexing (DWDM) and Optical Time Division Multiplexing (OTDM) systems. Furthermore, recent advances in technology have also opened up new possibilities for FOAs in a multitude of applications, including the generation of single and multi-wavelength outputs [3, 4], wavelength conversion [5] and wide-band spectral sources [6].

The development of in-line optical amplification was necessitated by the need to overcome the switching and processing limitations of electronic regenerators which were the dominant means of amplification at the time [7, 8]. Initially, research efforts focused on methods such as Raman amplification [9, 10] Semiconductor Optical Amplifiers (SOAs) [11, 12] and Fiber Optic Parametrical Amplifiers (FOPAs) [13, 14] to amplify optical signals, but the cost and complexity of these methods made them commercially impractical. It was not until the early 1990s that a low-cost and commercially viable

alternative was developed in the form of the Erbium Doped Fiber Amplifier (EDFA) [1]. EDFAs are capable of providing a wide amplification bandwidth and can be easily spliced to conventional silica fibers, making them the backbone of many optical networks worldwide.

Current research efforts have now focused towards the development of compact, high performance and low cost EDFAs. In this regard, new fibres such as thulium, phosphorus, tellurite, bismuth and photonic crystal fibres [15]-[20] have been explored to increase the erbium ion concentration in the fiber without detrimental effects such as concentration quenching [21] and cluster formation [22]. However, these new fibres are not without their drawbacks, for instance thulium and bismuth based fibers that cannot be spliced easily to conventional SMFs. In this regard, Zirconia has been seen as a highly promising candidate in the development of compact, high erbium concentration EDFAs. Zirconia or ZrO_2 ions co-doped in silica fibers possess a high index of refraction that has been reported of around 1.45 over the visible and near infrared spectrum [23, 24]. As such, ZrO_2 ions tend to exhibit wide emission and absorption bandwidths, as predicted by the Fuchtbauer-Ladenberg relationship [25, 26] and JuddOfelt theory [27, 28]

and therefore can amplify more DWDM channels than lower index materials. Furthermore, zirconia has excellent mechanical strength and is chemical corrosion resistance as well as being non-hygroscopic, is easily spliced to SMFs and exhibits excellent transmission in the visible and near infrared; giving the zirconia doped EDFA practical applications in the real world. The fabrication and characterization of an Erbium Doped Zirconia-Yttria-Alumino Silicate Fiber (EDZF) is the focus of the first part of this work.

Additionally, zirconia co-doped fibers have also been shown to exhibit significant non-linear characteristics. These non-linear characteristics, which are not seen in conventional Single-Mode Fibres (SMFs) or EDFAs, [1] have tremendous potential for the development of various new applications such as multi-wavelength outputs and also wavelength conversion. Of particular interest is the Four-Wave Mixing (FWM) effect. In the absence of significant photo-absorption effects, FWM is a type of optical Kerr effect, and occurs when light at two or more different wavelengths is launched into a fiber [1]. The FWM effect is observed when signals at different wavelengths are launched into a fiber, and the interaction of these two signals gives rise to a new signal (known as an idler), the wavelength of which does not coincide with any of the others [29, 30]. The FWM effect has tremendous potential for the development of new fiber based wavelength sources, and is the focus of the later part of this work.

2 ZIRCONIA YTTRIA-ALUMINO SILICATE GLASS FABRICATION

The EDZF is fabricated in three stages. In the first stage, a conventional silica preform is fabricated using the Modified Chemical Vapour Deposition (MCVD) technique, whereby SiCl_4 and P_2O_5 vapors are passed through a slowly rotating silica tube that is heated by an external burner. The burner heats the length of the tube as it rotates and, due to the high temperature generated, the chloride in the SiCl_4 and P_2O_5 vapors oxidizes, depositing a porous phospho-silica layer along the inner wall of the silica tube. The optimum deposition temperature range for the MCVD process is 1350 - 1400 °C, with a variation of the pre-sintering temperature from 1300 to 1450 °C. The fabricated silica tube, with its deposited porous phospho-silica layer, then undergoes a solution doping process using dopant precursors of suitable strength to obtain the optimized process parameters for making a fiber with a Numerical Aperture (NA) of approximately 0.17 - 0.20. The glass modifiers, ZrO_2 , Y_2O_3 , Al_2O_3 and Er_2O_3 are individually mixed with alcohol and water at a ratio of 1:5 to form the complex ions $\text{ZrOCl}_2 \cdot 8\text{H}_2\text{O}$, $\text{YCl}_3 \cdot 6\text{H}_2\text{O}$, $\text{AlCl}_3 \cdot 6\text{H}_2\text{O}$ and $\text{ErCl}_3 \cdot 6\text{H}_2\text{O}$ respectively and are then incorporated into the host matrix using the solution doping technique. Small quantities of Y_2O_3 and P_2O_5 are also added to the glass matrix to act as nucleating agents, functioning to increase the phase separation of the Er_2O_3 doped micro-crystallites that will form in the core matrix of the optical fiber preform.

During the fabrication process, it is crucial to note that, in a bulk glass matrix, pure zirconia exists in three distinct crystalline phases over different temperature ranges. At very

high temperatures, above 2350 °C, ZrO_2 has a cubic structure whereas, at intermediate temperatures between 1170 and 2350 °C, a tetragonal structure is observed. At low temperatures, below approximately 1170 °C, ZrO_2 takes on a monoclinic structure. The transformation of the crystalline structure from tetragonal to monoclinic is very rapid and is accompanied by a 3 to 5 percent volume increase. This rapid increase can result in extensive cracking in the material - as was observed in the doped core region of the preform after the fabrication - and is highly detrimental, as it destroys the mechanical properties of fabricated components during cooling. In order to overcome this problem, several oxides, such as MgO , CaO , and Y_2O_3 that dissolve in the zirconia crystal structure can be used to slow down or eliminate these crystal structure changes; in this work a minor quantity of Y_2O_3 is used.

In the final stage of the fiber fabrication process, the fabricated preform that has undergone the solution doping process is annealed at 1100 °C for 3 hours in a closed furnace, under heating and cooling rates of 20 °C/min, to generate ErO_2 doped ZrO_2 rich micro-crystalline particles. The resulting annealed preform is collapsed into a solid rod at a temperature higher than 2000 °C and is drawn into a fiber strand with a diameter $125 \pm 0.5 \mu\text{m}$, using a conventional fiber drawing tower. During the drawing process, the preform (and the fiber obtained) is exposed to a temperature of around 2000 °C for only a few minutes. Due to the high cooling rate of the material and the melting temperature of the ZrO_2 crystals being above 2200 °C, the ZrO_2 nano-crystalline host is retained within the silica glass matrix. Both the primary & secondary coatings were applied on-line to increase the tensile strength, as well as to reduce the moisture ingress from external sources. During the fiber drawing procedure, proper control of the fiber diameter, coating thickness and coating concentricity along the whole length of the fabricated fiber gives the optimization required for the production of a high quality optical fiber. The thickness of the primary coating (Desolite DP-1004), as well as that of the secondary coating (Desolite DS-2015), and the coating uniformity were ensured by adjusting the flow pressure of the inlet gases into the primary and secondary coating resin vessels during the drawing of the fiber, as well as by properly aligning the position of primary and secondary coating cup units.

3 EZDF CHARACTERISATION

In bulk zirconia-silicate glass, phase-separation has been observed at temperatures below the onset of crystallization - which also results in structural inhomogeneity [31, 32]. Phase separation, or immiscibility, is a phenomenon that is known to exist in amorphous binary systems [33]; however in some ZrO_2 - SiO_2 systems immiscibility exists even in the stable liquid phase above the melting point. The phase diagram of ZrO_2 - SiO_2 systems was evaluated using Fact-Sage software, and it was determined that a stable immiscibility zone exists in the range between 60 and 80 mole % SiO_2 . This stable immiscibility zone extends to temperatures lower than the glass melting point - and gives a metastable immiscibility zone in a wide composition range where phase separation occurs normally in an amorphous state. In the EZDF, it may be expected

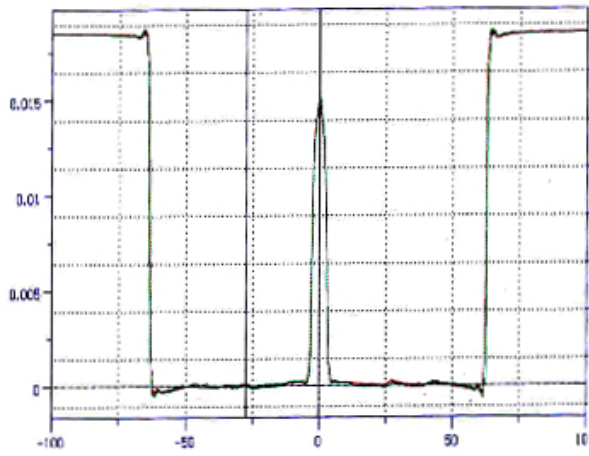


FIG. 1 Refractive index profile of fiber (ZEr-B).

Perform No	Al ₂ O ₃ (mole %)	ZrO ₂ (mole %)	Er ₂ O ₃ (mole %)
ZEr-A	0.25	0.65	0.155
ZEr-B	0.24	2.10	0.225

TABLE 1 Doping levels within core region of the preforms

that the separated ZrO₂ and Al₂O₃ phases would mix together into a homogeneous mixture before crystallization could occur during heating at high temperature, since the homogeneous amorphous mixture of compositions, ZrAl_xO_y, is generally thermodynamically more stable than the two separate phases. In this work two Er₂O₃ doped fibers, designated ZEr-A and ZEr-B, were fabricated. Both fibers contain 0.24-0.25 mole % of Al₂O₃, with the ZrO₂ and Er₂O₃ dopant concentration increased from 0.65 to 2.21 mole % and from 0.155 to 0.225 mole % for ZEr-A and ZEr-B respectively. The doping levels of the two fibers are obtained through an Electron Probe Micro-Analysis (EPMA) for both the fabricated fiber samples and is given in Table 1, whilst the physical parameters of the fibers are given in Table 2.

The measured refractive index profile of fiber ZEr-B is shown in Figure 1. The spectroscopic properties such as absorption coefficient, fluorescence and fluorescence decay curves of the fabricated fibers are measured, and it can be observed that the peak absorption of the two types of fiber at 978 nm are found to be 15.0 and 22.0 dB/m respectively. The spectral attenuation curve of fiber ZEr-B is shown in Figure 2, as the non-linear properties of this fiber will be analysed in the following section.

The fluorescence spectra of the fiber samples were measured with lateral pumping, for a pump power level of 100 mW at 980 nm. The fluorescence curves for both fibers are shown in Figure 3 and the fluorescence decay curves of both fibers are shown in Figure 4.

The two fibers (ZEr-A and ZEr-B) show almost the same fluorescence live-times of 10.93 and 10.86 ms respectively. Fiber ZEr-B, which has higher doping levels of Er₂O₃ and ZrO₂ shows slight shorter fluorescence life-time. These results indicate that the concentration-quenching phenomenon that is

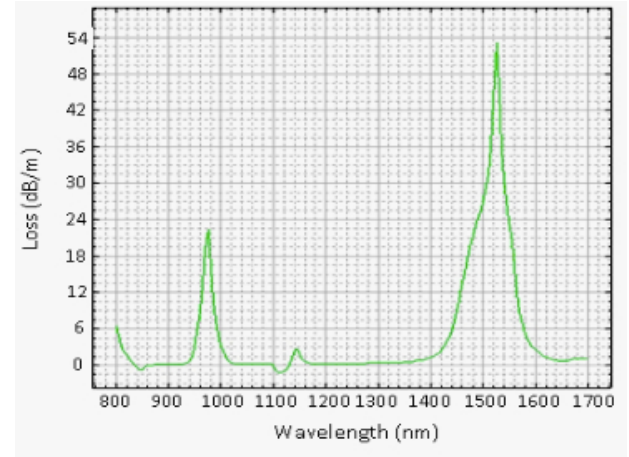


FIG. 2 Spectral attenuation curve of fiber (ZEr-B).

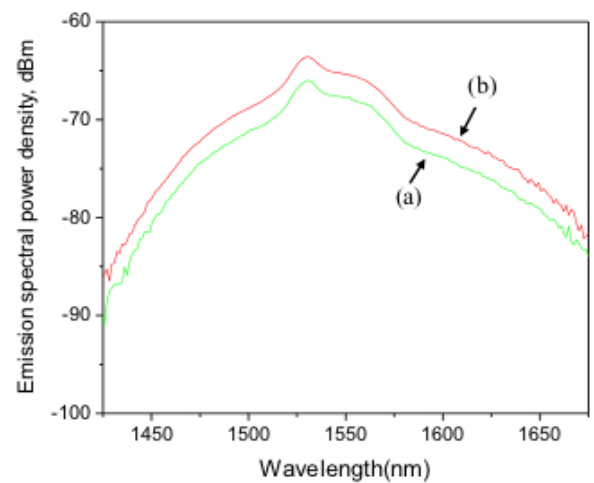


FIG. 3 Fluorescence curves of (a) fiber ZEr-A and (b) fiber ZEr-B at a pump power level of 100 mW.

typical of Er³⁺ ions is strongly reduced through an increase in the doping levels of ZrO₂. In the generation of the FWM effect in the zirconia-erbium doped silica fiber, the ZEr-B is used instead of the ZEr-A due to the higher ZrO₂ concentration, which will provide a better non-linear interaction.

4 GENERATION OF THE FWM EFFECT IN THE EZDF

The generation of the FWM effect in nonlinear fibers can be explained by using the coupled differential equations for the propagating amplitudes, including the contributions to phase mismatch due to XPM and SPM [34]. A well-known formula used for FWM estimation was originally derived by Hill et. al. [35] and reformulated later to include the phase-mismatch dependent efficiency by Shibata et. al. [36]. In the FWM process in glass, two chosen wavelengths (λ_{pump} and λ_{signal}) will generate a converted wavelength $\lambda_{\text{converted_signal}} = 2\lambda_{\text{pump}} - \lambda_{\text{signal}}$. To analyze the nonlinearity in the EZDF, the nonlinear coefficient, γ , is estimated by using;

$$\gamma = \sqrt{P_{\text{textFMW}} \eta P_S P_P^2} e^{-\alpha L} L_{\text{textef}} f^2 \quad (1)$$

Fiber Number	Core Composition	Core Diameter	Fiber Type	NA	A-eff	RI of core
ZEr-A	SiO+Al ₂ O ₃ +P ₂ O ₅ -ZrO ₂ - Y ₂ O ₃ +Er ₂ O ₃	10.5	Circular core with normal resin	0.17	87 μ^2	1.46625
ZEr-B	SiO+Al ₂ O ₃ +P ₂ O ₅ -ZrO ₂ - Y ₂ O ₃ +Er ₂ O ₃	10.0	Circular core with normal resin	0.20	75 μ^2	1.47025

TABLE 2 Fiber parameters

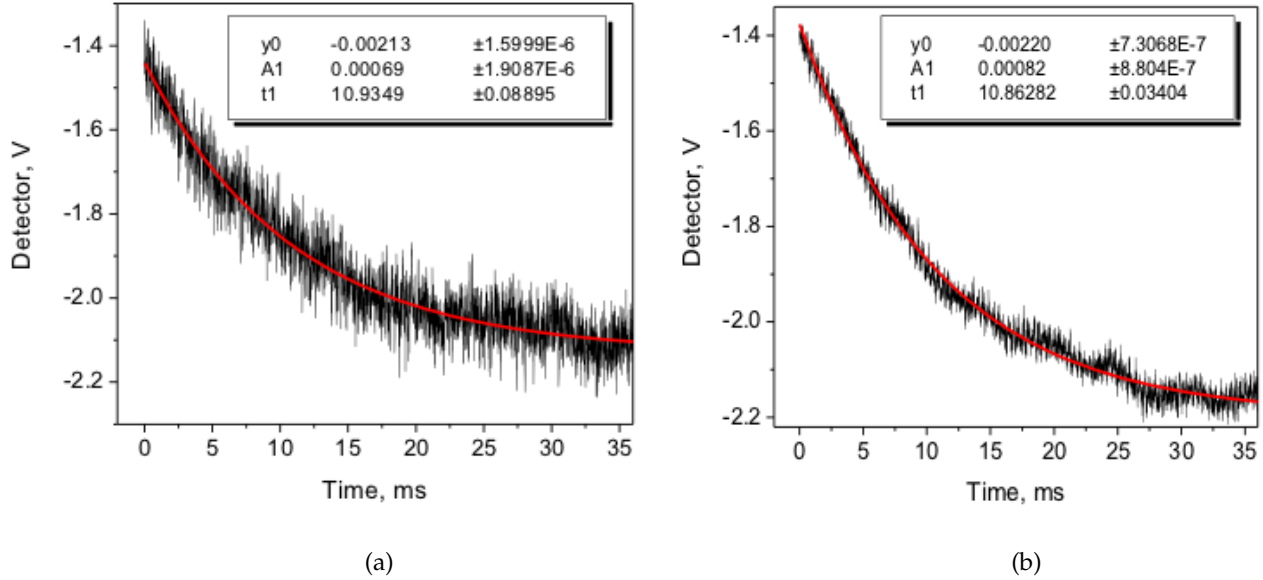


FIG. 4 The fluorescence decay curve of two EDFs (a) ZEr-A and (b) ZEr-B at a pump power level of 100 mW.

where P_{FWM} is the FWM power, P_p is the input pump power, P_s is the input signal power, L is the fiber length and α is the fiber attenuation coefficient. The effective length of the fiber L_{eff} takes into account the decrease in power due to attenuation - and is defined as;

$$L_{\text{eff}} = \frac{1 - e^{-\alpha L}}{\alpha} \quad (2)$$

The normalized FWM efficiency, η , is written as;

$$\eta = \frac{\alpha^2}{\alpha^2 + \Delta\beta^2} \left[1 + \frac{2e^{-\alpha L} (1 - \cos(\Delta\beta L))}{(1 - e^{-\alpha L})^2} \right] \quad (3)$$

where is the phase $\Delta\beta$ mismatch that is given by;

$$\Delta\beta = \frac{2\pi\lambda^2}{c} D \Delta f^2 \quad (4)$$

with the dispersion parameter, $D = \frac{-2\pi c}{\lambda^2} \beta^2$, where β^2 is the group velocity dispersion parameter. From equation (4), it can be seen that P_{FWM} is at its minima when $\Delta\beta \frac{L}{2} = k\pi$, where k is an integer. This occurs due to the phase mismatch between the signals propagating inside the fiber and occurs at every $\frac{2\pi}{\beta}$ meters. The P_{FWM} minima can also be determined as a product of the channel spacing, such that:

$$\Delta f_k = \sqrt{\frac{kc}{\lambda^2 DL}} \quad (5)$$

As the magnitude of the nonlinearity in the fiber only shifts the P_{FWM} minima, therefore an analysis of the FWM signal power minima can be used to determine the dispersion of the optical fiber, whilst the nonlinearity can be estimated from the total fiber attenuation. The physical setup for measuring the

P_{FWM} minima is simple and only requires two laser diodes with a tuning range of less than 1 nm each and a EZDF of the proper length. The channel spacing at which P_{FWM} reaches its first minima is a necessary measurement in calculating the dispersion of the fiber and is given as:

$$D = \frac{c}{\lambda^2 \Delta f^2 L} \quad (6)$$

From equations (1) to (6), the theoretical FWM power can now be calculated as

$$P_{\text{FWM}} = \eta \gamma^2 P_p^2 P_s e^{-\alpha L} L_{\text{eff}}^2 \quad (7)$$

γ is determined by bi-directional measurements of the FWM power, while the chromatic dispersion is determined from the wavelength detuning of the FWM Power Conversion Efficiency (PCE). Both measurements use the same experimental setup as given by the schematic in Figure 5.

In the setup, two Yokogawa (AQ2200) Tunable Laser Sources (designated TLS1 and TLS2), with tuning ranges from 1460 nm to 1640 nm and linewidths of 0.015 nm are used as signal sources. The pump signal P_1 (or P_p), is generated by TLS 1 at a fixed wavelength of 1560 nm and an average output power of 12.8 dBm. A second signal, P_s is generated from TLS2 with a wavelength varying from 1561 nm to 1565 nm at an average power level of 10.8 dBm. Both P_1 and P_s are combined using a 3 dB coupler and a Polarization Controller (PC) to adjust the polarization of the input signals in order to obtain the maximum FWM efficiency. Additionally, two Laser Diode (LD) pumps at wavelengths of 1460 nm and 1490 nm are also launched into the EZDF using a WDM to excite the Er^{3+} ions just enough so that they are transparent to the

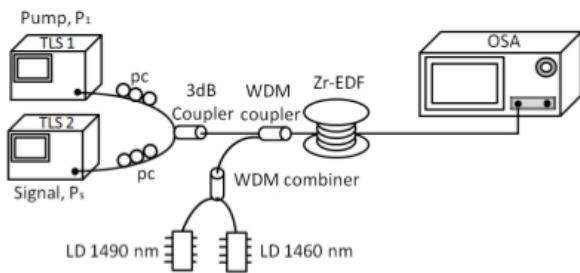


FIG. 5 Schematic diagram for generating FWM effects in the EZDF

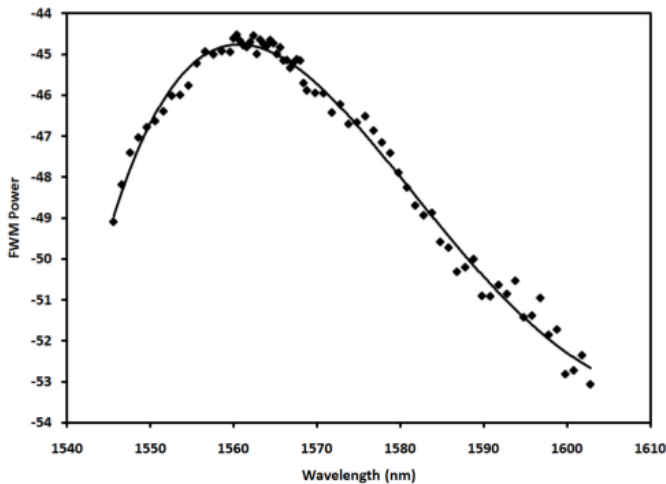


FIG. 6 The spectrum of the converted signal (FWM power) against the wavelength of the pump against converted wavelength for the ZEr-B optical fiber sample.

signals used for the generation of the FWM (the suppression of the Er^{3+} ions is necessary as the EZDF sample incorporates both ZrO_2 and Er_2O_3 , however this work is only interested in the non-linear effects generated by the ZrO_2 in the fibre). A 4 m long ZEr-B fiber with an Erbium concentration of 3000 ppm is used. The ZEr-B fiber has a core refractive index value of 1.466 and an effective area of $87 \mu\text{m}^2$ along with a propagation loss, α of 0.68 dB/m, which is obtained using the cut-back method. The refractive index and glass core size of the ZEr-B fiber used are important parameters that will be used to determine the nonlinearity of the fiber. Finally, a Yokogawa Optical Spectrum Analyzer (OSA) with 0.02 nm resolution bandwidth is used to measure the generated FWM spectrum.

5 RESULTS AND DISCUSSION

The power of signals generated by the FWM process is dependent the wavelength of the pump and input signal. In this work, the pump and signal wavelengths are detuned by 0.4 nm. The pump and signal powers are set at +15 dBm and +13 dBm respectively and are optimized for the maximum possible power using a PC. Figure 6 shows the power of the signal obtained from the FWM process against the pump wavelength.

It can be seen that the power of the converted signal begins to increase from a low value of -48 dBm at a pump wavelength of 1545 nm to a peak power of -45 dBm at 1565 nm. The power

of the converted signal does not change significantly between 1558 nm to 1565 nm, with only minor fluctuations of approximately 0.5 dB being observed. After this region however, the power decreases rapidly as the pump power continues to increase towards the L-band region. The reason for this is that the gain spectrum of ZEr-B provides the highest gains at a wavelength around 1560 nm. As such, the pump signal is set at a wavelength of 1560 nm, as this will ensure the generation of the FWM output will fall within the flat region. The wavelength value of 1560 nm is also used in the measurement of the nonlinearity coefficient of ZEr-B.

Figure 7 shows the overlay spectrum of the converted signals along with the pump and signal wavelengths. The spectrum shown is as obtained from the OSA with a +25 dB fixed attenuator, the attenuator serving to protect the OSA from spikes in the signal which could potentially damage it. The pump wavelength is left constant at 1560 nm and -9.9 dBm power while the signal wavelengths are varied from 1561 nm to 1565 nm in steps of 1 nm. The power of the signal wavelength is maintained at -10.5 dBm. From Figure 7, it can be seen that two sidebands C_1 and S_2 are generated by the pump and signal wavelengths. At a signal wavelength of 1561 nm, two converted wavelengths are observed at 1559 nm (C_1) and 1562 nm (S_2), a shift of 2 and 1 nm respectively on either side of the signal. As the signal wavelength increases to 1562 nm, the converted wavelengths also shift accordingly to 1558 nm (C_1) and 1564 nm (S_2), giving a shift of 4 and 2 nm respectively. This trend is seen to continue as the signal wavelength continues to be varied until 1565 nm, which sees the C_1 move towards a wavelength of 1555 nm in steps of 1 nm, and S_2 increasing in steps of 2 nm to a wavelength of 1570 nm. It is also observed that when the signal wavelength increases at a fixed pump wavelength, the power of the generated sidebands drops. This can be attributed to the gain spectrum of the ZEr-B fiber such that the longer signal wavelengths move away from the optimum gain region of the fiber. The channel spacings obtained in Figure 8 are essential in determining the fiber non-linear coefficient, dispersion and slope dispersion of the ZEr-B fiber, which is seen in the following results.

Figure 8 shows the power of the converted signal, C_1 against the wavelength of the input signal. The pump is left constant at a wavelength of 1560 nm and the signal wavelength is varied from 1550 nm to 1559 nm with a frequency spacing 0.2 nm. To ensure the maximum power is obtained for the converted signal, the two PCs as shown in Figure 6 are adjusted to provide the optimum output power. As can be seen from the figure, the power of the converted signal is initially low at about -58 dBm. However, as the signal wavelength increases, so does the power of the converted signal, reaching a power of approximately -45 dBm at a wavelength of 1559 nm. Further increases in the input signal wavelength do not result in any change to the converted signal power. It can be seen that the experimental results agree well with the theoretical predictions for ZEr-B. It is observed that the difference in the power of the converted signal in Figure 9 and that of Figure 8 is attributed to the use of the +25 dB attenuator.

The analysis of FWM power in a function of channel spacing can be used to estimate the fiber chromatic dispersion

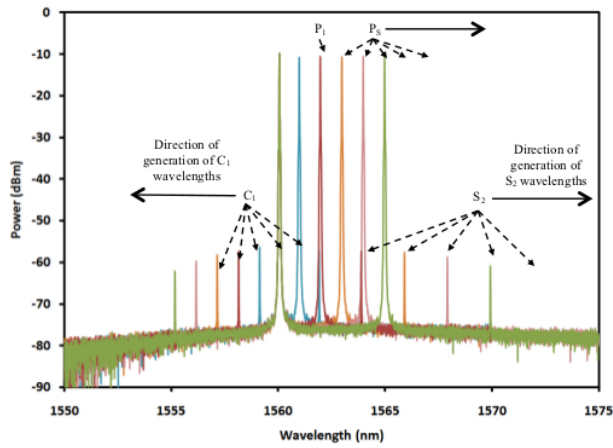


FIG. 7 The typical output spectra at P_1 and P_s , as well as their converted signals (sideband fields) C_1 and S_2 when wavelength of P_1 is fixed at 1560 nm and the wavelength of P_s is varied from 1561 nm to 1565 nm for the ZEr-B optical fiber sample.

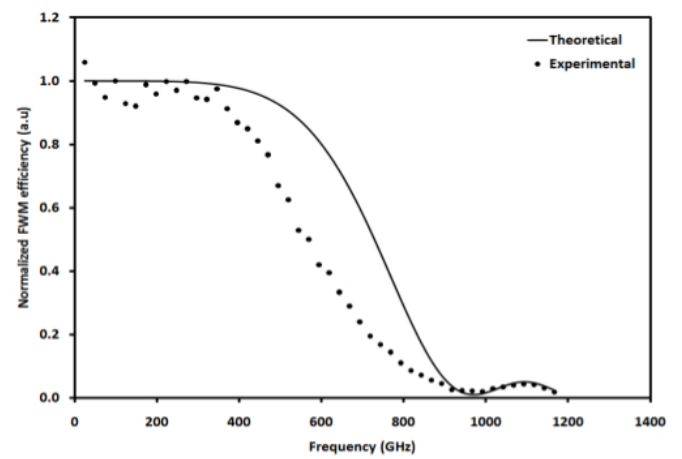


FIG. 9 Normalized FWM efficiency against the input signal frequency for the ZEr-B optical fiber sample.

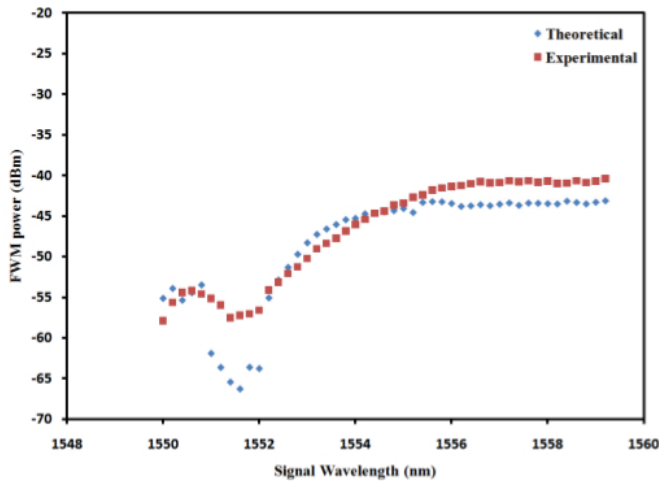


FIG. 8 FWM conversion efficiency versus wavelength detuning for the ZEr-B optical fiber sample.

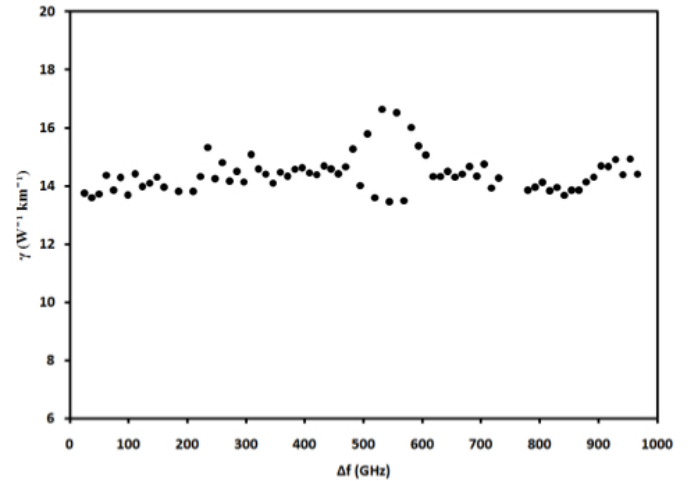


FIG. 10 Nonlinear coefficients with varying the frequency spacing as obtained using the ZEr-B optical fiber sample.

and dispersion slope. Figure 9 shows the normalized FWM efficiency against the input signal frequency. It can be seen that as the channel spacing (frequency) is increased from 30 GHz to 400 GHz, the FWM efficiency remains relatively the same, with fluctuations of about 0.5 a.u. However, above 400 GHz, the FWM efficiency begins to drop, reaching almost 0 at 1000 GHz. These measurements are in agreement with the theoretical predictions for the ZEr-B fiber. From equation (6) and the Figure 9, a chromatic dispersion and slope dispersion value of 28.45 ps/nm.km and 3.63 ps/nm².km respectively is obtained for ZEr-B.

Using the signal power, pump power, converted power and the normalized FWM efficiency, the nonlinear coefficient for Zr-EDF is estimated using equation (1). In this equation, the FWM efficiency is important in getting the value of nonlinear coefficient where it used equation (3) for found the value. Therefore, a nonlinear coefficient value of 14 W⁻¹km⁻¹ is obtained for the ZEr-B. Figure 10 shows the variation of the nonlinear coefficient against the channel spacing.

From Figure 10, it can be seen that the non-linear coefficient

remains the same for almost all channel spacing values, with the largest variation being approximately 2 dBm between the region of 500 to 600 GHz. This gives the ZEr-B fiber a high potential as a medium for a variety of applications such as wavelength conversion and wavelength generation.

6 CONCLUSIONS

The fabrication of an EDZF is described in the work, followed by an analysis of its application as a non-linear medium for the generation of the FWM effect. The fabrication of the EZDF follows the conventional approach with the creation of a standard silica preform using the MCVD technique. Glass modifiers and nucleating agents are then added to the silica preform using the solution doping technique and the resulting preform is annealed and drawn into a fiber strand with a diameter $125 \pm 0.5 \mu\text{m}$. In this work, two EZDF samples are fabricated and designated as ZEr-A and ZEr-B, with ZrO₂ and Er₂O₃ dopant concentrations of 0.65 to 2.21 mole % and 0.155 to 0.225 mole % respectively and numerical apertures of between 0.17 to 0.20 as well as peak absorptions of 15.0

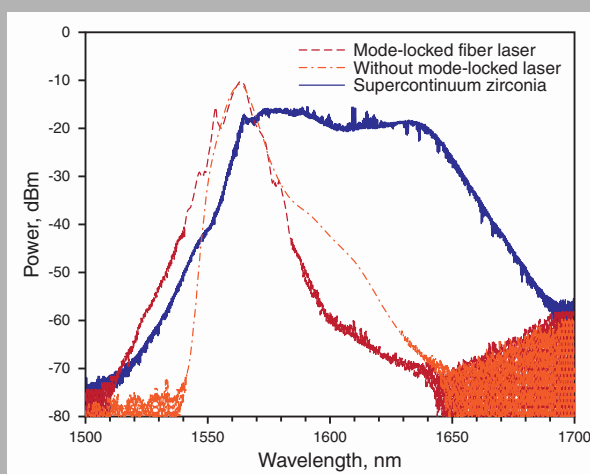
and 22.0 dB/m respectively at 978 nm. In investigation FWM effect, a 4 m long portion of ZEr-B with a propagation loss of 0.68 dB/m and an erbium concentration of 3000 ppm is used. FWM power levels of approximately -45 dBm at around 1565 nm are obtained and agree well with the theoretical predicted values. The ZEr-B fiber also shows a non-linear coefficient of $14 \text{ W}^{-1}\text{km}^{-1}$ along with chromatic and dispersion slopes of 28.45 ps/nm.km and 3.63 ps/nm².km that are well in accordance to the theoretical values.

References

- [1] G. E. Keiser, "A Review of WDM Technology and Applications," *Opt. Fiber Technol.* **5**, 3–39 (1999).
- [2] M. Wasfi, "Optical Fiber Amplifiers – Review," *Int. J. Comm. Netw. Infor. Sec.* **1**, 42–47 (2009).
- [3] H. Ahmad, M. Z. Zulkifli, A. A. Latif, K. Thambiratnam, and S. W. Harun, "17-channels S band multiwavelength Brillouin/Erbium Fiber Laser Co-Pump with Raman source," *Laser Phys.* **19**, 2188–2193 (2009).
- [4] D. Richardson, J. Nilsson, and W. Clarkson, "High Power Fiber Lasers: Current Status and Future Perspectives [Invited]," *J. Opt. Soc. Am. B* **27**, 63–92 (2010).
- [5] K. Inoue, and H. Toba, "Wavelength Conversion Experiment using Fiber Four-Wave Mixing," *IEEE Photonic. Tech. L.* **4**, 69–72 (1992).
- [6] E. Yahel, and A. Hardy, "Amplified Spontaneous Emission in High-Power, Er^{3+} . Yb^{3+} Codoped Fiber Amplifiers for Wavelength-Division-Multiplexing Applications," *J. Opt. Soc. Am. B* **20**, 1198–1203 (2003).
- [7] D. Cotter, and A. D. Ellis, "Asynchronous Digital Optical Regeneration and Networks," *J. Lightwave Technol.* **16**, 2068–2080 (1998).
- [8] S. Abbott, "Review of 20 Years of Undersea Optical Fiber Transmission System Development and Deployment since TAT-8," in *Proceedings to Optical Communication, 2008. ECOC 2008. 34th European Conference on*, 1–4 (ECOC, Brussel, 2008).
- [9] K. Rottwitz, and J. H. Povlsen, "Analysing the Fundamental Properties of Raman Amplifiers in Optical Fibers," *J. Lightwave Technol.* **23**, 3597–3613 (2005).
- [10] J. H. Lee, Y. M. Chang, Y. G. Han, H. Chung, S. H. Kim, and S. B. Lee, "A Detailed Experimental Study on Single Pump Raman/EDFA Hybrid Amplifiers: Static, Dynamic, and System Performance Comparison," *J. Lightwave Technol.* **23**, 3848 (2005).
- [11] P. Doussiere, A. Jourdan, G. Soulage, P. Garabedian, C. Graver, T. Fillion, E. Derouin, and D. Leclerc, "Clamped Gain Travelling Wave Semiconductor Optical Amplifier for Wavelength Division Multiplexing Applications," in *Proceedings to Semiconductor Laser Conference, 1994., 14th IEEE International*, 185–186 (IEEE, Maui, 1994).
- [12] K. Morito, "Output-Level Control of Semiconductor Optical Amplifier by External Light Injection," *J. Lightwave Technol.* **23**, 4332–4341 (2005).
- [13] T. Torounidis, P. A. Andrekson, and B.-E. Olsson, "Fiber-optical parametric amplifier with 70-dB gain," *IEEE Photonic. Tech. L.* **18**, 1194–1196 (2006).
- [14] J. M. Chavez Boggio, P. Dainese, F. Karlsson, and H. L. Fragnito, "Broad-Band 88% Efficient Two-Pump Fiber Optical Parametric Amplifier," *IEEE Photonic. Tech. L.* **15**, 1528–1530 (2003).
- [15] Y. Ohishi, A. Mori, M. Yamada, H. Ono, Y. Nishida, and K. Oikawa, "Gain Characteristics of Tellurite-Based Erbium-Doped Fiber Amplifiers for 1.5- μm Broadband Amplification," *Opt. Lett.* **23**, 274 (1998).
- [16] S. Jiang, B.-C. Hwang, T. Luo, K. Seneschal, F. Smektala, S. Honkanen, J. Lucas, and N. Peyghambarian, "Net Gain of 15.5 dB from a 5.1 cm-Long Er^{3+} Doped Phosphate Glass Fiber," in *Proceedings to Optical Fiber Communications*, PD5–1 (IEEE, Baltimore, 2000).
- [17] A. Cucinotta, F. Poli, and S. Selleri, "Design of Erbium-Doped Triangular Photonic-Crystal-Fiber-Based Amplifiers," *IEEE Photonic. Tech. L.* **16**, 2027 (2004).
- [18] S. Aozasa, H. Masuda, and M. Shimizu, "S-band Thulium-Doped Fiber Amplifier Employing High Thulium Concentration Doping Technique," *J. Lightwave Technol.* **24**, 3842–3848 (2006).
- [19] S. W. Harun, N. Tamchek, S. Shahi, and H. Ahmad, "L-band Amplification and Multi-Wavelength Lasing with Bismuth-Based Erbium Doped Fiber," *Prog. Electromagn. Res.* **6**, 1–12, (2009).
- [20] S. D. Emami, P. Hajireza, F. Abd-Rahman, H. A. Abdul-Rashid, H. Ahmad, and S. W. Harun, "Wide-Band Hybrid Amplifier Operating in S-Band Region," *Prog. Electromagn. Res.* **102**, 301–313 (2010).
- [21] E. Snoeks, P. G. Kik, and A. Polman, "Concentration Quenching in Erbium Implanted Alkali Silicate Glass," *Opt. Mater.* **5**, 159 (1996).
- [22] D. M. Gill, L. McCaughan, and J. C. Wright, "Spectroscopic Site Determinations in Erbium-Doped Lithium Niobate," *Phys. Rev. B* **53**, 2334 (1996).
- [23] M. C. Paul, S. W. Harun, N. A. D. Huri, A. Hamzah, S. Das, M. Pal, S. K. Bhadra, H. Ahmad, S. Yoo, M. P. Kalita, A. J. Boyland, and J. K. Sahu, "Wideband EDFA Based on Erbium Doped Crystalline Zirconia Yttria Alumino Silicate Fiber," *J. Lightwave Technol.* **28**, 2919–2924 (2011).
- [24] M. C. Paul, S. W. Harun, N. A. D. Huri, A. Hamzah, S. Das, M. Pal, S. K. Bhadra, H. Ahmad, S. Yoo, M. P. Kalita, A. J. Boyland, and J. K. Sahu, "Performance comparison of Zr-based and Bi-based erbium-doped fiber amplifiers," *Opt. Lett.* **35**, 2882–2884 (2010).
- [25] J. R. Armitage, "Spectral Dependence of the Small-Signal Gain around 1.5 μm in Erbium Doped Silica Fiber Amplifiers," *IEEE J. Quantum Electron.* **26**, 423–425 (1990).
- [26] B. Pedersen, A. Bjarklev, J. H. Povlsen, K. Dybdal, and C. C. Larsen, "The design of erbium-doped fiber amplifiers," *J. Lightwave Technol.* **9**, 1105–1112 (1991).
- [27] J. Yang, S. Dai, Y. Zhou, L. Wen, L. Hu, and Z. Jiang, "Spectroscopic Properties and Thermal Stability of Erbium-Doped Bismuth-Based Glass for Optical Amplifier," *J. Appl. Phys.* **93**, 977–983 (2003).
- [28] P. Peterka, B. Faure, W. Blanc, M. Karásek, and B. Dussardier, "Theoretical Modelling of S-band Thulium-Doped Silica Fibre Amplifiers," *Opt. Quant. Electron* **36**, 201–212 (2004).
- [29] K. Kikuchi, and C. Lorattanasane, "Design of Highly Efficient Four-Wave Mixing Devices using Optical Fibers," *IEEE Photonic. Tech. L.* **6**, 992–994 (1994).
- [30] O. Aso, A. Shin-Ichi, T. Yagi, M. Tadakuma, Y. Suzuki, and S. Namiki, "Broadband Four-Wave Mixing Generation in Short Optical Fibres," *Electron. Lett.* **36**, 709–711 (2000).
- [31] G. D. Wilk, R. M. Wallace, and J. M. Anthony, "Hafnium and Zirconium Silicates for Advanced Gate Dielectrics," *J. Appl. Phys.* **87**, 484–492 (2000).
- [32] G. Rayner, R. Therrien, and G. Lucovsky, "The structure of plasma-deposited and annealed pseudo-binary ZrO_2 - SiO_2 alloys," *Proc. Mater. Res. Soc. Symp.* **611**, C1.3.1–C1.3.9 (2000).
- [33] P. F. James, "Liquid-Phase Separation in Glass-Forming Systems," *J. Mater. Sci.* **10**, 1802–1825 (1975).

- [34] G. P. Agrawal, *Nonlinear Fiber Optics* (Academic Press, London, 1995).
- [35] K. O. Hill, D. C. Johnson, B. S. Kawasaki, and R. I. MacDonald, "CW Three-Wave Mixing in Single-Mode Fibers," J. Appl. Phys. **49**, 50980-51006 (1978).
- [36] N. Shibata, R. P. Braun, and R. G. Warrts, "Phase-Mismatch Dependence of Efficiency of Wave Generation through Four-Wave Mixing in a Singlemode Fiber," Quantum Electron. **23**, 1205-1211 (1987).

Abstract: We propose and demonstrate the generation of a supercontinuum (SC) spectrum from a 10 m long silica fiber co-doped with zirconia-yttria-alumino and erbium (Zr-EDF) as a non-linear medium. The proposed system utilizes a 2 m long Zr-EDF in a ring laser configuration to generate mode-locked pulses at 1560 nm based on the non-polarization rotation (NPR) technique. The fiber laser generates a mode-locking spectrum from 1526 to 1640 nm with a peak power of -10 dBm at approximately 1565 nm as well as a 6.1 nm bandwidth at the 3 dB level. The generated mode-locked pulses have average and peak powers of 15 mW and 1 kW respectively with a repetition rate of 23.2 MHz. These pulses are subsequently used to generate the SC spectrum from the 10 m Zr-EDF, with the SC spectrum obtained having a 200 nm bandwidth from 1500 nm as well as a large 3-dB bandwidth of 68.2 nm. The SC pulse width is 0.59 ps with a symmetrical shape at about 1600 nm and a 3-dB bandwidth of approximately 0.12 ps. This is the first report of a zirconia host employed as a non-linear medium for SC generation.



The spectra from the mode-locked fiber laser, ASE, and SC

© 2012 by Astro Ltd.

Published exclusively by WILEY-VCH Verlag GmbH & Co. KGaA

Supercontinuum from Zr-EDF using Zr-EDF mode-locked fiber laser

H. Ahmad,^{1,*} N.A. Awang,^{1,2} M.Z. Zulkifli,¹ K. Thambiratnam,¹ M.C. Paul,³ S. Das,³ and S.W. Harun⁴

¹ Photonics Laboratory, Department of Physics, University of Malaya, 50603 Kuala Lumpur, Malaysia

² Faculty of Science, Technology, and Human Development, Universiti Tun Hussein Onn Malaysia, 86400 Batu Pahat, Johor, Malaysia

³ Fiber Optics and Photonics Division, Central Glass & Ceramic Research Institute-CSIR, Kolkata-32, India

⁴ Department of Electrical Engineering, Faculty of Engineering, University of Malaya, 50603 Kuala Lumpur, Malaysia

Received: 22 June 2011, Revised: 4 July 2011, Accepted: 7 July 2011

Published online: 2 November 2011

Key words: supercontinuum; zirconia-based erbium-doped fiber; mode-locked fiber laser

1. Introduction

Since its demonstration in the early 1970s by R.R. Alfano and S.L. Shapiro [1,2], supercontinuum (SC) generation and the spectral broadening of partially or fully coherent light signals in optical waveguides has been the focus of significant research efforts. SC generation in particular has attracted much attention owing to the enormous spectral broadening experienced by laser pulses, which have many useful applications in telecommunications [3], spectroscopy [4], frequency metrology [5], optical coherence tomography [6], and device characterization [7].

SC generation is a complex physical phenomenon involving the interaction of classical nonlinear optical effects such as self-phase modulation (SPM), cross phase modulation (CPM), four wave mixing (FWM), and stimulated Raman scattering (SRS) [8]. R.R. Alfano and S.L. Shapiro first reported the generation of an SC output using 5 mJ/ps pulses at 530 nm in BK7 bulk glass to obtain a white light spectrum covering the entire visible range from 400 to 700 nm. However, this approach is highly complex and requires the intricate alignment and coupling of various optical components as well as the use of high energy ultra-short pulses. Instead, a more practi-

* Corresponding author: e-mail: harith@um.edu.my

cal approach would be to use the tight spatial confinement of lower energy pulses within a suitably nonlinear waveguide, as the higher nonlinearity of the material lowers the power levels required for SC generation. J.K. Ranka et al. [9] demonstrated SC generation in a photonic crystal fiber (PCF) with an extremely small solid-core, generating an SC spanning over 550 THz in spectral width. Since then, there has been growing interest in SC generation using optical fibers and microstructured optical fibers fabricated from highly nonlinear glasses such as PCFs and highly nonlinear dispersion shifted fibers (HNLFs) [10–18] and in dual-core microstructured fibers [19]. On top of these, there are also reports on all fiber SC generation [20] and also SCs with high power outputs [21,22]. There have been investigations of SC generation in the UV region from 509 to 640 nm using tapered PCFs [23] and also numerical simulations of mid-infrared SC generation of up to 5 μm in a single-mode fluoride fiber [24]. However, there are very limited reports on the use of standard optical fibers as a medium for SC generation. It will be of interest to have SC generation in standard silica fibers that can be conveniently spliced into standard single-mode fibers (SMFs) as this approach is inexpensive. There is a need to investigate new types of optical fibers that can provide SC generation which also have a high non-linear coefficient and based on standard silica hosts as well as its variations.

In this paper, the generation of an SC spectrum is proposed and demonstrated using a new type of optical fiber; a zirconia-erbium-doped fiber (Zr-EDF). The Zr-EDF is fabricated using a ternary glass host, zirconia-yttria-aluminum (Zr-Al-Y) co-doped silica fiber. The combination of both Zr and Al allows for a higher erbium doping concentration, thus allowing the fabrication of a short-length erbium-doped fiber amplifier (EDFA). Besides its usage as an amplifying medium, the Zr-EDF also exhibits high non-linearity characteristics as demonstrated in this paper, as a medium for SC generation. The Zr-EDF is pumped with a passively mode-locked Zr-EDF fiber laser generating ultra-short pulses.

2. Experimental setup

The experimental setup for SC generation from a Zr-EDF is shown in Fig. 1. In this work, two Zr-EDF lengths are used; first, a 2 m long Zr-EDF is used to create a passively mode-locked fiber laser, and its output is then propagated through a 10 m long Zr-EDF in order to generate the SC spectrum. The Zr-EDFs are fabricated from a silica fiber co-doped with zirconia-yttria-alumino using the modified chemical vapor deposition (MCVD) technique as well as erbium ions using a solution doping approach. The addition of zirconia and aluminum ions into the glass host allows for a high erbium doping concentration of about 1500 ppm to be obtained without any clustering of the rare-earths ions, while small amounts of Y_2O_3 and P_2O_5 ions serve as the nucleating agents to increase the phase separation between the erbium ion-doped micro crystallites in

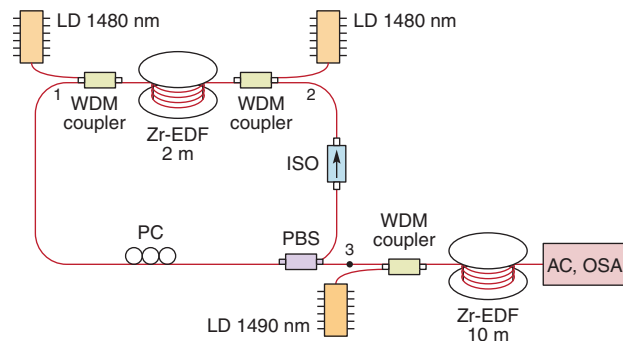


Figure 1 (online color at www.lphys.org) Schematic diagram for generating mode-locked fiber laser and SC in a Zr-EDF. LD – laser diode, WDM – wavelength division multiplexor, PBS – polarization beam splitter, AC – autocorrelator, OSA – optical spectrum analyzer, PC – polarization controller, and Zr-EDF – zirconia based erbium-doped fiber

the core matrix of optical fiber preform [25,26]. The advantage of the zirconia-based host is that it is useful in generating ultra-short pulses as a result of its wide-band characteristic.

The mode-locked fiber is based on the non-linear polarization rotation (NPR) technique and uses an inexpensive fiber-based polarization beam splitter (PBS) as opposed to the typical approach of a polarization dependent isolator (PDI) sandwiched in between two fiber-based polarization controllers (PCs). The 2 m long Zr-EDF has a pump absorption rate of about 13.5 dB/m at 1480 nm and is connected to the common ports of two 1480/1550 nm wavelength division multiplexers (WDMs). The 1480 nm ports of the WDMs are connected to two 1480 nm pump laser diodes (LDs) that are set to operate at 150 mW and configured in a bi-directional pumping scheme to provide a total pump power of about 300 mW. The 1550 nm output of the first WDM, Port 1 is connected to a fiber-based PC, which is then connected to a fiber-based 50:50 PBS. The slow axis port of the PBS is connected to a polarization insensitive isolator and then connected back to Port 2 of the second WDM as to complete the ring cavity of the mode-locked fiber laser, with a total cavity length of approximately 5.5 m. The PC acts as the mode-locking element [27,28] and is used to adjust the polarization of the signal that travels in the slow-axis in order to provide self-start mode-locking. The generation of the mode-locked pulses is based on the NPR technique, where an intense optical pulse propagating in a non-polarization maintaining optical fiber can experience non-linear changes in the polarization state due to the self-phase and cross-phase modulation as well as some uncontrolled birefringence in the fiber. This behavior is similar to that of saturable absorbers, giving an intensity dependent loss.

The short-pulses generated from the fiber laser have an average power of 15 mW with a repetition rate of

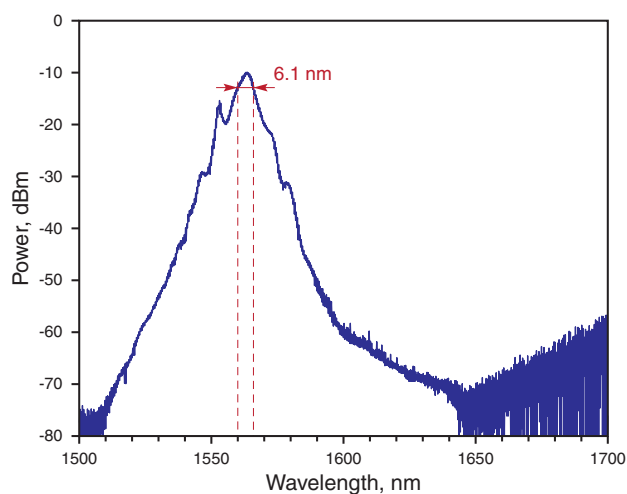


Figure 2 (online color at www.lphys.org) Optical spectra of the output laser pulse

23.2 MHz, giving a peak power of about 1 kW, which is extracted through the fast axis output of the PBS. This output is then connected to the 1550 nm port of a third WDM, which is joined to a 10 m long Zr-EDF which acts as the medium for SC generation. The 1490 nm LD is used to pump the erbium ions in the Zr-EDF as to make it transparent, thus allowing the input mode-locked pulses to pass through without being absorbed and therefore able to interact with the glass host of the Zr-EDF to generate the SC output. The output of the Zr-EDF is then connected to a Yokogawa AQ6370B optical spectrum analyzer (OSA) with a resolution of 0.02 nm and an Alnair auto-correlator. The mode-locked pulses are very stable and can operate for several hours without breaking up as well as being immune to external vibrations. This translates the generation of an SC spectrum with a similar degree of high stability. The experimental results are presented in the following section.

3. Results and discussions

The generation of the mode-locked pulses from the Zr-EDF laser can be achieved by adjusting the PC, with self-starting mode-locked pulse at 1560 nm being obtained at a LD power of 130 mW and above. With appropriate adjustments of the PC, the mode-locked pulses are generated based on the NPR technique, which is largely due to SPM and CPM occurring in the fiber, along with some uncontrolled birefringence. This effect is similar to the behavior of saturable absorbers, which gives intensity dependent loss [29]. The mode-locking spectrum that is generated by the Zr-EDF is shown in Fig. 2, giving a span from 1525 to 1640 nm with a bandwidth of 6.1 nm at the 3 dB level. It has a peak power of about -10 dBm at a wavelength of 1560 nm.

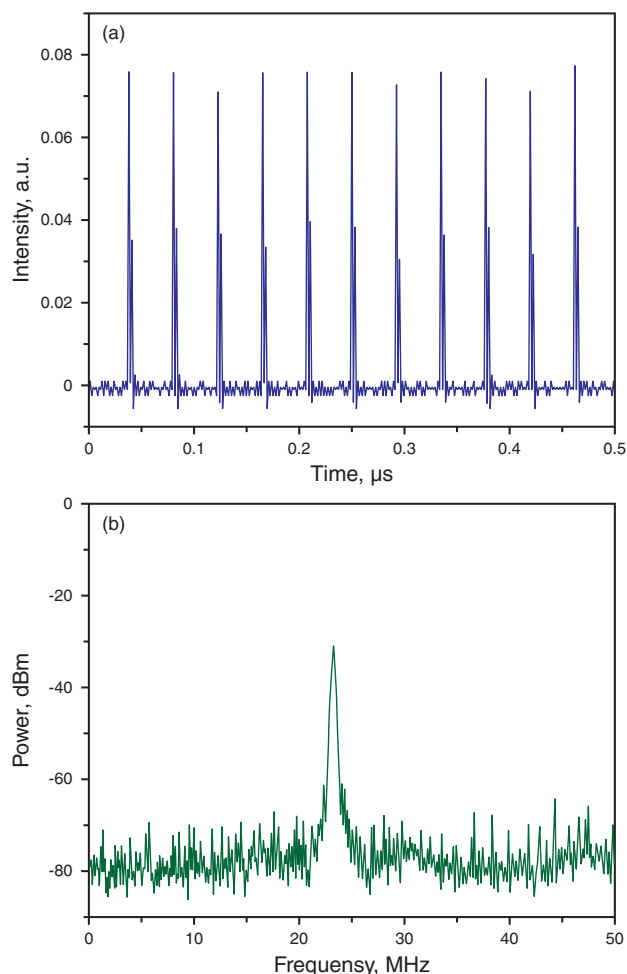


Figure 3 (online color at www.lphys.org) Spectrum of the output laser pulses at (a) – sampling oscilloscope and (b) – RF spectrum analyzer

The generated mode-locked pulses are shown in Fig. 3. Fig. 3a shows the sampling oscilloscope trace with a repetition rate of 23.2 MHz. From the trace, there are also side-pulses that are a consequence of the technique based on saturable absorbers and these can be removed by the proper adjustment of the PC. From Fig. 3b, the repetition rate as obtained using a radio frequency (RF) spectrum analyzer together with a 6 GHz bandwidth photo-detector, which is taken from the 5% port of a 95:5 fused bi-conical coupler. The measured frequency is about 23.2 MHz, similar to that calculated value using Fig. 3a. The repetition rate of the mode-locked fiber laser depends on the fiber cavity length and in this setup the length is about 5.5 m. A shorter cavity length will increase the repetition rate. The present cavity length gives a positive dispersion near the 1560 nm region [27] thus providing operation in the normal dispersion regime, which is normally referred to as a stretched pulse mode-locked fiber laser.

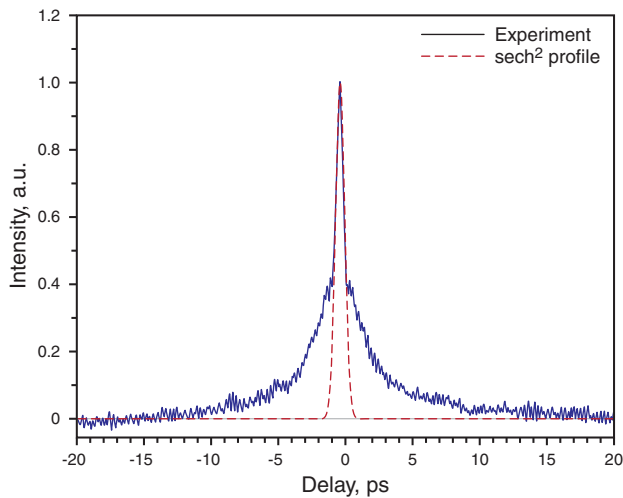


Figure 4 (online color at www.lphys.org) The spectra of femtosecond pulses obtained experimentally (from the Alnair auto-correlator output) and using a hyperbolic secant squared (sech^2) profile, giving a pulse width of 0.59 ps

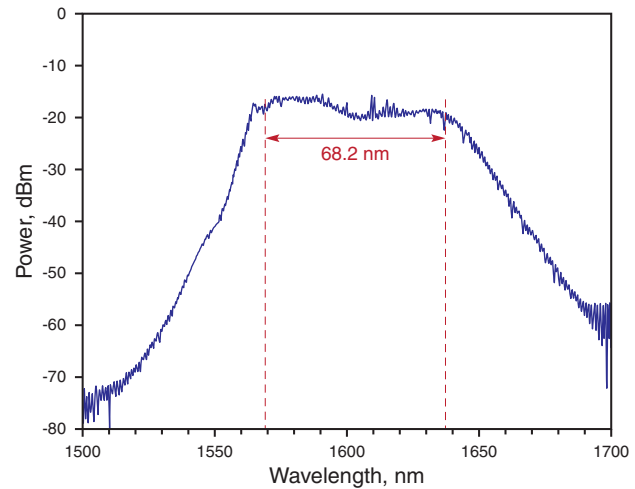


Figure 6 (online color at www.lphys.org) SC output generated from the 10 m long Zr-EDF

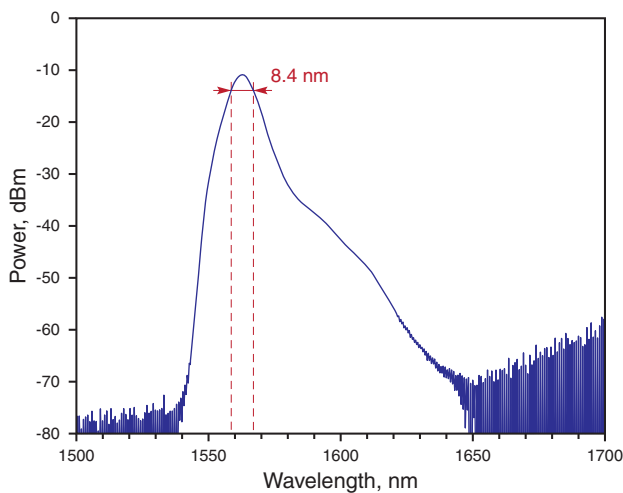


Figure 5 (online color at www.lphys.org) The ASE spectrum of Zr-EDF with Port 3 disconnected

The duration of the mode-locked pulses from the Zr-EDF laser is obtained using the Alnair auto-correlator and is shown in Fig. 4. Using a hyperbolic secant squared (sech^2) profile; a pulse duration of 0.59 ps is measured when the system is optimally configured.

The average power measured is 15 mW with a peak power of 1 kW. The energy per pulse is about 0.6 nJ. These mode-locked pulses are then connected to a 10 m Zr-EDF as in Fig. 1 for SC generation.

Another measurement of interest would be the amplified spontaneous emission (ASE) spectrum from the 10 m long Zr-EDF, which is taken by disconnecting Port 3 in

Fig. 1 such that it is measured at the output end that is connected to the OSA. The spectrum is shown in Fig. 5 when it is pumped at 170 mW from the LD at 1490 nm, which is connected to the third WDM. The purpose of this ASE spectrum is to provide a comparison with the SC spectrum generated.

The generated ASE spectrum spans from about 1540 to 1650 nm, with a peak power of approximately -11 dBm at 1565 nm. The measured 3 dB bandwidth or full-width at half-maximum (FWHM) of the ASE spectrum is about 8.4 nm.

The SC spectrum is generated by connecting the output of the mode-locked ring fiber laser to Port 3 of the third WDM, which is connected to the 10 m long Zr-EDF and the LD pump power is adjusted such that the doped fiber becomes transparent with gain factor of only 1. This is to allow the usage of the ternary glass host, zirconia-yttria-aluminum co-doped silica fiber as a non-linear medium of interest. The mode-locked pulses are made to travel into the Zr-EDF and the SC output generated is shown in Fig. 6. The SC spectrum wavelength spans from 1500 to 1700 nm, with a bandwidth as large as 68.2 nm at 3-dB level when excited by mode-locked pulses at 1560 nm with a pulse width of 0.59 ps. The SC spectrum shifted towards the longer wavelength as similarly observed in most case [30]. From the Fig. 6, it has a symmetrical shape of around 1600 nm.

The pulse width of the SC is characterized using a similar autocorrelator and the measurement is taken using the 5% port of the 95:5 fused bi-conical coupler as to limit the input power to less than 1 mW. The pulse width has a FWHM of about 0.12 ps using the hyperbolic secant squared (sech^2) technique, as a result of pulse compression. This normally occurs when for the case of opera-

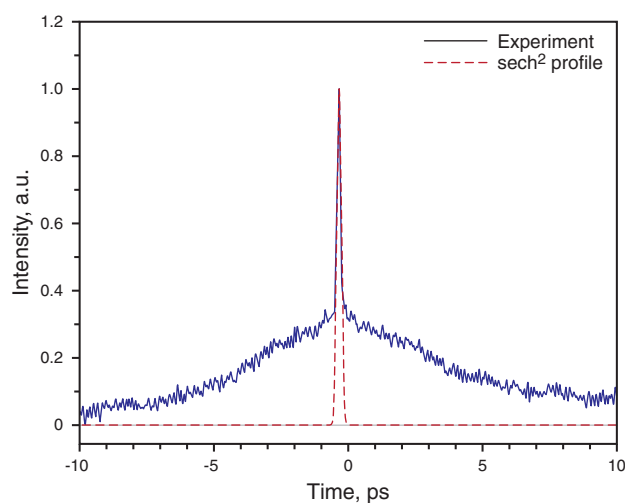


Figure 7 (online color at www.lphys.org) The SC pulse width obtained experimentally and using a hyperbolic secant squared (sech^2) profile, giving a pulse-width of 0.12 ps

tion in the anomalous dispersion region. This is shown in Fig. 7.

Fig. 8 shows the comparison of the spectrum from the mode-locked fiber laser, the ASE spectrum as taken from the 10 m Zr-EDF, which is disconnected from the mode-locked ring fiber laser system and the SC spectrum of the zirconia host when mode-locked pulses is injected into the medium. This clearly indicates that the measured SC spectrum is due to the non-linear behavior of the zirconia host and not from the ASE of the Zr-EDF or the wavelength spectrum of the mode-locked pulses.

In this paper, the Zr-EDF is capable of generating an SC output when mode-locked pulses are injected into the medium. This indicates that the zirconia host acts as a non-linear medium. Typically, for SC generation, highly non-linear fibers, dispersion shifted fibers and photonic crystal fibers are used as the medium. This is the first report whereby a zirconia host; Zr-EDF is shown to have a non-linear behavior and able to generate SC. The system can be configured as a compact SC generator using short lengths of the Zr-EDF. The current fiber has a zero dispersion wavelength at around the 1300 nm region. By proper design, and shifting the zero-dispersion wavelength into the shorter region, will be able to generate a wider SC spanning from the visible to infrared.

4. Conclusion

In this work, SC generation from a silica based zirconia host is proposed and demonstrated. The proposed system utilizes a 2 m long Zr-EDF based laser in a ring cavity to generate self-starting mode-locked pulses at 1560 nm, which are then used to generate the SC spectrum from a

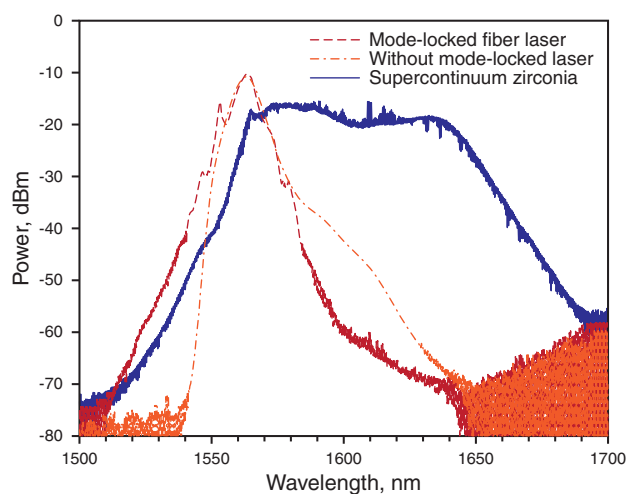


Figure 8 (online color at www.lphys.org) The spectra from the mode-locked fiber laser, ASE, and SC

10 m long Zr-EDF. The fiber laser is based on the NPR technique and generates a mode-locking spectrum from 1526 to 1640 nm with a 6.1 nm bandwidth at 3-dB level and a peak power of -10 dBm at about 1560 nm. The mode-locked pulses generated have an average power of 15 mW with a peak power of 1 kW as well as 0.6 nJ energy per pulse at a repetition rate of 23.2 MHz. The SC spectrum obtained ranges from 1500 to 1700 nm, with a large 3-dB bandwidth of 68.2 nm. The SC has a pulse width of 0.59 ps with a symmetrical shape at about 1600 nm as well as a 3-dB bandwidth of approximately 0.12 ps. This is the first report of a silica-based zirconia host used as a non-linear medium for SC generation.

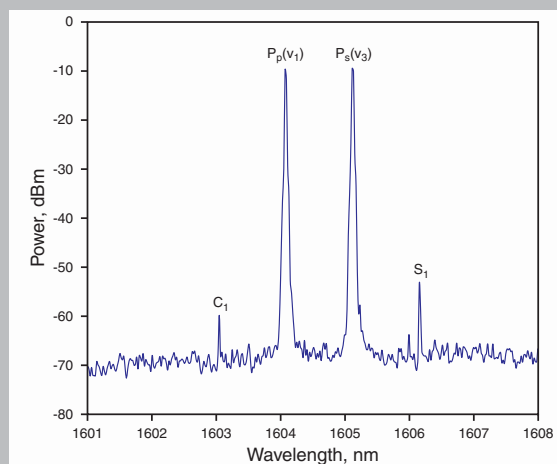
Acknowledgements The authors would like to express their gratitude to the University of Malaya, Malaysia for providing the funding for this work and the Central Glass & Ceramic Research Institute, India for the optical fiber.

References

- [1] R.R. Alfano and S.L. Shapiro, *Phys. Rev. Lett.* **24**, 584 (1970).
- [2] R.R. Alfano and S.L. Shapiro, *Phys. Rev. Lett.* **24**, 592 (1970).
- [3] J.M. Dudley, G. Genty, and S. Coen, *Rev. Mod. Phys.* **78**, 1135 (2006).
- [4] J. Shah, *Ultrafast Spectroscopy of Semiconductors and Semiconductor Nanostructures*, 2nd ed., Springer Series in Solid-State Sciences, vol. 115 (Springer, 1999).
- [5] B.R. Washburn, S.A. Diddams, N.R. Newbury, J.W. Nicholson, M.F. Yan, and C.G. Jørgensen, *Opt. Lett.* **29**, 250 (2004).
- [6] W. Drexler, U. Morgner, F.X. Kärtner, C. Pitris, S.A. Boppart, X.D. Li, E.P. Ippen, and J.G. Fujimoto, *Opt. Lett.* **24**, 1221 (1999).

- [7] R.T. Neal, M.D.C. Charlton, G.J. Parker, C.E. Finlayson, M.C. Netti, and J.J. Baumberg, *Appl. Phys. Lett.* **83**, 4598 (2003).
- [8] G. Brambilla, F. Koizumi, V. Finazzi, and D.J. Richardson, *Electron. Lett.* **41**, 795 (2005).
- [9] J.K. Ranka, R.S. Windeler, and A.J. Stentz, *Opt. Lett.* **25**, 25 (2000).
- [10] A.K. Abeeluck, S. Radic, K. Brar, J.-C. Bouteiller, and C. Headley, in: *Proc. of the Optical Fiber Communication Conference*, Atlanta, GA, USA, March 22–28, 2003 (OFC 2003), paper ThT1.
- [11] J.W. Nicholson, A.K. Abeeluck, C. Headley, M.F. Yan, and C.G. Jørgensen, *Appl. Phys. B* **77**, 211 (2003).
- [12] A.K. Abeeluck, C. Headley, and C.G. Jørgensen, *Opt. Lett.* **29**, 2163 (2004).
- [13] R. Buczynski, D. Pysz, R. Stepień, A.J. Waddie, I. Kujawa, R. Kasztelan, M. Franczyk, and M.R. Taghizadeh, *Laser Phys. Lett.* **8**, 443 (2011).
- [14] M.R.A. Moghaddam, S.W. Harun, R. Akbari, and H. Ahmad, *Laser Phys. Lett.* **8**, 369 (2011).
- [15] R. Buczynski, H.T. Bookey, D. Pysz, R. Stepień, I. Kujawa, J.E. McCarthy, A.J. Waddie, A.K. Kar, and M.R. Taghizadeh, *Laser Phys. Lett.* **7**, 666 (2010).
- [16] D.A. Sidorov-Biryukov, K.A. Kudinov, A.A. Podshivalov, and A.M. Zheltikov, *Laser Phys. Lett.* **7**, 355 (2010).
- [17] S.-P. Chen, J.-H. Wang, H.-W. Chen, Z.-L. Chen, J. Hou, X.-J. Xu, J.-B. Chen, and Z.-J. Liu, *Laser Phys.* **21**, 519 (2011).
- [18] Y. Gu, L. Zhan, D.-D. Deng, Y.-X. Wang and Y.-X. Xia, *Laser Phys.* **20**, 1459 (2010).
- [19] R. Buczynski, D. Pysz, T. Martynkien, D. Lorenc, I. Kujawa, T. Nasilowski, F. Berghmans, H. Thienpont, and R. Stepień, *Laser Phys. Lett.* **6**, 575 (2009).
- [20] S.M. Kobtsev and S.V. Kukarin, *Laser Phys.* **20**, 372 (2010).
- [21] H.W. Chen, S.P. Chen, and J. Hou, *Laser Phys.* **21**, 191 (2011).
- [22] S.M. Kobtsev, S.V. Kukarin, and S.V. Smirnov, *Laser Phys.* **20**, 375 (2010).
- [23] S.P. Stark, A. Podlipensky, N.Y. Joly, and P.St.J. Russell, *J. Opt. Soc. Am. B* **27**, 592 (2010).
- [24] L. Liu, G.S. Qin, Q.J. Tian, D. Zhao, and W.P. Qin, *Opt. Express* **19**, 10041 (2011).
- [25] M.C. Paul, S.W. Harun, N.A.D. Huri, A. Hamzah, S. Das, M. Pal, S.K. Bhadra, H. Ahmad, S. Yoo, M.P. Kalita, A.J. Boyland, and J.K. Sahu, *J. Lightwave Technol.* **28**, 2919 (2010).
- [26] M.C. Paul, S.W. Harun, N.A.D. Huri, A. Hamzah, S. Das, M. Pal, S.K. Bhadra, H. Ahmad, S. Yoo, M.P. Kalita, A.J. Boyland, and J.K. Sahu, *Opt. Lett.* **35**, 2882 (2010).
- [27] H.A. Haus, K. Tamura, L.E. Nelson, and E.P. Ippen, *IEEE J. Quantum Electron.* **31**, 591 (1995).
- [28] Z.C. Luo, A.P. Luo, W.C. Xu, C.X. Song, Y.X. Gao, and W.C. Chen, *Laser Phys. Lett.* **6**, 582 (2009).
- [29] V.J. Matsas, T.P. Newson, D.J. Richardson, and D.N. Payne, *Electron. Lett.* **28**, 1391 (1992).
- [30] X. Liu, C. Xu, W.H. Knox, J.K. Chandalia, B.J. Eggleston, S.G. Kosinski, and R.S. Windeler, *Opt. Lett.* **26**, 358 (2001).

Abstract: The generation and performance of the four-wave mixing (FWM) effect in zirconia-erbium doped fibers (Zr-EDFs) is investigated and compared for linear and ring cavities. A 3 m long Zr-EDF with an erbium ion concentration of 3000 ppm and non-linear coefficient value of $14.0 \text{ W}^{-1}\text{km}^{-1}$ serves as the non-linear medium in this work. The ring configuration generates sidebands approximately 20 dB higher than the linear configuration, whilst the linear configuration provides a more stable sideband power as the signal wavelength changes. An enhanced ring configuration is also proposed and demonstrated, using only a single tunable laser source (TLS) as the pump wavelength and a 100 m long highly non-linear fiber (HNLF) with a non-linear coefficient of $10.8 \text{ W}^{-1}\text{km}^{-1}$. The enhanced ring configuration is capable of generating up to 10 sidebands through the FWM effect with channel spacings of approximately 1 nm each. The proposed enhanced ring design will find many applications as multi-wavelength sources for communications and sensing.



The spectrum of the generated FWM effect in the ring cavity configuration with sideband frequencies generated at C_1 and S_1

© 2012 by Astro, Ltd.

Four-wave mixing in zirconia-erbium doped fiber – a comparison between ring and linear cavities

H. Ahmad,^{1,*} K. Thambiratnam,¹ N.A. Awang,^{1,3} Z.A. Ghani,⁴ and S.W. Harun²

¹ Photonics Research Centre, University of Malaya, 50603 Kuala Lumpur, Malaysia

² Department of Electrical Engineering, Faculty of Engineering, University of Malaya, 50603 Kuala Lumpur, Malaysia

³ Faculty of Science, Technology and Human Development, Universiti Tun Hussein Onn Malaysia, 86400 Batu Pahat, Johor, Malaysia

⁴ Faculty of Applied Science, Universiti Teknologi MARA, 40450 Shah Alam, Selangor Darul Ehsan, Malaysia

Received: 6 March 2012, Revised: 30 April 2012, Accepted: 5 May 2012

Published online: 19 September 2012

Key words: four-wave mixing; zirconia-erbium doped fibers; ring fiber laser; highly non-linear fiber

1. Introduction

The development of fiber based multi-wavelength sources for optical communications and sensing applications has recently garnered significant interest due to their low cost and compatibility with current optical systems [1–4]. Many techniques have been undertaken to generate these sources, ranging from simple methods such as the slicing of amplified spontaneous emission (ASE) from erbium doped fiber amplifiers (EDFAs) [5,6], and semiconductor

optical amplifiers (SOAs) [7] to more complex approaches such as stimulated Brillouin scattering (SBS) [8,9].

While these approaches can generate the desired multi-wavelength output they suffer from a number of drawbacks, such as high cost (in the case of the EDFA and SOA, which typically requires an arrayed waveguide grating (AWG) and special erbium doped fibers or expensive SOAs to generate the required ASE or too narrow channel spacings (in the case of SBS generated multi-wavelength outputs).

* Corresponding author: e-mail: harith@um.edu.my

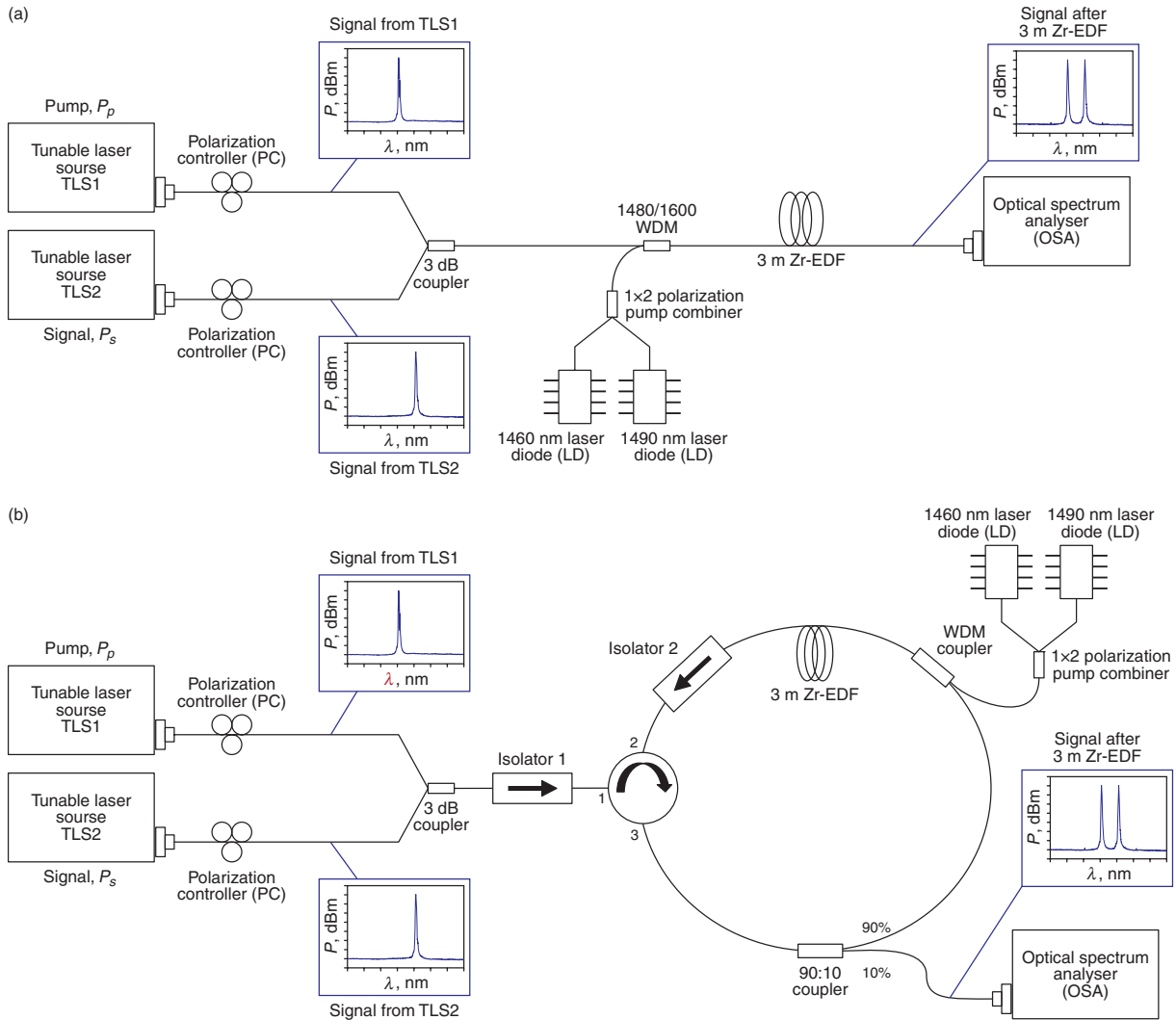


Figure 1 (online color at www.lasphys.com) Schematic diagram for generating FWM effects in the Zr-EDF (a) linear configuration (b) ring configuration. The insets show the spectrum of the power, P (dBm) against the wavelength, λ (nm) for the signals obtained at the various parts of the setups

Recently, $\chi^{(3)}$ non-linear phenomena such as four-wave mixing (FWM) and self-phase modulation (SPM) have been seen as a viable approach towards generating cheap multi-wavelength sources with suitable channel spacings [10,11]. These processes the optical Kerr effect, and were originally impairments towards high data-rate optical fiber communication [12–14]. However, continued research soon developed significantly useful applications based on $\chi^{(3)}$ non-linear phenomena, in particular the FWM effect, such as parametric amplification, wavelength conversion and wavelength oscillation [15–17]. The FWM effect is most prominent in fibers with a high non-linearity coefficient value, and was initially observed in fibers such as photonic crystal fibers (PCFs) [18] as well

as tellurite, chalcogenide, chalcogenide and bismuth based glasses [19–27].

However, generating the FWM effect in these fibers can be hard due to the requirement of phase matching in order to maintain optimum efficiency. It is difficult to maintain phase matching over long lengths of fiber, as is typically the case with fibers above. In this regard, the zirconia-erbium doped fiber (Zr-EDF) is a promising non-linear gain medium for FWM generation, exhibiting non-linear behavior in only short fiber lengths. Zr-EDFs were originally designed for highly doped EDFAs without the detrimental effects of concentration quenching [28] and cluster formation [29], but have also shown significant non-linear characteristics which are not typi-

cally observed in conventional EDFAs [30], in particular the FWM effect. The generation of the FWM effect in the Zr-EDF has tremendous potential for various new applications such as multi-wavelength outputs and wavelength conversion. Furthermore, as Zr-EDFs tend to exhibit wide emission and absorption bandwidths as predicted by the Fuchtbauer-Ladenberg relationship [31,32] and Judd-Ofelt theory [33,34], more wavelength division multiplexing (WDM) channels can be amplified, thereby allowing for the generation of wide-bandwidth multi-wavelength outputs. This factor, combined with excellent mechanical strength, chemical corrosion resistance and non-hygroscopic properties makes the Zr-EDF a suitable for real-world applications.

In this work, the generation and performance of the FWM effect in linear and ring configuration Zr-EDF based fiber lasers is investigated and compared. A 3 m long Zr-EDF with an erbium ion concentration of 3000 ppm and non-linear coefficient value of $14.0 \text{ W}^{-1}\text{km}^{-1}$ serves as the non-linear medium in this work. An enhanced ring configuration is also investigated, using a 100 m long highly non-linear fiber (HNLF) with a nominal zero dispersion wavelength (ZDW) at 1531 nm and nonlinear parameter of $10.8 \text{ W}^{-1}\text{km}^{-1}$. The signal from a single tunable laser source (TLS) interacts with the dominant lasing wavelength in the ring cavity to generate the FWM effect and create a multi-wavelength comb. The proposed configuration has multiple applications as a multi-wavelength source with consistent channel spacing for sensing and communications tasks.

2. Experimental setup

The experimental setups of the ring and linear cavity configurations for generating the FWM effect are shown in Fig. 1. The linear cavity configuration is shown in Fig. 1a, whilst the ring cavity configuration is given in Fig. 1b.

In the linear configuration, a TLS, designated TLS1 in Fig. 1a acts as the pump source, P_p , with an output power of 12.8 dBm and operating at 1604 nm. The second TLS, designated as TLS2 in Fig. 1a acts as the signal source, P_s , with an average output power of 12.0 dBm. Unlike TLS1, the output wavelength of TLS2 is not fixed, and can be tuned from 1601 to 1611 nm in this work. Both TLS units have maximum and minimum wavelengths of 1460 and 1640 nm respectively, with a linewidth of 0.015 nm. The separate outputs of both TLS1 and TLS2 are channeled into two different polarization controllers (PCs) as to optimize the beam for maximum FWM efficiency. The optimized output from the PCs are then combined using a 3 dB coupler with the output end connected to one of the ports of the 1480/1600 nm WDM coupler. Two pump lasers, at 1460 and 1490 nm and operating at 90 mW each is combined using a 1×2 polarization pump combiner, with the output connected to the second port of the WDM coupler (these two wavelengths are used due to the availability of

the pump sources at the time, however the same results will be obtained using a single 1480 nm laser diode operating at the same output power). The output port of the WDM coupler is then connected to a 3 m long Zr-EDF. The advantage of zirconia co-dopants is that it allows for higher erbium ion concentrations to be achieved, which in this case is approximately 3000 ppm. The Zr-EDF used has a core refractive index of 1.466 and an effective area of $87 \mu\text{m}^2$ with a propagation loss, α at 0.68 dB/m using the cut-back measurement method. The fiber has a non-linear coefficient, γ value of $14.0 \text{ W}^{-1}\text{km}^{-1}$, which is higher than the conventional PCF γ value of $11.0 \text{ W}^{-1}\text{km}^{-1}$ [18]. The fiber also has a higher chromatic dispersion of 28.45 ps/nm/km and lower dispersion slope of $3.63 \text{ ps/nm}^2\text{.km}$ as compared to a conventional silica fiber (which has a chromatic dispersion and dispersion slope of about 17.0 ps/nm/km and $0.092 \text{ ps/nm}^2\text{/km}$ respectively). The 1460 and 1490 nm pumps are used to invert the population of the erbium ions so as to make fiber transparent to incoming signals in the wavelength region from 1500 to 1600 nm. By making the fiber transparent, the erbium ions play no role, and thus any interaction is purely between the incoming signals and the zirconia dopant ions in the Zr-EDF as to allow the observation of non-linear effects. The pump and signal wavelengths, P_1 and P_2 provides the interacting sources for generating the FWM effect in the Zr-EDF, and the output is observed using an optical spectrum analyzer (OSA) with a resolution of 0.02 nm (Yokogawa AQ6370B) connected after the Zr-EDF.

The ring cavity configuration of Fig. 1b differs slightly from the linear cavity as shown in Fig. 1a, whereby the output from the 3 dB coupler is connected through an optical isolator (Isolator 1) to Port 1 of a 3-port optical circulator. The ring cavity consists of the same 3 m Zr-EDF with one end connected to another optical isolator (Isolator 2) which is in turn connected to Port 2 of the optical circulator. The optical isolator is placed in such a way as to enforce oscillations in the anti-clockwise direction. The Zr-EDF is being pumped so as to invert the erbium ion population as was done in the linear configuration using the 1460 and 1490 nm laser diodes, with a cumulative output power of 180 mW. The pump power is injected into the ring cavity through the 1460/1600 nm WDM with the output port connected to the EDF and the other input port of the WDM connected to the 90% port of a 90:10 fused coupler. The common port of the 90:10 fused coupler is connected to Port 3 of the optical circulator, thus completing the ring cavity. The 10% port of the fused coupler is connected to an OSA. As in the discussion for the case of the linear cavity, the Zr-EDF is pumped so as to make the fiber transparent to signals in the region of 1500 to 1600 nm. As such, P_p and P_s will now interact only with zirconia dopant ions and generate the FWM effect. P_p and P_s enters the ring cavity through Port 1 and is then re-emitted at Port 2, where it is then reflected back onto itself because of Isolator 2. The reflected signal will be emitted at Port 3 of the optical circulator and travels to the 90:10 fused coupler, where 90% of the signal will con-

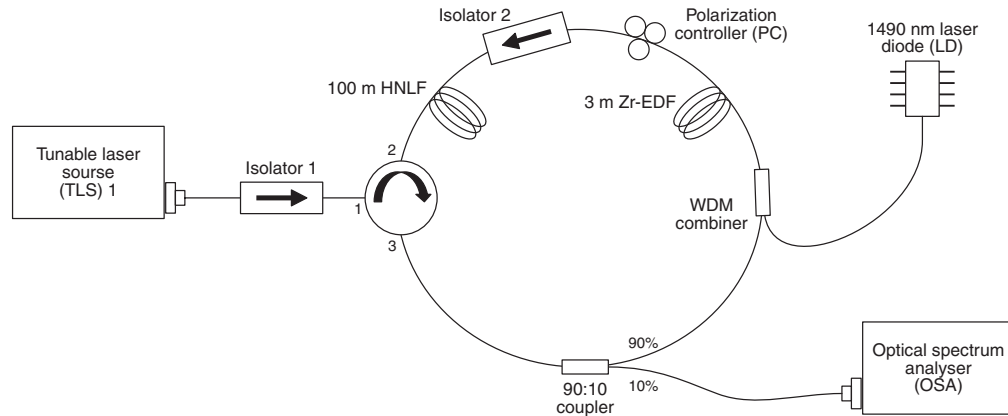


Figure 2 Experimental setup for the proposed a Zr-EDF based multi-wavelength ring laser

tinue to propagate to the Zr-EDF. The resulting interaction between P_p , P_s , and zirconia ions will result in the generation of side-bands from the FWM effect. P_p , P_s , and the generated side-bands now travel through Isolator 2 and the optical circulator until they reach the 90:10 fused coupler, where 90% of the generated signal continues to propagate in the ring cavity, while 10% is extracted for further analysis.

Besides Fig. 1a and Fig. 1b, Fig. 2 provides the extended improvement of Fig. 1b as to provide a higher output signal and also for multi-wavelength generation. The configuration of Fig. 2 is based on Fig. 1b and is therefore similar in design, with only two design modifications.

The first modification is the addition of a 100 m long HNLF with a nominal ZDW at 1531 nm as well as a loss coefficient, dispersion slope and nonlinear parameter of 0.73 dB/km, 0.007 ps/nm²/km and 10.8 W⁻¹km⁻¹, respectively, which acts as a medium to boost up the FWM signal generated by the ring cavity. The cavity design is also slightly simpler, with only a single TLS (TLS1), with the signal of TLS1 entering Port 1 of the optical circulator and exiting at Port 2. It is then reflected by the isolator into Port 2 and out through Port 3 where it will pass a 90:10 fused coupler in the anti-clockwise direction. The signal will be amplified by the Zr-EDF which is pumped as in Fig. 1b. A PC is used to optimize the generation of signals based on the FWM effect. The results obtained are presented in the following section.

3. Results and discussion

In the case of non-degenerate FWM, two pump frequencies at v_1 and v_2 co-propagate with a signal frequency of v_3 . In this scenario, the three propagating frequencies will generate a fourth frequency v_4 , where $v_4 = v_1 + v_2 - v_3$. In the special case of degenerate FWM, whereby two high-

intensity waves at frequencies $v_1 = v_2$ and $v_3 = v_4$ interact, the mixing process generates two new waves at frequencies of $2v_1 - v_3$ and $2v_3 - v_1$ [35]. In the case of the linear cavity configuration of Fig. 1a, using the equation for the degenerate case, with the frequency v_1 equals to the pump frequency (wavelength of 1604.0 nm) and v_3 is the signal frequency (1605.0 nm) the calculated value for the generated sideband C_1 equals to a wavelength of 1603.0 nm. For S_1 , the wavelength value obtained is 1606.3 nm. This augurs well with the measured value from Fig. 3, with two sidebands observed at 1603.1 nm (C_1) and 1606.1 nm (S_1). The powers of the C_1 and S_1 are -79.5 and -79.1 dBm respectively, approximately 67 dB lower than the pump and signal waves of -12.0 dBm.

In the case of the ring configuration of Fig. 1b, the generated sidebands C_1 and S_1 are observed at 1603.0 and 1606.2 nm as shown in Fig. 4. As with the case of the linear cavity, the wavelengths of the generated sidebands correspond closely with the predicted values of 1603.0 and 1606.3 nm for C_1 and S_1 , respectively (which is expected as the pump and signal frequencies have been kept constant for both configurations). In the ring configuration however, the power of the generated sidebands is much higher, with C_1 having a power of -59.8 dBm and S_1 having a power of -53.4 dBm. This is an increase of power of between 19.7 to 25.4 dB as compared to that of the linear cavity configuration. Furthermore, the generated sidebands are 50 dB lower than the pump and signal waves, which is of a better value as compared to the linear cavity. The higher powered sidebands in the ring configuration can be attributed to the multiple passes occurring in the cavity.

Fig. 5 shows the power of the C_1 sideband as a function of the changing signal wavelength. It can be seen that the power of the C_1 sideband in the linear configuration is low, at -77 dBm, and drops to -80 dBm as the wavelength of P_s is changed from 1601 to 1611 nm. The power of C_1 however remains relatively unchanged for the entire wave-

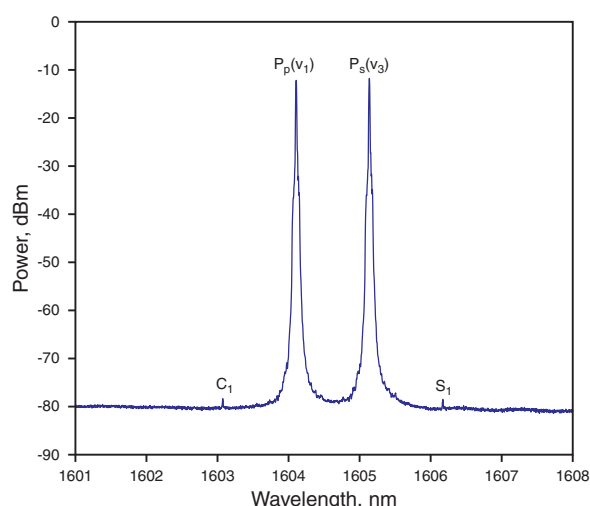


Figure 3 (online color at www.lasphys.com) The spectrum of the generated FWM effect in the linear cavity configuration, with sideband frequencies generated at C_1 and S_1

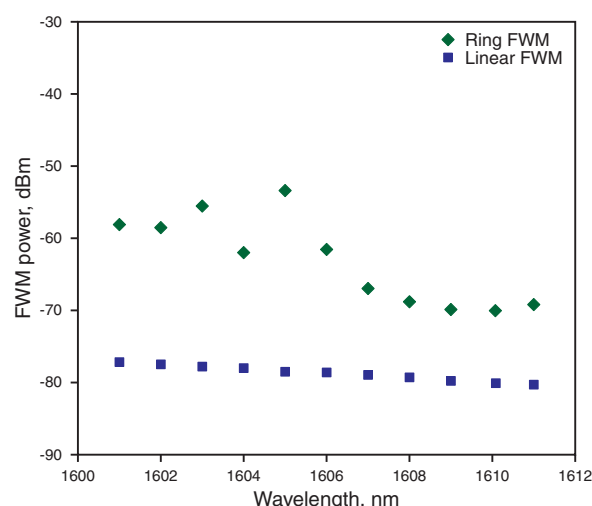


Figure 5 (online color at www.lasphys.com) The power of the C_1 sideband against of signal wavelength in the ring configuration

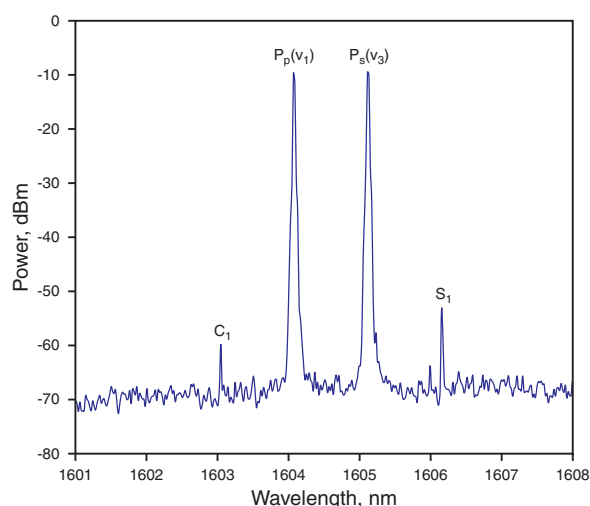


Figure 4 (online color at www.lasphys.com) The spectrum of the generated FWM effect in the ring cavity configuration with sideband frequencies generated at C_1 and S_1

length span. The power of the C_1 sideband generated in the ring configuration on the other hand is higher at an average of -62 dBm. However, the power of the generated sideband fluctuates substantially between a low of -69 dBm to a high of -53 dBm as the wavelength of P_s is changed from 1601 to 1611 nm. It can therefore be inferred that the ring cavity provides a better output power as compared to the linear cavity, whilst the linear cavity has the advantage

of a nearly flat output power against the changing of the signal wavelengths.

From this work, the FWM effect can be utilized to generate a multi-wavelength output as given in the experimental setup of Fig. 2. In this setup, the dominant wavelength oscillating in the ring cavity is used as the pump wavelength, with the TLS providing the signal wavelength. The dominant wavelength is obtained by operating the system without any input from the TLS; thus the lasing wavelength with the highest intensity that is oscillating in the ring cavity is the dominant wavelength. The interaction between the high intensity pump and signal wavelengths fulfills the conditions for degenerate FWM, thereby generating sidebands at $2v_1 - v_3$ and $2v_3 - v_1$. As the sidebands generated are also of high intensity (although not as high as the originating pump and signal wavelengths), further sidebands are now obtained, giving a multi-wavelength comb as shown in Fig. 6a, Fig. 6b, and Fig. 6c.

At a laser diode (LD) drive current of 184 mA, as in Fig. 6a, the dominant wavelength is obtained at 1606.2 nm, designated as the signal wavelength, P_s , with a power of -4.8 dBm. The pump wavelength P_p is obtained from the TLS at 1605.2 nm and a power of 12.0 dBm (although the power of P_p that oscillates in the ring cavity is only 4.3 dBm as a result of losses in the setup). Both P_p and P_s interact through the degenerate FWM process to generate two sidebands, C_1 and S_1 at 1604.2 and 1607.1 nm, respectively, agreeing well with its predicted values of 1604.2 and 1607.2 nm. As both C_1 and S_1 are of sufficiently high power, S_1 is able to interact with P_s to further generate two new signals at 1605.2 and 1608.1 nm (coinciding with the predicted values of 1605.3 and 1608.0 nm). The wavelength at 1605.3 nm over-

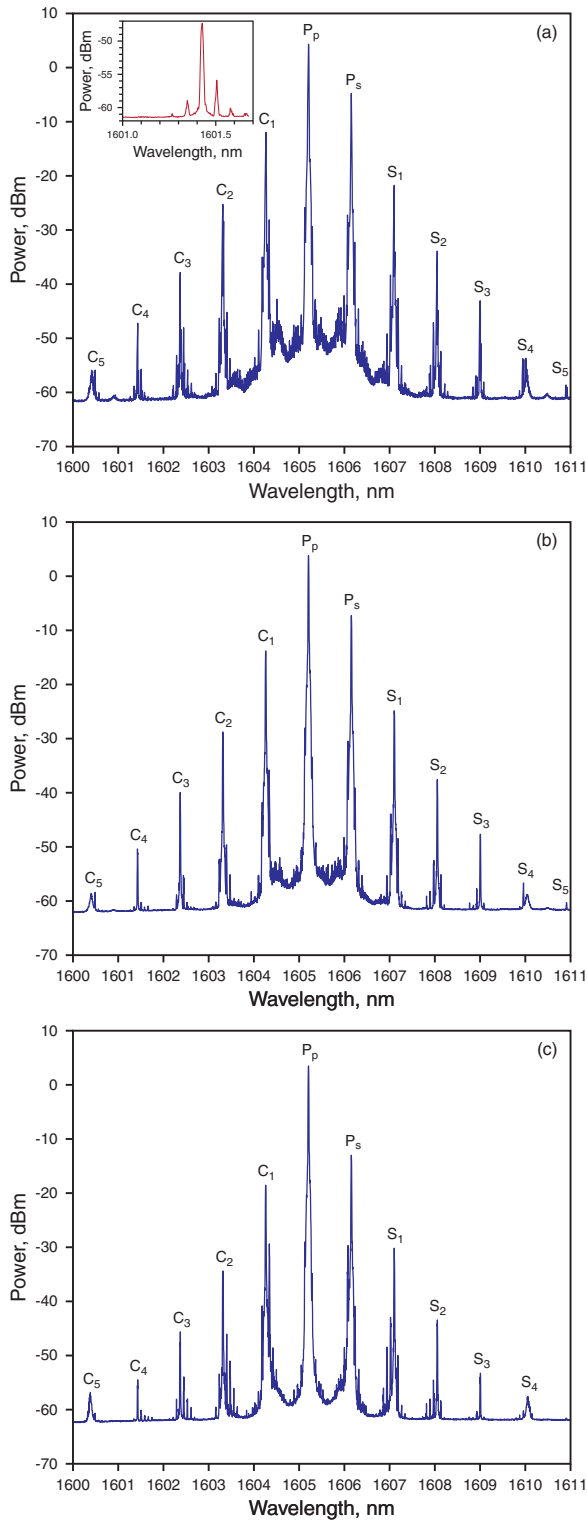


Figure 6 (online color at www.lasphys.com) Output spectrum of the proposed Zr-EDF based multi-wavelength ring laser at different LD drive currents of (a) 184 mA, (b) 170 mA, and (c) 160 mA

laps with P_p , while the wavelength at 1608.1 nm forms a new sideband, designated S_2 . Similarly, S_1 and S_2 are also able to interact with each other due to their adequate power levels, thereby generating another two wavelengths at 1606.1 and 1609.0 nm as predicted. As before, the wavelength generated at 1606.1 nm overlaps with P_s , while the wavelength at 1609.0 nm forms a new sideband, S_3 . S_3 and S_2 will also interact to form wavelengths new wavelengths at 1608.1 and 1609.9 nm, whereby the wavelength at 1608.1 nm will overlap with the already oscillating wavelength of 1607.1 nm, and the wavelength at 1609.9 nm forming a new sideband, S_4 . The power of S_4 is low at only -54 dBm, though it is still able to interact with S_3 to generate a new sideband, S_5 at 1610.9 nm (with the other wavelength generated overlapping the oscillating wavelength of S_2), subsequent interactions are not observed. The same process repeats itself with the generation of sidebands in the shorter wavelengths, from C_1 with a wavelength of 1604.3 nm to C_5 with a wavelength of 1600.4 nm. All generated sidebands agree well with their theoretically predicted values.

At a lower LD drive current of 170 mA, a similar wavelength comb is observed in Fig. 6b with no difference in the wavelengths of P_p and P_s or the generated sidebands S_1 to S_5 and C_1 to C_5 . However, the power of P_s is lower at only -9.8 dBm, as compared to -4.8 dBm in Fig. 6a. P_p is also lower at 2.2 dBm. This lower power is attributed to less gain available due the lower LD pump power, and thus the generated sidebands are also of lower power as predicted. A result of this lower power is an almost non-existent S_5 sideband, with S_5 being only a small spike of -60 dBm in Fig. 6b. C_5 however has a peak power of -59.6 dBm, only slight lower than its power of -57.8 dBm as observed in Fig. 6a. At the lowest LD drive current of 160 mA, as shown in Fig. 6c, the same wavelength comb is observed, with no changes to the wavelengths of P_p , P_s , or its sidebands. However, due to the low powers of P_p and P_s (2.5 and -12.9 dBm, respectively), the subsequent sidebands generated are also of lower power and thus S_4 now cannot interact properly with S_3 to generate new sidebands. Therefore no lasing wavelength is observed after S_4 . From this, it can be inferred that as the drive current continues to be lowered, less and less sidebands will be generated due to insufficient power for the FWM effect, as would be expected.

Furthermore, for each lasing wavelength in Fig. 6a to Fig. 6c, several closely spaced lasing lines are also observed to be generated around the main lasing wavelength. These lasing lines, which are more visible towards the longer and shorter wavelengths, are observed to have spacings of approximately 0.08 nm, and can therefore be attributed to the Brillouin effect. The inset of Fig. 6a shows the wavelength C_3 along with the Brillouin generated sidebands.

It is observed that in this setup, the Zr-EDF plays two roles; to initiate the FWM effect in the fiber as well as to act as a gain medium for the generated wavelengths. A multi-wavelength fiber laser based on this configuration

would have many uses in telecommunications and sensing applications where consistent channel spacing is required.

4. Conclusion

In this work, the generation and performance of the FWM effect in the linear and ring cavity is investigated. A 3 m long Zr-EDF with a erbium ion concentration of 3000 ppm and non-linear coefficient value of $14 \text{ W}^{-1}\text{km}^{-1}$, as well as chromatic dispersion and dispersion slope of 28.45 ps/nm/km and $3.63 \text{ ps/nm}^2/\text{km}$ is used as the non-linear medium. The Zr-EDF is pumped by 1460 and 1490 nm laser diodes as to make the fiber transparent to incoming signals in the wavelength region from 1500 to 1600 nm. The pump and signal wavelengths are set to 1604.0 and 1605.0 nm at -12.0 dBm , and generates two sidebands, C_1 and S_1 at 1603.1 and 1606.1 nm respectively, in agreement with the theoretically predicted values. For the linear cavity, the C_1 and S_1 powers are -79.5 and -79.1 dBm , while for the ring cavity higher C_1 and S_1 powers of -59.8 and -53.4 dBm are obtained, an increase of 19.7 to 25.4 dB respectively. The linear configuration however shows a more stable sideband power as the wavelength of the signal changes in comparison to the ring configuration. The FWM effect is also examined in an enhanced ring configuration, using only a single TLS and a 100 m long HNLF with a nominal ZDW at 1531 nm and nonlinear parameter of $10.8 \text{ W}^{-1}\text{km}^{-1}$. The enhanced configuration uses the dominant wavelength in the ring cavity as the signal wavelength, while the TLS provides the pump wavelength. The resulting FWM interaction can generate up to 10 sidebands, but reducing the gain of the Zr-EDF by lowering the pump LD drive current will reduce the number of sidebands generated. Additional lasing wavelengths with very close spacings are also observed around each generated sideband and attributed to the Brillouin effect. The proposed configuration provides a multi-wavelength source with consistent channel spacing for many applications in sensing and telecommunications.

Acknowledgements We would like to thank M. Paul of the Central Glass and Ceramic Research Institute (CGCRI), India for providing the Zr-EDF. We would also like to thank the University of Malaya for providing the HIR Grant (Terahertz, UM/C/HIR/MOHE/SC/O1), MOHE for funding this project.

References

- [1] H. Ahmad, M.Z. Zulkifli, A.A. Latif, K. Thambiratnam, and S.W. Harun, *Laser Phys.* **19**, 2188 (2009).
- [2] J. Chow, G. Town, B. Eggleton, M. Ibsen, K. Sugden, and I. Bennion, *IEEE Photon. Technol. Lett.* **8**, 60 (1996).
- [3] X.P. Dong, S.P. Li, K.S. Chiang, M.N. Ng, and B.C.B. Chu, *Electron. Lett.* **36**, 1609 (2000).
- [4] L. Talaverano, S. Abad, S. Jarabo, and M. López-Amo, *J. Lightwave Technol.* **19**, 553 (2001).
- [5] S. Shahi, S.W. Harun, A.H. Sulaiman, K. Thambiratnam, and H. Ahmad, *Microwave Opt. Technol. Lett.* **51**, 110 (2009).
- [6] S.W. Harun, F.A. Rahman, K. Dimiyati, and H. Ahmad, *Laser Phys. Lett.* **3**, 495 (2006).
- [7] H. Ahmad, K. Thambiratnam, A.H. Sulaiman, N. Tamchek, and S.W. Harun, *Laser Phys. Lett.* **5**, 726 (2008).
- [8] S. Shahi, S.W. Harun, K. Dimiyati, M.R. Tamjis, and H. Ahmad, *Microwave Opt. Technol. Lett.* **52**, 1416 (2010).
- [9] M.P. Fok and C. Shu, *Opt. Express* **14**, 2618 (2006).
- [10] S.W. Harun, R. Parvizi, S. Shahi, and H. Ahmad, *Laser Phys. Lett.* **6**, 813 (2009).
- [11] X.F. Yang, X.Y. Dong, S.M. Zhang, F.Y. Lu, X.Q. Zhou, and C. Lu, *IEEE Photon. Technol. Lett.* **17**, 2538 (2005).
- [12] R.-J. Essiambre, B. Mikkelsen, and G. Raybon, *Electron. Lett.* **35**, 1576 (1999).
- [13] I. Shake, H. Takara, K. Mori, S. Kawanishi, and Y. Yamabayashi, *Electron. Lett.* **34**, 1600 (1998).
- [14] N. Kashyap, P.H. Siegel, and A. Vardy, *IEEE Trans. Inf. Theory* **52**, 64 (2006).
- [15] S.O. Konorov, E.E. Serebryannikov, D.A. Akimov, A.A. Ivanov, M.V. Alfimov, and A.M. Zheltikov, *Phys. Rev. E* **70**, 066625 (2004).
- [16] L. Deng and M.G. Payne, *Phys. Rev. Lett.* **91**, 243902 (2003).
- [17] G.P. Agrawal, *Nonlinear Fiber Optics* (Academic, San Diego, 2001).
- [18] X.M. Liu, X.Q. Zhou, and C. Lu, *Phys. Rev. A* **72**, 013811 (2005).
- [19] J.S. Wang, E.M. Vogel, and E. Snitzer, *Opt. Mater.* **3**, 187 (1994).
- [20] M.E. Marhic, I. Morita, M.-C. Ho, Y. Akasaka, and L.G. Kazovsky, *Electron. Lett.* **35**, 2045 (1999).
- [21] H. Masuda, A. Mori, K. Shikano, K. Oikawa, K. Kato, and M. Shimizu, in: *Conference on Optical Fiber Communication Anaheim, CA, USA, March 17–22, 2002 (OFC 2002)*, paper ThB6.
- [22] D. Marchese, M. De Sario, A. Jha, A.K. Kar, and E.C. Smith, *J. Opt. Soc. Am. B* **15**, 2361 (1998).
- [23] J.A. Moon and D.T. Schaafsma, *Fiber Integr. Opt.* **19**, 201 (2000).
- [24] M. Asobe, H. Kobayashi, H. Itoh, and T. Kanamori, *Opt. Lett.* **18**, 1056 (1993).
- [25] M. Asobe, T. Kanamori, K. Naganuma, H. Itoh, and T. Kaino, *J. Appl. Phys.* **77**, 5518 (1995).
- [26] T. Hasegawa, T. Nagashima, and N. Sugimoto, *Opt. Commun.* **281**, 782 (2008).
- [27] K.K. Qureshi, S.-H. Wang, P.K.A. Wai, H.Y. Tam, C. Lu, and N. Sugimoto, *Opt. Commun.* **275**, 223 (2007).
- [28] E. Snoeks, P.G. Kik, and A. Polman, *Opt. Mater.* **5**, 159 (1996).
- [29] D.M. Gill, L. McCaughan, and J.C. Wright, *Phys. Rev. B* **53**, 2334 (1996).
- [30] G.E. Keiser, *Opt Fiber Technol.* **5**, 3 (1999).
- [31] J.R. Armitage, *J. Quantum Electron.* **26**, 423 (1990).
- [32] B. Pedersen, A. Bjarklev, J.H. Povlsen, K. Dybdal, and C.C. Larsen, *J. Lightwave Technol.* **9**, 1105 (1991).
- [33] J.H. Yang, S.X. Dai, Y.F. Zhou, L. Wen, L.L. Hu, and Z.H. Jiang, *J. App. Phys.* **93**, 977 (2003).
- [34] P. Peterka, B. Faure, W. Blanc, M. Karásek, and B. Dussardier, *Opt. Quantum Electron.* **36**, 201 (2004).
- [35] J. Toulouse, *J. Lightwave Technol.* **23**, 3625 (2005).

Fabrication and application of zirconia-erbium doped fibers

H. Ahmad,¹ K. Thambiratnam,^{1,*} M. C. Paul,² A. Z. Zulkifli,¹ Z. A. Ghani,³ and S. W. Harun¹

¹Photonics Research Centre, University of Malaya, 50603 Kuala Lumpur, Malaysia

²Fiber Optics and Photonics Division, Central Glass & Ceramic Research Institute-CSIR, Kolkata, India

³Faculty of Applied Sciences, Universiti Teknologi MARA, Puncak Alam, Shah Alam, 40450 Selangor Darul Ehsan, Malaysia

*kavintheran@gmail.com

Abstract: In this work, the fabrication of a Zirconia-Erbium co-Doped Fiber (Zr-EDF) and its application in the generation of non-linear effects as well as use in a compact pulsed fiber laser system is described. The Zr-EDF is fabricated by the Modified Chemical Vapor Deposition (MCVD) technique in combination with solution doping to incorporate the glass modifiers and nucleating agent. The resulting preforms are annealed and drawn into fiber strands with a $125.0 \pm 0.5 \mu\text{m}$ diameter. Two Zr-EDFs, ZEr-A and ZEr-B, are fabricated with erbium ion concentrations of 2800 and 3888 ppm/wt and absorption rates of 14.5 and 18.3 dB/m at 980 nm respectively. Due to its higher erbium dopant concentration, a 4 m long ZEr-B is used to demonstrate the generation of the Four-Wave-Mixing (FWM) effect in the Zr-EDF. The measured FWM power levels agree well with theoretical predictions, giving a maximum FWM power - 45 dBm between 1558 nm to 1565 nm, and the generated sidebands are as predicted. The non-linear coefficient of ZEr-B is measured to be $14 \text{ W}^{-1}\text{km}^{-1}$, with chromatic and slope dispersion values of 28.45 ps/nm.km and 3.63 ps/nm².km respectively. The ZEr-B is also used together with a graphene based saturable absorber to create a compact, passively Q-switched fiber laser. Short pulses with a pulse width of 8.8 μs and repetition rate of 9.15 kHz are generated at a pump power of 121.8 mW, with a maximum average output power of 161.35 μW and maximum pulse energy value of 17.64 nJ. The fabricated Zr-EDF has many potential applications in multi-wavelength generation as well as in the development of compact, pulsed laser sources.

©2012 Optical Society of America

OCIS codes: (140.3500) Lasers, erbium; (140.3510) Lasers, fiber; (160.2290) Fiber materials; (160.4330) Nonlinear optical materials; (060.4370) Nonlinear optics, fibers; (060.7140) Ultrafast processes in fibers.

References and links

1. G. E. Keiser, "A review of WDM technology and applications," *Opt. Fiber Technol.* **5**(1), 3–39 (1999).
2. R. Ramaswami, "Optical fiber communication: from transmission to networking," *IEEE Commun. Mag.* **40**(5), 138–147 (2002).
3. M. Wasfi, "Optical fiber amplifiers – review," *Int. J. Commun. Netw. Inf. Secur.* **1**, 42–47 (2009).
4. D. Richardson, J. Nilsson, and W. Clarkson, "High power fiber lasers: current status and future perspectives [Invited]," *J. Opt. Soc. Am. B* **27**(11), B63–B92 (2010).
5. H. Ahmad, M. Z. Zulkifli, A. A. Latif, K. Thambiratnam, and S. W. Harun, "17-channels S band multiwavelength brillouin/erbium fiber laser co-pump with Raman source," *Laser Phys.* **19**(12), 2188–2193 (2009).
6. K. Inoue and H. Toba, "Wavelength conversion experiment using fiber four-wave mixing," *IEEE Photon. Technol. Lett.* **4**(1), 69–72 (1992).
7. E. Yahel and A. Hardy, "Amplified spontaneous emission in high-power, $\text{Er}^{3+}/\text{Yb}^{3+}$ codoped fiber amplifiers for wavelength-division-multiplexing applications," *J. Opt. Soc. Am. B* **20**(6), 1198–1203 (2003).

8. M. J. Yadlowsky, E. M. Deliso, and V. L. Da Silva, "Optical fibers and amplifiers for WDM systems," *Proc. IEEE* **85**(11), 1765–1779 (1997).
9. E. Snoeks, P. G. Kik, and A. Polman, "Concentration quenching in erbium implanted alkali silicate glass," *Opt. Mater.* **5**(3), 159–167 (1996).
10. D. M. Gill, L. McCaughan, and J. C. Wright, "Spectroscopic site determinations in erbium-doped lithium niobate," *Phys. Rev. B Condens. Matter* **53**(5), 2334–2344 (1996).
11. M. C. Paul, S. W. Harun, N. A. D. Huri, A. Hamzah, S. Das, M. Pal, S. K. Bhadra, H. Ahmad, S. Yoo, M. P. Kalita, A. J. Boyland, and J. K. Sahu, "Wideband EDFA based on erbium doped crystalline zirconia yttria alumino silicate fiber," *J. Lightwave Technol.* **28**(20), 2919–2924 (2010).
12. M. C. Paul, S. W. Harun, N. A. D. Huri, A. Hamzah, S. Das, M. Pal, S. K. Bhadra, H. Ahmad, S. Yoo, M. P. Kalita, A. J. Boyland, and J. K. Sahu, "Performance comparison of Zr-based and Bi-based erbium-doped fiber amplifiers," *Opt. Lett.* **35**(17), 2882–2884 (2010).
13. J. R. Armitage, "Spectral dependence of the small-signal gain around 1.5 μm in erbium doped silica fiber amplifiers," *IEEE J. Quantum Electron.* **26**(3), 423–425 (1990).
14. B. Pedersen, A. Bjarklev, J. H. Povlsen, K. Dybdal, and C. C. Larsen, "The design of erbium-doped fiber amplifiers," *J. Lightwave Technol.* **9**(9), 1105–1112 (1991).
15. J. Yang, S. Dai, Y. Zhou, L. Wen, L. Hu, and Z. Jiang, "Spectroscopic properties and thermal stability of erbium-doped bismuth-based glass for optical amplifier," *J. Appl. Phys.* **93**(2), 977–983 (2003).
16. P. Peterka, B. Faure, W. Blanc, M. Karásek, and B. Dussardier, "Theoretical modeling of S-band thulium-doped silica fiber amplifiers," *Opt. Quantum Electron.* **36**(1-3), 201–212 (2004).
17. R.-J. Essiambre, B. Mikkelsen, and G. Raybon, "Intra-channel cross phase modulation and four-wave-mixing in high speed TDM systems," *Electron. Lett.* **35**(18), 1576–1578 (1999).
18. I. Shake, H. Takara, S. Kawanishi, and Y. Yamabayashi, "Optical signal quality monitoring method based on optical sampling," *Electron. Lett.* **34**(22), 2152–2154 (1998).
19. N. Kashyap, P. H. Siegel, and A. Vardy, "Coding for the optical channel: the ghost-pulse constraint," *IEEE Trans. Inf. Theory* **52**(1), 64–77 (2006).
20. S. Harun, R. Parvizi, S. Shahi, and H. Ahmad, "Multi-wavelength erbium-doped fiber laser assisted by four-wave mixing effect," *Laser Phys. Lett.* **6**(11), 813–815 (2009).
21. X. F. Yang, X. Dong, S. Zhang, F. Lu, X. Zhou, and C. Lu, "Multi-wavelength erbium doped fiber laser with 0.8 nm spacing using sampled Bragg grating and photonic crystal fiber," *IEEE Photon. Technol. Lett.* **17**(12), 2538–2540 (2005).
22. H. Ahmad, M. C. Paul, N. A. Awang, S. W. Harun, M. Pal, and K. Thambiratnam, "Four-wave-mixing in zirconia-yttria-aluminum erbium codoped silica fiber," *J. Eur. Opt. Soc. Rapid Publ.* **7**, 12011 (2012).
23. D. Popa, Z. Sun, T. Hasan, F. Torrisi, F. Wang, and A. C. Ferrari, "Graphene Q-switched, tunable fiber laser," *Appl. Phys. Lett.* **98**(7), 073106 (2011).
24. R. J. Williams, N. Jovanovic, G. D. Marshall, and M. J. Withford, "All-optical, actively Q-switched fiber laser," *Opt. Express* **18**(8), 7714–7723 (2010).
25. W.-J. Cao, H.-Y. Wang, A.-P. Luo, Z.-C. Luo, and W.-C. Xu, "Graphene-based, 50 nm wide-band tunable passively Q-switched fiber laser," *Laser Phys. Lett.* **9**(1), 54–58 (2012).
26. M. L. Siniava, M. N. Siniavsky, V. P. Pashinin, A. A. Mamedov, V. I. Konov, and V. V. Kononenko, "Laser ablation of dental materials using microsecond Nd:YAG laser," *Laser Phys.* **19**(5), 1056–1060 (2009).
27. H. Q. Shangquan, L. W. Casperson, A. Shearin, K. W. Gregory, and S. A. Prahl, "Drug delivery with microsecond laser pulses into gelatin," *Appl. Opt.* **35**(19), 3347–3357 (1996).
28. F. Wang, A. G. Rozhin, V. Scardaci, Z. Sun, F. Hennrich, I. H. White, W. I. Milne, and A. C. Ferrari, "Wideband-tunable, nanotube mode-locked, fibre laser," *Nat. Nanotechnol.* **3**(12), 738–742 (2008).
29. A. G. Rozhin, V. Scardaci, F. Wang, F. Hennrich, I. H. White, W. I. Milne, and A. C. Ferrari, "Generation of ultra-fast laser pulses using nanotube mode-lockers," *Phys. Status Solidi B* **243**(13), 3551–3555 (2006).
30. T. R. Schibli, K. Minoshima, H. Kataura, E. Itoga, N. Minami, S. Kazaoui, K. Miyashita, M. Tokumoto, and Y. Sakakibara, "Ultrashort pulse-generation by saturable absorber mirrors based on polymer-embedded carbon nanotubes," *Opt. Express* **13**(20), 8025–8031 (2005).
31. F. Bonaccorso, Z. Sun, T. Hasan, and A. C. Ferrari, "Graphene photonics and optoelectronics," *Nat. Photonics* **4**(9), 611–622 (2010).

1. Introduction

The advent of the in-line optical amplifier in the later part of the 20th century acted as a catalyst for the exponential growth of optical communications around the world. In-line optical amplifiers or Fiber Optical Amplifiers (FOAs) were instrumental in overcoming the constraints inherent in electronic regenerators and allowed for the amplification of multiple signals simultaneously, thereby making possible the commercial communications networks that span the globe today [1–3]. Furthermore, recent technological advances have also opened up a variety of new prospects for FOAs, such as the generation of single and multi-

wavelength fiber lasers [4,5], wavelength converters [6] and wide-band spectral sources [7], thus making the FOA a focal point of research and development.

The Erbium Doped Fiber Amplifier (EDFA) has long been the dominant technology for the development of FOAs due to its relatively low-cost per wavelength, low complexity and high stability [1,8]. However, the EDFA does have its limitations; most notably is that the concentration of erbium ions, the active medium of the FOA, cannot be increased significantly without encountering detrimental effects such as concentration quenching [9] and cluster formation [10]. In order to overcome this problem, and to address the rising need for compact and lower cost FOAs, research has now turned towards the exploration of new materials to act as hosts or co-dopants for the purpose of creating highly-doped EDFAs. In this regard, the element zirconium is a highly promising candidate towards achieving this goal. Zirconium ions co-doped in a silica host matrix demonstrate a high refractive index of over 1.45 in the visible and near infrared spectrum [11,12], thereby displaying wider emission and absorption bandwidths and allowing more channels to be amplified as compared to materials with a lower refractive index. This behavior is in accordance with the Fuchtbauer–Ladenberg relationship [13,14] and Judd–Ofelt theory [15,16]. Additionally, silica fibers co-doped with zirconium ions possess significant mechanical strength, are not hygroscopic and are able to resist to chemical corrosion. They also demonstrate excellent compatibility with conventional silica based optical fibers, thus making them useful for real-world applications.

Furthermore, zirconium co-doped fibers have demonstrated substantial non-linear characteristics. While detrimental towards high data-rate optical communications [17–19], non-linear phenomenon such as Four-Wave Mixing (FWM) and Self-Phase Modulation (SPM) have tremendous potential for the development of new, cost-effective applications such as multi-wavelength sources, wavelength converters and supercontinuum sources [20,21]. The FWM effect is of significant interest, due to its tremendous prospective in the development of stable and low cost multi-wavelength sources with channel spacings that are suitable for Dense Wavelength Division Multiplexing (DWDM) applications. However, generating the FWM effect is challenging due to the need to maintain phase matching between the propagating wavelengths, and the long lengths of fiber needed to generate the FWM effect make maintaining phase matching difficult. In this regard, the zirconium co-doped fiber is a promising candidate for generating the FWM effect, exhibiting non-linear behavior in only short fiber lengths [22] and therefore able to overcome the complexities of phase matching.

In this work, the fabrication and characterization of a Zirconium-Erbium co-Doped Fiber (Zr-EDF) is described, as well as its application as a non-linear gain medium and compact, linear gain medium for pulsed fiber lasers. The next section will examine the fabrication process, while the following section will detail the characterization of the physical and optical characteristics of the Zr-EDF. The successive sections will outline the application of the Zr-EDF, first as a non-linear gain medium for the generation of the FWM effect, and secondly as a short-length gain medium in a compact, passively Q-switched fiber laser using a graphene based Saturable Absorber (SA).

2. Fabrication

The fabrication of the Zr-EDF is a three-stage process. The process begins with the fabrication of a conventional silica preform using the Modified Chemical Vapor Deposition (MCVD) technique. Figure 1(a) shows the setup of the MCVD system, while Fig. 1(b) shows the actual system. The fiber preform is fabricated by passing SiCl_4 and POCl_3 vapors through a slowly rotating silica tube. An external flame source moves along the length of the tube as it rotates, heating the tube and its contents to a temperature of between 1350°C and 1400°C. This high temperature causes the chloride vapors to oxidize, and results in the deposition of a porous phospho-silica layer along the inner diameter of the silica tube.

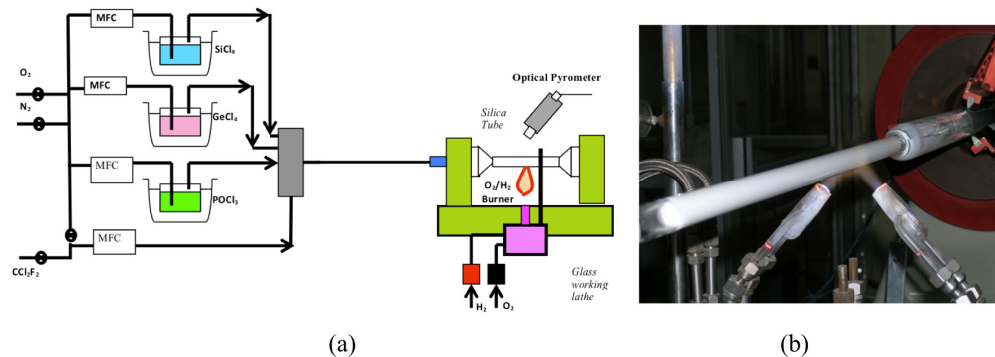


Fig. 1. (a) Setup of the MCVD system and (b) the formation of the silica preform.

Once an even phospho-silica layer is obtained along the inner wall of the silica tube, the second stage of the fabrication process begins. In this stage, the silica tube with the porous phospho-silica layer on its inner wall undergoes a solution doping process where the glass modifiers ZrO_2 , Y_2O_3 , Al_2O_3 and Er_2O_3 are added. These modifiers are first mixed with an alcohol and water solution at a 1:5 ratio to form the complex ions $\text{ZrOCl}_2 \cdot 8\text{H}_2\text{O}$, $\text{YCl}_3 \cdot 6\text{H}_2\text{O}$, $\text{AlCl}_3 \cdot 6\text{H}_2\text{O}$ and $\text{ErCl}_3 \cdot 6\text{H}_2\text{O}$ that is then incorporated into the glass matrix of the silica tube by solution doping. At this stage also, small quantities of Y_2O_3 and P_2O_5 are added to the glass matrix to function as nucleating agents as well as to increase the phase separation of the Er_2O_3 doped micro-crystallites that form in the core matrix of the optical fiber preform. The concentration of the dopant constituents is optimized so as to give a fiber with a Numerical Aperture (NA) of 0.17 to 0.20. The addition of Y_2O_3 also serves a secondary purpose, which is to slow down or eliminate changes in the ZrO_2 crystal structure. This is because in a bulk glass matrix, pure zirconium can exist in three distinct crystalline phases, depending on the temperature range. At temperatures of above 2350°C , the ZrO_2 crystallites take on a cubic structure, while at lower temperatures of between 1170 and 2350°C they form a tetragonal structure instead and at temperatures of below 1170°C form a mono-clinic structure. The detrimental effect of these changes arises during the shift from the tetragonal to monoclinic phases, which is very fast and accompanied by an increase in volume of between 3 to 5%. This rapid increase causes significant cracking in the developed fiber during the cooling process (observed primarily in the core region, as this is where the concentration of ZrO_2 crystallites is the highest) and destroys the mechanical properties of the fiber. Adding a small amount of Y_2O_3 , or oxides such as MgO , CaO can slow or stop down the changes in the crystalline structure, thereby preserving the mechanical strength and integrity of the fiber.

The final phase of the fabrication process involves the annealing of the fabricated preform after the solution deposition process. The preform is annealed at a temperature of 1100°C over a duration of 3 hours in a closed furnace, with a heating and cooling rate of $20^\circ\text{C}/\text{min}$ so as to create Er_2O_3 and ZrO_2 rich micro-crystallites. Once the preform has been annealed, it is collapsed into a solid rod at a temperature of more than 2000°C and then drawn into a fiber strand with a $125.0 \pm 0.5\mu\text{m}$ diameter through a conventional fiber-drawing tower. The temperature of 2000°C is below the melting temperature of the ZrO_2 crystallites but above the melting temperature of glass, thus allowing the ZrO_2 crystallites to retain their crystalline structure inside the silica glass matrix. Once the fiber has been drawn, the primary and secondary coatings, Desolite DP-1004 and Desolite DS-2015 is added to the fiber and the coating uniformity is assured by controlling the flow pressure of the inlet gases into the primary and secondary coating resin vessels during the drawing process, as well as the proper alignment of the primary and secondary coating cup units. The fiber diameter is also closely controlled during the drawing process to ensure that a high quality fiber is produced.

3. Optical characteristics of the Zr-EDF

Characterization of the Zr-EDF is carried out at both the preform stage and also using the completed fiber. Using selected preform samples, morphology of the core region was analyzed using a Field-Emission Gun Scanning Electron Microscopy (FEGSEM), while dopant concentration of each sample was determined using Electron Probe Microanalyses (EPMA). Two different preforms were prepared with different Er_2O_3 and ZrO_2 dopant levels by changing the composition of $\text{ErCl}_3 \cdot 6\text{H}_2\text{O}$ and $\text{ZrOCl}_2 \cdot 8\text{H}_2\text{O}$ during solution doping process, while the Al_2O_3 content is kept constant for both fiber samples. These preforms, and the resultant fibers drawn from them are designated as ZEr-A and ZEr-B. As the ZrO_2 crystallites are able to sustain their crystalline structures at high temperatures, above the temperature required to collapsed the silica rod and draw the fiber from the preform, therefore the existence of some ZrO_2 crystallites are expected within the host matrix of the preform. The microstructure of the doping region of ZEr-A and ZEr-B, which are developed without any thermal treatment or annealing, are given in Fig. 2.

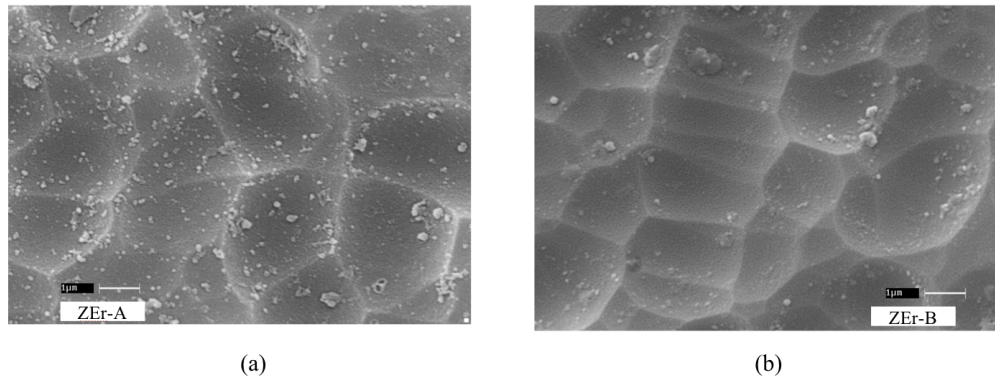


Fig. 2. The microstructure of the core region of the (a) ZEr-A preform and (b) the ZEr-B preform.

The boundaries of the ZrO_2 crystallites in the glass matrix of the optical preform can be seen clearly in the figure, and it is observed that the boundaries of the ZrO_2 crystallites are larger and better defined in ZEr-B than similar crystallites in ZEr-A. This is attributed to the higher concentration of ZrO_2 used in the fabrication of ZrO_2 . The results of the EPMA analysis of the dopant concentrations for the fabricated fibers are given in Table 1, which shows the Al_2O_3 , ZrO_2 and Er_2O_3 dopant concentrations in ZEr-A and ZEr-B. Both fiber preforms have approximately the same Al_2O_3 dopant levels of about 24 to 25 mol%. However, the ZEr-B fiber has a much higher ZrO_2 dopant concentration, almost quadruple that of ZEr-A, as well as close an Er_2O_3 dopant concentration almost twice as high as that of ZEr-A.

Table 1. Dopant Concentration within Preform Core Region (ZEr-A and ZEr-B)

Preform	Al_2O_3 (mol%)	ZrO_2 (mol%)	Er_2O_3 (mol%)
ZEr-A	0.25	0.65	0.155
ZEr-B	0.24	2.10	0.225

The physical characteristics of ZEr-A and ZEr-B are given in Table 2. Both fibers have almost similar characteristics, except for a slightly different NA and effective area (A_{eff}), with ZEr-A having an NA and A_{eff} of 0.17 μm and 87 μm^2 respectively while ZEr-B has values of 0.20 and 75 respectively. Both fibers are also observed to have significantly higher background

losses than standard erbium doped fibers, with ZEr-A and ZEr-B having background losses of 145 dB/km and 175 dB/km respectively at 1300 nm. These losses are much higher than that of standard erbium doped fibers, which have typical values of around 10 to 15 dB/km, and arises due to scattering from the nano-crystalline phases in the fibers.

Table 2. Physical Characteristics of the Completed Fibers (ZEr-A and ZEr-B)^a

Preform	Core Composition	Core Diameter (μm)	Fiber Type	NA	A _{eff} (μm ²)	Background Loss at 1300 nm (dB/km)
ZEr-A	SiO + Al ₂ O ₃ + P ₂ O ₅ -ZrO ₂ -Y ₂ O ₃ + Er ₂ O ₃	10.5	Circular core with normal resin	0.17	87	145
ZEr-B	SiO + Al ₂ O ₃ + P ₂ O ₅ -ZrO ₂ -Y ₂ O ₃ + Er ₂ O ₃	10.0	Circular core with normal resin	0.20	75	175

^aNote: the fibers ZEr-A and ZEr-B are of similar type to that of MEr-1 and MEr-3 respectively as in [11].

In the characterization of the completed optical fibers, the absorption and fluorescence lifetimes of the fabricated fibers are analyzed. The peak absorption of the fibers at 978 nm are determined to be 14.5 and 18.3 dB/m respectively for ZEr-A and ZEr-B, translating to an of erbium ion concentration of 2800 and 3888 ppm/wt for the respective fibers. The fluorescence curves of both the ZEr-A and ZEr-B annealed preforms and drawn fibers are shown in Fig. 3(a), while the fluorescence decay curves of both fibers are given in Fig. 3(b). The fluorescence curves are obtained by laterally pumping the fibers at a 980 nm pump power of 100 mW, and it can be seen that the both the ZEr-A and ZEr-B fibers have fluorescence peaks at 1530 nm, as is expected from as the active medium for both fibers is erbium. The ZEr-B has a slightly higher emission power density as compared to the ZEr-A, which is expected due to the higher Er₂O₃ dopant concentration of ZEr-B. It is also observed that the spectral broadening of the drawn fibers are larger than that of the preforms; this is attributed to the phase change of the Er₂O₃ from micro-crystallites in the annealed preform into nano-crystallites as the fiber is drawn. The decay curves of both fibers are approximately the same as expected due to the active medium of both fibers being the same. However, the decay curve of ZEr-B shows that it has a slight shorter fluorescence lifetime. Taking this fact into account, together with the higher doping levels of Er₂O₃ and ZrO₂ in ZEr-B, indicates that the concentration-quenching phenomenon that is typical of erbium ions is strongly reduced through an increase in the doping levels of ZrO₂.

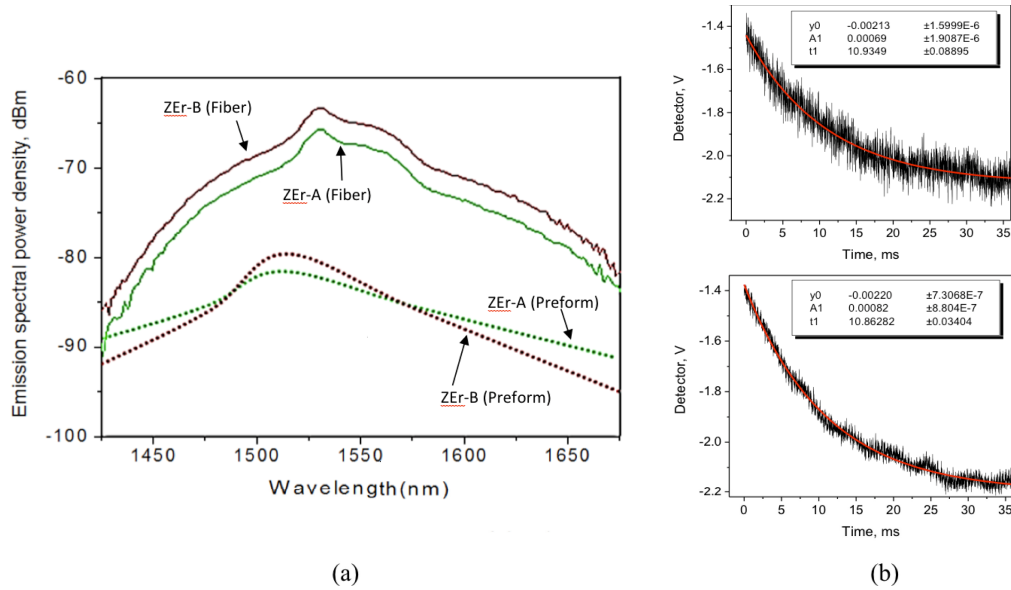


Fig. 3. (a) Fluorescence curve of ZEr-A and ZEr-B annealed preforms and drawn fibers, and (b) decay curves of ZEr-A (above) and ZEr-B (below). (Figures used with permission (these figures are reproduced and modified with the permission of the publisher of [22].))

Based on the characterization of the Zr-EDF, it can be seen that the addition of zirconium ions into the glass matrix of the Erbium Doped Fiber (EDF) allows for the fabrication of highly doped fibers, which have many potential applications in the development of compact devices. The following sections will examine the applications of the Zr-EDF, in particular its non-linear characteristics and also its usage as a compact medium for the generation of short pulses.

4. Four-wave-mixing in the Zr-EDF

In addition to providing high gain in a short fiber length, the Zr-EDF has also garnered increasing interest due to its significant non-linear characteristics that arise from the addition of zirconium ions into the glass matrix of the EDF [1]. The FWM effect is of particular interest when it comes to the non-linear effects of the Zr-EDF, as it has significant potential for new applications such as multi-wavelength generation and wavelength conversion. The FWM effect is an optical Kerr effect, and occurs when two or more wavelengths propagate simultaneously in non-linear medium. The interaction of these wavelengths results in the scattering of the incident photons, which in turn produces a fourth photon, known as an idler, at a wavelength that does not coincide with the incident wavelengths as given by Eq. (1) [22]:

$$\lambda_{\text{new_signal}} = 2\lambda_{\text{pump}} - \lambda_{\text{signal}}, \lambda_{\text{new_signal}} = 2\lambda_{\text{pump}} + \lambda_{\text{signal}} \quad (1)$$

where λ_{pump} and λ_{signal} are the pump and signal wavelengths respectively, while $\lambda_{\text{new_signal}}$ is the wavelength of the signal generated by the FWM process. The power of the generated signal, P_{FWM} can be computed as:

$$P_{\text{FWM}} = \eta \gamma^2 P_p^2 P_s e^{-\alpha L} L_{\text{eff}}^2 \quad (2)$$

where P_p is the input pump power and P_s is the input signal power. L_{eff} is the effective length of the fiber and is given as $L_{\text{eff}} = \frac{1-e^{-\alpha L}}{\alpha}$, with L being the fiber length and α is the

fiber attenuation coefficient. The normalized FWM efficiency η , is given as $\eta = \frac{\alpha^2}{\alpha^2 + \Delta\beta^2} [1 + \frac{2e^{-\alpha L}(1 - \cos(\Delta\beta L))}{(1 - e^{-\alpha L})^2}]$, where the phase mismatch, $\Delta\beta = \frac{2\pi\lambda^2}{c} D\Delta f^2$. The dispersion parameter can be given as $D = \frac{-2\pi c}{\lambda^2} \beta^2$ and β^2 is the group velocity dispersion parameter. The γ parameter is determined by bi-directional measurements of the FWM power, while the chromatic dispersion is determined from the wavelength detuning of the FWM Power Conversion Efficiency (PCE). Figure 4 shows the experimental setup used in the generation and measurement of the FWM effect:

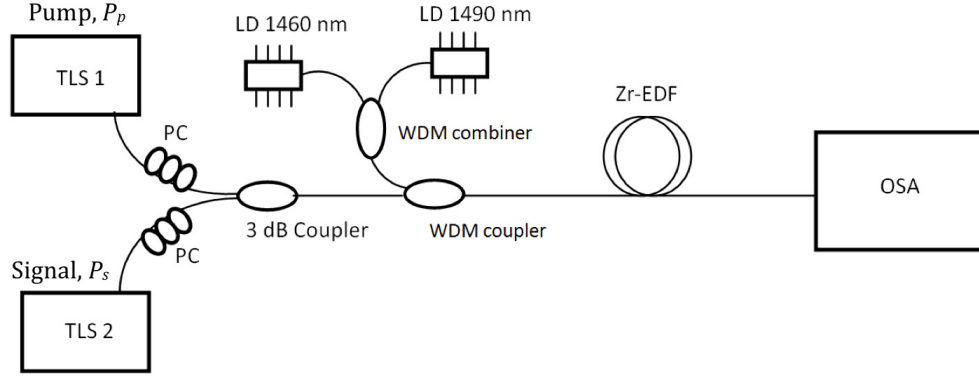


Fig. 4. Experimental setup for FWM generation and measurement in the Zr-EDF (a similar configuration as in [22]).

In the setup, two Tunable Laser Sources (designated TLS1 and TLS2) are used as the pump and signal sources. Each TLS has a tuning range from 1460 nm to 1640 nm and linewidth of 0.015 nm. TLS1 is used to generate the pump beam, P_p , fixed at 1560 nm with an average output power of 12.8 dBm. The signal beam, P_s has an average power 10.8 dBm with wavelengths of between 1552 nm to 1557 nm, and is generated by TLS2. P_p and P_s are combined by a 3 dB coupler with Polarization Controllers (PCs) used to obtain the maximum FWM efficiency. Two Laser Diodes (LDs) pumps at 1460 nm and 1490 nm are used to pump the Zr-EDF through a Wavelength Division Multiplexer (WDM) in order to suppress the erbium ions and allow interaction between the propagating beams and the host medium which contain the zirconium ions. A 4 m long ZEr-B fiber, with the characteristics as described in Tables 1 and 2, is used as the non-linear medium. An Optical Spectrum Analyzer (OSA) with a 0.02 nm resolution bandwidth completes the optical circuit and is used to measure the generated FWM spectrum.

Figure 5(a) shows both the theoretical as well as the actual value of P_{FWM} for different P_p wavelengths. It can be seen that the actual values of P_{FWM} agree well with the theoretically predicted values of Eq. (2), with the highest P_{FWM} value of about -45 dBm obtained at a P_p region of between 1558 nm to 1565 nm. Similarly, the wavelengths of the idlers generated agree well with their predicted values, as shown in Fig. 5(b). With the wavelength of P_p fixed and the wavelength of P_s varied by 1 nm, two sets of idler wavelengths are formed at C and S , with C corresponding to $\lambda_{new_signal} = 2\lambda_{pump} - \lambda_{signal}$ and S corresponding to $\lambda_{new_signal} = 2\lambda_{pump} + \lambda_{signal}$.

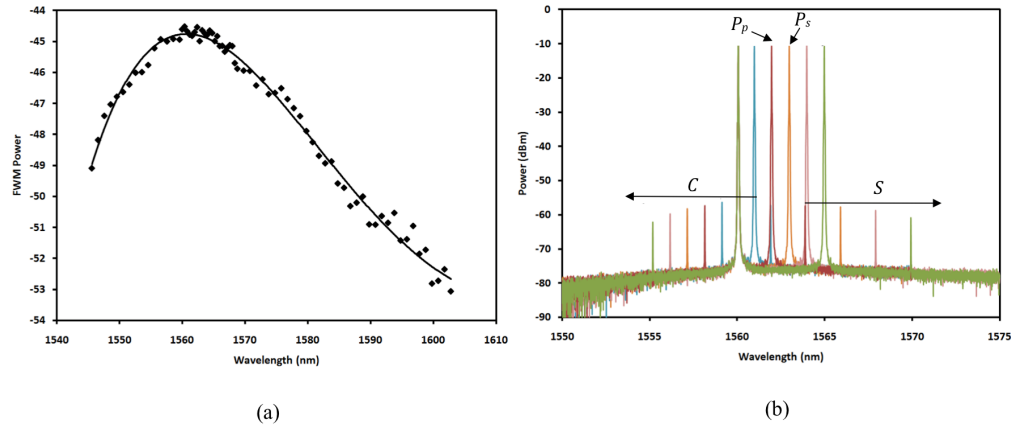


Fig. 5. (a) Theoretical and actual values of P_{FWM} against different P_p wavelengths, and (b) generation of idler wavelengths C and S at different P_s wavelengths. (These figures are reproduced with the permission of the publisher of [22].)

From the obtained values of P_{FWM} , C and S , the non-linear coefficient as well as the chromatic and dispersion slopes can be determined. In the case of the ZEr-B fiber, the obtained non-linear coefficient, chromatic slope and dispersion slope is determined to be $14 \text{ W}^{-1}\text{km}^{-1}$, 28.45 ps/nm.km and $3.63 \text{ ps/nm}^2.\text{km}$ respectively. Furthermore, the non-linear coefficient remains constant for all wavelengths propagating in the fiber, thus giving the ZEr-B fiber a very high potential for use in a multitude of applications such as wavelength conversion and wavelength generation.

5. Generation of short pulses using the Zr-EDF

In addition to its non-linear characteristics, the high concentration of erbium ions in a short length of fiber also provides the Zr-EDF with a significant advantage in the development of compact pulse fiber lasers. These lasers have recently garnered significant attention, and of particular interest are Q-switched fiber lasers, which provide high-energy pulses for applications such as in medicine, range-finding and sensing [23–27]. In this regard, a compact passively Q-switched pulse fiber laser can be realized by combining the Zr-EDF with an SA based on graphene, due to its relatively easy fabrication and low-cost [28–30].

Figure 6 shows the setup of the fiber laser, using a 3 m long ZEr-B fiber as the linear gain medium together with a graphene based SA as the Q-switching mechanism, as well as the setup used to create the graphene layer that will act as the SA for this work.

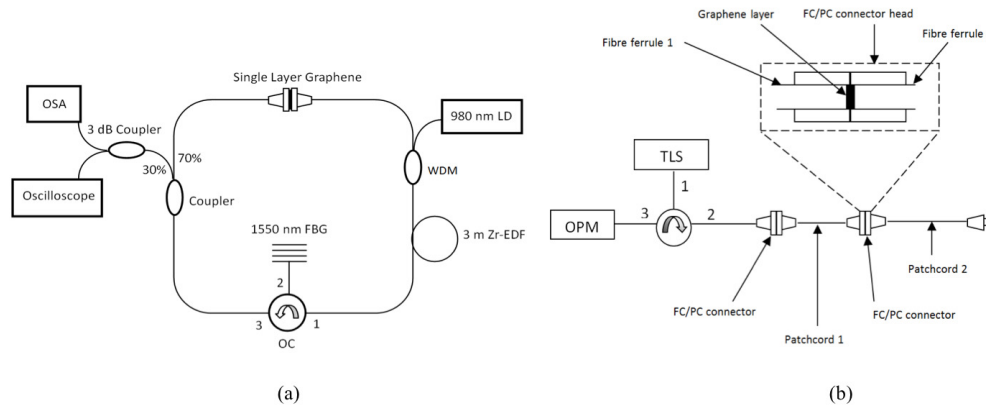


Fig. 6. (a) Setup of the passively Q-switched ZEr-B fiber ring laser using a graphene based SA, and (b) the setup for the deposition of the graphene layer onto the fiber ferrule.

As shown in Fig. 6(a), the ZEr-B fiber is pumped by a 980 nm laser diode through a 980 / 1550 nm WDM. The ZEr-B fiber is also connected to an Optical Circulator (OC), which is in turn connected to a Fiber Bragg Grating (FBG) with a center wavelength of 1550 nm and a reflectivity of approximately 98.9% that acts to lock the wavelength propagating in the laser cavity. A 70:30 coupler is used to extract a portion of the signal for analysis, while the graphene based SA is placed within the cavity to generate the desired pulses. The extracted signal passes through a 3 dB coupler, with one half being directed to an OSA and the other half connected to a photodiode and oscilloscope. The graphene based SA is fabricated by depositing an emulsion containing graphene flakes suspended in a N-Methyl Pyrrolidone (NMP) onto the face of Fiber Ferrule 1 as illustrated in Fig. 6(b). A 1550 nm beam, at a high power of about 11 dBm then illuminates the fiber ferrule, causing some of the NMP solution to evaporate and leaving a thick layer of graphene. Fiber Ferrule 1 is then connected to Fiber Ferrule 2 so as to sandwich the graphene layer and the TLS turned on, while the output power is recorded by the Optical Power Meter (OPM). After some time, the TLS is shut off and Fiber Ferrule 2 removed. During this process, a portion of the graphene is transferred between the fiber ferrules, thus making the layer of graphene on Fiber Ferrule 1 thinner. Fiber Ferrule 2 is cleaned and the process repeated until the power of the OPM is 4.1% of the power of the input beam, with the reflection for a single layer of graphene contributing approximately 0.1% [31] and Fresnel reflection contributing the remaining 4.0%. Once this power is achieved, the assembly of Fiber Ferrules 1 and 2 now form the SA.

The compact ZEr-B based Q-switch laser performs adequately, generating pulses with a pulse width of 8.8 μ s and repetition rate of 9.15 kHz at a pump power of 121.8 mW. The pulses generated are also stable over time and display minimal noise. Figure 7 provides a snapshot of an individual pulse generated as well as the pulse train obtained at a pump power of 121.8 mW.

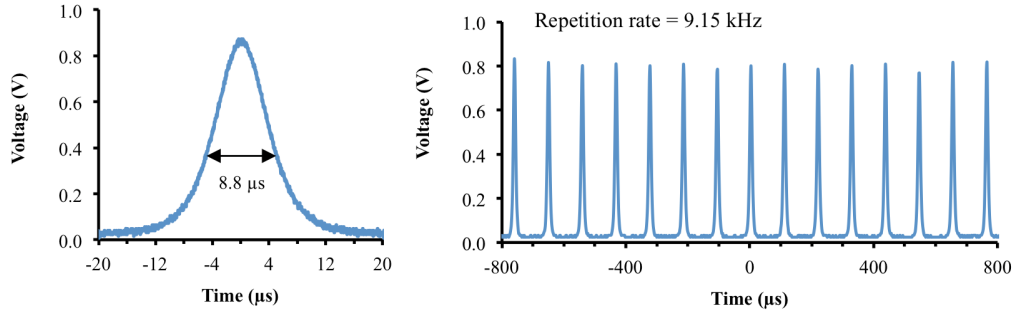


Fig. 7. Q-switched pulse width (*left*) and pulse train (*right*) obtained at a pump power of 121.8 mW.

Figures 8(a) and 8(b) show the pulse width and pulse repetition rate as a function of pump power as well as the average output power against pump power for the ZEr-B based Q-switched fiber laser. As can be seen in Fig. 8(a) the pulse width decreases while the repetition rate increases with as the pump power is raised. Although the availability of equipment limits the testing to a maximum pump power of 121.8 mW, the trends demonstrated by the fiber laser indicate that higher pump powers will undoubtedly result in smaller pulse widths and higher repetition rates. Furthermore, the average output power and pulse energy of the fiber laser also increases as the pump power is increased, as shown in Fig. 8(b). This increase is observed to be linear, with a slope value of about 0.45 μW/mW, and a maximum average output power of 161.35 μW (although it is expected that with a higher pump power and optimized cavity length, a higher average output power can be obtained). The pulse energy also increases linearly, with a slope of about 0.83 nJ/mW and a maximum pulse energy value of 17.64 nJ. These characteristics are typical of a highly doped erbium based fiber laser.

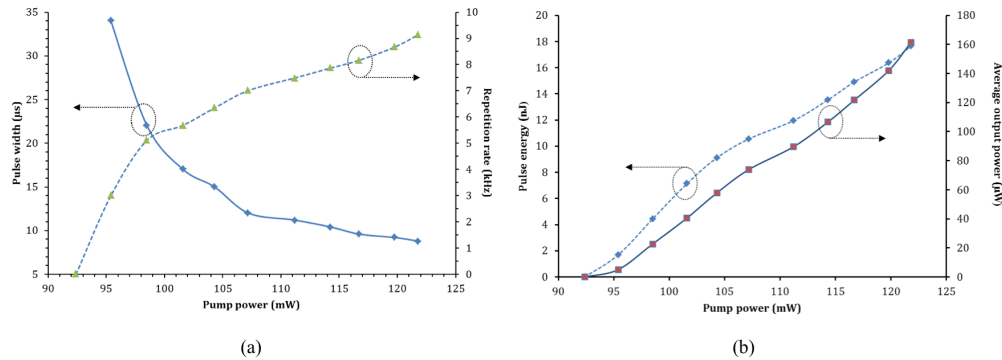


Fig. 8. (a) Repetition rate and pulse width of the ZEr-B Q-switched fiber laser against different pump powers and (b) average output power and pulse energy of the ZEr-B Q-switched fiber laser against different pump powers.

It can be seen that the Zr-EDF, in particular the ZEr-B variant has a very high potential for a multitude of applications, from the development of multi-wavelength sources from its non-linear behavior to the fabrication of compact pulsed laser sources. The exploration into the capabilities of the Zr-EDF is only at its beginning; there is no doubt that additional research in the future will yield many more useful applications for this type of fiber.

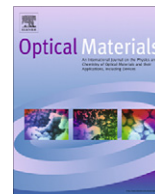
6. Conclusion

The fabrication and characterization of the Zr-EDF is described, as well as its uses in generating the FWM effect and also as a compact, passively Q-switched fiber laser. The Zr-EDF is made by first fabricating a conventional silica preform using the MCVD technique at

between 1350°C and 1400°C, following which glass modifiers and nucleating agents such as ZrO_2 , Y_2O_3 , Al_2O_3 , Er_2O_3 and P_2O_5 are added by solution doping. The resulting preform is then collapsed and annealed at a temperature of more than 2000°C to produce an optical fiber with a diameter of $125.0 \pm 0.5 \mu\text{m}$. Two Zr-EDFs are fabricated, designated ZEr-A and ZEr-B with erbium ion concentrations of 2800 and 3888 ppm/wt and absorption rates of 14.5 and 18.3 dB/m at 978 nm respectively. In the generation of the FWM effect, a 4 m long ZEr-B is used as the non-linear gain medium, and generates an FWM output with a power of - 45 dBm when pumped between 1558 nm to 1565 nm as predicted theoretically. The wavelengths of the generated sidebands also agree well with theoretical predictions, showing stability and potential applications as a multi-wavelength source. The ZEr-B is has a non-linear coefficient of $14 \text{ W}^{-1}\text{km}^{-1}$ and chromatic and slope dispersion values of 28.45 ps/nm.km and 3.63 ps/nm².km. The ZEr-B is also used to create a compact, passively Q-switched fiber laser together with a graphene based saturable absorber, and is capable of generating short pulses with a pulse width of 8.8 μs and repetition rate of 9.15 kHz at a pump power of 121.8 mW. The proposed fiber laser has a maximum average output power of 161.35 μW and maximum pulse energy value of 17.64 nJ, and has significant potential for further development as a compact, pulsed laser source.

Acknowledgments

The authors wish to express their gratitude to MOHE for their funding (UM.C/HIR/MOHE/SC/01) as well as to N. A. Awang of the Faculty of Science, Technology and Human Development, Universiti Tun Hussein Onn Malaysia, 86400 Batu Pahat, Johor Darul Takzim for her assistance and support in this work.



Q-switched Zr-EDF laser using single-walled CNT/PEO polymer composite as a saturable absorber

H. Ahmad^{*}, A.Z. Zulkifli, K. Thambiratnam, S.W. Harun

Photonics Research Centre, University of Malaya, 50603 Kuala Lumpur, Malaysia

ARTICLE INFO

Article history:

Received 9 July 2012

Received in revised form 27 August 2012

Accepted 5 September 2012

Available online 25 October 2012

Keywords:

Zirconia–Erbium Doped Fiber
Single-Walled Carbon Nanotube
Saturable absorber

ABSTRACT

In this work, we propose and demonstrate a compact, Zirconia–Erbium Doped Fiber (Zr-EDF), a new type of fiber with zirconia dopants added to the silica glass host to significantly increase erbium ion concentrations in the glass matrix. Q-switched behavior is obtained by using a Single-Walled Carbon Nanotube/Polyethylene Oxide composite sandwiched between two fiber ferrules as a saturable absorber. The Zr-EDF fiber laser has a nearly flat amplified spontaneous emission spectrum from 1545 to 1565 nm, unlike conventional erbium doped fibers. The pulse train generated has a maximum repetition rate and pulse width of 14.20 kHz and 8.6 μ s respectively. The highest average output power of the system is 270.0 μ W, with a corresponding pulse energy of 19.02 nJ. The proposed system is compact, cost-effective and rugged and has applications in range-finding, medicine and in industry.

© 2012 Elsevier B.V. All rights reserved.

1. Introduction

The development of compact fiber lasers with short pulse widths, high energy pulsed outputs have received significant attention for their potential in a multitude of applications. In order to generate these pulses, Q-switching and mode-locking are the two most common techniques employed. Mode-locking of the fiber laser is usually done when ultra-fast pulses of typically less than 1 ns are desired, such as in optical communications [1]. Q-switching techniques on the other hand are employed when the desired pulses need not be very short, or in cases where long pulses would be of better advantage, such as in sensing, range-finding and medicine [1–5]. Furthermore, Q-switching also allows for pulses with higher pulse energies to be generated, and does not entail the delicate balancing of cavity losses required for mode-locking, thus increasing operational efficiency and reducing the complexity of the fiber laser.

Q-switched pulses can be generated in a fiber laser by either active or passive modulation. Active modulation uses acoustic- or electro-optic modulators integrated within the laser cavity to generate the desired pulse output [6,7], while passive modulation uses Saturable Absorbers (SAs) [8] such as Semiconductor Saturable Absorption Mirrors (SESAMs) [9,10] to achieve the desired effect. The advantage of SAs as a Q-switching device is due to its compactness and ease of operation. Lately, Single-Walled Carbon Nanotubes (SWCNTs) and graphene have garnered significant interest for their use as SAs in Q-switched fiber lasers, due to their low

saturation intensity, relatively easy fabrication and low-cost [11–13]. While graphene has lately made significant in-roads as a SA due to its broad operational bandwidth [14,15], SWCNTs still find substantial use as SAs in many practical applications, especially in fiber based systems. This is primarily due to the ease of fabricating SWCNT SAs, whereby in the case of graphene based SAs, the fabrication is done by the Chemical Vapor Deposition (CVD) technique and then optically deposited onto the fiber ferrule [14]. SWCNT SAs on the other hand can be fabricated by using commercially available SWCNTs, suspended in a host material such as Polyvinyl Alcohol (PVA) and simply depositing them onto the fiber ferrule. This makes SWCNT SAs easy to fabricate and very rugged, which is well described in the review paper of reference [16]. Furthermore, the performance and stability of SWCNT SAs are well-known and proven, thus lending high confidence to their application [17,18].

In this work we propose and demonstrate a compact, Q-switched fiber laser using a SWCNT based SA together with a highly-doped, Zirconia–Erbium Co-doped Fiber (Zr-EDF) as the linear gain medium. The Zr-EDF is a new type of fiber that is formed from a ternary glass host consisting of zirconia ions co-doped in a silica fiber. The addition of the zirconium ions reduces the effects associated with high erbium dopant concentrations in an optical fiber, such as concentration quenching [19], thereby allowing high erbium ion concentrations in a short length of fiber. Furthermore, the Zr-EDF is based on a silica glass host, making it easy to splice to conventional telecommunications grade fibers, as opposed to other highly doped fibers such as those based on Bismuth glass hosts [20]. The SWCNT SA is also fabricated using a new host material, Polyethylene Oxide (PEO). PEO has the advantage of a lower melting point as compared to the typically used PVA, and also

^{*} Corresponding author. Tel.: +60 3 79677133; fax: +60 3 79674146.

E-mail address: harith@um.edu.my (H. Ahmad).

has excellent dispersion in water, making fabrication process easier while having no adverse effects on the performance of the SWCNT in the PEO host [21]. This is the first time, to the knowledge of the authors, that the Zr-EDF is used in conjunction with the SWCNT/PEO composite SA to create a compact, passively Q-switched fiber laser.

2. Fabrication of the Zr-EDF and SWCNT/PEO

In this work, two main components play a crucial role in generating the Q-switched pulses, namely the Zr-EDF gain medium and the SWCNT/PEO SA. The next sub-sections provide brief descriptions on the fabrication of the Zr-EDF and also the SWCNT/PEO composite.

2.1. Zr-EDF fabrication

The Zr-EDF is a silica based Erbium Doped Fiber (EDF) that is co-doped with ZrO_2 ions, allowing for very high Er^{3+} dopant concentrations in a short length of fiber to be realized. This gives the Zr-EDF a very important advantage as compact devices can be developed from it. Furthermore, the silica fiber host offers the advantage of good mechanical strength, similar to that of conventional Single-Mode-Fibers (SMFs) as well as compatibility with conventional SMFs, thus allowing for the development of compact and high performance optical amplifiers or fiber lasers as compared to those of Bismuth-based fibers.

The Zr-EDF is obtained from a fiber preform fabricated from a ternary glass host consisting of zirconia–yttria–aluminum ions co-doped in a silica fiber. The fabrication of the Zr-EDF takes place in three stages. In the first stage, a standard silica preform is fabricated using the Modified Chemical Vapor Deposition (MCVD) technique by passing SiCl_4 and P_2O_5 vapors over a slowly rotating silica tube. This process is carried out at a temperature of 1350–1400 °C and creates a silica tube with a porous phospho-silica layer deposited along its inner wall. In the second stage, the glass modifiers ZrO_2 , Y_2O_3 , Al_2O_3 and Er_2O_3 are first mixed with alcohol and water (at a 1:5 ratio) to form the complex ions $\text{ZrOCl}_2 \cdot 8\text{H}_2\text{O}$, $\text{YCl}_3 \cdot 6\text{H}_2\text{O}$, $\text{AlCl}_3 \cdot 6\text{H}_2\text{O}$ and $\text{ErCl}_3 \cdot 6\text{H}_2\text{O}$, and are then added to the silica tube using the solution doping technique. At this stage also, small amounts of Y_2O_3 and P_2O_5 are added into the glass matrix to serve as nucleating agents and further increase the phase separation of the Er_2O_3 micro-crystallites in the core matrix, although the zirconia and aluminum ions alone are enough to achieve the desired Er^{3+} dopant concentrations. The addition of the Y_2O_3 will also help

to dissolve the crystalline structure of the zirconia ions, and this will prevent cracking in the optical fiber as it cools. In the final stage of the fabrication process, the preform that has undergone the solution doping process is annealed at 1100 °C for 3 h. The annealed preform is then collapsed into a solid rod at 2000 °C and drawn using a conventional drawing tower to form a fiber with a diameter of $125 \pm 0.5 \mu\text{m}$. This process has been clearly explained in reference [19].

2.2. SWCNT/PEO fabrication

The second part of this paper is the fabrication of the SA, which acts as a Q-switched device. Generally, the SAs based on SWCNTs or graphene are housed in a host material such as PVA instead of being applied directly to the face of the fiber ferrule [22,23]. In this report, an alternative approach is taken, using PEO as the host material. The advantage of this material is that it is water-soluble, has good uniformity and is also easier to fabricate for use as a host.

The SA is formed by sandwiching a SWCNT/PEO composite in between two fiber ferrules. The SWCNT used in this research is 99% pure and is acquired from Cheap Tubes Inc. The SWCNTs are between 3 and 30 μm in length, and on average have diameters of between 1 and 2 nm. The PEO and Sodium Dodecyl Sulfate (SDS) solutions, which have average molecular weights of $1 \times 10^6 \text{ g/mol}$ and 288.38 g/mol are obtained from Sigma-Aldrich, and combined with the SWCNTs to form the SWCNT/PEO composite. The SWCNT, in a 1% SDS solution, is ultrasonically dispersed at 50 W for a period of 30 min and then forms the composite by solution casting. The resulting composite is then formed onto the fiber ferrule by dropping the liquid solution and allowing it to dry in air over a period of 24 h. Fig. 1a shows the image of the SWCNT/PEO layer on the facet of the ferrule under 20 times magnification. Raman spectroscopy is also used to provide confirmation of the SWCNT, with the spectrum of the Raman shift shown in Fig. 1b. The Raman shift obtained has a similar pattern as that obtained by Dresselhaus et al. [24]. Furthermore, the values G at 1598 cm^{-1} , D at 1362 cm^{-1} and G' at 2684 cm^{-1} indicate that it is a Single-Walled Carbon Nanotube.

The two peaks at 186 cm^{-1} and 287 cm^{-1} are in the Radial Breathing Modes (RBM), which correspond to the nanotube diameter and occur at low wavenumbers [25]. The usage of the above SA, having SWCNT in a PEO matrix material is as a Q-switching element and discussed in the following section.

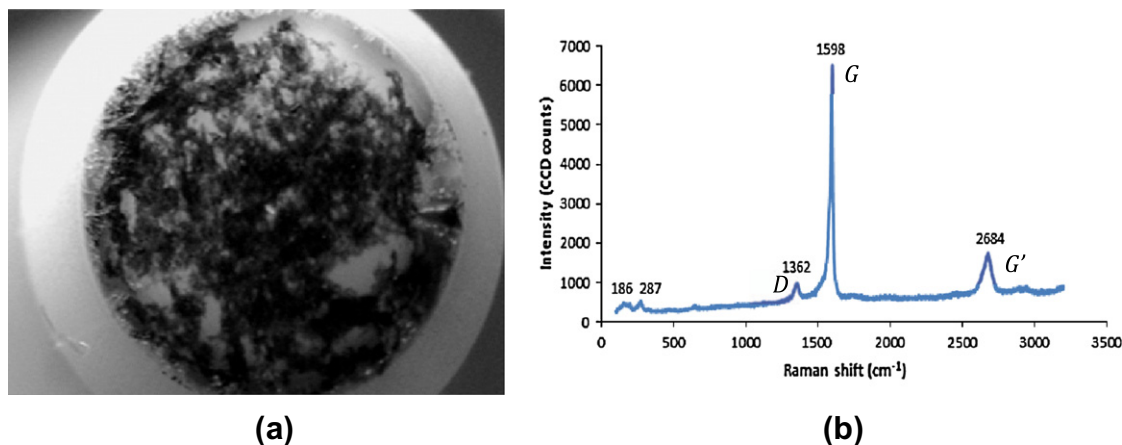


Fig. 1. (a) SWCNT/PEO composite polymer deposited on the facet of the fiber ferrule and (b) the Raman spectroscopy taken indicating the Single-Walled Carbon Nanotube layer.

3. Experimental setup for Q-switching

The configuration of the proposed Q-switched Zr-EDF laser using a SWCNT/PEO composite as a saturable absorber is shown in Fig. 2:

It consists of a 3 m long of highly doped Zr-EDF at 2800 wt ppm as the gain medium, with an absorption coefficient of 14.5 dB/m at 980 nm. The high Er^{3+} dopant concentration is achieved by co-doping the silica fiber with Zirconia–Yttria–Aluminum (Zr–Y–Al) ions, thereby reducing the detrimental effects of concentration quenching. The Zr-EDF is pumped by a 980 nm pump laser diode through a 980/1550 nm Wavelength Division Multiplexer (WDM), with the common port connected to one end of the Zr-EDF. The other end of the Zr-EDF is then connected to Port 1 of the Optical Circulator (OC). Port 2 of the OC is connected to a Fiber Bragg Grating (FBG) with a centre wavelength of 1550 nm and a reflectivity of approximately 98.9% as well as a 3 dB bandwidth of 0.24 nm. Port 3 of the OC is then connected to a 70:30 coupler, with the 70% port connected to one end of the ferrule assembly containing the SWCNT/

PEO composite. The other end of this assembly is then connected to the 1550 nm port of the WDM to complete the ring cavity. The 30% port of the coupler is connected to a 3 dB coupler, with one output connected to an Optical Spectrum Analyzer (OSA) with a resolution of 0.03 nm while the other output is connected to an Oscilloscope.

The pump power to the Zr-EDF is varied until a maximum value of 177.75 mW. The generated Amplified Spontaneous Emission (ASE) at both ends of the Zr-EDF will be forced to travel in a clockwise direction because of the OC placed in the optical circuit. The presence of the FBG is to select a particular wavelength of interest to oscillate in the cavity, and this selection can be tuned applying strain or temperature. The filtered wavelength is reflected by the FBG into the cavity through the OC, where it now encounters the 70:30 coupler. The propagating wavelength emitted by the 70% port now travels to the SWCNT/PEO based SA, where the Q-switched pulses are generated. The Q-switched pulses then travel to the WDM and continue to propagate in the ring cavity, thus forming the fiber laser. The portion of the propagating signal extracted by the 30% port of the optical coupler is used for the analysis of the optical and pulse properties of the signal.

4. Results and discussion

The output ASE generated by the 3 m long Zr-EDF taken at different pump powers is shown in Fig. 3. From the figure, it can be seen that the ASE spectrum generated is very broad, stretching from approximately 1525 nm to more than 1605 nm, with a reasonable power output, which has a nearly flat output spectrum as compared to erbium doped in a silica only host. The measurements are taken at different pump powers from 7.3 mW to 177.8 mW, which show a peak at 1535 nm, before decreasing until about 1545 nm and then having a nearly flat plateau region until about 1565 nm. For pumping powers of more than 100.0 mW, the measured excess pump is 0.2 mW and above, which indicates that the gain medium is completely pumped or at least nearly completely pumped. This makes the Zr-EDF a very interesting medium, as only short Zr-EDF lengths are required for performance comparable to that of much longer conventional EDFs. Furthermore, its nearly flat gain spectrum around the C-band region will be attractive for Dense Wavelength Division Multiplexing (DWDM) and metro applications and in this experiment, a compact module employing an uncooled laser diode with a maximum power setting of 141.8 mW is used as the pump source.

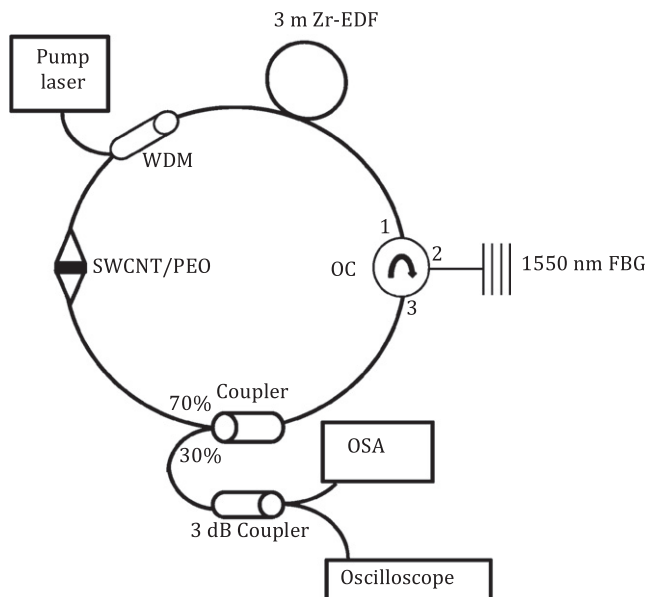


Fig. 2. Experimental setup for Q-switched Zr-EDF fiber ring laser with SWCNT/PEO as the SA.

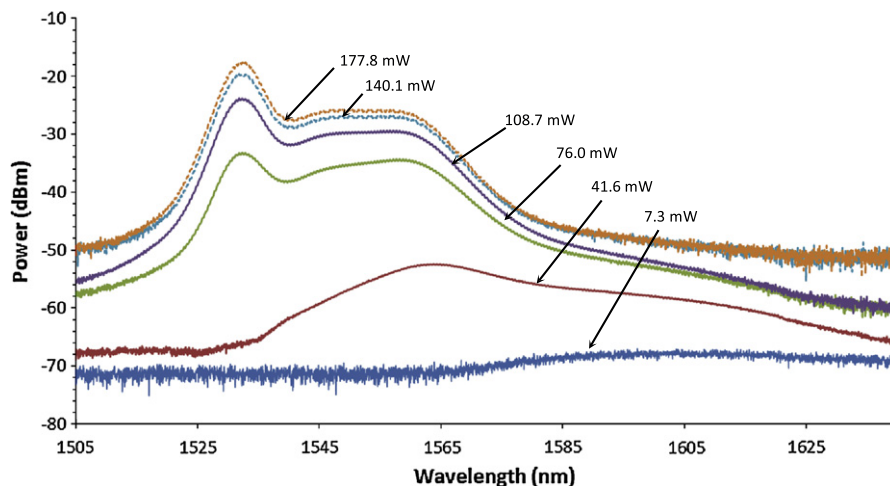


Fig. 3. ASE spectrum of the 3 m Zr-EDF pumped at different pump powers from 7.3 mW to 177.8 mW.

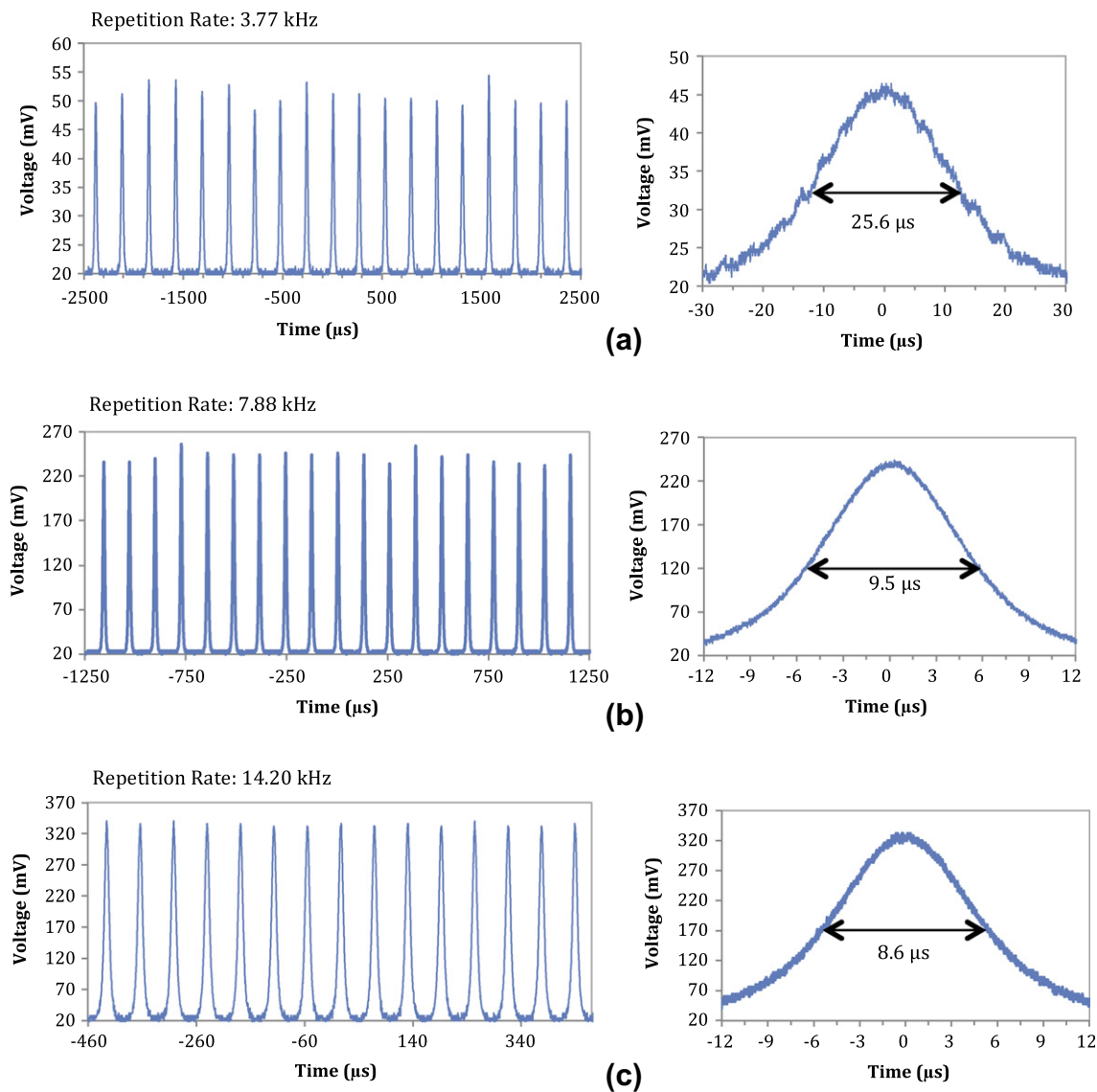


Fig. 4. Repetition rate and pulse width of the generated pulses as measured by the oscilloscope at pump powers of (a) 95.1 mW, (b) 110.3 mW and (c) 141.8 mW.

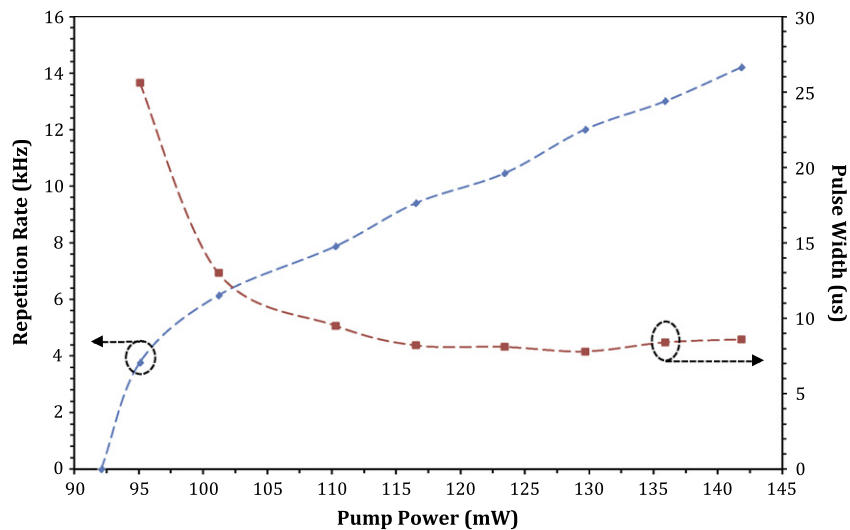


Fig. 5. Pulse repetition rate (kHz) and pulse width (μ s) for different pump powers.

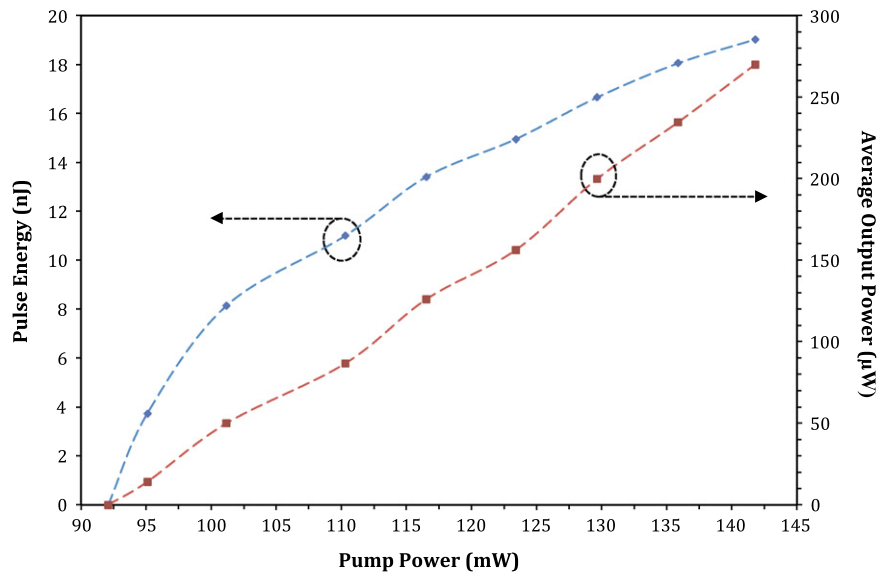


Fig. 6. Pulse energy (nJ) and average output power (μW) of the fiber laser as a function of the pump power.

The repetition rates and pulse widths of the pulses generated by the system are shown in Fig. 4 for different pump powers. At a pump power of 95.1 mW, around the threshold region, a train of pulses with a repetition rate of 3.77 kHz is obtained, as shown in Fig. 4a. The pulses generated at this pump power show slight fluctuations from peak-to-peak. The corresponding measured pulse width is about 25.6 μs . Increasing the pump power to 110.3 mW also increases the repetition rate of the generated pulse train, with a repetition rate of 7.88 kHz, doubling the value at a pump power of 95.1 mW, as shown in Fig. 4b. The pulses generated are also more stable, with less fluctuation between peaks. The corresponding pulse width obtained at this drive current is shorter at approximately 9.5 μs , which is close to half of the value obtained in the earlier case.

At the highest pump power of 141.8 mW, the repetition rate of the pulses generated is approximately 14.20 kHz, almost twice the value obtained at the previous pump power. The pulses obtained are also very stable, and show very little peak-to-peak fluctuations. The pulse width obtained at this pump power is also shorter at 8.6 μs , only a slight difference from the pulse width obtained at a pump power of 110.3 mW.

Fig. 5 shows the measurement of the pulse repetition rate and the pulse width as a function of the pump power to the Zr-EDF. From the Figure, it can be said that the repetition rate grows predictably with the increase in the pump power, giving a maximum repetition rate 14.20 kHz at a pump power of 141.8 mW. The overall slope of the repetition rate plot is about 0.25 kHz/mW. It can also be inferred from the figure that the threshold value for obtaining the pulse train is about 92.5–95.0 mW of the output power from the pump laser. The plot of Fig. 5 indicates clearly that the repetition rate can be tuned by changing the pump power.

In the case of the pulse width, it initially decreases with the pump power, with only a slight change between pump powers of 110.3 mW to the maximum pump power of 141.8 mW, following an exponential decay pattern. At around the threshold value, the pulse width is 25.6 μs , and decreases to 8.6 μs at the highest pump power. At the higher pump powers, the minor changes in the pulse width as the pump power is increased, along with linear changes in the repetition rate both indicate that the SWCNT/PEO SA is operating in an almost saturated condition.

Fig. 6 shows the average output power and pulse energy of the Zr-EDF fiber laser with the SWCNT/PEO SA.

From the Figure, it is clearly shown that the average output power of the fiber laser increases almost linearly against the pump power, giving an average output power of 270.0 μW at a maximum pump power of 141.8 mW. The change of the average output power against the pump power is linear, with a slope of 5.48 $\mu\text{W}/\text{mW}$. Also from the Figure, it can be observed that the pulse energy increases with the pump power, steeply in the initial stage with a slope value of about 0.66 nJ/mW, and subsequently increasing slowly above a pump power value of 101.2 mW with a slope of approximately 0.27 nJ/mW. The maximum pulse energy obtained is 19.02 nJ at a pump power of 141.8 mW.

The proposed fiber laser in this work can be used in applications requiring a compact fiber laser with a Q-switched output. The use of the Zr-EDF allows a short length of fiber to be used, thus giving a very compact system. Furthermore, by using the SWCNT/PEO sandwiched between two fiber ferrules, which can be easily incorporated into the setup, provides an inexpensive pulse laser system that is also very rugged and can be used in applications such as range-finding, medicine and industrial applications.

5. Conclusion

A compact Q-switched fiber laser based on a highly doped Zr-EDF and compact SWCNT/PEO SA is demonstrated. The Zr-EDF used as the gain medium is a new type of fiber, co-doped with zirconia ions to facilitate very high erbium ion dopant concentrations in a short length of fiber. The SA is created from SWCNTs deposited on PEO, which has several advantages over the conventionally used PVA host material. The ASE spectrum generated from the fiber laser has a nearly flat plateau from 1545 to 1565 nm in the 5 dB power range. The Q-switched pulse train is obtained above a threshold pump power of 92.5–95.0 mW, and at the maximum pump power of 141.8 mW a repetition rate of 14.20 kHz is obtained, with a corresponding pulse width of 8.6 μs . The average output power of the fiber laser is 270.0 μW at 141.8 mW, and the maximum pulse energy obtained is 19.02 nJ. The proposed fiber laser is compact and low-cost as well as being very rugged, and can be used in a multitude of applications such as range-finding, medical and industrial usage.

Acknowledgements

We would like to acknowledge the funding for this project under the grant UM.C/HIR/MOHE/SC/01. We would also like to

thank M.C. Pal and the Central Glass and Ceramic Research Institute, Kolkata, India, for the fiber sample as well as F. Ahmad for assisting in the preparation of the saturable absorber.

References

- [1] D. Popa, Z. Sun, T. Hasan, F. Torrisi, F. Wang, A.C. Ferrari, *Appl. Phys. Lett.* 98 (2011) 073106.
- [2] R.J. Williams, N. Jovanoic, G.D. Marshall, M.J. Withford, All-optical, actively Q-switched fiber laser, *Opt. Express* 18 (2010) 7714.
- [3] W.-J. Cao, H.-Y. Wang, A.-P. Luo, Z.-C. Luo, W.-C. Xu, *Laser Phys. Lett.* 9 (2012) 54.
- [4] M.L. Siniava, M.N. Siniavsky, V.P. Pashinin, A.A. Mamedov, V.I. Konov, V.V. Kononenko, *Laser Phys.* 19 (2009) 1056.
- [5] H.Q. Shangguan, L.W. Casperson, A. Shearin, K.W. Gregory, S.A. Prahl, *Appl. Opt.* 35 (1996) 3347.
- [6] D. Hudson, K. Holman, R. Jones, S. Cundiff, J. Ye, D. Jones, *Opt. Lett.* 30 (2005) 2948.
- [7] A.G. Kuznetsov, S.A. Babin, *Laser Phys.* 20 (2010) 1266.
- [8] L.G. Luo, P.L. Chu, *Opt. Commun.* 161 (1999) 257.
- [9] P.P. Jiang, D.Z. Yang, Y.X. Wang, T. Chen, B. Wu, Y.H. Shen, *Las. Phys. Lett.* 6 (2009) 384.
- [10] V.N. Filippov, A.N. Starodumov, A.V. Kir'yanov, *Opt. Lett.* 26 (2001) 343.
- [11] F. Wang, A.G. Rozhin, V. Scardaci, Z. Sun, F. Hennrich, I.H. White, W.I. Milne, A.C. Ferrari, *Nat. Nanotechnol.* 3 (2008) 738.
- [12] A.G. Rozhin, V. Scardaci, F. Wang, F. Hennrich, I.H. White, W.I. Milne, A.C. Ferrari, *Phys. Status Solidi B* 243 (2006) 3551.
- [13] T.R. Schibli, K. Minoshima, H. Kataura, E. Itoga, N. Minami, S. Kazaoui, K. Miyashita, M. Tokumoto, Y. Sakakibara, *Opt. Express* 13 (2005) 8025.
- [14] F. Bonaccorso, Z. Sun, T. Hasan, A.C. Ferrari, *Nat. Photon.* 4 (2010) 611.
- [15] T. Hasan, F. Torrisi, Z. Sun, D. Popa, V. Nicolosi, G. Privitera, F. Bonaccorso, A.C. Ferrari, *Phys. Status Solidi B* 247 (2010) 2953.
- [16] T. Hasan, Z. Sun, F. Wang, F. Bonaccorso, P.H. Tan, A.G. Rozhin, A.C. Ferrari, *Adv. Mater.* 21 (2009) 3874.
- [17] D.-P. Zhou, L. Wei, B. Dong, W.-K. Liu, *IEEE Photon., Technol. Lett.* 22 (2010) 9.
- [18] B. Dong, J. Hao, J. Hu, C.-Y. Liaw, *Opt. Fiber Technol.* 17 (2011) 105.
- [19] M.C. Paul, S.W. Harun, N.A.D. Huri, A. Hamzah, S. Das, M. Pal, S.K. Bhadra, H. Ahmad, S. Yoo, M.P. Kalita, A.J. Boyland, J.K. Sahu, *Opt. Lett.* 35 (2010) 2882.
- [20] S. Zheng, C. Zhang, S. Jian, *Opt. Fiber Technol.* 18 (2012) 161.
- [21] M. Park, H. Kim, J.P. Youngblood, S.W. Han, E. Verploegen, A.J. Hart, *Nanotechnology* 22 (2011) 415703.
- [22] X. Zhang, T. Liu, T.V. Sreekumar, S. Kumar, V.C. Moore, R.H. Hauge, R.E. Smalley, *Nano Lett.* 3 (2003) 1285.
- [23] V. Scardaci, A.G. Rozhin, F. Hennrich, W.I. Milne, A.C. Ferrari, *Phys. E: Low-Dimens. Syst. Nanostruct.* 37 (2007) 115.
- [24] M.S. Dresselhaus, G. Dresselhaus, R. Saito, A. Jorio, *Phys. Reports* 409 (2005) 47.
- [25] G. Wang, B. Wang, J. Park, Y. Wang, B. Sun, J. Yao, *Carbon* 4 (2009) 242.

Q-Switching and Mode-Locking in Highly Doped $\text{Zr}_2\text{O}_3\text{--Al}_2\text{O}_3\text{--Er}_2\text{O}_3$ -Doped Fiber Lasers Using Graphene as a Saturable Absorber

Kavintheran Thambiratnam, *Member, IEEE*, Harith Ahmad, Farah Diana Muhammad, Mohd. Zamani Zulkifli, Ahmad Zarif Zulkifli, Mukul Chandra Paul, and Sulaiman Wadi Harun

Abstract—The application of graphene as a saturable absorber (SA) for generating Q-switched and mode-locked pulses in a Zirconia–Erbium-doped fiber (Zr-EDF) laser is explored. Graphene-based SAs have a very wide operational range, which complements the extended operational bandwidth of the Zr-EDF. The Zr-EDF has an erbium concentration of about 4320 ppm, with absorption rates of 22.0 and 58.0 dB/m at 987 and 1550 nm. The system is capable of generating Q-switched pulses with pulsewidths and energies of 4.6 μs and 16.8 nJ, respectively, as well as peak powers of 3.6 mW at a repetition rate of 50.1 kHz. The Zr-EDF laser can also generate mode-locked pulses with pulsewidths, average output powers, pulse energies, and peak powers of 730 fs, 1.6 mW, 23.1 pJ, and 31.6 W, respectively, at a repetition rate of 69.3 MHz. Both the Q-switched and mode-locked output pulses are highly stable, allowing for their application in a multitude of real-world applications.

Index Terms—Graphene-based saturable absorber, mode-locking, Q-switching, Zirconia–Erbium-doped fiber (Zr-EDF).

I. INTRODUCTION

COMPACT, ultrafast fiber lasers have recently become the focus of substantial research efforts due to their significant applications in a multitude of research fields such as communications, metrology, manufacturing and material processing as well as medicine and health [1]–[4]. Ultrafast fibers are usually mode-locked or Q-switched, and enabled by active modulation techniques [5]–[7]. While these systems are able to generate the desired ultrafast pulses, they are typically complex and costly, and thus, not particularly suited for deployment in compact systems or high-density networks. In this regard, passively mode-locked and Q-switched fiber lasers are seen as a viable alternative toward actively modulated systems, with high potential for practical, real-world applications.

Passively modulated fiber lasers can be achieved by techniques such as the nonpolarization rotation technique [8] and semiconductor saturable absorber mirrors (SESAMs) [9], [10]. However, these approaches can be difficult to implement, requiring fine adjustments to the cavity design, or incurring varying degrees of cost and complexity, thereby limiting their usage. Recently however, graphene has emerged as a practical, highly cost-effective and easily fabricated solution toward generating ultrafast pulses in fiber lasers [11]–[15]. Used as a saturable absorber (SA), a single atomic layer of graphene can generate the desired Q-switched or mode-locked pulses without complexity and costs, such as those incurred by SESAMs. Furthermore, graphene-based SAs possess impressive optical characteristics such as ultrafast recovery times and a very wide operational wavelength range, due to the gapless behavior of the graphene atomic layer [11], [12], giving them a significant advantage over other techniques used for passive modulation in fiber lasers.

In order to create a compact pulsed fiber laser, the graphene-based SA can be combined with an active fiber laser that is short in length but with a high active ion dopant concentration. The erbium-doped fiber (EDF) has long been the dominant means in the development of fiber laser and amplifiers, but short, highly doped EDFs cannot be realized due to the detrimental effects of cluster formation and concentration quenching in silica-based EDFs [16], [17]. Specialty fibers, such as bismuth–erbium-doped fibers (Bi-EDFs) are able to overcome this limitation, allowing for high erbium ion concentrations to be realized, but instead suffer from problems such as difficulties in splicing and incompatibility with conventional, silica fibers. In this regard, Zirconia has recently come to light as a viable dopant material for increasing the Erbium ion concentration in fibers without the effects of clustering and concentration quenching, while at the same time maintaining the integrity and compatibility of conventional silica fibers [18]. Zirconia–Erbium codoped fibers (Zr-EDFs), or $\text{Zr}_2\text{O}_3\text{--Al}_2\text{O}_3\text{--Er}_2\text{O}_3$ fibers also possess a slightly wider emission and absorption bandwidth than conventional EDFs, thus, complementing the gapless bandwidth of the graphene layer.

In this study, the application of graphene as an SA is examined in the development of Q-switched and mode-locked fiber lasers using the Zr-EDF as the active gain medium. The Zr-EDF used has an erbium ion concentration of 4320 ppm, with absorption rates of about 22.0 and 58 dB/m at 987 and 1550 nm, respectively. The Q-switched Zr-EDF laser with the graphene SA is capable of generating pulses at a repetition rate of 50.1 kHz with

Manuscript received April 20, 2013; revised July 1, 2013; accepted July 1, 2013. This work was supported by the University of Malaya under Grants UM.C/625/1/HIR/MOHE/SCI/29 and RG143-12AET.

K. Thambiratnam, H. Ahmad, F. D. Muhammad, M. Z. Zulkifli, A. Z. Zulkifli, and S. W. Harun are with the Photonics Research Centre, University of Malaya, Kuala Lumpur, 50603 Malaysia (e-mail: kavintheran@gmail.com; harith@um.edu.my; faradibah90@yahoo.com; mohdzamani82@yahoo.com; zain_73@yahoo.com; swharun@um.edu.my).

M. C. Paul is with the Central Glass and Ceramic Research Institute, Kolkata 700032 India (e-mail: mcpal@cgcricri.res.in).

Color versions of one or more of the figures in this paper are available online at <http://ieeexplore.ieee.org>.

Digital Object Identifier 10.1109/JSTQE.2013.2272459

pulsewidths, pulse energies and pulse peak powers of 4.6 μs , 16.8 nJ, and 3.6 mW, respectively. When operated in the mode-locking regime, the Zr-EDF laser is capable of generating pulses at an average output power of 1.6 mW and pulsewidth of 730 fs, as well as a pulse energy of 23.1 pJ, and a peak power of 31.6 W. The repetition rate of the pulses is approximately 69.3 MHz, corresponding to a pulse spacing of around 14.5 ns in the pulse train. The generated pulses are observed to be quite stable, giving them a high potential for real-world applications requiring compact, pulsed fiber lasers.

II. FABRICATION OF THE ZR-EDF

The Zr-EDF is fabricated in the same manner as a conventional EDF using the modified chemical vapor deposition technique. A silica tube is prepared before-hand, and mounted on a glass lathe. SiCl_4 and P_2O_5 vapors are then passed through the silica tube as it is externally heated to between 1350 and 1400 $^\circ\text{C}$ so as to deposit a porous phospho-silica layer on the inner surface of the tube. The tube then undergoes the solution doping process, where glass modifiers in the form of the complex ions $\text{ZrOCl}_2 \cdot 8\text{H}_2\text{O}$, $\text{YCl}_3 \cdot 6\text{H}_2\text{O}$, and $\text{AlCl}_3 \cdot 6\text{H}_2\text{O}$ are added, along with the active ions in the form of $\text{ErCl}_3 \cdot 6\text{H}_2\text{O}$ in an alcohol:water solution at a ratio of 1:5. Quantities of Y_2O_3 and P_2O_5 is also added at this stage to act as nucleating agents, which are necessary to increase the phase-separation of the Er_2O_3 rich microcrystallites present in the core of the fiber, while small amounts of MgO and CaO are added to prevent rapid structural changes that can degrade the mechanical integrity of the fiber. Once the solution doping process has been completed, the obtained preform is annealed at 1100 $^\circ\text{C}$, and subsequently, heated to over 2000 $^\circ\text{C}$ to collapse the fiber into a glass rod, which is then drawn. In the final step of the fabrication process, the drawn fiber is coated with a protective polymer buffer. The detailed fabrication process of the Zr-EDF has been reported in [19] and [20].

Morphological characterization of the fabricated Zr-EDF is done using a field-emission gun scanning electron microscopy (FEGSEM) as well as a conventional microscope. Observation of the fabricated Zr-EDF under standard magnification, using the microscope shows a typical fiber with a very distinct core, less than 10 μm in diameter, surrounded by a cladding of approximately 125 μm in diameter. Further observation using the FEGSEM provides ZrO_2 crystalline microstructures, which also contain the Er_2O_3 dopants to be easily observed. The microscopic view of the fiber is shown in Fig. 1(a), while the image of the Zr-EDF captured by the FEGSEM is shown in Fig. 1(b).

The dopant levels within the Zr-EDF are obtained using electron probe microanalysis (EPMA), which gives an Er_2O_3 dopant level of 0.225 mol% or about 4320 ppm. Spectral analysis of the fiber indicates spectral attenuation at 980 and 1550 nm, as is to be expected due to the presence of erbium ions in the glass host, as well as a fluorescence life-time of 10.86 ms. The peak absorption of the fiber is measured to be 22.0 dB/m at 987 nm, and about 58.0 dB/m at 1550 nm. The chromatic dispersion value of the Zr-EDF is determined to be +28.45 $\text{ps} \cdot \text{nm}^{-1} \cdot \text{km}^{-1}$ [18].

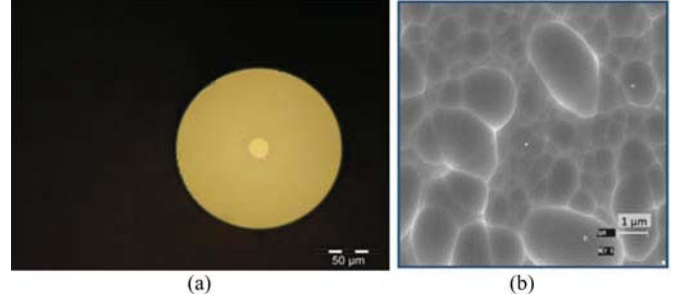


Fig. 1. (a) Microscopic view of the Zr-EDF, and (b) observation of the Zr-EDF using the FEGSEM. Under the FEGSEM, the ZrO_2 and Er_2O_3 rich microcrystalline structures are clearly visible and well defined.

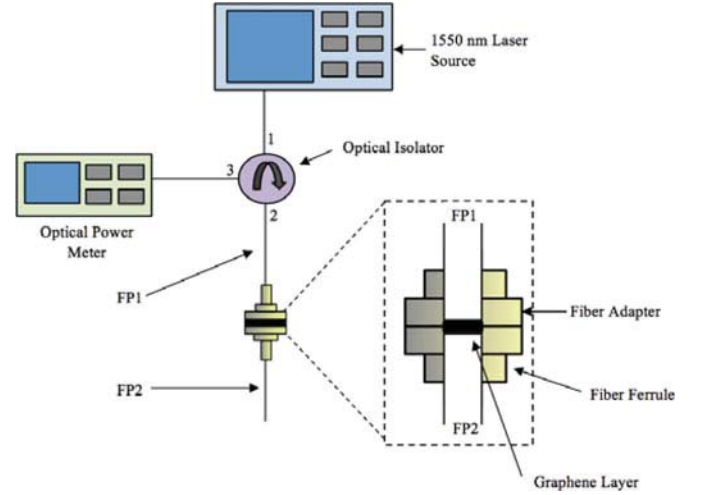


Fig. 2. Setup of the optical deposition system, which is used to create the graphene layer on the face of the fiber ferrule.

III. FABRICATION OF THE GRAPHENE SA

The graphene-based SA used in this study is formed from graphene flakes that are adhered to the face of an optical fiber ferrule through the optical deposition technique. The graphene is obtained from Graphene Research Ltd. in the form of graphene flakes, suspended in an N-methylpyrrolidone solution. The graphene flakes have an average particle size of 550 nm, with an average flake thickness of 0.35 nm.

In order to form the graphene SA, the graphene layer must first be deposited onto the face of a fiber ferrule. A patchcord, with FC/PC terminations is prepared and designated as FP1. The creation of the graphene layer is done using the optical deposition process, using the setup as shown in Fig. 2.

The optical deposition system consists of a 1550-nm laser source, which is connected to Port 1 of an optical circulator (OC). One end of FP1 is connected to Port 2 of the OC, while the other end is left bare; it is on this end that the graphene layer will be deposited on. Port 3 of the OC is connected to an optical power meter, which is used to measure the reflected power from the graphene layer during the deposition process. To deposit the graphene layer, the unconnected end of FP1 is immersed in the aqueous solution containing the graphene flakes. The 1550-nm laser is activated, at a power of 11 dBm

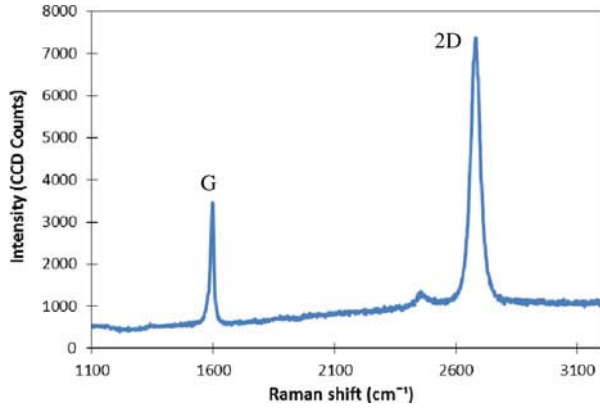


Fig. 3. Raman spectrum of a nearly single layer of graphene deposited on the fiber ferrule.

and allowed to transmit for approximately 3 min. This will cause a thick graphene layer to deposit onto the surface of the ferrule as an effect of optical thermophoresis [21]. After 3 min, the laser is deactivated and the immersed ferrule, now with the attached graphene layer is carefully removed from the solution. Subsequently, this ferrule is now connected to one end of another FC/PC terminated patchcord using an adaptor, and the 1550-nm laser is activated, at the same power level for 3 min. FP2 is then removed and cleaned, before being reconnected and the process repeated in cycles of 3 min. During this time, the reflected power is measured using the OPM, and once the reflected power is measured to be about 4.1% of the transmitted power, the process is stopped. The reflection of 4.1% arises from the reflection of the graphene layer at $\sim 0.1\%$ [12] and Fresnel reflection, from the unconnected ferrule of FP2 at $\sim 4.0\%$.

The deposited graphene layer is examined by Renishaw InVia Raman spectrometer, at 532 nm (2.33 eV) over a 10-s period and a grating value of 1800 lines/mm. The incident power and the depth of field are set at 5 mW and 1 μm , respectively. The charge coupled device (CCD) used together with the Raman spectrometer has a 100x objective lens and numerical aperture of 0.8, giving a spot size of 0.5 μm . The Raman spectrum of the deposited graphene is shown in Fig. 3, which exhibits the two intensity peaks at 1597 and 2684 cm^{-1} .

The peak at 1597 cm^{-1} corresponds closely to the expected G peak for graphene, which is usually at 1580 cm^{-1} . Similarly, the intense peak at 2684 cm^{-1} corresponds to the 2-D peak for graphene, which is typically at 2700 cm^{-1} [22], [23], indicating the desired graphene layer is present on the face of the fiber ferrule. Furthermore, the ratio of G to 2-D does not exceed 1, thus, indicating that a nearly single layer of graphene has been deposited, about two or three layers, whereas a multiple layers of graphene will result in a G to 2-D ratio of more than 1.

The spot image of the graphene layer, which complements the Raman spectra obtained, is shown in Fig. 4(a), while the inspection of the graphene layer on the face of the fiber ferrule is shown in Fig. 4(b).

The ferrule of FP1, which has the deposited graphene multilayer on its surface, is now connected to an FC/PC patchcord using an adaptor to form the SA assembly. The application of

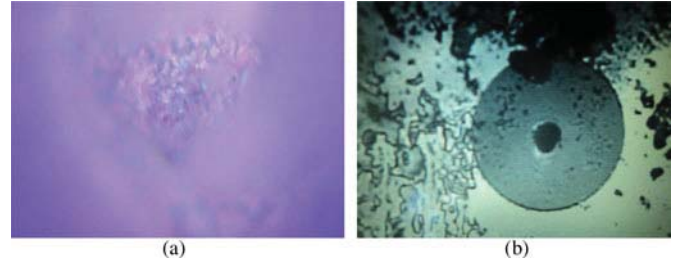


Fig. 4. (a) Spot image of the graphene layer, and (b) observation using an optical fiber scope, which shows the fiber ferrule with the graphene layer. The graphene layer is visible as the black area over what would be the core of the fiber. The oily residue, at the left hand and the edges of the image are the leftover traces of the N-methylpyrrolidone solution.

the SA in generating Q-switched and mode-locked pulses is detailed in the following sections.

IV. GENERATION OF Q-SWITCHED PULSES IN THE ZR-EDF LASER WITH A GRAPHENE-BASED SA

Q-switching allows for the development of pulsed fiber lasers with short pulsewidths and high pulse energies. Q-switched fiber lasers are typically employed where ultrafast pulses are not necessary, or where longer pulses would be more advantageous, such as in medical applications, range finding, and sensing [24]–[27]. Graphene-based SAs can be used in combination with highly doped Zr-EDFs to realize a compact Q-switched fiber laser, with pulsewidths of 4.6 μs and repetition rates of up to 50 kHz.

Fig. 5 shows the setup of a passively Q-switched Zr-EDF laser with a graphene-based SA. A 2-m long Zr-EDF is used as the active gain medium for the ring fiber laser, and is pumped by a 980-nm laser diode (LD) with a maximum operating power of approximately 100 mW. The 980-nm LD is configured to pump the Zr-EDF in a forward-pumping scheme, and is connected to the 980-nm port of a 980/1550 nm wavelength division multiplexer (WDM). The common output of the WDM is connected one end of the Zr-EDF. The other end of the Zr-EDF is connected to an optical isolator, which is used to force signal propagation in the clockwise direction only. The output of the isolator is in turn connected to a polarization controller (PC), which serves to control the polarization state of the propagating signal so as to optimize the signal output level. The PC is connected to a 90:10 fused coupler, with the 90% port connected to the SA assembly, which is responsible for generating the Q-switched pulses. Finally, the output of the SA is connected to the 1550-nm port of the fused coupler, thus completing the ring cavity. The 10% port of the fused coupler is used to extract a portion of the oscillating signal for analysis, and is connected to a Yokogawa AQ6317 optical spectrum analyzer (OSA) with a resolution of 0.02 nm for spectral measurements. For the purpose of analyzing the pulse train characteristics of the laser's output, a LeCroy 352A oscilloscope together with an optoelectronic (OE) converter is used in place of the OSA.

The optical spectrum of the Q-switched pulses obtained from the Zr-EDF laser, operating at a pump power of about 100 mW, is shown in Fig. 6(a). The output spectrum is obtained using

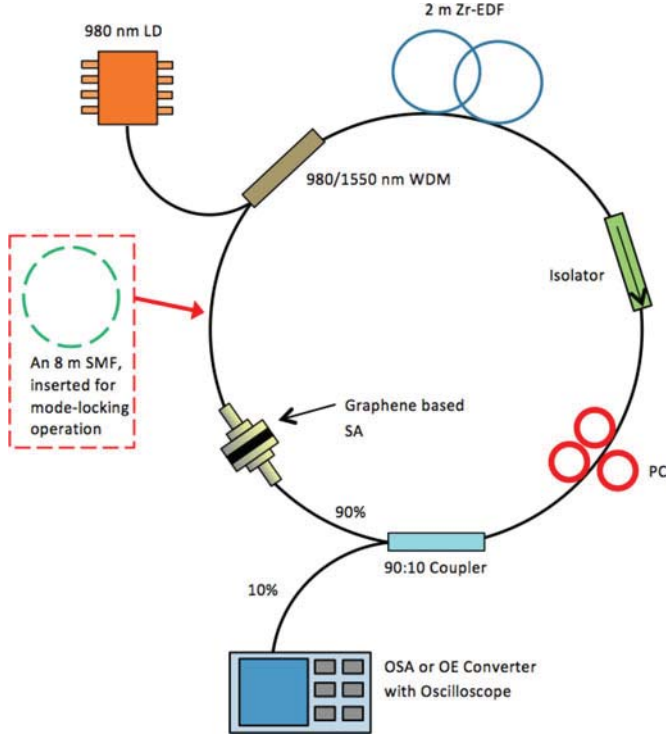


Fig. 5. Setup of the passively Q-switched Zr-EDF laser with a graphene based SA. The 8 m long SMF is added to the setup to allow the Zr-EDF laser to operate in the mode-locking regime, although will only be focused on in the later part of this manuscript.

the OSA, and shows a wide laser bandwidth, spanning from 1559.2 to 1562.7 nm at a power of -40 dBm. This gives the generated laser spectrum a bandwidth of approximately 3.5 nm, which can be attributed to multimode oscillations and cavity perturbations [28]. The laser peak is at 1560.8 nm, with a peak power of about -3.1 dBm and a linewidth of about 0.04 nm at -20 dBm. Fig. 6(b) shows the train of laser pulses obtained from the Q-switched Zr-EDF laser, using the OE converter and oscilloscope. Operating at the same pump power of 100 mW, a pulse train with a repetition rate of 50.1 kHz is obtained. The intensity of the peaks is almost constant at 15 mV, indicating that the output of the laser is adequately stable.

Fig. 7 shows the average output power against the pump power of the graphene-based Q-switched Zr-EDF laser. It can be seen that above a pump power of more than 50 mW, the average output power of the fiber laser responds almost linearly to the increase in the pump power, with an increments of about 0.15 mW for every 10 mW rise in pump power. The maximum average output power is approximately 0.9 mW, which is obtained at the highest pump power of 100 mW, while extrapolating the linear response of the laser gives a lasing threshold at about 48 mW. The Q-switching threshold is determined to be at 56 mW.

The pulse repetition rate and pulsewidth of the Q-switched Zr-EDF laser for different pump powers is shown in Fig. 8. The repetition rate is observed to increase almost linearly with the pump power, from 21.3 kHz at a pump power of 56 mW, to a maximum repetition rate of 50.1 kHz at 100 mW, with increasing between 3 and 7 kHz for every additional 10 mW

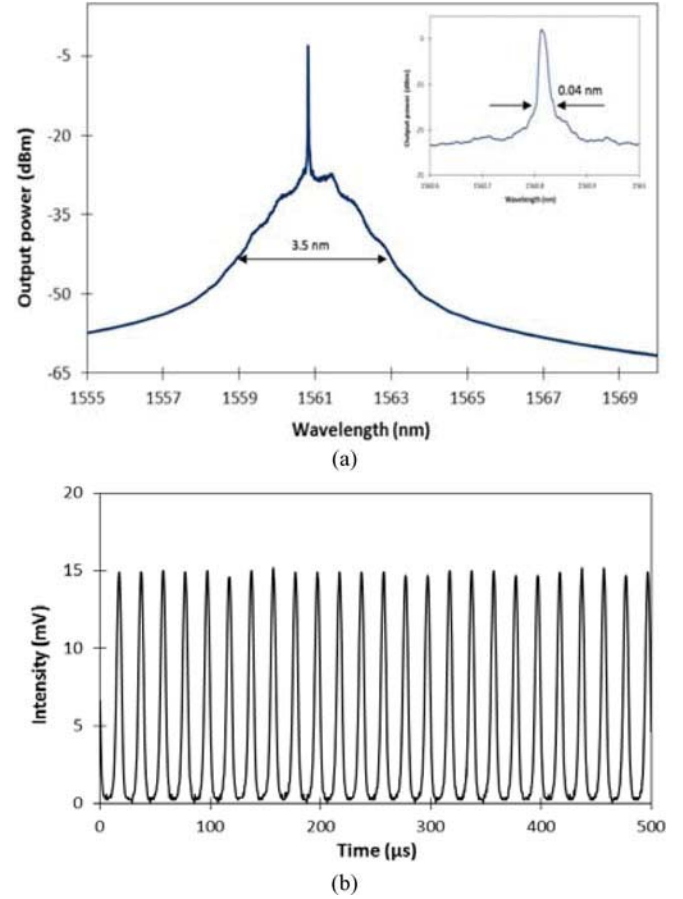


Fig. 6. (a) Output spectrum. (b) Output pulse train of the graphene based Q-switched Zr-EDF fiber laser taken at pump power of 100 mW.

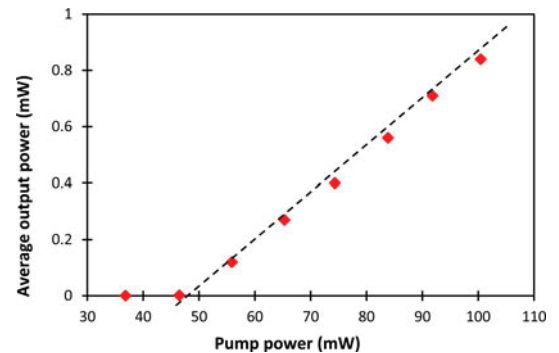


Fig. 7. Average output power against the pump power.

of pump power. It is expected that higher repetition rates can be obtained with higher pump powers; however, this work is limited by a maximum available pump power of 100 mW. The pulsewidth responds inversely to the pump power, as expected, decreasing from 11.1 to 4.6 μ s as the pump power increases from 56 to 100 mW.

The pulse energy and pulse peak power of the Zr-EDF's laser output is shown in Fig. 9. The pulse energy rises steeply from 5.6 to 13.4 nJ as the pump power changes from ~ 56 to ~ 74 mW. Above a pump power of 74 mW, however, the increase in the pump power becomes slower, rising from 15.3 nJ at a

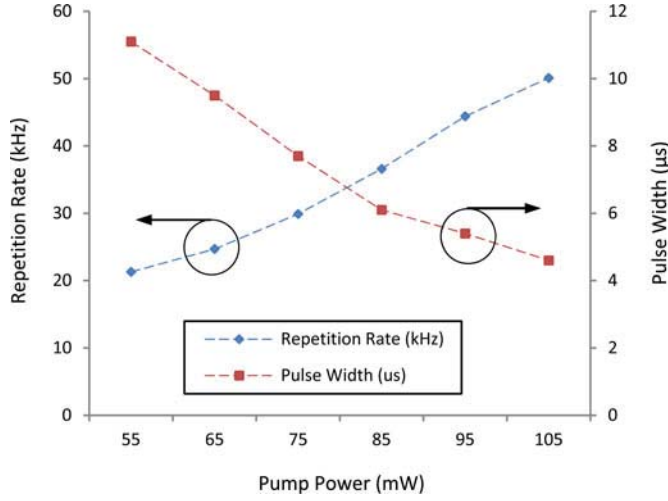


Fig. 8. Pulse repetition rate and pulsewidth against the pump power.

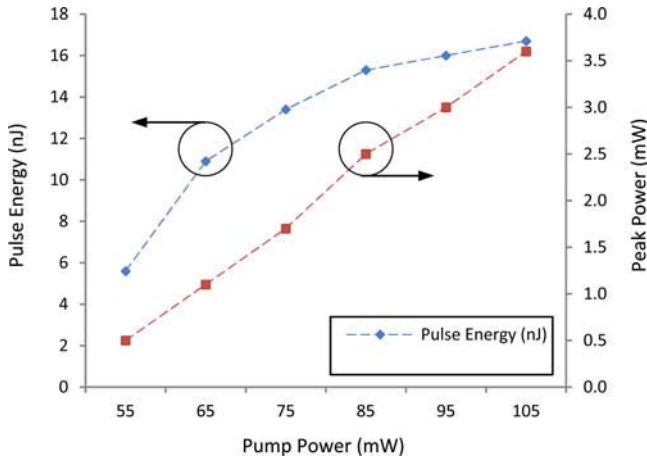


Fig. 9. Pulse energy and peak power against the pump power.

pump power of 84 mW to only 16.8 nJ at the highest pump power of 100 mW.

In the case of the peak power, it is observed to increase linearly with the pump power, from a minimum value of 0.5 mW and a maximum value of 3.6 mW as the pump power is changed from 56 to 100 mW. This gives an increment rate of about 0.6 mW in the peak power of the system for every 10 mW increase in the pump power.

V. GENERATION OF MODE-LOCKED PULSES IN THE ZR-EDF LASER WITH A GRAPHENE-BASED SA

Mode locked fiber lasers are able to generate ultrafast pulses of less than 1 ps, making them highly desirable for communications applications [11]. A passively mode-locked Zr-EDF laser with a graphene-based SA can be realized by slightly modifying the setup as shown in Fig. 5, whereby an 8-m long single mode fiber (SMF) is inserted in between the SA and the 1550-nm port of the WDM. This changes the GVD of the cavity. The Zr-EDF has a dispersion coefficient of $+28.45 \text{ ps}^2 \cdot \text{nm}^{-1} \cdot \text{km}^{-1}$, giving the cavity a GVD coefficient of $-36.86 \text{ ps}^2/\text{km}$. On the other hand, the dispersion coefficient of the SMF-28 is $+17 \text{ ps}^2 \cdot \text{nm}^{-1} \cdot \text{km}^{-1}$,

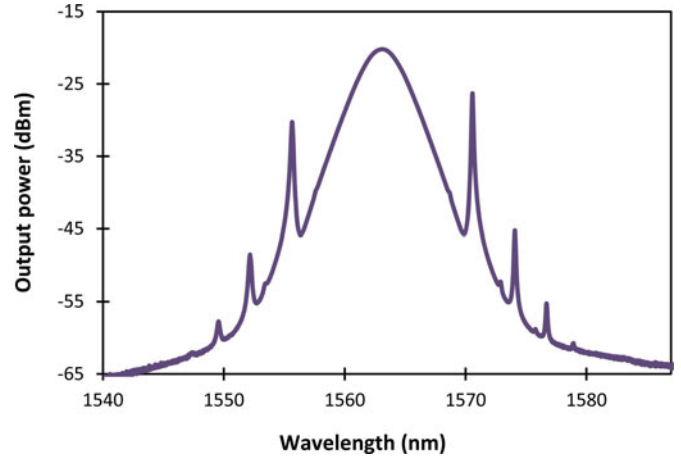


Fig. 10. Optical spectrum of the Zr-EDF mode-locked fiber laser at a pump power of 100 mW.

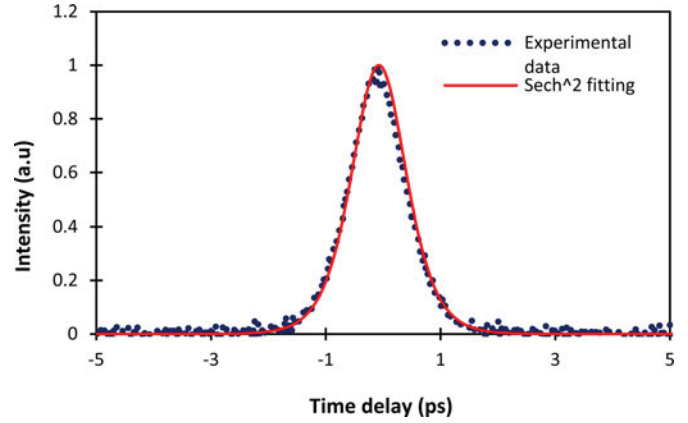
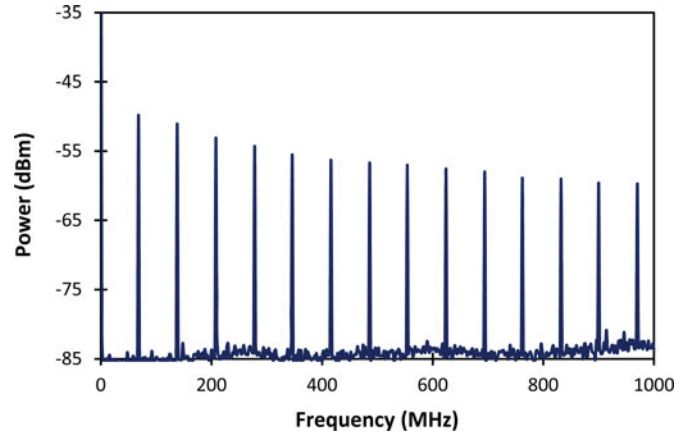
Fig. 11. Autocorrelation trace of the mode-locked pulse, with sech^2 fitting.

Fig. 12. RF spectrum of the mode-locked laser output measured with 1-GHz span.

giving a GVD coefficient of $-22.02 \text{ ps}^2 \cdot \text{km}$. With the addition of the 8-m long SMF, the total GVD for the entire cavity is now -0.294 ps^2 , taking into account the remaining SMF lengths in the cavity as well as the GVD of the Zr-EDF. This puts the cavity in the anomalous dispersion region, and allows the laser to operate in a soliton mode-locking regime. The optical spectrum

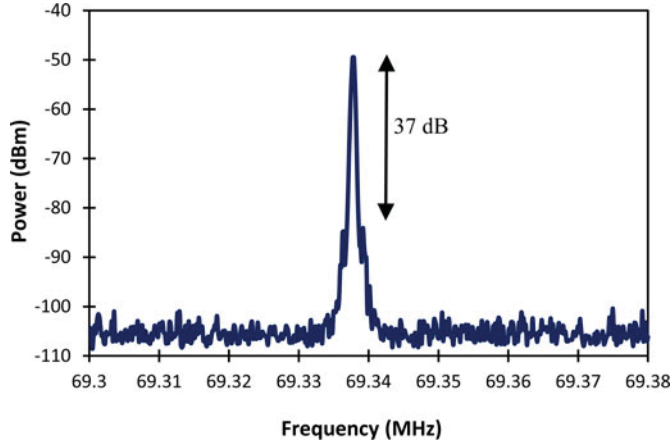


Fig. 13. RF spectrum at the fundamental repetition rate of 69.3 MHz with a 80-kHz frequency span and resolution of 300 Hz.

and pulse train of the generated pulses are analyzed by an OSA and an OE converter together with an oscilloscope. For the additional measurement of the mode-locked time characteristics, an Anair HAC-200 autocorrelator is used, while the spectrum of the output pulses in frequency domain is measured using an Anritsu MS2683A radio frequency spectrum analyzer (RFSa).

Soliton mode-locking behavior is observed in the Zr-EDF laser at a threshold pump power of 90 mW. As such, all subsequent measurements are taken at a pump power of 100 mW. Fig. 10 shows the optical spectrum of the mode-locked pulses, which spans from 1545 to 1580 nm with a 3-dB bandwidth of 3.6 nm at a central wavelength at 1563 nm. Multiple Kelly's sidebands are also observed, confirming that the system is operating in the soliton regime. No crease patterns or continuous wave (CW) lasing peaks are observed at the midpoint or at any other part of the output spectrum, further confirming that the laser is operating in the mode-locking regime. This is highly desirable, as the presence of CW components will affect the stability of the mode-locked pulses [29]. The formation of the Kelly's sidebands is attributed to the periodical perturbation of the intracavity [30], which confirms the attainment of the anomalous dispersion, soliton-like mode locking operation. At this power, the mode-locked pulses have an average output power of 1.6 mW, with a pulse energy of 23.1 pJ and peak power of 31.6 W. The repetition rate is 69.3 MHz, corresponding to a pulse spacing of around 14.5 ns in the pulse train.

Fig. 11 shows the second harmonic generation autocorrelation trace, with estimated pulse duration of 730 fs at the full-width half maximum (FWHM) point. The autocorrelation trace shows that the experimentally obtained values agree well with the theoretical sech^2 fitting, with no pulse breaking or pulse pair generation. A time-bandwidth product of 0.32 is obtained from the product 3 dB bandwidth of 3.6 nm (or 0.44 THz) and the pulse FWHM. The obtained value is slightly higher than the expected transform limit of 0.315.

Fig. 12 shows the mode-locked laser spectrum in the frequency domain, obtained from the RFSa. The output pulse is observed over a 1-GHz-span radio frequency (RF) spectrum, and is seen to be highly stable, with no Q-switching perturba-

tions. This is deduced from the evenly spaced frequency interval in the RF spectrum that is free from spectral modulation [31]. It can also be seen that the laser has achieved CW mode locking laser oscillation, due to the absence of low-repetition-rate modulations in the output pulse train that result in relaxation oscillations [32], [33]. The RF repetition rate of the pulse is approximately 69.3 MHz, agreeing well with the measurements obtained from the oscilloscope.

Fig. 13 shows the fundamental harmonic frequency of the mode-locked laser output at 69.3 MHz as measured with an 80-kHz frequency span and a resolution of 300 Hz. The measured RF spectrum indicates that the mode-locked laser output works in its fundamental regime, with the estimated peak-to-pedestal ratio being about 37 dB.

The generated pulses are stable and consistent, thus, giving the Zr-EDF laser a multitude of uses as either a Q-switched or mode-locked laser for practical applications.

VI. CONCLUSION

The application of graphene-based SAs in Q-switched and mode-locked Zr-EDF lasers is detailed. The Zr-EDF lasers are based on a 2-m long Zr-EDF with an active ion concentration of approximately 4320 ppm and has an absorption rate of 22.0 dBm at 978 nm as well as 58.0 dBm at 1550 nm. The graphene SA is fabricated by optical deposition of graphene flakes onto a fiber ferrule, which is then sandwiched against another fiber ferrule to form the SA. The Zr-EDF laser has a lasing threshold of 48 mW, and a Q-switching threshold of 56 mW. Q-switched pulses with a pulsewidth of 4.6 μs and a pulse energy and pulse peak power of 16.8 nJ and 3.6 mW, respectively. The repetition rate of the Q-switched pulses is approximately 50.1 kHz. When operating in the mode-locking regime, the Zr-EDF laser has a mode-locking threshold of 90 mW, with the generated pulses having an average output power, pulse energy and peak power of approximately 1.6 mW, 23.1 pJ, and 31.6 W, respectively, as well as a pulsewidth of 730 fs. The repetition rate of the pulses is 69.3 MHz, corresponding to a channel spacing of 14.5 ns in the pulse train. The generated pulses are stable and consistent, and allow them to be confidently deployed in multiple practical applications.

REFERENCES

- [1] J. Clowes, "Next generation light sources for biomedical applications.," *Opt. Photon.*, vol. 3, pp. 36–38, 2008.
- [2] L. Shah and M. E. Fermann, "High power femtosecond fiber chirped pulse amplification system for high speed micromachining," *J. Las. Micro/Nanoeng.*, vol. 1, no. 3, pp. 176–180, 2006.
- [3] H. Ohta, S. Nogiwa, N. A. Oda, and H. Chiba, "Highly sensitive optical sampling system using timing-jitter-reduced gain-switched optical pulse," *Electron. Lett.*, vol. 33, no. 25, pp. 2142–2143, 1997.
- [4] T. R. Schibli, K. Minoshima, F. L. Hong, H. Inaba, A. Onae, H. Matsumoto, I. Hartl, and M. E. Fermann, "Frequency metrology with a turnkey all-fiber system," *Opt. Lett.*, vol. 29, no. 21, pp. 2467–2469, 2004.
- [5] W. Seitz, R. Ell, U. Morgner, T. R. Schibli, F. X. Kärtner, M. J. Lederer, and B. Braun, "All optical active mode locking with a nonlinear semiconductor modulator," *Opt. Lett.*, vol. 27, no. 24, pp. 2209–2211, 2002.
- [6] K. Kieu and M. Mansuripur, "Active Q-switching of a fiber laser with a microsphere resonator," *Opt. Lett.*, vol. 31, no. 24, pp. 3568–3570, 2006.

- [7] Y. M. Chang, J. Lee, Y. M. Jhon, and J. H. Lee, "Active Q-switching in an erbium-doped fiber laser using an ultrafast silicon-based variable optical attenuator," *Opt. Exp.*, vol. 19, no. 27, pp. 26911–26916, 2011.
- [8] E. A. Kuzin, B. I. Escamilla, D. E. Garcia-Gomez, and J. W. Haus, "Fiber laser mode locked by a Sagnac interferometer with nonlinear polarization rotation," *Opt. Lett.*, vol. 26, no. 20, pp. 1559–1561, 2001.
- [9] O. Okhotnikov, A. Grudinin, and M. Pessa, "Ultra-fast fibre laser systems based on SESAM technology: New horizons and applications," *New J. Phys.*, vol. 6, no. 177, 2004.
- [10] G. Steinmeyer, D. H. Sutter, L. Gallmann, N. Matuschek, and U. Keller, "Frontiers in ultrashort pulse generation: Pushing the limits in linear and nonlinear optics," *Science*, vol. 286, no. 5444, pp. 1507–1512, 1999.
- [11] Z. Sun, T. Hasan, F. Torrisi, D. Popa, G. Privitera, F. Wang, F. Bonaccorso, D. M. Basko, and A. C. Ferrari, "Graphene mode-locked ultrafast laser," *ACS Nano*, vol. 4, no. 2, pp. 803–810, 2010.
- [12] F. Bonaccorso, Z. Sun, T. Hasan, and A. C. Ferrari, "Graphene photonics and optoelectronics," *Nat. Photon.*, vol. 4, no. 9, pp. 611–622, 2010.
- [13] Q. Bao, H. Zhang, Y. Wang, Z. Ni, Y. Yan, Z. X. Shen, K. P. Loh, and D. Y. Tang, "Atomic-layer graphene as a saturable absorber for ultrafast pulsed lasers," *Adv. Funct. Mater.*, vol. 19, no. 19, pp. 3077–3083, 2009.
- [14] Z. Sun, D. Popa, T. Hasan, F. Torrisi, F. Wang, E. J. R. Kelleher, J. C. Travers, V. Nicolosi, and A. C. Ferrari, "A stable, wideband tunable, near transform-limited, graphene-mode-locked, ultrafast laser," *Nano Res.*, vol. 3, no. 9, pp. 653–660, 2010.
- [15] Y. Yap, R. D. La Rue, C. Pua, S. Harun, and H. Ahmad, "Graphene-based Q-switched pulsed fiber laser in a linear configuration," *Chin. Opt. Lett.*, vol. 10, no. 4, p. 041405, 2012.
- [16] D. M. Gill, L. McCaughan, and J. C. Wright, "Spectroscopic site determinations in erbium-doped lithium niobate," *Phys. Rev. B Condens. Mater.*, vol. 53, no. 5, pp. 2334–2344, 1996.
- [17] E. Snoeks, P. G. Kik, and A. Polman, "Concentration quenching in erbium implanted alkali silicate glass," *Opt. Mater.*, vol. 5, no. 3, pp. 159–167, 1996.
- [18] H. Ahmad, K. Thambiratnam, M. C. Paul, A. Z. Zulkifli, Z. A. Ghani, and S. W. Harun, "Fabrication and application of zirconia-erbium doped fibers," *Opt. Mater. Exp.*, vol. 2, no. 12, pp. 1690–1701, 2012.
- [19] H. Ahmad, M. C. Paul, N. A. Awang, S. W. Harun, M. Pal, and K. Thambiratnam, "Four-wave-mixing in zirconia-yttria-aluminum erbium codoped silica fiber," *J. Euro. Opt. Soc.—Rap. Public.*, vol. 7, p. 12011, 2012.
- [20] M. C. Paul, G. Sobon, J. Sotor, K. M. Abramski, J. Jagiello, R. Kozinski, L. Lipinska, and M. Pal, "A graphene-based mode-locked nano-engineered zirconia-yttria-aluminosilicate glass-based erbium-doped fiber laser," *Las. Phys.*, vol. 23, no. 3, p. 035110, 2013.
- [21] W. J. Cao, H. Y. Wang, A. P. Luo, Z. C. Luo, and W. C. Xu, "Graphene-based, 50 nm wide-band tunable passively Q-switched fiber laser," *Las. Phys. Lett.*, vol. 9, no. 1, pp. 54–58, 2012.
- [22] A. C. Ferrari, J. C. Meyer, V. Scardaci, C. Casiraghi, M. Lazzeri, F. Mauri, S. Piscanec, D. Jiang, K. S. Novoselov, S. Roth, and A. K. Geim, "Raman spectrum of graphene and graphene layers," *Phys. Review Lett.*, vol. 97, no. 18, p. 187401, 2006.
- [23] D. Graf, F. Molitor, K. Ensslin, C. Stampfer, A. Jungen, C. Hierold, and L. Wirtz, "Spatially resolved Raman spectroscopy of single and few layer graphene," *Nano Lett.*, vol. 7, no. 2, pp. 238–242, 2007.
- [24] H. Ahmad, M. Z. Zulkifli, F. D. Muhammad, A. Z. Zulkifli, and S. W. Harun, "Tunable graphene-based Q-switched erbium-doped fiber laser using fiber Bragg grating," *J. Mod. Opt.*, vol. 60, no. 3, pp. 202–212, 2013.
- [25] L. Q. Zhang, Z. Zhuo, J. X. Wang, and Y. Z. Wang, "Passively Q-switched fiber laser based on graphene saturable absorber," *Las. Phys.*, vol. 22, no. 2, pp. 433–436, 2012.
- [26] D. Popa, Z. Sun, T. Hasan, F. Torrisi, F. Wang, and A. C. Ferrari, "Graphene Q-switched, tunable fiber laser," *Appl. Phys. Lett.*, vol. 98, no. 7, pp. 073106-1–073106-3, 2011.
- [27] J. Y. Huang, S. C. Huang, H. L. Chang, K. W. Su, Y. F. Chen, and K. F. Huang, "Passive Q-switching of Er-Yb fiber laser with semiconductor saturable absorber," *Opt. Exp.*, vol. 16, no. 5, pp. 3002–3007, 2008.
- [28] H. Ahmad, F. D. Muhammad, M. Z. Zulkifli, and S. W. Harun, "Graphene-oxide-based saturable absorber for all-fiber Q-switching with a simple optical deposition technique," *IEEE Photon. Technol. Lett.*, vol. 4, no. 6, pp. 2205–2213, 2012.
- [29] G. Sobon, J. Sotor, and K. M. Abramski, "All-polarization maintaining femtosecond Er-doped fiber laser mode-locked by graphene saturable absorber," *Las. Phys. Lett.*, vol. 9, no. 8, pp. 581–586, 2012.
- [30] M. L. Dennis and I. N. Duling, "Experimental study of sideband generation in femtosecond fiber laser," *IEEE J. Quantum Electron.*, vol. 30, no. 6, pp. 1469–1477, 1994.
- [31] C. Honninger, R. Paschotta, F. M. Genoud, M. Moser, and U. Keller, "Q-switching stability limits of continuous wave passive mode locking," *J. Opt. Soc. Am. B.*, vol. 16, no. 1, pp. 46–56, 1999.
- [32] F. Wang, A. G. Rozhin, V. Scardaci, Z. Sun, F. Hennrich, I. H. White, W. I. Milne, and A. C. Ferrari, "Wideband-tunable, nanotube mode-locked, fibre laser," *Nat. Nanotechnol.*, vol. 3, pp. 738–742, 2008.
- [33] U. Keller, K. J. Weingarten, F. X. Kärtner, D. Kopf, B. Braun, I. D. Jung, R. Fluck, C. Hönninger, N. Matuschek, and J. Aus der Au, "Semiconductor saturable absorber mirrors (SESAMs) for femtosecond to nanosecond pulse generation in solid-state lasers," *IEEE J. Sel. Top. Quant. Electron. (JSTQE)*, vol. 2, no. 3, pp. 435–453, 1996.



Kavintheran Thambiratnam received the B.Sc. and M.Sc. degrees in physics from the University of Malaya, Kuala Lumpur, Malaysia and is currently working toward the Ph.D. degree in photonics at the same institution. He is the author of more than 20 publications in international journals and conference proceedings. His research interests include fiber amplifiers and fiber-optic sensors, with a particular interest in the applications of optical sensors toward biological applications.



Sciences, Malaysia.

Harith Ahmad received the Ph.D. degree in laser technology from the University of Wales, Swansea, U.K., in 1983. He is currently a Professor with the Department of Physics, University of Malaya, Kuala Lumpur, Malaysia, where he has actively pursued research activities in the field of photonics since 1983. He is the author of more than 300 professional papers in international journals and conference proceedings. His research interests include lasers, fiber-based devices for telecommunications, and fiber-based sensor devices. Dr. Ahmad is a Fellow of the Academy of



Farah Diana Muhammad received the B.Sc. degree in pure science (physics) from the University of Technology, Malaysia, in 2011. She is currently working toward the Ph.D. degree at Photonics Research Centre, University of Malaya, Kuala Lumpur, Malaysia, where she is working in the field of the photonics applications of graphene, including the mode locking, supercontinuum, Q-switching, and single longitudinal mode fiber laser.



Mohd. Zamani Zulkifli received the B.Sc. degree in instrumentation physics from University Putra Malaysia, Selangor, Malaysia, in 2005 and subsequently the M.Sc. and Ph.D. degrees from the University of Malaya, Kuala Lumpur, Malaysia. He has authored a number of publications in international journals and has also presented his work at many conferences. His research interests include instrumentation and fiber amplifiers and fiber-optic sensors.



Ahmad Zarif Zulkifli received the Bachelor's degree in electrical and electronics engineering from Universiti Teknologi Malaysia, Johor Bahru, Malaysia, in 2008, and subsequently obtained the Master's degree in telecommunications engineering from the University of Malaya, Kuala Lumpur, Malaysia, by 2011. He is currently working toward the Ph.D. degree in the same research Centre. His research interests include passively pulsed fibers using saturable absorbers such as graphene and carbon nanotubes.



Mukul Chandra Paul received the M.Sc. degree in inorganic chemistry from Burdwan University, Burdwan, India, in 1989 and the Ph.D. degree in the field of development of radiation sensitive fibers for evaluation of their radiation response behavior at room temperature from Central Glass and Ceramic Research Institute (CGCRI), Kolkata, India, in 2003. Since 1997, he has been a Research Scientist with the Fiber Optics and Photonics division of CGCRI. He has published around 100 papers in international scientific journals/conferences, authored five patents and six book chapters. His research interests include development of different specialty optical fibers through material composition of the doping host based on the chemistry of glass and ceramic.

Sulaiman Wadi Harun, photograph and biography not available at the time of publication.